A 230 GHz Focal Plane Array Using a Wide IF Bandwidth SIS Receiver

John Daniel Garrett

New College

University of Oxford

A thesis submitted for the degree of

Doctor of Philosophy

Trinity 2018

The test of the machine is the satisfaction it gives you. There isn't any other test. If the machine produces tranquility it's right. If it disturbs you it's wrong until either the machine or your mind is changed.

— Robert M. Pirsig
Zen and the Art of Motorcycle Maintenance

Abstract

Superconductor-Insulator-Superconductor (SIS) mixers offer the best noise properties of any heterodyne mixing technique at millimetre wavelengths. In astronomy, they are used for sensitive spectroscopy, which is vital for understanding the properties of the cold interstellar medium, including regions of star formation activity. Modern SIS receivers have noise properties that are $\sim$3 times the quantum limit, and it is now becoming increasingly difficult to lower the noise properties any further. In this thesis, I investigate two techniques that extend the capability of SIS receivers.

The first technique is extending the instantaneous bandwidth of the receivers, i.e., the intermediate frequency bandwidth (IFBW). For spectral line sources, wide IFBW expands the survey depth to allow multiple emission lines to be observed simultaneously. Here, I present a new SIS mixer device at 230 GHz. The planar circuit was minimised to reduce any parasitic capacitances that may limit the IFBW. Experimentally, the device provides excellent noise temperatures down to 36 K and an IFBW extending from approximately 0–11 GHz. Simulation software was developed to better understand the performance of this device, and it suggests that the IFBW can be extended to higher frequencies if the IF measurement chain is upgraded.

The second technique that I investigate is increasing the number of receivers in the focal plane of the receiver, i.e., adding more pixels. There are many challenges involved in this task including how to fit multiple receivers into a small space, how to properly cool the receiver, and how to deliver the local-oscillator signal. Here, I present a new 1×4 focal plane array. This array is acting as a demonstrator for a new array architecture that can be expanded into many more pixels in the future. It uses cascaded waveguide power splitters to divide the local-oscillator signal, and then waveguide directional couplers to combine the LO with the astronomical signals.

Finally, I present CO(J=1$\rightarrow$0) measurements from 34 galaxies in the 5MUSES survey. These measurements trace the amount of cold molecular gas present in these galaxies. By comparing these measurements to other metrics that trace star formation activity (e.g., infrared luminosity), I was able to form empirical relationships between the observed quantities. I also combined these results with other star formation studies from nearby and high redshift galaxies to form scaling relationships spanning a large fraction of cosmic time.

Statement of Originality

I completed the work presented in this thesis under the supervision of Prof. Ghassan Yassin at the University of Oxford between October 2014 and August 2018. Everything in this thesis is my own original work, except where stated otherwise. I have not submitted any of this work for any other degree, diploma or qualification at any other institution of higher education.

The design of the 230 GHz receiver in Chapter 3 was initially developed by Dr. Boon Kok Tan. This receiver has been presented in: (J. Garrett, *et al.* [1]), and (J. Garrett, *et al.* [2]).

The design of the array block in Chapter 5 was initially developed by Dr. Jamie Leech. The array has been presented in: (J. Leech, *et al.* [3]), and (J. Garrett, *et al.* [4]).

The work in Chapter 6 was completed under the supervision of Dimitra Rigopoulou and in collaboration with Isabella Cortzen and Georgios Magdis from the University of Copenhagen. The work that we completed together been submitted for publication in: (I. Cortzen, *et al.* [5]).

John Garrett
August 2018

Acknowledgements

First and foremost, I would like to thank my supervisor, Prof. Ghassan Yassin. Throughout my DPhil project, your guidance helped me to overcome obstacles and explore new ideas. Thank you for believing in me and giving me the chance to come work in your group.

I would also especially like to thank Dr. Boon Kok Tan. You have been an excellent mentor for me over the past 4 years. Whether troubleshooting in the lab or debating new theories over a pint, thank you for helping me develop my ideas and grow as a researcher.

Within our group, I thank Jamie and Sumedh for their feedback and patient explanations. I also owe Rik a massive thank you for helping me on countless occasions setting up the experiments in this thesis.

I thank Garret and Ashling (a.k.a., Viper and Jester) for everything that they do behind the scenes. As soon as I met you two at the open day, I knew that I would be in good hands.

I would also like to thank Rupe and Alex for all the bops, guest nights, gym sessions, office parties and all-around good times over the last few years. There are too many cherished memories to think of just one, but thank you for your friendship. Additionally, I thank Andre for our dark jokes, Wednesday lunches and video games in the MCR.

I am very grateful to my family for everything that they have done to get me to where I am today. I thank my parents for their life-long encouragement and support, and I thank my brother for the fun trips we've recently had in Italy, Switzerland and Devon. Good luck on your own PhD!

Finally, I owe Dani so much for her love and support. Between proofreading papers, dealing with my neurotic behaviour while I've been writing this thesis, and moving across the world with me; thank you for everything.

Contents

List of Figures

List of Tables

Chapter 1

Introduction

In this thesis, we investigate new techniques to increase the sensitivity of Superconductor/Insulator/Superconductor (SIS) receivers. These receivers are commonly used in astronomy for high resolution spectroscopy at frequencies between ∼100 GHz and ∼1.3 THz. Among other applications, these measurements are vital for studying the emission lines from cold molecular gas in the interstellar medium. Here, we present two new SIS receiver projects centred around 230 GHz. The first is an SIS receiver with wide instantaneous bandwidth, which allows multiple emission lines to be observed simultaneously. The second is an array of SIS receivers, which allows for more pixels to be contained within a single telescope, thereby increasing the mapping speed and field-of-view. In addition to this work, we also present observations of molecular gas in intermediate redshift galaxies, i.e., galaxies that are approximately 300 million to 5 billion light-years away.

1.1 Millimetre-wave astronomy

In the coldest regions of the interstellar medium, there are dense clouds of molecular gas and dust. Many of these clouds are so cold that they radiate no light in the visible spectrum and the dust blocks the light from background stars (e.g., Fig. 1.1a). The largest clouds, known as *Giant Molecular Clouds* (GMCs), can extend up to ∼300 light-years in diameter with masses up to $\sim 10^6$ times the mass of our sun. All stars, including our Sun, were likely born deep inside GMCs as massive clumps of gas collapsed due to their own gravity. This process is seen in some nearby GMCs, including the Eagle Nebula shown in Fig. 1.1b. Then, as nuclear fusion begins in the cores of the nascent stars, the stellar radiation illuminates the GMC, ionises the surrounding gas and destroys the stellar nursery.

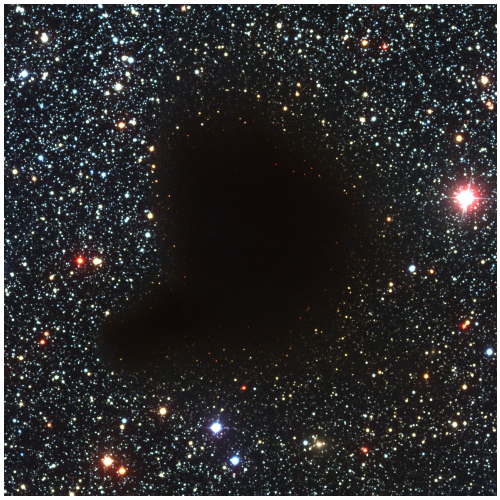

(a) An image of a nearby molecular cloud (Barnard 68) taken with the VLT telescope[1]. The centre of the cloud blocks all of the visible light from the background stars.

(b) An image of the Eagle Nebula taken with the Hubble Space Telescope[1]. The GMC that originally formed the young stars is now being destroyed by intense stellar radiation.

Figure 1.1: Dense clouds of molecular gas and dust.

Before the young stars illuminate the molecular gas and disassociate it into its atomic form, the gas is completely dark in the visible spectrum. To properly study GMCs, the molecular gas has to be observed directly. This is done by measuring the spectral emission lines from the molecular gas, which mostly appear at millimetre and submillimetre wavelengths[2] (mm-wave and submm-wave, respectively). While molecular hydrogen (H_2) is the most abundant molecule, it lacks a permanent dipole moment. This then means that it requires very high excitation temperatures ($T \gtrsim 300$ K) to radiate any emission lines. These temperatures are unattainable deep inside GMCs where the ambient temperature is close to $T \sim 10$ K. Instead, carbon monoxide (CO) is used to trace the molecular gas because CO is both abundant and easily excited at low temperatures. (The first few emission lines of CO and H_2 are plotted in Fig. 1.2 along with black body radiation from cold dust at $T \sim 10$ K.) By measuring the spectral profile of CO and other molecules, we can then infer the physical and chemical properties of the molecular gas, which is vital for studying GMCs, star formation, and galactic evolution.

[1]Credit for Fig. 1.1a: ESO.
Credit for Fig. 1.1b: NASA, ESA, and the Hubble Heritage Team (STScI/AURA).

[2]Here, the millimetre-wavelength spectrum is defined as electromagnetic radiation with wavelengths between $1 < \lambda < 10$ mm (or frequencies between $30 < \nu < 300$ GHz), and the submillimetre wavelength spectrum is defined as wavelengths between $0.1 < \lambda < 1$ mm (or frequencies between $0.3 < \nu < 3$ THz).

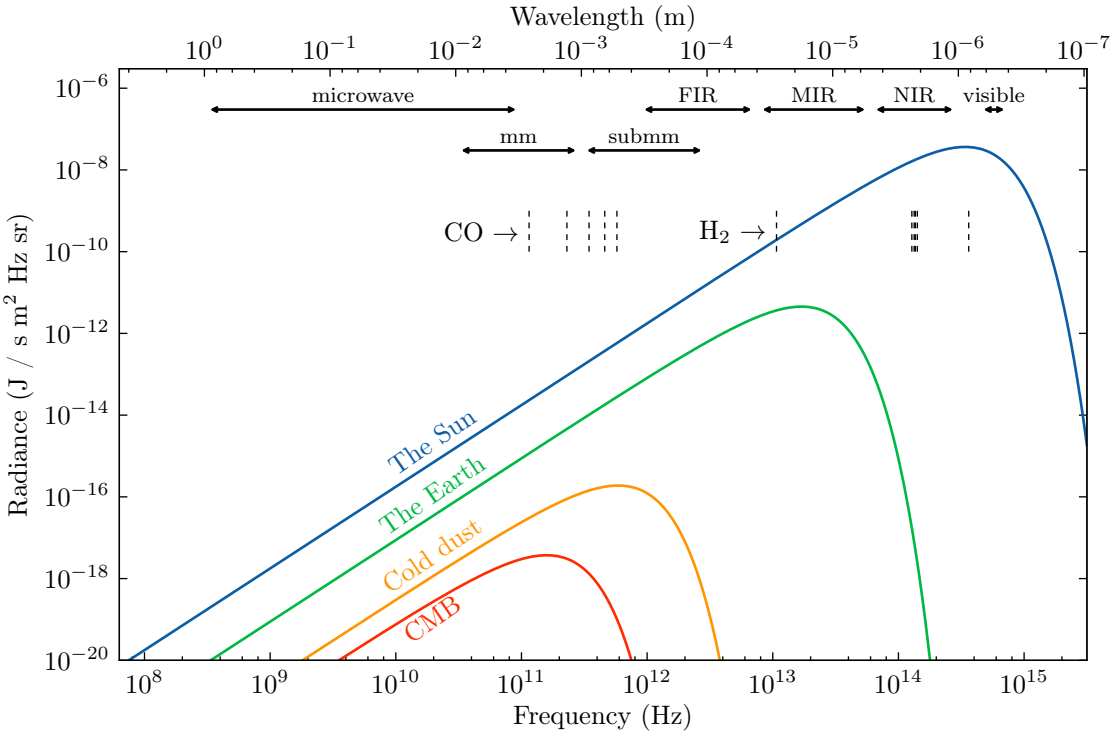

Figure 1.2: Black body radiation that approximately corresponds to the Sun (T∼5,800 K), the Earth (T∼288 K), cold dust (T∼10 K), and the cosmic microwave background (CMB; T∼2.7 K). The first five CO(J+1→J) rotational lines are also plotted along with five low energy H_2 emission lines. Different frequency bands are labelled including the microwave (0.3–300 GHz), millimetre-wave (mm-wave; 30–300 GHz), submillimetre-wave (submm-wave; 0.3–3 THz), far infrared (FIR; 0.9–7.5 THz), mid-infrared (MIR; 7.5–60 THz), near infrared (NIR; 60–300 THz), and visible light (430–770 THz) bands.

Observing at millimetre wavelengths, however, is challenging because the astronomical signals are typically very weak, partially attenuated by water vapour in our atmosphere (e.g., Fig. 1.3), and easily obscured by thermal noise in the receiver. For these reasons, millimetre-wave telescopes are built at high elevations with receivers that operate at temperatures close to absolute zero. The receivers also require extremely high spectral resolution[3], on the order of $R \equiv \nu/\Delta\nu \sim 10^3$–$10^8$, to measure the profile of the spectral lines. This is necessary because the molecular lines are very narrow and they often exist within crowded spectra. High spectral resolution allows us to distinguish between the individual lines, which may vary greatly in relative power, and to view the structural information contained within their profiles. For example, if we measure the emission line from a gas in a distant rotating galaxy, the profile will exhibit a double-horned feature due to the Doppler shift. This can be used to

[3]Spectral resolution is defined as: $R \equiv \nu/\Delta\nu$ where ν is the centre frequency and $\Delta\nu$ is the frequency resolution, i.e., the width of the smallest frequency channel.

determine the radius of the galaxy, but only if the emission line is sampled with an adequate spectral resolution.

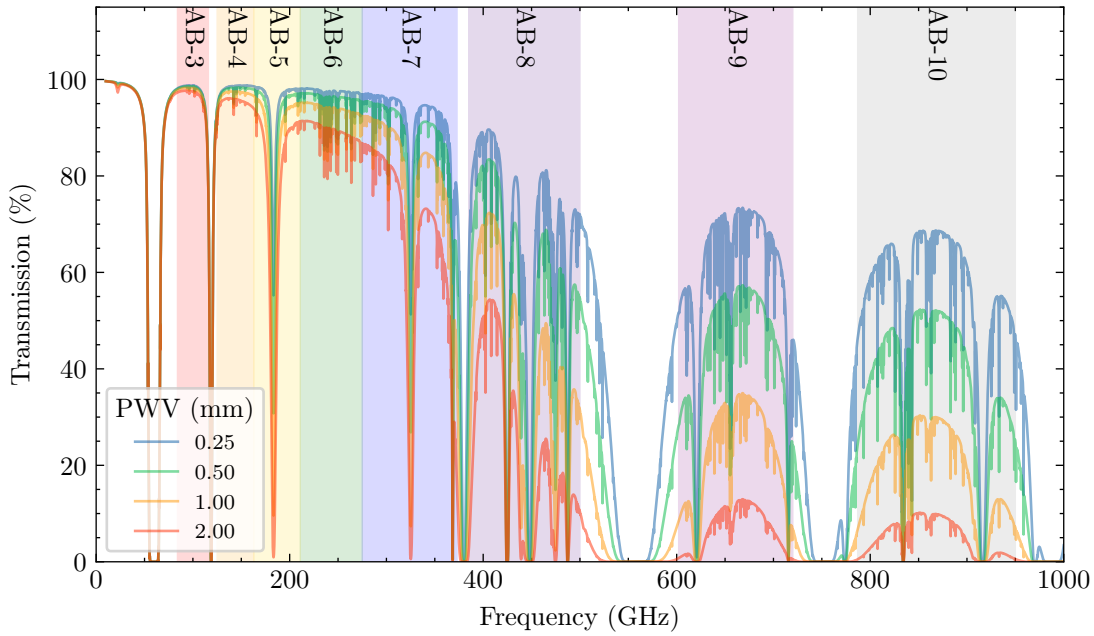

Figure 1.3: Atmospheric transmission at the site of the Atacama Large Millimeter Array (ALMA) on Llano de Chajnantor (elevation: 5,040 m). The transmission depends heavily on the precipitable water vapour (PWV). At this site, the average PWV is ∼1 mm, but it drops below 0.5 mm for around 25% of the year. The ALMA frequency bands (AB) are labelled at the top of the figure. This data was downloaded from the ALMA Science Portal (online: https://almascience.eso.org/about-alma/atmosphere-model).

In general, there are two categories of mm-wave receivers: bolometers, which measure the total incident power over a range of frequencies; and heterodyne receivers, which are able to measure the amplitude and phase of the signal as a function of frequency. Bolometers can be used in conjunction with diffraction gratings or Fabry-Pérot spectrometers for resolutions up to $R \sim 10^3$, but higher resolution is only really possible through coherent down-conversion with heterodyne mixers. These mixers shift the spectral content of the astronomical signals down to a lower frequency, while also preserving the phase information. Then, once down-converted, the signals can be digitally sampled at any spectral resolution, typically $R \sim 10^3$–10^8, using standard electronics.

In addition to high spectral resolution, heterodyne mixing also has the added benefit that it can be used for *aperture synthesis interferometry*. This allows multiple telescopes to act together, where the effective diameter of the primary mirror is

the largest separation distance between any two telescopes, i.e., the maximum baseline. Well-known mm-wave interferometers include the Submillimeter Array (SMA) in Hawaii, the Northern Extended Millimeter Array (NOEMA) in the French Alps, and the Atacama Large Millimeter/submillimeter Array (ALMA) in the Chilean Andes. Out of these, ALMA is by far the largest and the most sensitive. It consists of 66 radio dishes spread across the Chajnantor plateau at an elevation of 5,040 m. The maximum baseline of ALMA is ∼15 km, which allows it to achieve extremely high angular resolution, on the order of ∼30 milliarcseconds (mas). Two example of images taken by ALMA in its maximum baseline configuration are shown in Fig. 1.4. The first is Arp 220, which is the closest known *ultra-luminous infrared galaxy* (ULIRG), and the second is the protoplanetary disk HL Tau.

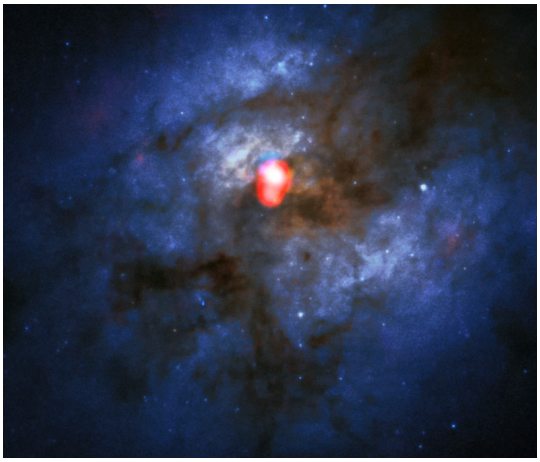

(a) Arp 220[4]: the closest known ULIRG. Red is from ALMA at λ=2.6 mm, and blue/green is from Hubble. ALMA has been vital for studying the nucleus of this galaxy (e.g., [6–8]), which is completely obscured by dust in optical wavelengths.

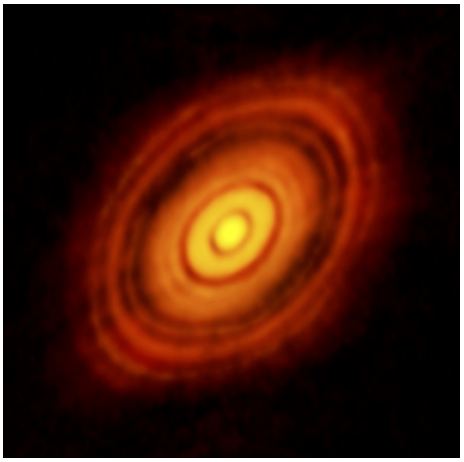

(b) HL Tau: a protoplanetary disk. The young star (age $\leq$1−2 Myr) is surrounded by a ∼140 AU diameter disk. The dark bands could be caused by planets forming in the disk, but this is an ongoing debate. (Credit: ALMA Partnership, *et al.* [9].)

Figure 1.4: High angular resolution images taken with ALMA.

Beyond "local" interferometry, the data from multiple telescopes from around the world can also be combined through *very long baseline interferometry* (VLBI). Then, the maximum baseline is only limited by Earth's diameter (∼12, 734 km). Examples at radio frequencies include the Very Large Baseline Array (VLBA) and the European VLBI Network (EVN), which combine some of the largest radio telescopes in the world (e.g., the Effelsberg 100-m Radio Telescope in Germany, the Lovell Telescope in the

[4]Credit for Fig. 1.4a: ALMA(ESO/NAOJ/NRAO)/NASA/ESA and The Hubble Heritage Team (STScI/AURA).

U.K., the Arecibo Observatory in Puerto Rico, and the Green Bank Telescope in West Virginia). At millimetre wavelengths, the most ambitious VLBI network is the Event Horizon Telescope (EHT). This network is combining almost all of the major mm-wave telescopes in an attempt to resolve the event horizon of a supermassive black hole (SMBH). Two candidates for this telescope are the SMBH at the centre of our Milky Way (Sgr A*) and the SMBH at the centre of the supergiant elliptical galaxy M87. Of these two, Sgr A* has a slightly larger angular diameter at 53 microarcseconds (µas), but the SMBH in M87 is not much smaller at 22 µas, despite being much farther away. As seen in Fig. 1.5, the EHT network has the highest angular resolution of any telescope ever built. To achieve a similar resolution at optical wavelengths would require a 3.5 km baseline, which is impossible with current technology.

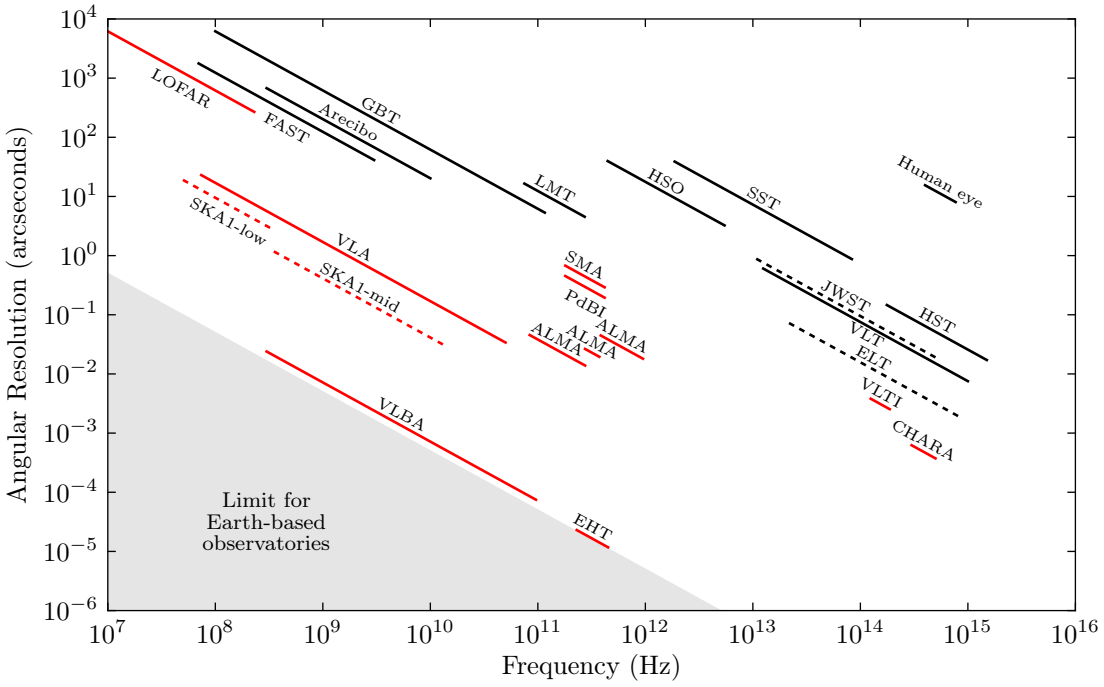

Figure 1.5: The angular resolution of various telescopes and interferometers. Current observatories are shown as black lines, observatories under construction are shown as dashed lines, and interferometers are shown in red. For single dish telescopes, the angular resolution was calculated as λ/D where D is the diameter of the primary mirror. For interferometers, the angular resolution was calculated as λ/B where B is the maximum baseline of the array. This is highly idealised and does not take into account other systematic effects. Note that ALMA is divided into 3 sections because the maximum baseline depends on the frequency band (using values from the ALMA Cycle 5 Technical Handbook [10]).

1.2 Heterodyne mixing

In astronomy, heterodyne mixers are operated by combining the signal-of-interest at frequency ω_{RF} with the pure sinusoidal signal from a local-oscillator (LO) at frequency ω_{LO}. Provided that the mixer has a non-linear response, a beat frequency at $|\omega_{\mathrm{RF}} - \omega_{\mathrm{LO}}|$ is generated, known as the intermediate frequency (IF) signal. A simple block diagram of this process is shown in Fig. 1.6a. As previously discussed, down-conversion is required in the case of mm-wave astronomy because the frequency of the astronomical signals is too high to sample directly. After down-conversion, however, the frequency of the IF signal is low enough that it can be amplified, filtered and injected into a digital spectrometer.

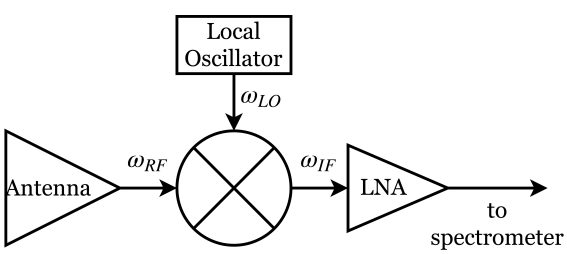

(a) A block diagram of a typical mm-wave heterodyne receiver. The signal-of-interest ω_{RF} mixes with the local-oscillator signal ω_{LO} to produce the intermediate frequency signal ω_{IF}. The IF signal power is amplified using a low-noise amplifier (LNA) before passing on to the rest of the IF circuit.

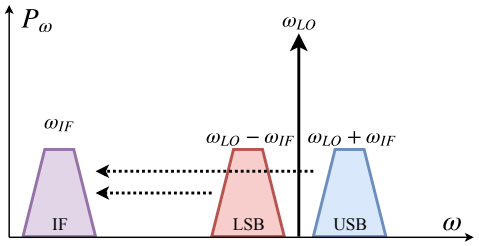

(b) The spectrum resulting from dual sideband (DSB) down-conversion. The upper sideband (USB; blue) and lower sideband (LSB; red) are down-converted to the same IF spectrum (purple).

Figure 1.6: Heterodyne mixing at millimetre wavelengths.

The frequency spectrum of a down-conversion mixer is depicted in Fig. 1.6b, with the signals-of-interest shown in blue and red. Using standard terminology, the spectral content around $(\omega_{\mathrm{LO}} + \omega_{\mathrm{IF}})$ is known as the upper sideband (USB), and the spectral content around $(\omega_{\mathrm{LO}} - \omega_{\mathrm{IF}})$ is known as the lower sideband (LSB). In general, there are three different mixing schemes: (a) single-sideband (SSB) mixing, where only one sideband is down-converted; (b) sideband separating (2SB) mixing, where each sideband is down-converted to its own IF output; and (c) dual-sideband (DSB) mixing, where the upper and lower sidebands are down-converted to the same IF spectrum. Fig. 1.6b depicts DSB mixing because the USB and LSB overlap in the IF spectrum.

The sensitivity of heterodyne receivers is given by the Dicke radiometer equation,

$$T_{\mathrm{min}} = \frac{T_{\mathrm{N}}}{\sqrt{\Delta\nu \cdot \Delta t}} \tag{1.1}$$

where T_{min} is the minimum detectable temperature[5], T_{N} is the noise temperature of the receiver system, $\Delta\nu$ is the instantaneous bandwidth, and Δt is the integration time. From this equation, we can see that the noise temperature is extremely important since the integration time required for a given sensitivity is proportional to $1\,/\,T_{\text{N}}^2$. For example, if the noise temperature can be cut in half, the required observing time drops by a factor of 4. Likewise, the instantaneous bandwidth $\Delta\nu$ is also important since the integration time is proportional to $1\,/\,\Delta\nu$. This instantaneous bandwidth is the bandwidth of the IF signal in Fig. 1.6b, which is why it is also known as the IF bandwidth or IFBW.

Each component in the receiver chain contributes some amount of noise to the overall receiver noise temperature T_{N}. To calculate T_{N}, we then have to cascade these noise contributions back to the input of the receiver using:

$$T_{\text{N}} = T_1 + \left(\frac{T_2}{G_1}\right) + \left(\frac{T_3}{G_1 \cdot G_2}\right) + \left(\frac{T_4}{G_1 \cdot G_2 \cdot G_3}\right) + \ldots \tag{1.2}$$

where T_i and G_i are the noise temperature and the gain of the i^{th} component, respectively. Note that a lossy component ($G_i < 1$) has the effect of amplifying the noise contribution from all of the following components (i.e., T_{i+1}, T_{i+2}, etc.), and conversely, a high gain component ($G_i \gg 1$) is able to conceal the noise contribution from components farther down the line. This is why most microwave-frequency receiver chains begin with a high-quality low noise amplifier (LNA). Unfortunately, these are not available above ~100 GHz, which means that the first electronic component in a mm-wave receiver is normally the heterodyne mixer itself.

For a typical mm-wave receiver, the cascaded noise temperature can be simplified to:

$$T_{\text{N}} = T_{\text{RF}} + \frac{T_{\text{M}}}{G_{\text{RF}}} + \frac{T_{\text{IF}}}{G_{\text{RF}}\, G_{\text{M}}} \tag{1.3}$$

where the "RF" subscript refers to everything on the high-frequency side of the mixer (mostly optical components), "M" refers to the mixer itself, and "IF" refers to everything on the low-frequency side (mostly electronic components). At mm-wave frequencies, all of the RF components are passive and the overall RF gain is below unity ($G_{\text{RF}} < 1$). The RF noise is then calculated by cascading the effective noise

[5]It is common in radio astronomy to represent the power per unit bandwidth ($P{\cdot}\Delta\nu$) as a temperature, defined as: $T \equiv P{\cdot}\Delta\nu/k_{\text{B}}$ where k_{B} is the Boltzmann constant. This is done regardless of whether or not the signal is thermal in origin.

temperature of each component, which is related to the loss through:

$$T_{\rm eff} = (L-1)\,T_{\rm phys} \tag{1.4}$$

where L is the loss (equal to $1/G$) and $T_{\rm phys}$ is the physical temperature. At low frequencies, the RF noise is often comparable to the other noise contributions, but at submillimetre wavelengths, it easily dominates $T_{\rm N}$ due to the additional loss from water vapour in the atmosphere. The noise from the IF components, on the other hand, is usually dominated by the low noise amplifier (LNA), which is normally the next component in the receiver chain after the mixer. Therefore, to create a high sensitivity mm-wave receiver, we require low loss RF components, low noise IF components, and a high conversion efficiency and low noise mixing element. Note however that all heterodyne mixers are constrained by the quantum limit of sensitivity, imposed by Heisenberg's uncertainty principle. For DSB mixers, this limit is:

$$T_{\rm Q} = \frac{h\,\nu}{2\,k_{\rm B}} \sim \left(\frac{2.4\ {\rm K}}{100\ {\rm GHz}}\right)\cdot\nu \tag{1.5}$$

where h is Planck's constant and $k_{\rm B}$ is the Boltzmann constant. This corresponds to a lower limit of $T_{\rm N}^{\rm DSB} \geq 5.5$ K at 230 GHz. If instead we wish to measure an emission line that only appears in one sideband, the other sideband only contributes additional noise, so the minimum noise temperature for SSB operation is twice as high: $T_{\rm N}^{\rm SSB} \geq 11$ K (assuming that the conversion efficiency is the same for both sidebands).

Superconducting Detectors

At millimetre wavelengths, most heterodyne receivers use superconducting detectors for down-conversion. These detectors are operated well below the transition temperature of the metals at which point electrons bind together into Cooper pairs. If enough energy is supplied to break a Cooper pair, two free electrons are released, called quasiparticles. Superconducting detectors that rely on this effect include Superconductor/Insulator/Superconductor (SIS) junctions, which are used between 100 GHz $\lesssim \nu \lesssim$ 1.3 THz, and hot electron bolometers (HEBs), which are used at frequencies well above 1 THz. SIS mixers operating below 1 THz almost exclusively use niobium junctions, which have a gap frequency of ∼700 GHz (i.e., the frequency at which photons can break the Cooper pairs). However, from quantum theory, heterodyne mixing is still possible in niobium SIS mixers up to ∼1.4 THz and even higher

with new materials such as niobium nitride (NbN) and niobium titanium nitride (NbTiN).

1.3 SIS mixers

Superconductor/Insulator/Superconductor (SIS) tunnel junctions are currently the gold standard for heterodyne mixing from ∼100 GHz to +1 THz. As their name suggests, they consist of two superconductors that are separated by a thin insulation barrier (Fig. 1.7). If the barrier is sufficiently thin, i.e., on the order of ∼10 Å, the electrons can quantum tunnel between the superconductors without dissipating any energy. Either of the charge carriers can tunnel across the insulation barrier (i.e., Cooper pairs or quasiparticles); however, SIS junctions are designed specifically for quasiparticle tunnelling and so Cooper pair tunnelling is suppressed using a magnetic field. The theory behind SIS mixers will be covered in much more detail in Chp. 2.

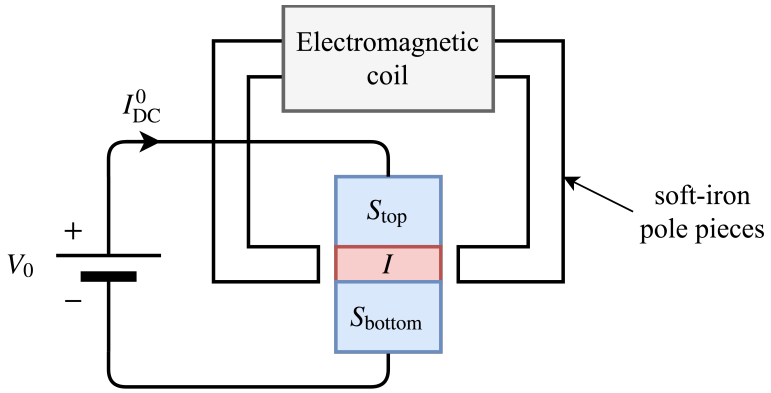

Figure 1.7: A diagram of a simple SIS junction. Two superconductors (S) are separated by a thin insulation barrier (I) that is approximately 10 Å thick. A positive DC bias voltage V_0 results in quasiparticles tunnelling from S_{bottom} to S_{top} (and therefore a positive DC current I^0_{DC}). The electromagnet is used to suppress Cooper pair tunnelling. The soft-iron pole pieces focus the field across the junction.

In order for a single electron to tunnel through the insulation barrier, its energy state has to overlap with an empty state in the opposite electrode. In a normal metal/insulator/normal metal (NIN) junction, this leads to a linear current–voltage relationship because the density of states is approximately constant for small excitation energies. Quasiparticles, however, have an energy gap in their density of states due to the formation of Cooper pairs (Fig. 1.8a). On either side of the Fermi energy level E_{F}, there are no available quasiparticle states from $E_{\text{F}} - \Delta$ to $E_{\text{F}} + \Delta$. Therefore, as a bias voltage is applied to an SIS junction, initially there is no (or very little) tunnelling current. Then, once the bias voltge equals $V_0 \sim 2\Delta/e$, the tunnelling current

rises very sharply (Fig. 1.8b) as filled states in S_{bottom} begin to overlap with empty states in S_{top}, leading to the highly non-linear current–voltage relationship shown in Fig. 1.8b.

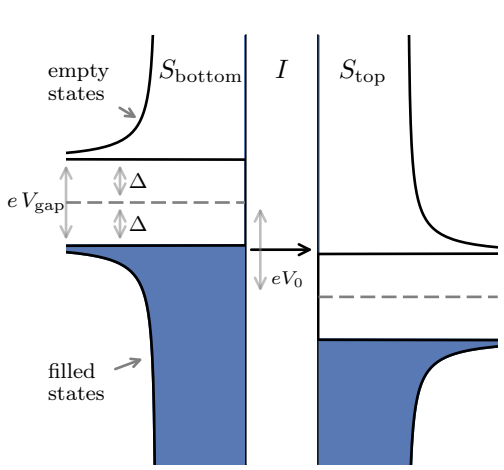

(a) For positive V_0, the quasiparticle tunnelling current is proportional to the number of filled states in S_{bottom} that overlap with empty states in S_{top}. However, the formation of Cooper pairs results in an energy gap ($e\,V_{\text{gap}}$) in the quasiparticle density of states. The SIS junction then needs to be biased at $|V_0| \gtrsim V_{\text{gap}}$ before any tunnelling will occur, resulting in a highly non-linear current–voltage relationship (Fig. 1.8b).

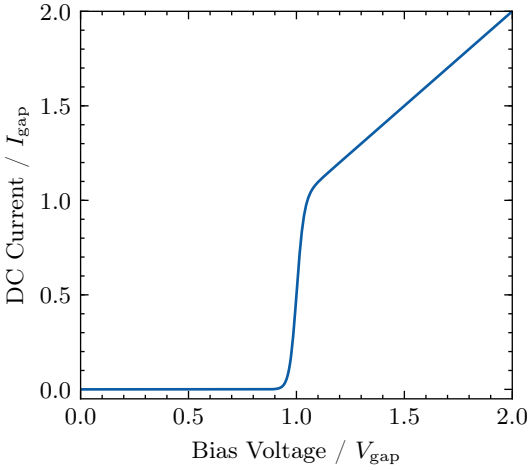

(b) The characteristic current–voltage relationship of an SIS junction, also known as the *DC I–V curve*. The current rises sharply at $V_0 \sim V_{\text{gap}}$, which corresponds to the binding energy of the Cooper pairs: $2\Delta \sim e\,V_{\text{gap}}$. Here, the current and voltage are normalised to the properties of the transition (V_{gap} and I_{gap}; explained in Chp. 2).

Figure 1.8: Quasiparticle tunnelling in an SIS junction.

The current–voltage (I–V) relationship shown in Fig. 1.8b is ideal for a variety of tasks, including heterodyne mixing. For a classical analysis, the I–V curve is all that is required in order to calculate the mixer's operation. At higher frequencies, however, quasiparticles absorb energy directly from the LO's photons and gain the energy necessary to tunnel through the insulation barrier even at voltages below V_{gap}, a process known as *photon-assisted tunnelling* (Fig. 1.9a and Fig. 1.9b). A quantum mechanical approach is then required to describe mixing at these frequencies. This was first provided by Tucker in 1979 [11] and later summarised by Tucker and Feldman in 1985 [12] (again, much more information will be provided in Chp. 2). From this quantum mechanical description, Tucker [11] found that SIS junctions are capable of quantum limited noise performance and conversion efficiencies greater than unity, i.e., $G_{\text{SIS}} > 1$. In practice, conversion gains above unity result in unstable mixer operation.

Instead, low noise temperatures and $G_{\mathrm{SIS}} \sim 1$ are desired for creating highly sensitive SIS mixers.

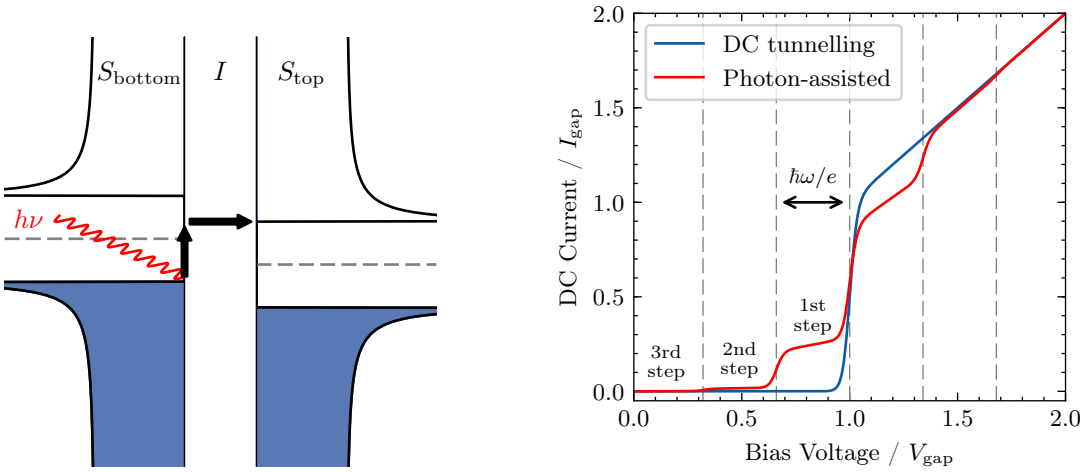

(a) Quasiparticles can absorb energy directly from the LO's photons in order to gain the necessary energy to tunnel through the insulation barrier, a process known as *photon assisted tunnelling*.

(b) Photon assisted tunnelling induces a step-like structure into the I–V curve. The width of each step is $h\nu/e$, where h is Planck's constant, ν is the frequency of the radiation, and e is the charge of an electron.

Figure 1.9: Photon assisted tunnelling in an SIS junction.

Modern SIS receivers

Modern SIS mixers offer the best noise performance of any heterodyne mixing technique between 100 GHz and +1 THz, and they are used in every major millimetre telescope listed in Table 1.1. SIS receivers are also now operating at frequencies close to 1 THz, with the recent cartridges for ALMA Band 10 producing noise temperatures that are approximately 4.4 times the quantum limit from 787 GHz to 950 GHz [13]. Efforts are now being made to create SIS mixers at frequencies up to 1.3 THz (e.g., [14]), with the possibility of adding additional ALMA frequency bands between 1−1.6 THz [15] in the future.

Below 400 GHz, state-of-the-art SIS receivers are now approximately 3 times the quantum limit (Fig. 1.10), and as a result, further improvements to the noise temperature are becoming increasingly difficult. SIS receivers at these frequencies are now dominated by noise from the atmosphere, the optical components and the low-noise amplifiers, so minor improvements to the mixer's noise temperature do not have a large effect on the overall sensitivity. There are, however, other ways to extend the capability of these receivers besides lowering the noise temperature, two of which

Table 1.1: Millimetre and submillimetre wavelength observatories employing SIS receivers.

Telescope[a]	Location	Elevation (m)	Dish diameter[b] (m)	Surface error (μm rms)
AST/RO†	Antarctica	2,800	1.7	9
SPT	"	2,800	10	20
LLAMA‡	Argentina	4,820	12	15
SST	"	2,490	1.5	20
SMT/HTT	Arizona	3,185	10	15
CARMA†	California	2,200	6×10.4	30
			9×6.1	30
			8×3.5	30
ALMA	Chile	5,040	54×12	25
			12×7	20
APEX	"	5,100	12	17
ACT	"	5,190	6	31
ASTE	"	4,800	10	19
NANTEN2	"	4,800	4	20
CCAT*	"	5,612	6	–
CCOSMA	China	4,300	3	30
NOEMA‡	France	2,550	12×15	50
JCMT	Hawaii	4,092	15	24
CSO†	"	4,140	10.4	13
SMA	"	4,080	8×6	13
Nobeyama 45 m	Japan	1,350	45	65
LMT	Mexico	4,640	50	31
IRAM 30 m	Spain	2,850	30	50
SOFIA	Airplane	13,700	2.7	
HSO	Satellite @ L2	–	3.5	2.5

Note: This table only includes telescopes with heterodyne receivers above 200 GHz. The telescopes are organised by location. Some of the information was pulled from [16].

[a] Telescopes: *Antarctic Submillimeter Telescope and Remote Observatory* (AST/RO), *South Pole Telescope* (SPT), *Large Latin American Millimeter Array* (LLAMA), *Solar Submillimeter Telescope* (SST), *Submillimeter Telescope* (SMT; previously the *Heinrich Hertz Telescope*/HHT), *Combined Array for Research in Millimeter-wave Astronomy* (CARMA), *Atacama Large Millimeter/submillimeter Array* (ALMA), *Atacama Pathfinder Experiment* (APEX), *Atacama Cosmology Telescope* (ACT), *Atacama Submillimeter Telescope Experiment* (ASTE), *Cerro Chajnantor Atacama Telescope* (CCAT), *China-Cologne Observatory for Submillimeter Astronomy* (CCOSMA; previously KOSMA), *Northern Extended Millimeter Array* (NOEMA; an extension of the *Plateau de Bure Interferometer*/PdBI), *James Clerk Maxwell Telescope* (JCMT), *Caltech Submillimeter Observatory* (CSO), *Submillimeter Array* (SMA), *Large Millimeter Telescope* (LMT), *Stratospheric Observatory for Infrared Astronomy* (SOFIA), and *Herschel Space Observatory* (HSO).

[b] Interferometers are denoted as (*number of dishes*)×(*dish diameter*).

† Decommissioned.

‡ Under construction.

* Proposed.

will be the focus of this thesis. Firstly, the instantaneous bandwidth $\Delta\nu$ of the receiver can be expanded. This is the bandwidth of the down-converted IF signal (i.e., the IF bandwidth or IFBW), which also sets the bandwidth of the lower and upper sidebands. For continuum sources, the integration time is proportional to $1 \,/\, \Delta\nu$ (recall Eqn. 1.1), and for spectral sources, wide IFBW expands the survey depth of a measurement to allow multiple emission lines to be observed at the same time. For example, if a receiver is able to observe simultaneously from 219.6 GHz to 230.5 GHz (a bandwidth of 10.9 GHz), four of the most common isotopes of CO can be captured during a single integration, i.e., the CO($J = 2 \rightarrow 1$) rotational lines of $^{12}C^{16}O$, $^{13}C^{16}O$, $^{12}C^{17}O$ and $^{12}C^{18}O$. The second technique that can be used to extend the capability of SIS receivers is increasing the number of pixels N_{pixels} contained within a single telescope. This is accomplished by installing an array of SIS receivers in the focal plane. Assuming that the receivers are operating independently, the time required to map a given target is then proportional to $1 \,/\, N_{\text{pixels}}$. Telescopes with focal plane arrays are very useful for surveys that cover large areas of the sky, the results of which can be used to identify interesting targets to observe in more detail with large single dish telescopes or interferometers.

1.4 Thesis outline

The primary objective of this DPhil project was to increase the sensitivity of SIS receivers through improved instantaneous bandwidth, multi-pixel focal plane arrays, and advanced SIS receiver simulations. The outline of this thesis is as follows:

Chapter 2 introduces the theory behind SIS mixing. The chapter begins by covering the basics of superconductivity and quantum tunnelling. Heterodyne mixing in SIS junctions is then described based on the quantum mechanical theory developed by Tucker and Feldman [11, 12]. The chapter concludes by describing the experimental methods that are used to characterise SIS mixers.

Chapter 3 presents a new SIS receiver centred at 230 GHz. The area of the planar circuit was minimised to limit the capacitance, which helps to extend the IF response. The chapter begins by presenting the design of the planar circuit and electromagnetic simulations. Then, the experimental results are presented, including the DC, RF and IF performance.

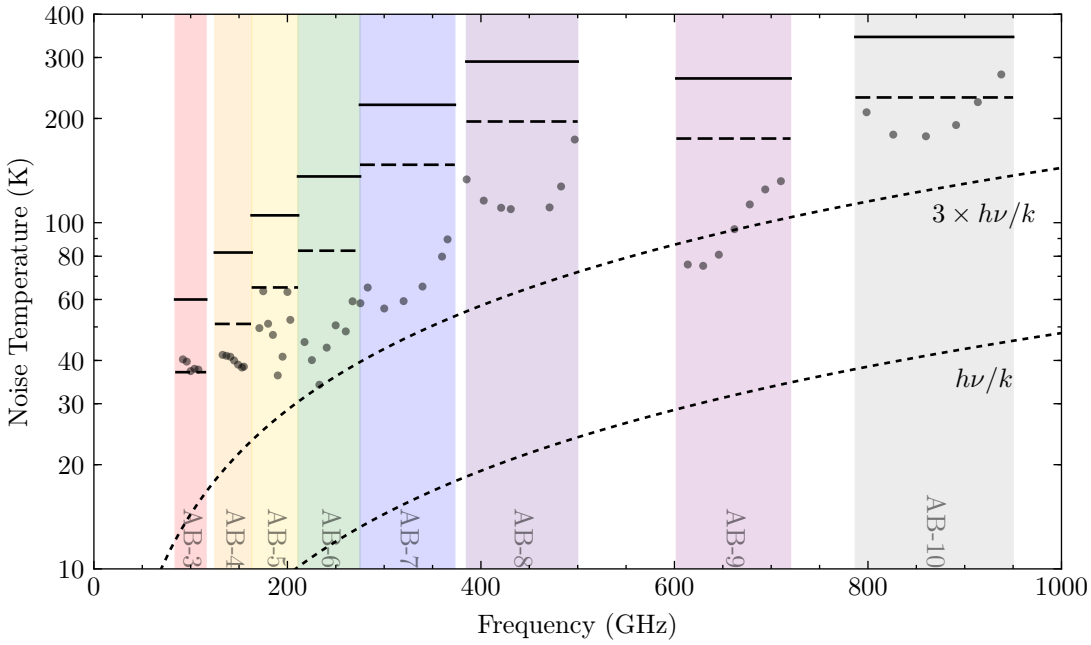

Figure 1.10: The noise temperature of the ALMA SIS receivers. The solid horizontal lines represent the ALMA noise temperature specifications, and the dashed lines are the values that must be met over at least 80% of the band. The dots are the measured noise temperature values from the literature: Band 3 (S. Claude, *et al.* [17]), Band 4 (S. Asayama, *et al.* [18]), Band 5 (B. Billade, *et al.* [19]), Band 6 (G. Ediss, *et al.* [20]), Band 7 (S. Mahieu, *et al.* [21]), Band 8 (W. Shan, *et al.* [22]), Band 9 (A. Baryshev, *et al.* [23]), and Band 10 (Y. Fujii, *et al.* [13]). Note that the Band 3 results are out-dated; more recent results can be found in [24], but this paper does not list the noise temperature versus LO frequency. Also note that Bands 3–7 are SSB receivers and Bands 8–10 are DSB receivers.

Chapter 4 presents a new software package called QMix, short for *Quasiparticle Mixing* software. This software simulates quasiparticle tunnelling in SIS junctions using multi-tone spectral domain analysis. The package was initially developed to investigate the operation of the device from Chp. 3 because this device has (a) a wide IF response, (b) a singular SIS junction that could be prone to saturation, and (c) low capacitance, which may not suppress the higher-order harmonics of the LO. This chapter includes basic SIS mixer simulations, which help to test and validate the software, as well as simulations of the 230 GHz device from Chp. 3.

Chapter 5 presents a new 1×4 focal plane array for operation at 230 GHz. The array was developed to test a new array architecture that can be expanded to many more pixels in the future. The array uses waveguide power splitters and directional couplers to distribute and inject the LO signal into the RF waveg-

uides. This chapter begins by describing the design, fabrication and assembly of the array, and then preliminary experimental results are presented.

Chapter 6 presents new CO(J=1→0) measurements from 34 intermediate redshift galaxies ($0.05 < z < 0.5$). The measurements were taken with the IRAM 30 m telescope in Pico Veleta, Spain. They are combined with infrared luminosity values from the 5MUSES survey [25] to formulate empirical scaling laws between the global properties. They are also compared to other star formation studies to extend the scaling laws across a large fraction of cosmic time.

Chapter 7 concludes this thesis by summarising Chapters 2–6 and suggesting future development to expand upon this work.

Chapter 2

SIS Mixer Theory

2.1 Introduction

Superconductor/Insulator/Superconductor (SIS) tunnel junctions are sandwich-like structures comprising two superconductors separated by a thin insulation barrier (Fig. 2.1). If the insulation barrier is sufficiently thin, the electron wave function of the superconductors overlaps the barrier and has a finite probability amplitude in the opposite electrode. This allows for quantum tunnelling, which can take the form of either charge carrier present within a superconductor: quasiparticle tunnelling (free electrons) or Cooper pair tunnelling (paired electrons). Using traditional nomenclature, "SIS junctions" rely on quasiparticle tunnelling, while "Josephson junctions" rely on Cooper pair tunnelling, although the physical constructions are identical.

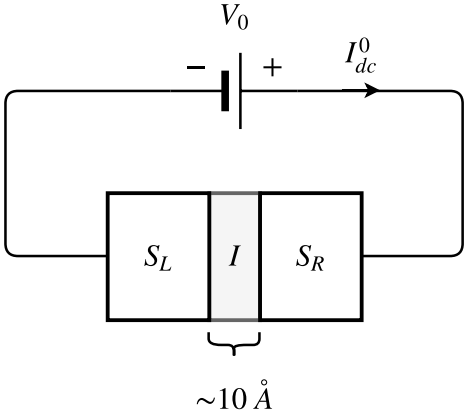

Figure 2.1: A simple SIS junction circuit. The superconductors on the left and right (S_{L} and S_{R}, respectively) are separated by a thin insulation barrier (I) that is approximately 10−20 Å thick. A positive DC voltage (V_0) results in quasiparticles tunnelling from S_{L} to S_{R} and a net DC current in the direction of I^0_{dc}.

In radio astronomy, SIS junctions are commonly used as heterodyne mixers to shift

the spectral content of signals from the millimetre-wave spectrum down to microwave frequencies that are favourable for digital processing. SIS junctions make excellent mixing elements because the quasiparticle tunnelling current is an extremely non-linear function of voltage, a requirement for good conversion efficiency. The first quantum mechanical description of SIS mixer operation was done by Tucker in 1979 [11] and later summarised by Tucker and Feldman in 1985 [12]. Two key predictions of this work are that SIS junctions can achieve (a) quantum limited mixing noise and (b) RF-to-IF conversion gain close to or even greater than unity [26], which is not possible with classical passive mixers. Both of these features are highly desirable for sensitive heterodyne measurements.

In this chapter, SIS mixer theory will be explored. To begin, the basics of superconductivity will be introduced in Sec. 2.2. Quasiparticle and Cooper pair tunnelling mechanism will then be described in Sec. 2.3 and Sec. 2.5, respectively. In Sec. 2.4, SIS mixer theory will be presented, and finally, the methods used to characterise SIS mixer performance will be explained in Sec. 2.6.

2.2 Superconductivity

When a superconductor is cooled below its critical temperature T_c, electron–phonon interactions allow pairs of electrons to form, called Cooper pairs [27, 28]. Each pair is composed of two electrons having opposing momenta and spin. Although seemingly counter-intuitive, Cooper pairs interact over a large enough distance that Coulomb repulsion is screened by the lattice and the electron-phonon interaction is strong enough to form a weak bond (Fig. 2.2).

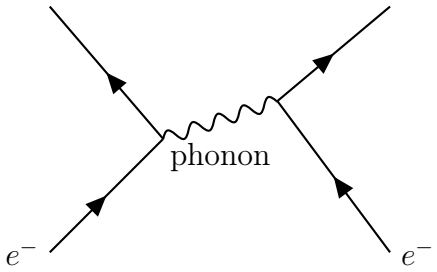

Figure 2.2: An electron-phonon interaction forming a Cooper pair. The phonon is a discrete vibration through the metal's positive ion lattice.

While the constituent electrons are fermions, which obey the Pauli exclusion principle, Cooper pairs are composite bosons. Therefore, all paired electrons can occupy

the same energy level and be described by a single wave function,

$$\psi(\mathbf{r}) = \sqrt{n_\mathrm{s}}\; e^{j\varphi(\mathbf{r})} \tag{2.1}$$

where n_s is the number of Cooper pairs and $\varphi(\mathbf{r})$ is the wave function's phase factor. Under a DC potential, Cooper pairs move coherently through the metal lattice with *exactly zero resistance.*

The binding energy of Cooper pairs 2Δ is governed by the strength of the phonon mediated attraction, and for type-II superconductors, such as niobium, it is on the order of several milli-electron volts. If an energy greater than 2Δ is absorbed by a Cooper pair, two quasiparticles are excited with total energy $E \geq 2\Delta$ relative to the superconductor's ground state. From Bardeen-Cooper-Schrieffer (BCS) theory [28], the excitation energy of one of these quasiparticles is

$$E = \sqrt{\Delta^2 + \xi^2} \tag{2.2}$$

where ξ is the normal-state quasiparticle energy relative to the Fermi level, E_F. The density of excitations of quasiparticles can then be found from:

$$\rho(E) = \mathcal{N}(\xi)\,\frac{\mathrm{d}\xi}{\mathrm{d}E} = \begin{cases} \mathcal{N}(0)\,\dfrac{|E|}{\sqrt{E^2-\Delta^2}} & \text{if } |E| > \Delta \\ 0 & \text{otherwise.} \end{cases} \tag{2.3}$$

where $\mathcal{N}(\xi)$ is the normal-metal density of states at an energy ξ relative to the Fermi energy[1] (Fig. 2.3a). Note that there are no states for $|E| \leq \Delta$ because it is energetically favourable for all of these electrons to condense into Cooper pairs. The range of energies within which single unpaired electrons do not exist is referred to as the superconductor's energy gap, $E_\mathrm{gap} = 2\Delta$. The probability that a given state is filled at temperature T is given by the Fermi function,

$$f(E) = \frac{1}{e^{E/k_\mathrm{B}T} - 1} \tag{2.4}$$

where k_B is the Boltzmann constant.

2.3 Quasiparticle tunnelling

The energy level diagram for an SIS junction can be created by combining the quasiparticle density of states with the Fermi function (Fig. 2.3a). This model is

[1]For small excitation energies ξ, we can assume $\mathcal{N}(\xi) = \mathcal{N}(0)$ is constant.

often called the semiconductor model due to the similarities with semiconductor energy level diagrams. At $T = 0$, all of the free electrons condense into Cooper pairs and no quasiparticle excitations exist. At any finite temperature, however, thermal excitations result in quasiparticles existing above the gap (i.e., at $E > \Delta$).

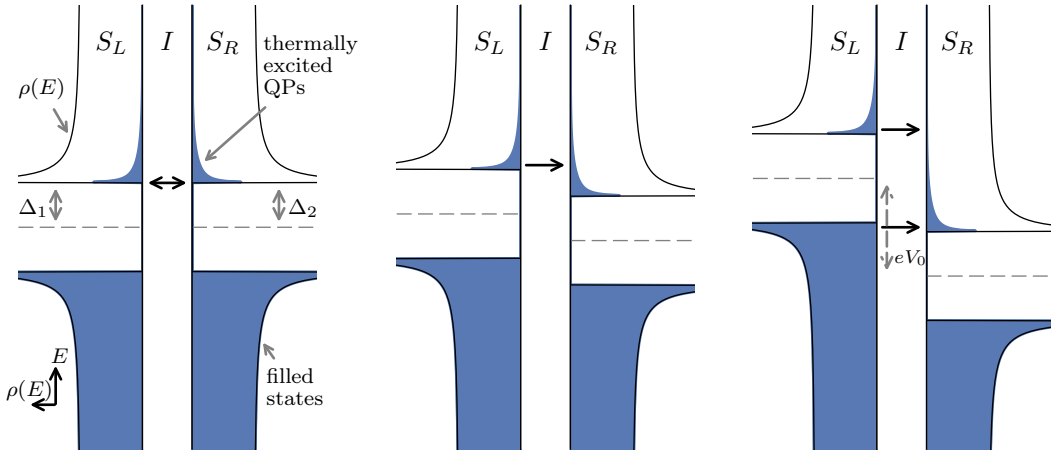

(a) $V_0 = 0$ (b) $0 < V_0 < V_{\text{gap}}$ (c) $V_0 \geq V_{\text{gap}}$

Figure 2.3: A density of states diagram for an SIS junction. The filled states are shown in blue and the empty states in white. The black arrows represent quasiparticles tunnelling through the insulation barrier. Note that the temperature is exaggerated in order to see the thermally excited quasiparticles. The labels correspond to the device shown in Fig. 2.1.

Quasiparticles can tunnel through the insulation barrier provided that (a) the new state has the same energy as the original state (conservation of energy), and (b) the new energy state is empty (Pauli exclusion principle). When a positive DC voltage is applied across the SIS junction (using the sign convention from Fig. 2.1), the potential of the left electrode increases by $+eV_0$ relative the right electrode. This results in the vertical translation seen in Fig. 2.3b. A small net tunnelling current will then flow from S_{L} to S_{R} due to the thermally excited quasiparticles. If V_0 is further increased to $2\Delta/e$, known as the gap voltage V_{gap}, enough potential energy is available to excite quasiparticles from below the gap (Fig. 2.3c), which results in a rapid rise in tunnelling current (Fig. 2.4). Above V_{gap}, the tunnelling current increases linearly with voltage and the SIS junction takes on its normal-state resistance R_{n}.

Overall, the DC tunnelling current is proportional to the number of filled states

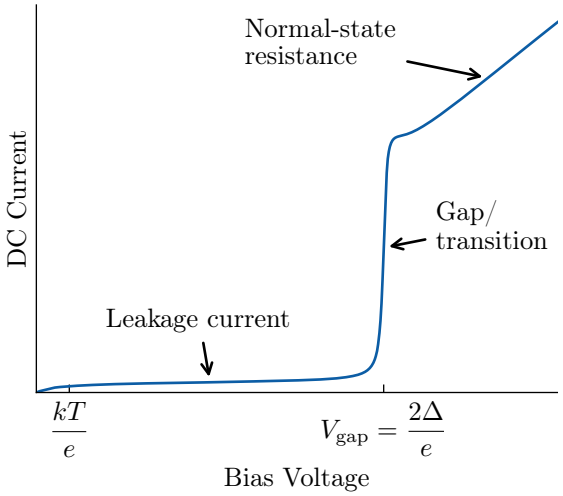

Figure 2.4: The DC current–voltage relationship (i.e., DC I–V curve) that arises from quasiparticle tunnelling in an SIS junction.

in one superconductor that overlap with empty states in the other superconductor:

$$I^0_{\text{dc}}(V_0) = \frac{1}{e\,R_{\text{n}}} \int_{-\infty}^{\infty} \{\rho_{\text{L}}\,(E - eV_0)\,f\,(E - eV_0)\,\rho_{\text{R}}\,(E)\,[1 - f\,(E)] - \rho_{\text{L}}\,(E - eV_0)\,[1 - f\,(E - eV_0)]\,\rho_{\text{R}}\,(E)\,f\,(E)\}\;dE \tag{2.5a}$$

$$= \frac{1}{e\,R_{\text{n}}} \int_{-\infty}^{\infty} \rho_{\text{L}}(E - eV_0)\,\rho_{\text{R}}(E)\;[f(E - eV_0) - f(E)]\;\;dE. \tag{2.5b}$$

Here I^0_{dc} is the DC tunnelling current, V_0 is the DC bias voltage, e is the charge of an electron, and ρ_{L} and ρ_{R} are the density of quasiparticle states in the left and right superconductors, respectively.

The current–voltage relationship shown in Fig. 2.4 is characteristic of an SIS junction and is commonly called the *DC I–V curve*. The I–V relationship of SIS junctions is more non-linear than any other passive device, which makes them ideal for a variety of applications, in particular, heterodyne mixing. The DC quasiparticle tunnelling was independently discovered by Giaever [29] and Nicol et al. [30] in 1960. Since the DC I–V curve provides an easy method to prove the existence of Cooper pairs and to measure their binding energy, these experiments were one of the first major confirmations of BCS theory[2].

[2]For his work, Giaever shared the 1973 Nobel Prize in Physics with Josephson who predicted Cooper pair tunnelling in 1962 [31], and Esaki who was the first to show quantum tunnelling in semiconductors in 1957 [32].

2.3.1 Photon-assisted tunnelling

In addition to electrical potentials and thermal excitation, quasiparticles can also be excited across the barrier by absorbing energy from individual photons (Fig. 2.5a). This was first shown experimentally by Dayem and Martin in 1962 [33], and then described mathematically by Tien and Gordon in 1963 [34]. To overcome the energy gap $E_{\mathrm{gap}} = 2\Delta$, the number of absorbed photons must be $n \geq (2\Delta - eV_0)/\hbar\omega$ where $\hbar = h/2\pi$, and ω is the angular frequency of the radiation. Since it is more probable to absorb m photons versus $m{+}1$ photons, a step-like structure is induced in the I–V curve (Fig. 2.5b). The width of each step corresponds to the photon equivalent voltage, $V_{\mathrm{ph}} = \hbar\omega/e$. Photon-assisted tunnelling is the basis of SIS heterodyne mixing, and will be covered in much more detail in Section 2.4.

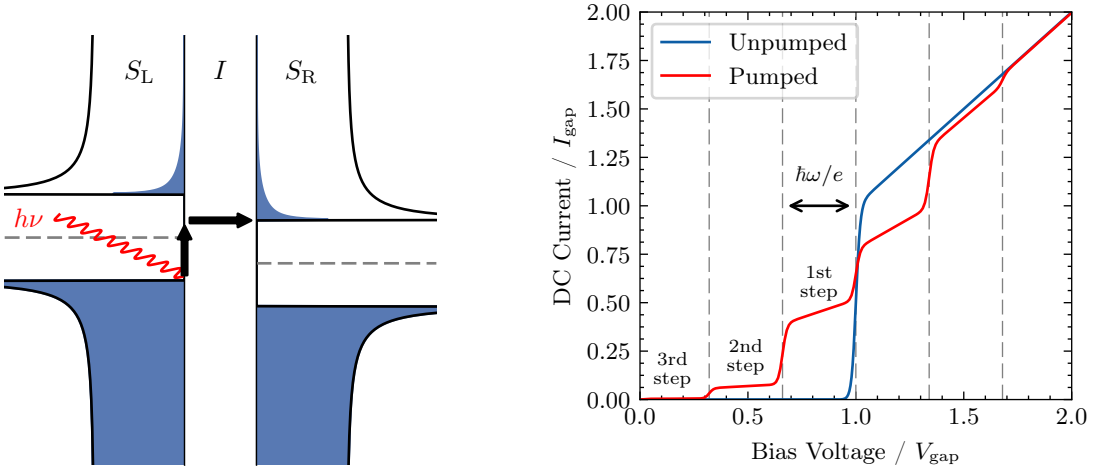

(a) An energy level diagram depicting photon-assisted tunnelling. The photon (red) gives a quasiparticle below the gap enough energy to tunnel through the insulation barrier even though $|V_0| < V_{\mathrm{gap}}$.

(b) The I–V curve resulting from photon-assisted tunnelling (i.e., the pumped I–V curve). The width of each step is equal to the photon equivalent voltage, $V_{\mathrm{ph}} = \hbar\omega/e$. In this example, $V_{\mathrm{ph}} = 0.34{\cdot}V_{\mathrm{gap}}$.

Figure 2.5: Photon-assisted tunnelling in an SIS junction.

2.3.2 Characteristic properties of DC quasiparticle tunnelling

An example of an experimental DC I–V relationship is shown Fig. 2.6 from a niobium/aluminium oxide/niobium (Nb/AlO_x/Nb) junction. The shape of the I–V relationship is influenced by the geometry, materials, construction and temperature of the junction. In order to characterise and compare the quality of different junctions, several performance metrics have been defined including gap voltage, normal

resistance, subgap leakage current, and gap linearity. These metrics are described below.

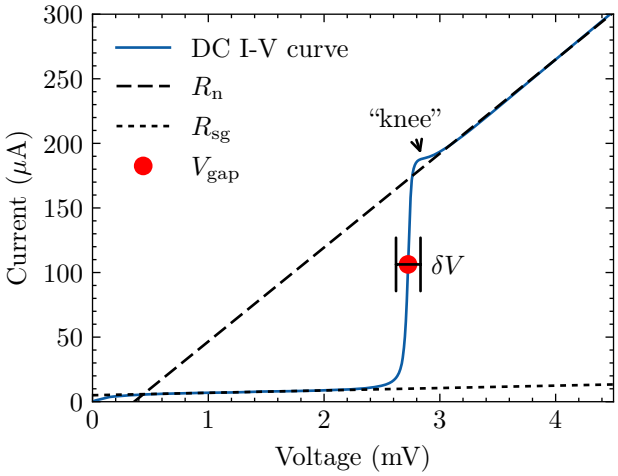

Figure 2.6: An experimental DC I–V curve taken from a Nb/AlO_x/Nb junction. Several characteristics of the I–V curve are labelled including the normal resistance (R_n), the subgap resistance (R_{sg}), the gap voltage (V_{gap}), and the width of the transition (δV).

Binding energy and gap voltage

The binding energy of Cooper pairs 2Δ comes from the electron-phonon interaction. This is a characteristic property of the superconducting material because the phonon exchange occurs via the underlying lattice of positive ions[3]. Although the binding energy is temperature dependent, below $T_c/2$ it is roughly equal to the value at $T = 0$ [35]:

$$2\,\Delta_0 = 3.528\,k_B\,T_c \tag{2.6}$$

where the "3.528" constant is the theoretical BCS gap ratio. Above $T_c/2$, the binding energy quickly drops with temperature as a significant number of quasiparticles are excited. This is described by the self-consistent BCS equation:

$$\frac{1}{\mathcal{N}(0)\,V} = \int_0^{\hbar\omega_D} d\xi\,\frac{1}{\sqrt{\xi^2+\Delta^2}}\,\tanh\left(\frac{\sqrt{\xi^2+\Delta^2}}{2\,k_B\,T}\right) \tag{2.7}$$

where ω_D is the Debye frequency, V is the strength of the attractive potential, and $\mathcal{N}(0)$ is the density of states at the Fermi energy. The $\mathcal{N}(0)\,V = \lambda_{ep}$ dimensionless

[3]Note that the electron-lattice interaction is also responsible for resistivity in the normal state. As such, good superconductors with high T_c typically have high resistance in the normal state, and noble metals, which have low resistance in the normal state, are not able to form Cooper pairs at *any* temperature.

product is a characteristic property of a given material and describes the strength of the electron–phonon coupling. The temperature dependence approximately follows

$$\frac{\Delta(T)}{\Delta_0} \approx \sqrt{\cos\left[\frac{\pi}{2}\left(\frac{T}{T_\mathrm{c}}\right)^2\right]}, \tag{2.8}$$

which is compared to the self-consistent BCS equation in Fig. 2.7.

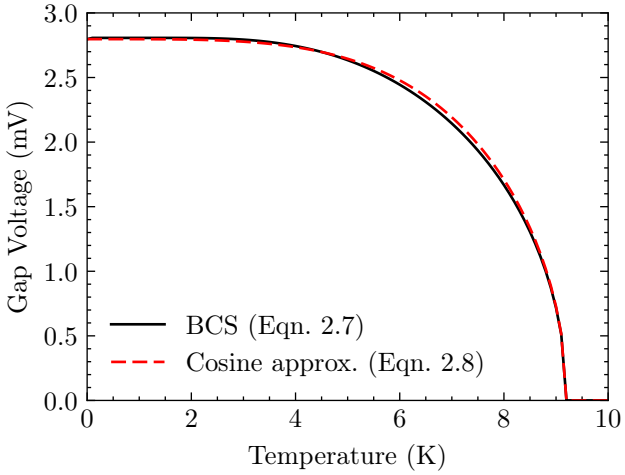

Figure 2.7: The gap voltage of niobium calculated from the self-consistent BCS equation (Eqn. 2.7) and the cosine approximation (Eqn. 2.8).

The binding energy can be recovered from an experimental DC I–V curve by measuring the location of the gap voltage V_gap (Fig. 2.6). This voltage corresponds to the binding energy of a Cooper pair, i.e., $eV_\mathrm{gap} = 2\Delta$. For a niobium/insulator/niobium junction, the gap voltage will be ∼2.8 meV, but it can be lower depending on the properties of the junction and the physical temperature. A high gap voltage suggests a low junction temperature and therefore low shot noise. Different superconducting materials, such as niobium nitride (NbN), can be used to further increase the binding energy, which becomes necessary at frequencies above the gap frequency of niobium, $\nu_\mathrm{gap} = eV_\mathrm{gap}/h \approx 680$ GHz.

Normal resistance

The normal resistance R_n is the resistance of the junction in its normal state, i.e., at a temperature above T_c. Experimentally, the normal resistance can be found by measuring the slope of the DC I–V curve $I^0_\mathrm{dc}(V_0)$ above the transition voltage:

$$R_\mathrm{n} = \left(\left.\frac{\mathrm{d}I^0_\mathrm{dc}}{\mathrm{d}V_0}\right|_{V_0 \gg V_\mathrm{gap}}\right)^{-1}. \tag{2.9}$$

This slope is represented by the dashed line in the example shown in Fig. 2.6. Since R_n is inversely proportional to junction area A_J, the $R_\mathrm{n}{\cdot}A_\mathrm{J}$ product is an important characteristic of a junction and is often referred to as the junction's transparency, $t_\mathrm{J} = R_\mathrm{n}{\cdot}A_\mathrm{J}$. By combining transparency with the gap voltage, the current density of the junction is defined as:

$$j_\mathrm{c} = \frac{V_\mathrm{gap}}{R_\mathrm{n} \cdot A_\mathrm{J}} = \frac{V_\mathrm{gap}}{t_\mathrm{J}}\,. \tag{2.10}$$

Normal resistance, transparency and current density are all dependent on the physical construction of the junction, especially the insulation barrier thickness.

Subgap leakage current

The leakage current seen below the transition voltage is primarily due to thermally excited quasiparticles. From BCS theory, this current is equal to [36]:

$$I_\mathrm{sg}(V_0) = \frac{2}{e\,R_\mathrm{n}} e^{-\frac{\Delta}{k_\mathrm{B}T}} \sqrt{\frac{2\Delta}{eV_0 + 2\Delta}}\,(eV_0 + \Delta)\,\sinh\left(\frac{eV_0}{2k_\mathrm{B}T}\right)\,K_0\left(\frac{e\,V_0}{2\,k_\mathrm{B}\,T}\right) \tag{2.11}$$

where K_0 is the 0^th order modified Bessel function of the second kind. Note that the subgap leakage current has an exponential relationship with temperature. Since leakage current is a major source of shot noise, SIS mixers must be kept as cold as possible to keep I_{sg} to a minimum (Fig. 2.8).

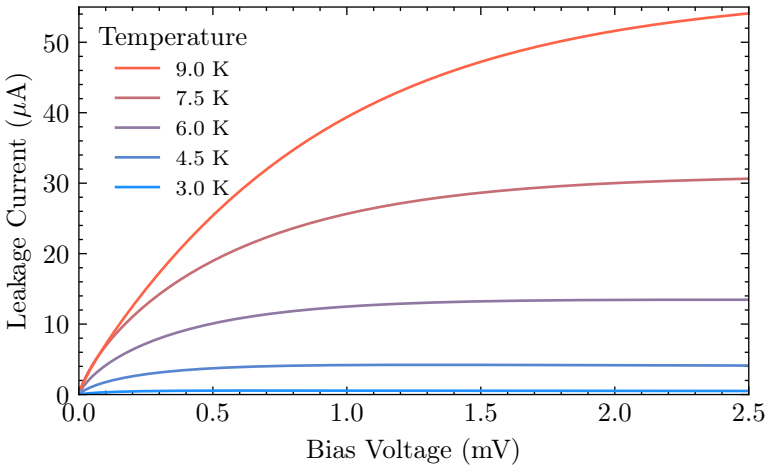

Figure 2.8: The subgap leakage current calculated from Eqn. 2.11 for different junction temperatures. This current gives rise to shot noise in an SIS mixer, so the temperature should be as low as possible to minimise the effect.

The quality factor of the DC I–V curve is defined as:

$$Q_\mathrm{IV} = \frac{I^0_\mathrm{dc}(V_0 + \delta V/2)}{I^0_\mathrm{dc}(V_0 - \delta V/2)} \tag{2.12}$$

where δV is the voltage width of the non-linearity. Alternatively, the resistance quality factor is defined as the ratio of subgap resistance (dotted line in Fig. 2.6) to normal resistance,

$$Q_{\mathrm{R}} = \frac{R_{\mathrm{sg}}}{R_{\mathrm{n}}}. \tag{2.13}$$

Using either definition, high Q-factors are desirable for good noise temperature and gain characteristics.

Gap linearity and proximity effect

Based on the superconducting density of states from Sec. 2.3, the DC I–V curve should be infinitely sharp at $V_0 = V_{\mathrm{gap}}$. Real DC I–V curves however have rounded transitions that take place gradually over finite voltage widths δV. One reason for this is inhomogeneities in the insulation barrier, which causes Δ to vary across the area of the junction. Another is quasiparticle lifetime broadening [37–40], where quasiparticles are able to exist within the energy gap for a finite time before condensing into Cooper pairs. Both of these effects can be represented by adding an imaginary component to the binding energy [37], such as:

$$\Delta = \Delta_1 - j\Delta_2. \tag{2.14}$$

For most junctions, Δ_2 is on the order of ~10 μeV. The rounding resulting from the imaginary term Δ_2 is shown in Figure 2.9.

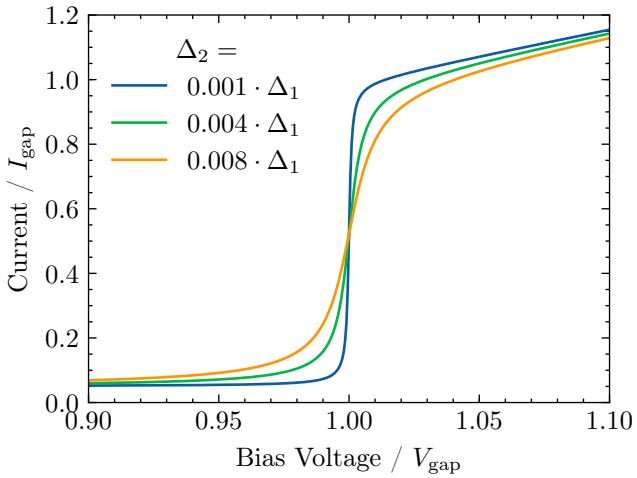

Figure 2.9: Rounding of the transition due to lifetime broadening and inhomogeneities in the insulation barrier.

Another cause for rounding can come from the proximity effect [41–44]. This is caused by the presence of leftover aluminium on the bottom electrode of the SIS junction. The actual junction construction is then $\mathrm{Nb/Al \cdot AlO_x/Nb}$. The density of states will then be different than in the ideal SIS junction, and can be calculated from McMillan's recursive equations [41]. (Lifetime broadening can also be incorporated into these equations by including the imaginary component of binding energy.) The proximity effect manifests itself as small knee seen just above the transition (visible in Fig. 2.6).

For good mixer performance, the transition should be as sharp as possible. The best and most non-linear transitions are found at low temperatures.

2.4 Heterodyne mixing with SIS junctions

We have seen in the previous subsections that SIS junctions have extremely non-linear properties, making them ideal for the detection of millimetre-wave signals, including heterodyne mixing. Heterodyne mixers are common electronic components that are used to shift signals either up or down in frequency (up-conversion and down-conversion, respectively). They operate by combining the signal-of-interest ω_{RF} with a pure sinusoidal signal from a local-oscillator ω_{LO}. If these signals are then passed together through a non-linear device, new signals at $|\omega_{\mathrm{RF}} + \omega_{\mathrm{LO}}|$ and $|\omega_{\mathrm{RF}} - \omega_{\mathrm{LO}}|$ are generated, known as the heterodynes. In millimetre-wave astronomy, the signals-of-interest are too high in frequency to be detected directly, so they are down-converted to an intermediate frequency (IF), $\omega_{\mathrm{IF}} = |\omega_{\mathrm{RF}} - \omega_{\mathrm{LO}}|$, which can be amplified, filtered and sampled by digital electronics.

At low frequencies, SIS mixer operation can be described classically, as you would a solid-state diode. At higher frequencies however, in the presence of high energy photons (i.e., when $\hbar\omega/e > \delta V$), the DC I–V curve is no longer sufficient to describe the junction's response, and a quantum mechanical description of quasiparticle tunnelling must be applied. To begin, if a voltage $V(t)$ is applied across an SIS junction where one electrode is grounded, the quasiparticle wave functions in the ungrounded electrode will be modulated by a phase factor[4]:

$$f(t) = \exp\left[\frac{-je}{\hbar}\int_0^t V(t')\,\mathrm{d}t'\right]. \tag{2.15}$$

[4]The phase factor $f(t)$ is the time-dependent portion of the wave function: $\psi_i(x,t) = \psi_i(x) \cdot f(t)$.

The Fourier transform of this phase factor, given by

$$W(\omega) = \int_{-\infty}^{\infty} f(t)\ e^{j\omega t}\ \mathrm{d}t\,, \tag{2.16}$$

can then be used to calculate the time-averaged tunnelling current using the Werthamer expression [45]:

$$\langle I(t)\rangle = \mathrm{Im} \int_{-\infty}^{\infty} W(\omega')\, W^*(\omega'')\ e^{-j(\omega'-\omega'')t}\, I_\mathrm{R}(V_0 + \hbar\omega'/e)\, d\omega'\, d\omega'' \tag{2.17}$$

where I_R is the complex response function of the SIS junction.

In order to recover the response function, note that in the DC case ($V(t)$=V_0), Eqn. 2.17 reduces to

$$I^0_\mathrm{dc}(V_0) = \mathrm{Im}\left\{I_\mathrm{R}(V_0)\right\}\ . \tag{2.18}$$

Therefore, the imaginary component of the response function can be found directly from the measured DC I–V curve. Then by assuming a causal relationship, the real component can be found from the Kramers-Kronig transform of $I^0_\mathrm{dc}(V_0)$ [46, 47],

$$\mathrm{Re}\left\{I_\mathrm{R}(V_0)\right\} \equiv I^0_\mathrm{kk}(V_0) = \frac{1}{\pi}\ \mathcal{P} \int_{-\infty}^{\infty} \frac{I^0_\mathrm{dc}(V') - V'/R_\mathrm{n}}{V' - V}\ \mathrm{d}V' \tag{2.19}$$

where $\mathcal{P}$ represents the Cauchy principal value.

Eqns. 2.15–2.19 provide a full description of quasiparticle tunnelling in the time-domain. Analysing heterodyne mixing in the time-domain, however, is difficult and computationally expensive, especially when the junction is highly non-linear. In the work presented by Tucker and Feldman [12], commonly known as the *Tucker theory*, the analysis is split in two: large-signal analysis to determine the steady-sate condition of the LO source, and small-signal analysis to calculate the conversion between the sideband frequencies. These are presented in the following two subsections.

2.4.1 Large-signal analysis

In Tucker theory, the large-signal analysis determines the SIS junction's response to a strong sinusoidal local-oscillator (LO) signal. Similar to the analysis of a transistor, the goal is to determine the operating point of the junction, linearise the operation, and then calculate the small-signal admittances and transconductances. The large-signal equivalent circuit is shown in Fig. 2.10 with the AC local-oscillator circuit on the left and the DC bias circuit on the right.

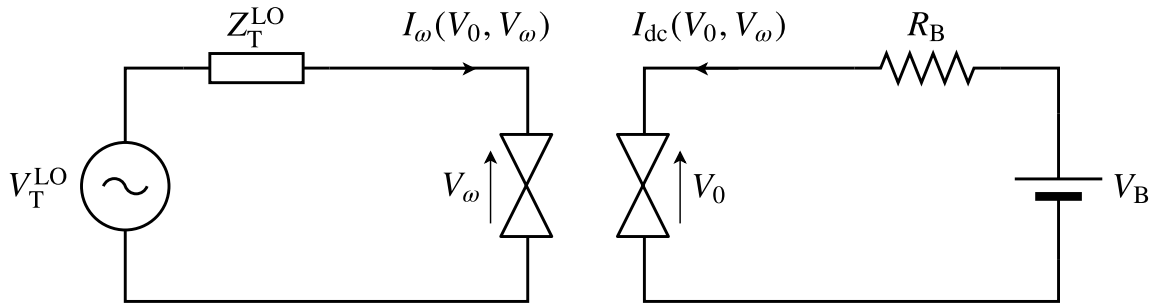

Figure 2.10: Large-signal equivalent circuits for AC and DC analysis (left and right, respectively). The circuit on the left consists of the Thévenin equivalent circuit for the local-oscillator (LO) signal and the AC properties of the junction. The circuit on the right consists of the bias circuit (B) and the DC properties of the junction. Note that the AC and DC tunnelling currents (I_ω and I_{dc}, respectively) both depend on the AC and DC voltages applied to the junction (V_ω and V_0, respectively).

Here, only the fundamental tone of the LO will be considered because all higher-order harmonics are assumed to be short-circuited by the junction's intrinsic capacitance. The voltage drop across the junction can then be written as:

$$V_{\mathrm{large}}(t) = V_0 + V_\omega \cos(\omega_{\mathrm{LO}} t) \tag{2.20}$$

where V_0 is the DC bias voltage and V_ω is the AC voltage amplitude due to the local-oscillator signal. The additional phase factor (Eqn. 2.15) due to the LO is then[5]:

$$f(t) = \exp\left[-\frac{je}{\hbar}\int_0^t V_{\mathrm{large}}(t') - V_0 \ \mathrm{d}t'\right] = \exp\left[-j\alpha \cdot \sin(\omega_{\mathrm{LO}} t)\right] \tag{2.21}$$

$$= \sum_{n=-\infty}^{\infty} J_n(\alpha)\ e^{-jn\omega_{\mathrm{LO}} t} \tag{2.22}$$

where $\alpha \equiv eV_\omega/\hbar\omega_{\mathrm{LO}}$ is the junction drive level, and J_n is the n^{th} order Bessel function of the first kind. The Fourier transform of Eqn. 2.22,

$$W(\omega') = \sum_{n=-\infty}^{\infty} J_n(\alpha) \cdot \delta(\omega' - n\,\omega_{\mathrm{LO}}), \tag{2.23}$$

can be inserted into the Werthamer expression (Eqn. 2.17) to calculate the quasiparticle tunnelling current:

$$I(t) = \mathrm{Im} \sum_{n,m} J_n(\alpha)\, J_{n+m}(\alpha)\, e^{jm\omega_{\mathrm{LO}} t}\, I_{\mathrm{R}}(V_0 + nV_{\mathrm{ph}}) \tag{2.24}$$

[5]By applying the Jacobi-Anger expansion: $e^{jz\sin\theta} \equiv \sum_{n=-\infty}^{\infty} J_n(z)\ e^{jn\theta}$.

where $V_{\rm ph} \equiv \hbar\omega_{\rm LO}/e$ is the equivalent photon voltage. The induced tunnelling current due to the LO signal therefore contains a DC component as well as AC components at harmonics of $\omega_{\rm LO}$.

The DC tunnelling current can be extracted from Eqn. 2.24 by setting $m = 0$:

$$I_{\rm dc}(V_0, V_\omega) = \sum_{n=-\infty}^{\infty} J_n^2(\alpha)\ I_{\rm dc}^0(V_0 + nV_{\rm ph}). \tag{2.25}$$

In this expression, n can be thought of as the number of absorbed photons, $J_n(\alpha)$ as the probability of absorbing n photons, and $V_0 + nV_{\rm ph}$ as the equivalent voltage when n photons are absorbed. This induces the step-like structure in the I–V curve where the width of each step is the photon equivalent voltage $V_{\rm ph}$. The resultant DC relationship, $I_{\rm dc}(V_0)$, is commonly known as the *pumped I–V curve*.

Similarly, the AC tunnelling current at $\omega = \omega_{\rm LO}$ can be obtained by adding together the currents at $m = -1$ and $m = +1$. The result will be a complex expression, $I_\omega = I'_\omega + jI''_\omega$, where the real and imaginary components are given by:

$$I'_\omega = \sum_{n=-\infty}^{\infty} J_n(\alpha)\left[J_{n-1}(\alpha) + J_{n+1}(\alpha)\right] \cdot I_{\rm dc}^0(V_0 + nV_{\rm ph}) \tag{2.26}$$

and

$$I''_\omega = \sum_{n=-\infty}^{\infty} J_n(\alpha)\left[J_{n-1}(\alpha) - J_{n+1}(\alpha)\right] \cdot I_{\rm kk}^0(V_0 + nV_{\rm ph})\,. \tag{2.27}$$

The AC components of the tunnelling current are plotted in Fig. 2.11a as a function of bias voltage. Note that the tunnelling current is typically purely real in the middle of the first photon step, meaning that the tunnelling current is in phase with the applied AC voltage.

So far, the tunnelling current has been calculated based on the voltage drop across the junction. Any real SIS junction, however, will be embedded within a complex circuit involving freespace components, waveguides, and planar circuits. Assuming that only linear components are used, the entire embedding circuit can be reduced to a Thévenin equivalent circuit (recall Fig. 2.10). If the embedding circuit's values are known (i.e., $V_{\rm T}^{\rm LO}$ and $Z_{\rm T}^{\rm LO}$), the challenge then is to solve for V_ω at each bias voltage V_0 that satisfies:

$$V_{\rm T}^{\rm LO} = I_\omega(V_0, V_\omega) \cdot Z_{\rm T}^{\rm LO} + V_\omega. \tag{2.28}$$

This is typically solved numerically because the AC tunnelling current expression is highly non-linear. Generally, capacitive values for $Z_{\rm T}^{\rm LO}$ result in lower dynamic

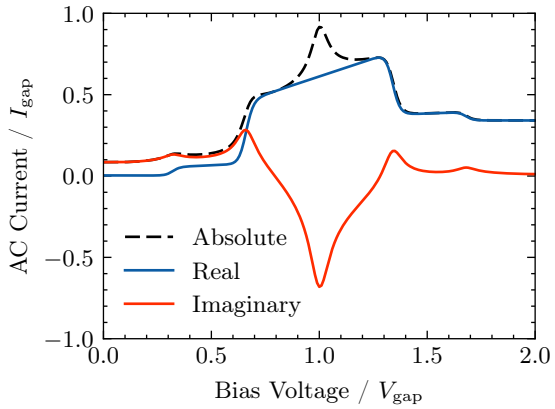

(a) AC tunnelling currents. Calculated assuming a constant junction drive level of $\alpha(V_0)$=1.

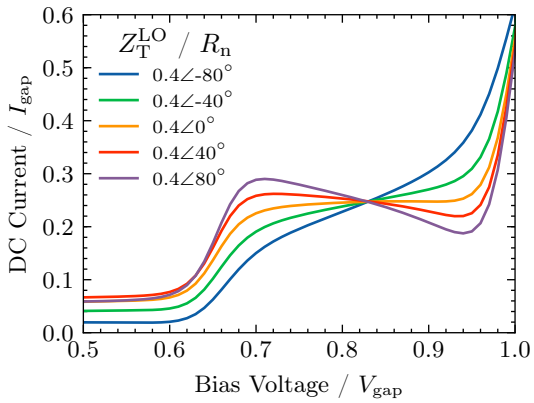

(b) The first photon step as a function of embedding impedance, i.e., the Thévenin impedance for the LO signal, Z_T^{LO}.

Figure 2.11: An example of large-signal analysis (calculated assuming a photon equivalent voltage of $V_{ph} = 0.35 \cdot V_{gap}$).

resistances while inductive values result in flat or even negative dynamic resistances (Fig. 2.11b). With V_ω known, or equivalently the junction drive level α, the small-signal circuit can be analysed.

2.4.2 Small-signal analysis

The small-signal analysis in Tucker theory assumes that once the operating point of the SIS junction has been determined, the circuit can be linearised to calculate the conversion between the sidebands. The small-signal circuit diagram for a 3-port heterodyne receiver is shown in Fig 2.12. This 3-port model is valid assuming that the higher-order harmonics are short-circuited by the junction's intrinsic capacitance. The port on the left represents the strong LO tone, while the ports on the right represent the small-signal frequencies. Each small-signal frequency is represented by a Norton equivalent circuit (i.e., an admittance Y_m and a current source $\mathscr{I}_m$) and a coefficient m where

$$\omega_m = |\omega_{IF} + m \cdot \omega_{LO}| \,. \tag{2.29}$$

For the 3-port model, we only consider the coefficients $m = -1$, $m = 0$ and $m = +1$. Using this notation, the upper sideband (USB) signal is at $\omega_1 = |\omega_{IF} + \omega_{LO}|$, the lower sideband (LSB) signal is at $\omega_{-1} = |\omega_{IF} - \omega_{LO}|$, and the IF output is at $\omega_0 = \omega_{IF}$. Note that there is no current source in the IF circuit because this is the output and we do not expect any input signal at this frequency. For a dual sideband mixer, the goal is to convert the signals at ω_1 and ω_{-1}, to the IF frequency ω_0.

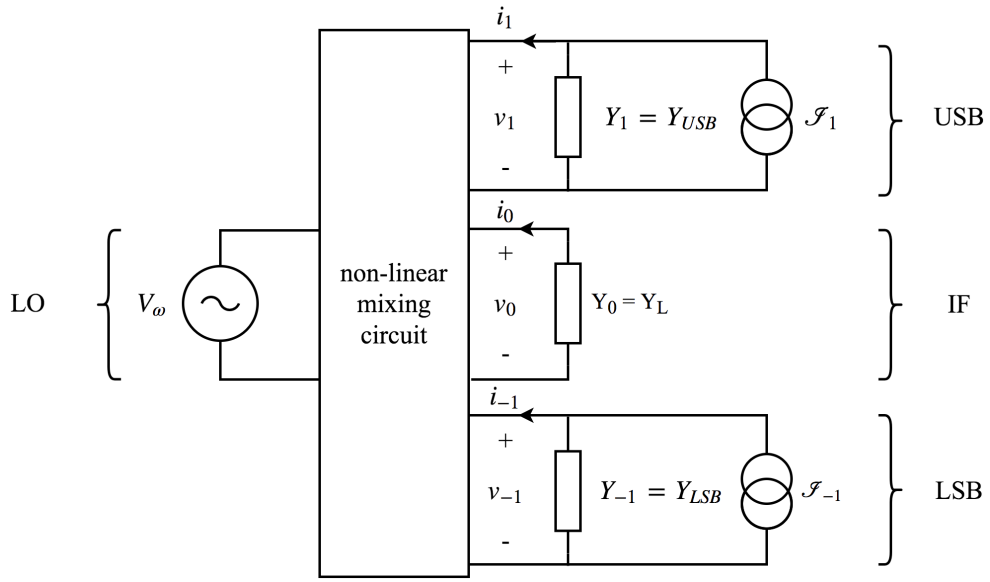

Figure 2.12: Small-signal circuit model for 3-port heterodyne mixing. The circuit for the LO is on the left, and the sideband signals are on the right.

The small-signal voltages and currents of all components can be combined and represented by

$$v_{\text{small}}(t) = \text{Re} \sum_m v_m \; e^{+j\omega_m t}, \quad \text{and} \tag{2.30}$$

$$i_{\text{small}}(t) = \text{Re} \sum_m i_m \; e^{+j\omega_m t}. \tag{2.31}$$

The conversion between i_m and v_m is represented by the linear relation:

$$i_m = \sum_{m'} Y_{mm'} v_{m'} \tag{2.32}$$

where $Y_{mm'}$ is the small-signal admittance matrix. The values of the small-signal admittances $Y_{mm'} = G_{mm'} + jB_{mm'}$ are found from [12]:

$$\begin{aligned} G_{mm'}(V_0, V_\omega) = & \frac{e}{2\,\hbar\,\omega_{m'}} \sum_{n,n'=-\infty}^{\infty} J_n(\alpha)\, J_{n'}(\alpha)\, \delta_{m-m',n'-n} \cdot \\ & \left\{ \left[+I^0_{\text{dc}} \left(V_0 + n' \frac{\hbar\,\omega}{e} + \frac{\hbar\,\omega_{m'}}{e} \right) - I^0_{\text{dc}} \left(V_0 + n' \frac{\hbar\,\omega}{e} \right) \right] + \right. \\ & \left. \left[-I^0_{\text{dc}} \left(V_0 + n \frac{\hbar\,\omega}{e} - \frac{\hbar\,\omega_{m'}}{e} \right) + I^0_{\text{dc}} \left(V_0 + n \frac{\hbar\,\omega}{e} \right) \right] \right\}, \end{aligned} \tag{2.33}$$

and

$$B_{mm'}(V_0, V_\omega) = \frac{e}{2\,\hbar\,\omega_{m'}} \sum_{n,n'=-\infty}^{\infty} J_n(\alpha)\, J_{n'}(\alpha)\, \delta_{m-m',n'-n} \cdot \left\{ \left[+I^0_{\rm kk}\left(V_0 + n'\frac{\hbar\,\omega}{e} + \frac{\hbar\,\omega_{m'}}{e}\right) - I^0_{\rm kk}\left(V_0 + n'\frac{\hbar\,\omega}{e}\right)\right] - \left[-I^0_{\rm kk}\left(V_0 + n\frac{\hbar\,\omega}{e} - \frac{\hbar\,\omega_{m'}}{e}\right) + I^0_{\rm kk}\left(V_0 + n\frac{\hbar\,\omega}{e}\right)\right]\right\} \tag{2.34}$$

where $\delta_{i,j}$ is the Kronecker delta function[6].

Once $Y_{mm'}$ is calculated, the conversion between small-signal current sources $\mathscr{I}_m$ and the different sidebands can be represented by the linear relation:

$$\mathscr{I}_m = \sum_{m'} (Y_{mm'} + Y_m \delta_{m,m'})\; v_{m'}. \tag{2.35}$$

For the 3-port case, Eqn. 2.35 can be represented in matrix form:

$$\begin{bmatrix} \mathscr{I}_1 \\ 0 \\ \mathscr{I}_{-1} \end{bmatrix} = \begin{bmatrix} Y_{1,1} + Y_{\rm USB} & Y_{1,0} & Y_{1,-1} \\ Y_{0,1} & Y_{0,0} + Y_L & Y_{0,-1} \\ Y_{-1,1} & Y_{-1,0} & Y_{-1,-1} + Y_{\rm LSB} \end{bmatrix} \begin{bmatrix} v_1 \\ v_0 \\ v_{-1} \end{bmatrix} \tag{2.36}$$

where $Y_{\rm USB} = Y_1$ and $Y_{\rm LSB} = Y_{-1}$ are the admittances of the upper and lower sideband circuits, respectively, and $Y_{\rm L} = Y_0$ is the admittance of the IF load. The small-signal voltages can then be found by inverting Eqn. 2.36:

$$\begin{bmatrix} v_1 \\ v_0 \\ v_{-1} \end{bmatrix} = \begin{bmatrix} Y_{1,1} + Y_{\rm USB} & Y_{1,0} & Y_{1,-1} \\ Y_{0,1} & Y_{0,0} + Y_L & Y_{0,-1} \\ Y_{-1,1} & Y_{-1,0} & Y_{-1,-1} + Y_{\rm LSB} \end{bmatrix}^{-1} \begin{bmatrix} \mathscr{I}_1 \\ 0 \\ \mathscr{I}_{-1} \end{bmatrix} \tag{2.37}$$

or

$$v_m = \sum_m Z_{mm'} \mathscr{I}_{m'} \tag{2.38}$$

where $Z_{mm'}$ represents the elements of the inverted matrix in Eqn. 2.37. From Eqn. 2.38, the output voltage at the IF frequency is then:

$$v_0 = Z_{00} \sum_m \lambda_{0m} \mathscr{I}_m \tag{2.39}$$

where λ_{0m} is given by

$$\lambda_{0m} = Z_{0m}/Z_{00}\,. \tag{2.40}$$

[6]The Kronecker delta function is: $\delta_{i,j} = \begin{cases} 1, & i = j \\ 0, & i \neq j \end{cases}$.

This results in an IF output power of $P_{\text{out}} = \frac{1}{2} G_{\text{L}} |v_0|^2$. By calculating the available power from the signal sidebands, the conversion efficiency is calculated as

$$G_{\text{c}} = \frac{P_{\text{out}}}{P_{\text{in}}} = 4 \left(G_{\text{USB}} + G_{\text{LSB}} \right) G_{\text{L}} \left| Z_{01} \right|^2 \tag{2.41}$$

where G_{USB}, G_{LSB} and G_{L} are the real components of Y_{USB}, Y_{LSB} and Y_{L}, respectively. The small-signal model can also be used to estimate the mixer's noise temperature, but this is outside the scope of this chapter (see [12]).

2.5 Cooper pair tunnelling

Although SIS mixers are designed specifically for quasiparticle tunnelling, Cooper pair tunnelling has practical implications on the mixers because pair tunnelling can contribute additional shot noise if it is not properly suppressed. Provided that two superconductors are weakly coupled, such as they are in SIS junctions, Cooper pairs are able to tunnel through the barrier without any loss in energy. Cooper pair tunnelling was first described mathematically by Josephson in 1962 [31] and then demonstrated experimentally by Anderson and Rowell in 1963 [48]. Josephson's tunnelling relations for voltage and current are given respectively by [31]

$$v(t) = \frac{\hbar}{2e} \frac{d\varphi}{dt} , \tag{2.42}$$

and

$$i(t) = I_{\text{c}} \sin(\varphi(t)) \tag{2.43}$$

where φ is the phase difference between the Cooper pair wave functions on either side of the barrier, and I_{c} is the critical current, which is characteristic of the materials, dimensions and temperature of an SIS junction. From [45], the critical current is given by:

$$I_{\text{c}} = \frac{\pi \, \Delta(T)}{2 \, e \, R_{\text{n}}} \tanh \left(\frac{\Delta(T)}{2 k_B T} \right) , \tag{2.44}$$

which reduces to $I_{\text{c}} \approx \pi \Delta_0 / 2 e R_{\text{n}}$ at low temperatures ($T \ll T_{\text{c}}$). To solve for the Cooper pair tunnelling current due to an applied voltage $v(t)$, Eqn. 2.42 and 2.43 can be combined to give

$$i(t) = I_{\text{c}} \sin \left(\varphi_0 + \frac{2e}{\hbar} \int_0^t v(t') \, dt' \right) \tag{2.45}$$

where φ_0 is a constant from the integration of $v(t)$ and equal to the phase difference between the two electrodes at $t = 0$.

Although Eqn. 2.45 shows that Cooper pair tunnelling is a highly non-linear function of voltage, several special cases can be identified. To begin with, if there is no applied potential, $v(t) = 0$, Eqn. 2.45 reduces to

$$i(t) = I_c \cdot \sin(\varphi_0) \ . \tag{2.46}$$

Therefore, even with zero voltage applied across the junction, the Cooper pair tunnelling current takes on a finite value between $-I_c$ and $+I_c$. This is the *DC Josephson effect*. Another special case can be found by applying a constant voltage across the junction, $v(t) = V_0$. In this case, Eqn. 2.45 becomes

$$i(t) = I_c \cdot \sin\left[\varphi_0 + 2\pi \cdot \left(\frac{2eV_0}{h}\right) \cdot t\right], \tag{2.47}$$

which has the form of a tunnelling current oscillating at a frequency of $2eV_0/h$ or $\sim$483.6 GHz/mV. This is the *AC Josephson effect*, and when it is combined with the resistance and capacitance of the junction, it manifests as additional DC tunnelling current (seen in Fig. 2.13).

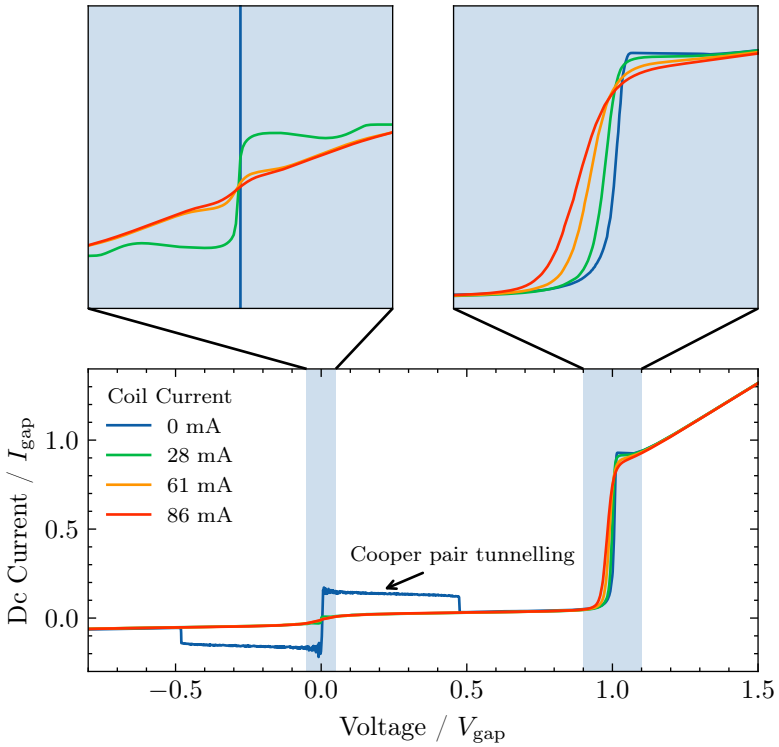

Figure 2.13: Cooper pair tunnelling in an SIS junction. A magnetic field can be applied to suppress this current; however, this has the added effect of rounding the transition. The figure on the top left magnifies the DC tunnelling current around the origin, and the figure on the top right magnifies the current around the gap voltage.

Suppressing Josephson tunnelling

Cooper pair tunnelling has be suppressed in SIS mixers because it produces additional shot noise. This can be done by applying an external magnetic field parallel to the insulation barrier. This introduces a spatial modulation of the phase difference φ and destroys Cooper pair coherence across the barrier at certain magnetic field intensities. The critical current's amplitude is related to the magnetic field by [35],

$$I_{\mathrm{c}}(x) = 2 \cdot I_{\mathrm{c}}(0) \left| \frac{J_1(x)}{x} \right| \tag{2.48}$$

where $x = \Phi/\Phi_0$, Φ is the magnetic flux passing through the insulation barrier, $\Phi_0 = h/2e$ is the quantum of magnetic flux, and J_1 is a Bessel function of the first kind. Therefore, minima are found whenever $J_1(x) = 0$. Higher minima result in better suppression; however, the magnetic field also has the effect of reducing the non-linearity of the junction (Fig. 2.13). Typically, the third minimum is a good compromise.

The Fiske step

One positive aspect of the AC Josephson effect is that it can be used to estimate the tuning frequency of an SIS mixer, i.e., the frequency at which there is very good coupling between the planar circuit and the SIS junction. Whenever $2\,e\,V_0{=}h\,\nu_{\mathrm{tune}}$, the AC Josephson effect matches the receiver's tuning frequency ν_{tune} leading to a small peak called the Fiske step. For example, if a mixer has a tuning frequency of 230 GHz, a spike should be seen at $\nu_{\mathrm{tune}}{\cdot}h/2e \sim 0.475$ mV. The SIS junction in Fig. 2.13 is tuned at two poles for broadband operation, so the Fiske step is not visible.

2.6 Characterising SIS mixer performance

There are three metrics that are commonly used to characterise the performance of SIS mixers: noise temperature, conversion efficiency, and instantaneous bandwidth. These can be calculated from the Y-factor technique, which is described below. Additionally, the tuning of the planar circuit can be analysed using the impedance recovery technique, described in Sec. 2.6.2, which heavily influences the noise temperature and gain.

2.6.1 Noise temperature

The Y-factor is a measure of a mixer's sensitivity. It is determined by pumping the mixer at a given LO frequency, exposing the mixer individually to hot and then cold black body radiation (at T_{H} and T_{C}, respectively) and comparing the down-converted IF output power P_{out} from each temperature. The ratio of output powers is the Y-factor, defined as:

$$Y \equiv \frac{P_{\mathrm{out}}(T_{\mathrm{H}})}{P_{\mathrm{out}}(T_{\mathrm{C}})}\,. \tag{2.49}$$

This Y-factor can either be calculated as a function of bias voltage (by integrating P_{out} across a range of IF frequencies with a detector diode), or as a function of IF frequency (by measuring P_{out} with a spectrum analyser). To fully characterise the RF performance of the mixer, these measurements are then completed at multiple LO frequencies across the tuning range of the receiver.

The noise properties of an SIS mixer are described by the equivalent input noise power per unit bandwidth, $P_{\mathrm{N}}/\Delta\nu$, and it is common practice to represent this noise power as a temperature: $T_{\mathrm{N}} \equiv P_{\mathrm{N}}/(k_{\mathrm{B}} \cdot \Delta\nu)$. Provided with a set of measurements made above the Rayleigh-Jeans limit[7], a straight line will connect the output power from the hot and cold load measurements (Fig. 2.14). The x-intercept then represents the noise temperature T_{N} referred back to the input of the system, and we can solve for T_{N} using

$$T_{\mathrm{N}} = \frac{T_{\mathrm{H}} - Y\,T_{\mathrm{C}}}{Y - 1}\,. \tag{2.50}$$

Note that if the black body loads are not above the Rayleigh-Jeans limit (i.e., if $T_{\mathrm{in}} \not\gg \hbar\omega/k_{\mathrm{B}} \approx 11$ K at 230 GHz), the Callen-Welton equations [49] must be used instead of Eqn. 2.50. These equations use the Planck formula for black body radiation instead of the Rayleigh-Jeans approximation.

An example of the Y-factor technique with experimental data is shown in Fig. 2.15. This experiment used a microwave absorber at room temperature ($T_{\mathrm{H}} \approx 295$ K) and a microwave absorber immersed in liquid nitrogen ($T_{\mathrm{C}} \approx 78.5$ K) for the hot and cold black body loads, respectively. In Fig. 2.15a, the IF output power resulting from the hot and cold loads is shown in red and blue, respectively. The ratio of these two powers, i.e., the Y-factor, is then shown in blue in Fig. 2.15b with the noise temperature calculated from Eqn. 2.50 shown in red. In this specific case, the best noise temperature was 37.7 K at a bias voltage of 2.2 mV.

[7] At temperatures above the Rayleigh-Jeans limit ($T \gg \hbar\omega/k_{\mathrm{B}}$), the black body spectral radiance is proportional to temperature. Therefore, the input power will also be proportional to the temperature, $P_{\mathrm{in}} \propto T_{\mathrm{in}}$.

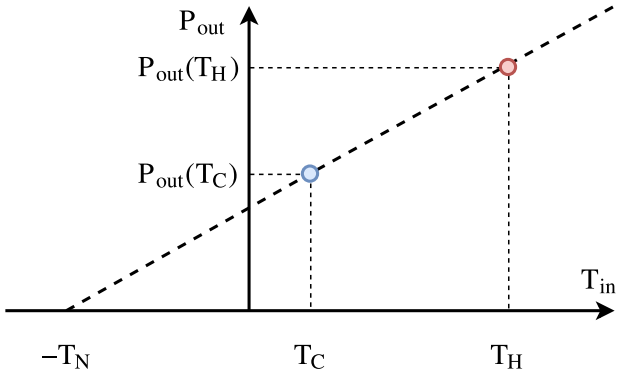

Figure 2.14: The Y-factor technique is used to calculate the noise temperature T_{N} of the receiver from measurements of hot and cold black body loads (at temperatures T_{H} and T_{C}, respectively). Here, T_{in} is the temperature of the black body load (the input signal) and P_{out} is the power of the down-converted IF signal. Note that P_{out} can either be measured as a function of bias voltage using a detector diode, or as a function of IF frequency using a spectrum analyser.

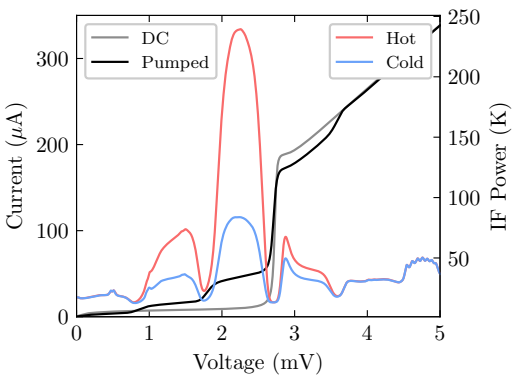

(a) The measured DC tunnelling current (left axis) and IF power from the hot and cold black body loads (right axis).

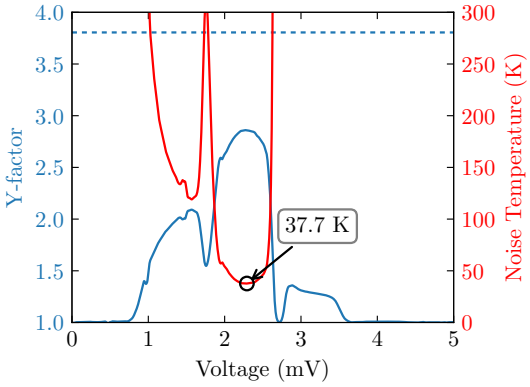

(b) The Y-factor and noise temperature calculations. The dashed line represents the maximum possible Y-factor: $Y_{\mathrm{max}} = T_{\mathrm{H}}/T_{\mathrm{C}}$.

Figure 2.15: An example of Y-factor analysis using experimental data. Here, the IF output power was filtered using a 4–6 GHz band pass filter and then integrated across this band using a detector diode.

Conversion efficiency

Before the down-converted signal from the SIS junction is measured, it first passes through multiple low noise amplifiers, filters and attenuators. Since the gains and losses of these components are not known exactly, the measured power is simply recorded in arbitrary units, A.U.. This is acceptable for noise temperature analysis since only relative powers are needed, but calculating the conversion efficiency requires calibrated values.

To calibrate the output power, the SIS junction can be operated as a calibrated noise source. This is possible because the quasiparticle tunnelling current gives rise to a well-defined shot noise with an effective temperature of [50]:

$$T_{\text{shot}}(V_0) = \frac{e}{2\,k_{\text{B}}}\, I^0_{\text{dc}}\, R_{\text{dyn}} \coth\left(\frac{e\,V_0}{2\,k_{\text{B}} T_{\text{amb}}}\right) \tag{2.51}$$

where I^0_{dc} is the DC tunnelling current, $R_{\text{dyn}} = \left(\mathrm{d}I^0_{\text{dc}}/\mathrm{d}V_0\right)^{-1}$ is the dynamic resistance, and T_{amb} is the ambient temperature of the SIS junction. At bias voltages above the gap, this shot noise increases linearly with a slope of $e/2k_{\text{B}}$ or 5.8 K/mV, and this linear relationship is seen in experimental data, e.g., Fig. 2.16. If a linear trend is fit to the slope of the shot noise in the experimental data, the IF output power can be calibrated by multiplying P_{out} by:

$$X_{\text{calibration}} = \frac{5.8\ [\text{K/mV}] \cdot \left(1 - |\Gamma_{\text{shot}}|^2\right)}{\text{experimental shot noise slope [A.U./mV]}}\,. \tag{2.52}$$

The result is the output power as a temperature, $T_{\text{out}} = P_{\text{out}} \cdot X_{\text{calibration}}$, measured in Kelvins. Note that the $\left(1 - |\Gamma_{\text{shot}}|^2\right)$ term in Eqn. 2.52 represents the impedance mismatch between the SIS junction and the IF circuit. The reflection coefficient is given by:

$$\Gamma_{\text{shot}} = \frac{Z_{\text{IF}} - R_{\text{dyn}}}{Z_{\text{IF}} + R_{\text{dyn}}} \tag{2.53}$$

where Z_{IF} is the input impedance of the IF circuit and R_{dyn} is the dynamic resistance of the SIS junction biased above the gap (approximately equal to the normal resistance). Since Z_{IF} changes with IF frequency, in this thesis we assume a reference plane with an input impedance equal to R_{n}, which allows us to ignore the reflection term in Eqn. 2.52. This is described in more detail in Appendix A.

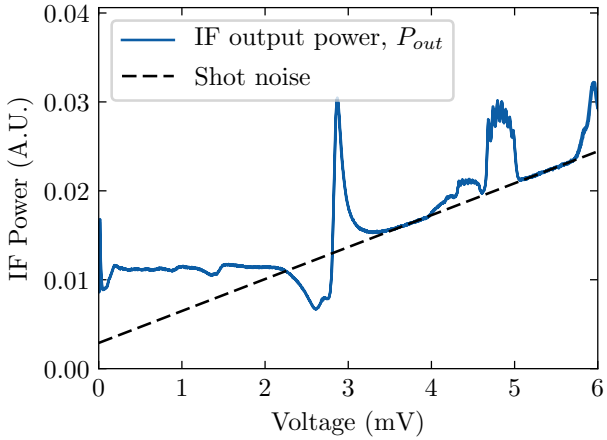

Figure 2.16: Measured IF output power (with no LO signal applied to the junction). Above the gap voltage, the IF output power increases at a constant 5.8 K/mV. This fact can be used to calibrate the output power using Eqn. 2.52.

With the IF output power calibrated, the conversion efficiency[8] is simply,

$$G_c = \frac{\Delta T_{\text{out}}}{\Delta T_{\text{in}}} = \frac{T_{\text{out}}(T_{\text{H}}) - T_{\text{out}}(T_{\text{C}})}{T_{\text{H}} - T_{\text{C}}}. \tag{2.54}$$

This value is equal to $G_c = G_{\text{RF}} \cdot G_{\text{SIS}}$ where G_{RF} is the gain of the RF circuit (everything on the RF side of the junction), and G_{SIS} is the conversion efficiency of the SIS junction. Tucker predicted in 1979 that SIS junctions can have conversion efficiencies greater than unity [11], which is impossible to achieve with classical passive mixers. Realistically however, SIS mixers with G_c>1 typically have unstable behaviour due to the negative dynamic resistance of the I–V curve, and conversion efficiencies just below unity are often more desirable.

Noise contributions

The noise temperature calculated from the Y-factor technique is the noise temperature of the entire system (T_{N} in Fig. 2.17). This noise is composed of multiple noise contributions from the various components in the receiver chain. Since T_{N} is the noise referred back to the input of the system, these noise contributions cascade as

$$T_{\text{N}} = T_1 + \frac{T_2}{G_1} + \frac{T_3}{G_1 G_2} + ... + \frac{T_n}{G_1 G_2 ... G_{n-1}} \tag{2.55}$$

[8] "Conversion efficiency" is used interchangeably with "conversion gain". Since the value is normally less than unity, I believe conversion efficiency is a more representative term. The variable G_c is used to represent both.

where T_i and G_i are the noise temperature and gain, respectively, of the i^{th} component (in order from input to output).

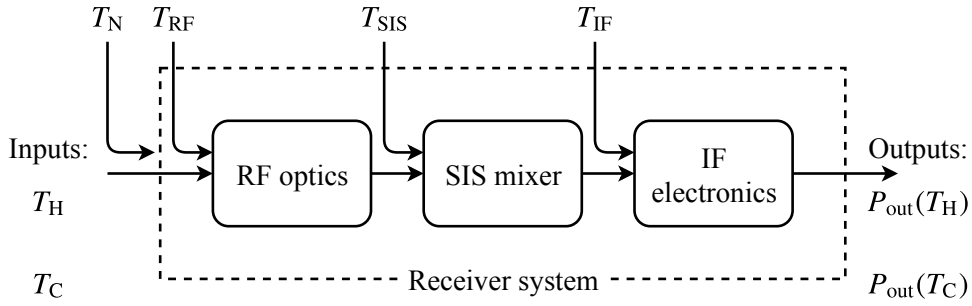

Figure 2.17: Noise cascading through an SIS receiver. Here, the receiver is divided into three main components: the RF sub-system (consisting of optical components and the planar circuit of the SIS device), the SIS mixer itself, and the IF sub-system (mainly electronic components). The overall noise temperature of the receiver T_N is the noise from the three sub-systems referred back to the input of the receiver. This is calculated in Eqn. 2.57.

In the case of an SIS receiver, the system can be divided into three main sub-systems: the RF sub-system, the SIS junction, and the IF circuit (Fig. 2.17). The noise contribution of the RF sub-system encompasses everything between the hot/cold loads and the SIS junction. This includes thermal noise from the beam splitter, the cryostat window, the horn, the waveguide and the device's planar circuit. These are all passive components, each of which adds an effective noise temperature of

$$T_{\text{eff}} = (L - 1)\, T_{\text{phys}} \tag{2.56}$$

where L is the component's loss (inverse of gain) and T_{phys} is the physical temperature. Conversely, the noise contribution of the IF circuit is dominated by an active component: the cryogenic LNA. The noise properties of the components after the LNA are mostly insignificant due to the LNA's large signal gain ($G_{\text{LNA}} \approx 30$ dB $= \times 1000$). Using Eqn. 2.55, the overall noise temperature of the system is then written as

$$T_N = T_{RF} + \frac{T_{SIS}}{G_{RF}} + \frac{T_{IF}}{G_{RF} \cdot G_{SIS}}\,, \tag{2.57}$$

which corresponds to Fig. 2.17.

RF noise contribution

Empirical tools have been developed to isolate the noise contributions of the different sub-systems. One such tool for the RF sub-system is the technique of intersecting lines [51]. For this technique, the hot/cold load measurements are completed for a

range of LO powers. As the LO power drops, the gain of the SIS mixer G_{SIS} also decreases. If the output power (P_{out}) is then plotted against the input load temperature (T_{in}) for each LO power level, the lines connecting the hot/cold measurements will intersect at $(-T_x, P_x)$. Ke and Feldman [52] explained that T_x represents the RF noise contribution because this is the noise component that is independent of LO power and therefore independent of mixer gain as well (whereas the IF and SIS noise contributions should be heavily dependent on mixer gain).

The technique of intersecting lines has the downside that it can be difficult to identify the intersection point. For N different LO powers, there will be $N(N-1)/2$ unique intersection points. Tong et al. [53] revised this technique so that noise temperature is instead plotted against relative conversion loss, $L_{\mathrm{c}} = G_{\mathrm{c}}^{-1}$. The equation for this line is then

$$T_{\mathrm{N}} = mL_c + T_x, \tag{2.58}$$

and the y-intercept is the noise component that is independent of mixer conversion gain (Fig. 2.18). This noise will mostly be due to passive attenuation in the RF optics, but it could also contain a component of the SIS noise contribution that is independent of conversion gain.

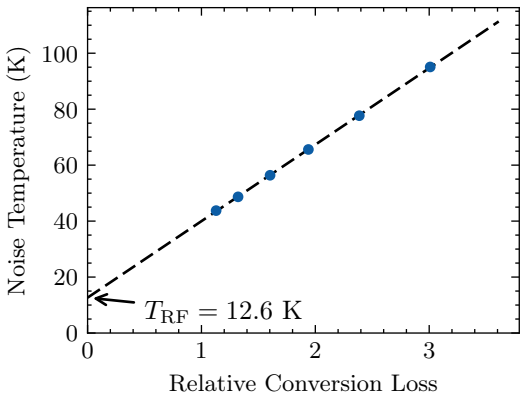

Figure 2.18: Calculating the RF noise contribution by using the technique of intersecting lines (the revised method developed by Tong et al. [53]). The y-intercept represents the noise contribution that is independent of mixer gain. This is the RF noise contribution.

IF noise contribution

In addition to calibrating the output power, the shot noise slope can also be used to estimate the IF noise contribution using the technique first suggested by Woody et al. [54]. If T_{out} is measured from an unpumped junction, the noise seen above the gap will be a combination of shot noise (T_{shot}), which is a function of V_0, and the

IF noise contribution (T_{IF}), which is not a function of V_0. The IF noise contribution can then be isolated by measuring the offset between T_{out} and the theoretical shot noise T_{shot}. In practice, this is done by fitting a line to the DC I–V curve above the gap and then finding the point at which this line crosses the x-intercept, V_{int}. This point is also the voltage where the shot noise slope would cross the x-intercept if T_{IF} were zero. Therefore, if a line is fit to T_{out} above the gap, the value of this line at V_{int} represents the IF noise contribution. An example of this technique is shown in Fig. 2.19.

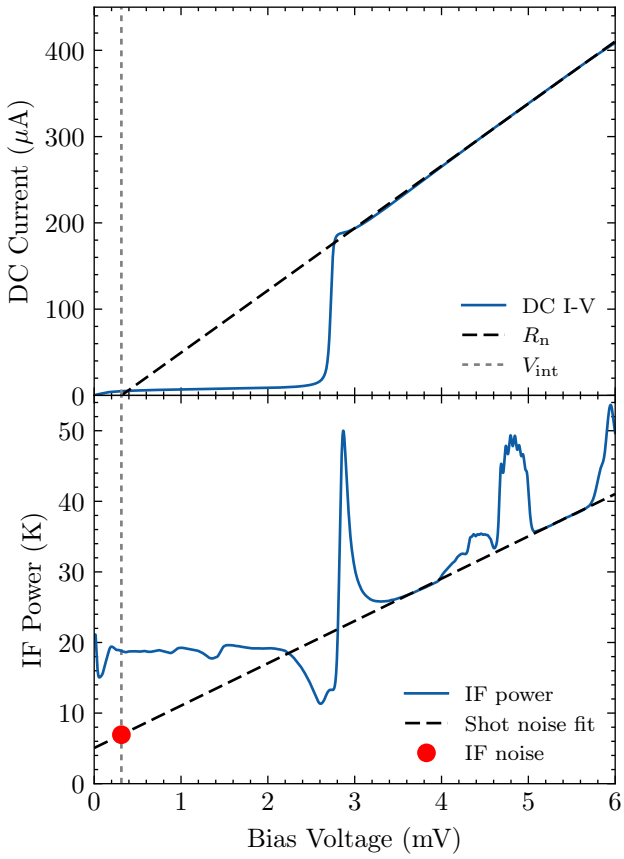

Figure 2.19: Estimating the IF noise T_{IF} from the shot noise slope. The top figure shows the DC I–V curve and the bottom figure shows the IF power (with no LO signal present). Above the gap, the IF power increases linearly. By extrapolating this line back to V_{int}, we are able to estimate the IF noise T_{IF}.

2.6.2 Impedance recovery

Modern SIS junctions are embedded within complex systems used to couple the freespace signals to the junction as efficiently as possible. This involves optical components, feed horns, waveguides and planar circuits. Since these components are purely

linear, they can be reduced to a Thévenin equivalent circuit (recall the large-signal circuit from Fig. 2.10). For maximum power transfer, the Thévenin impedance should be the complex conjugate of the junction's AC impedance. If there is an impedance mismatch, it will result in a loss in coupling and higher noise temperatures.

To ensure that the system has been designed properly, the embedding impedance can be recovered from the experimental pumped I–V curve. The technique described below is the "RF Voltage Match Method" developed by Skalare [55]. To begin, recall the AC and DC large-signal circuits from Fig. 2.10. The DC and pumped I–V curves are known directly from measured data: $I^0_{\rm dc}(V_0)$ and $I_{\rm dc}(V_0)$, respectively. The AC voltage across the junction, $V_{\omega i}$, can then be recovered by fitting the theoretical expression for the DC tunnelling current (Eqn. 2.25) to the experimental pumped I–V curve at each bias point, v_i. The junction can then be replaced by a linear impedance element, $Z_{\omega i}$, by dividing $V_{\omega i}$ by the AC tunnelling current, $I_{\omega i}$ (Eqn. 2.26).

The problem then is to find the best embedding circuit combination (i.e., $V_{\rm T}^{\rm LO}$ and $Z_{\rm T}^{\rm LO}$) that minimises the error function [55],

$$\epsilon = \sum_i (V_{\omega i} - |V'_{\omega i}|)^2 \tag{2.59}$$

over a given range of bias voltages. In Eqn. 2.59, $V_{\omega i}$ is the recovered AC junction voltage, and $V'_{\omega i}$ is the AC junction voltage that results from a given embedding circuit ($V_{\rm T}^{\rm LO}$ and $Z_{\rm T}^{\rm LO}$). S. Withington, *et al.* [56] expanded the work done by Skalare [55] to provide an easy to use error function:

$$\epsilon = \left(\sum_{i=1}^{N} |V_{\omega i}|^2\right) - \left(\sum_{i=1}^{N} \left|\frac{Z_{\omega i}\cdot V_{\omega i}}{Z_{\rm T}^{\rm LO}+Z_{\omega i}}\right|\right)^2 \cdot \left(\sum_{i=1}^{N} \left|\frac{Z_{\omega i}}{Z_{\rm T}^{\rm LO}+Z_{\omega i}}\right|\right)^{-1}. \tag{2.60}$$

This error function can be calculated over a range of embedding impedances to find the optimum value for $Z_{\rm T}^{\rm LO}$ (e.g., Fig. 2.20a). The embedding voltage can then be found from:

$$|V_{\rm T}^{\rm LO}| = \left(\sum_{i=1}^{N} \left|\frac{Z_{\omega i}}{Z_{\rm T}^{\rm LO}+Z_{\omega i}}\right|\right)^{-1}, \tag{2.61}$$

which in conjunction with $Z_{\rm T}^{\rm LO}$ completes the Thévenin circuit. These two values can then be combined to generate a simulated I–V curve (e.g., Fig. 2.20b).

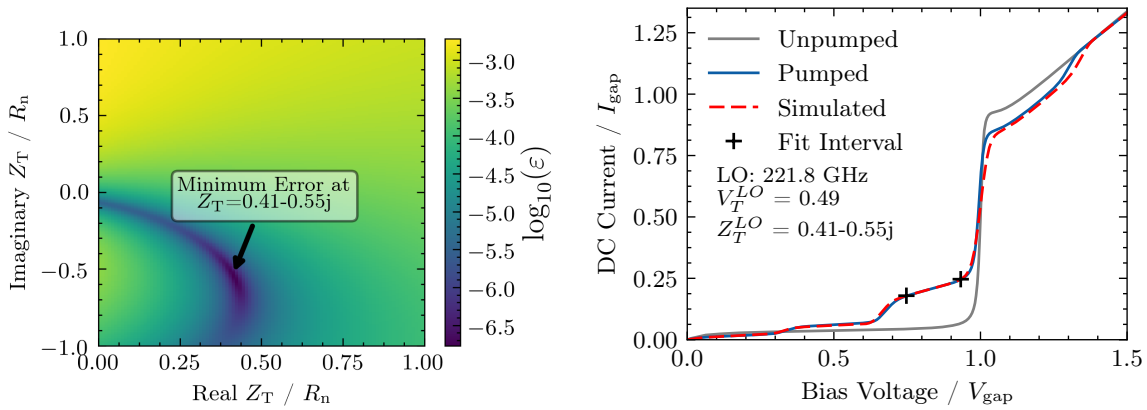

(a) The error surface calculated from Eqn. 2.60. The minimum error in this plot is the recovered embedding impedance Z_T^{LO}.

(b) Simulating an I–V curve from the recovered embedding circuit. Note that the error surface was only calculated over first photon step (i.e., the fit interval labelled above).

Figure 2.20: An example of impedance recovery.

2.7 Conclusion

Quasiparticle tunnelling in SIS junctions can be used to create state-of-the-art heterodyne mixers at millimetre-wave frequencies. Unlike with classical mixers, a quantum mechanical description is required to fully capture SIS mixer operation. This was first provided by Tucker who also showed that SIS mixers are capable of quantum limited noise temperatures and conversion efficiencies greater than unity. In reality however, the receiver noise temperatures will be increased by losses in the transmission lines that are used to couple power to the device. Experimentally, the noise temperature, gain and instantaneous bandwidth can be measured using the Y-factor method, while the tuning of the embedding circuit can be recovered from the pumped I–V curve. At frequencies below the gap, receiver noise temperatures of $\sim$3 times the quantum limit can be achieved.

Chapter 3

A 230 GHz Wide IFBW SIS Receiver

3.1 Introduction

Much of the recent work on SIS mixers has focused on broadening the IF bandwidth (IFBW) of the receivers. This is the bandwidth of the down-converted signal, which also sets the range of frequencies that can be measured simultaneously, without retuning the local-oscillator. Although wide IFBW does not increase a receiver's sensitivity for spectral lines, it does save imaging time in other ways. For example, wide IFBW expands the survey depth to allow multiple spectral lines to be measured simultaneously, reduces the likelihood that LO retuning is required when transitioning between sources with different redshifts, and facilitates calibration because the measured flux from continuum sources is larger.

Creating wide IFBW SIS mixers is challenging, in part, due to the intrinsic geometry of SIS junctions. At IF frequencies, the output impedance of an SIS junction can be represented by the dynamic resistance of the I–V curve [12] in parallel with the intrinsic capacitance of the SIS junction (Fig. 3.1). Together with additional capacitance from the RF circuit, this forms a low pass filter that limits the upper IF frequency range. To minimise this effect, the junction capacitance can be reduced by using small high current density junctions [57] or by instead fabricating multiple junctions in series [58]. Similarly, the capacitance of the RF circuit can be reduced by limiting the surface area of the circuit, but ultimately this leads to a trade-off between RF and IF bandwidth.

The IFBW can also be limited by the IF measurement chain, especially by the cryogenic isolator and low noise amplifier (LNA). Recently, the performance of cryogenic LNAs has greatly improved (e.g., [59, 60]); however, cryogenic isolators still

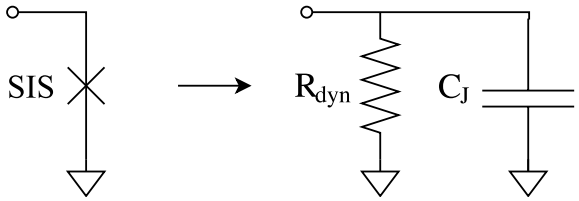

Figure 3.1: Lumped element representation of an SIS junction at IF frequencies. R_{dyn} is the dynamic resistance of the pumped I–V curve, and C_{J} is the intrinsic capacitance of the junction.

limit the IFBW to less than a decade of bandwidth. The isolator can be removed, but in this case the LNA should either be integrated directly into the SIS mixer block to reduce the electrical distance [24, 57, 61, 62] or an IF tuning circuit should be used to match the output impedance of the SIS device to the LNA [63]. There are practical limitations, however, to both of these techniques.

The current generation of SIS receivers, commissioned around 230 GHz, have IFBWs ranging between 4 and 8 GHz per sideband and polarisation (Table 3.1), and now receiver development is typically aiming for IFBWs of over 12 GHz. For example, the Submillimeter Array (SMA) currently uses receivers with a 4–12 GHz IF range [64], but they are planning on extending this to 4–16 GHz in the next phase of receiver development [65]. Likewise, the Atacama Large Millimetre Array (ALMA) has decided to extend the IF range of their receivers to 4–12 GHz [66, 67], and recently a group working on band-8 (RF: 385–500 GHz) has reported a high current density SIS mixer integrated with an LNA that has a 3–18 GHz IF range (i.e., a 15 GHz IFBW) [57].

Table 3.1: IFBW of commissioned SIS receivers around 230 GHz.

Telescope	Band/ Rx Name	RF range (GHz)	RFBW (GHz)	IF range (GHz)	IFBW (GHz)	Ref.
ALMA	5	167 – 211	44	4 – 8	4	10, 24
ALMA	6	211 – 275	64	5 – 10	5	10, 24
IRAM 30m†	B3	200 – 267	67	4 – 8	4	68, 69
SMA	230 GHz‡	194 – 240	46	4 – 12	8	64, 70
SMA	240 GHz‡	210 – 270	60	4 – 12	8	64, 70

Note: This table only includes receivers around 230 GHz because it is generally easier to achieve wide IFBW at higher RF frequencies. This is due to the smaller planar circuits and thereby smaller planar capacitances; although, the ratio of IF to RF bandwidth decreases dramatically at higher frequencies [67].

† Institut de Radioastronomie Millimétrique (IRAM) 30m telescope

‡ These receivers are also used on the James Clerk Maxwell Telescope (JCMT).

All of the receivers listed in the table above use waveguide probes to couple energy from the waveguide to the planar circuit. These require precisely tuned backshorts to maximise the coupling. An alternative is finline coupling, which facilitates mounting and does not require backshorts since the devices are mounted directly in the E-plane of the waveguide [71]. At 650 GHz, Tan et al. [63] achieved a 13 GHz IFBW with a finline device and an IF tuning circuit. At 230 GHz, Y. Zhou, *et al.* [72] also achieved a relatively wide IFBW with a finline device, but the IF spectrum featured a large resonance from 5 to 10 GHz.

In this chapter, a new 230 GHz SIS mixer is presented. The planar circuit of this device was optimised to produce a wide IFBW, and it uses a finline transition to couple to the waveguide. To begin, the design of the planar circuit is described in Sec. 3.2. Electromagnetic simulations of the SIS device are then presented in Sec. 3.3. Next, the fabrication process is described in Sec. 3.4, and the experimental system that was used to characterise the devices is specified in Sec. 3.5. The DC, RF and IF experimental results are presented separately in Sec. 3.6, 3.7 and 3.8, respectively. Finally, in Sec. 3.9, this chapter concludes with several suggestions to improve the SIS mixer and the experimental measurement system.

3.2 Design

The layout of the new SIS device is shown in Fig. 3.2a[1]. It is a single-ended device, meaning that the RF and LO signals enter together through the same waveguide (from the right in Fig. 3.2a). The entire device sits in the E-plane of the waveguide (Fig. 3.2b), and uses a finline transition to couple energy to the planar circuit. The area of the RF planar circuit was reduced as much as possible to minimise the planar circuit capacitance and maximise the IFBW; however, the SIS junction itself is relatively large with an area of $A_J = 1.5\ \mu m^2$.

The individual structures of the receiver are described below (see Fig. 3.2a):

– The unilateral finline couples energy from the waveguide to the slotline. It is a smoothly tapered transition from the finline with a 0.55 mm gap (a characteristic impedance of $Z_0 \approx 500\ \Omega$) to the slotline with a 2.5 µm gap ($Z_0 \approx 40\ \Omega$). The profile was synthesised with the Optimum Taper Method tool [73] to provide minimal return loss across a large RF bandwidth while also restraining the overall length.

[1]The planar circuit was designed by Dr. Tan [1].

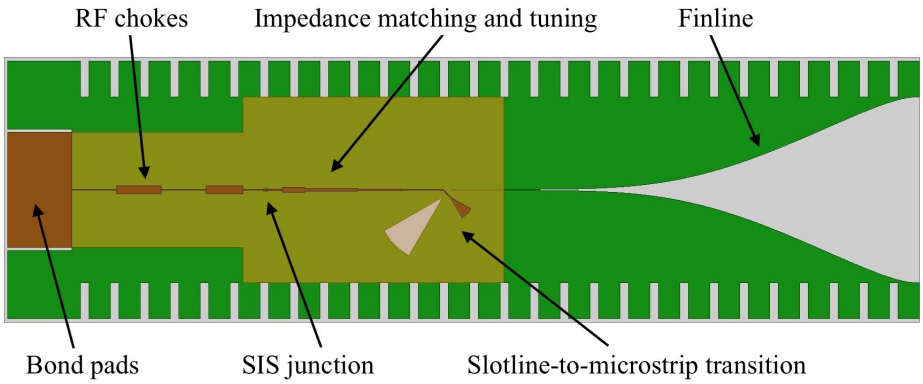

(a) Layout of the planar circuit.

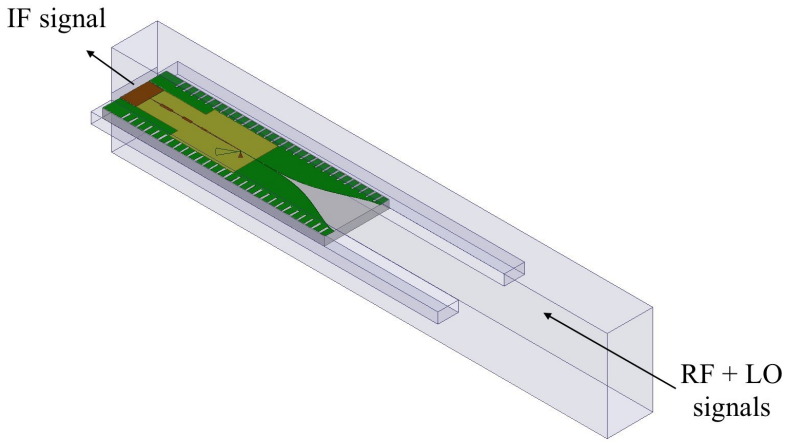

(b) The SIS device is mounted in the E-plane of the waveguide with slots on either side to support the device. It is a single-ended device, meaning that the RF and LO signals arrive through the same waveguide.

Figure 3.2: The new 230 GHz SIS device.

– The slotline-to-microstrip transition couples energy from the slotline to the microstrip. Two radial stubs were used to maximise the coupling, but the angle and length of the microstrip stub was reduced to minimise the capacitance of the planar circuit at IF frequencies.

– The impedance transformer matches the impedance of the slotline-to-microstrip transition ($Z_0 \approx 40\ \Omega$) to the normal resistance of the SIS junction ($R_\mathrm{n} \approx 14\ \Omega$). A standard three-stage Chebyshev transformer was used to provide a broad RF bandwidth. Inductive strips before and after the junction then tune the intrinsic capacitance of the SIS junction. They were designed to match at two frequencies

on either side of $\nu_c = 230$ GHz, again for broadband tuning.

- The junction is a 1.5 μm^2 circular niobium/aluminium oxide/niobium (Nb–AlO_x–Nb) SIS tunnel junction. The relatively large junction size was chosen to facilitate fabrication.
- The RF chokes prevent high frequency signals from leaking into the IF circuit. These signals can interfere with the LNA and increase the noise contribution from the IF circuit.
- The bond pads provide an area where bond wires can be attached to the device to carry out the down-converted signal to the rest of the IF chain.
- The serrations around help to eliminate surface currents that may travel along the outside edge of the device.

In [1], the performance of this SIS device was predicted by simulating the individual subsections of the planar circuit with electromagnetic simulation software and then importing the results into SuperMix [74], a software package designed to calculate the conversion efficiency and noise temperature of SIS devices. Inside SuperMix, the simulation results were cascaded to calculate the embedding impedances at each individual frequency. Excellent performance was estimated from 140–260 GHz in the RF spectrum (Fig. 3.3a) and 0–17 GHz in the IF spectrum (Fig. 3.3b). (Note that in Fig. 3.3b, the simulated noise temperature is low from DC to 25 GHz; however, this noise estimation ignores the IF noise contribution. In reality, the IF noise will increase dramatically past 17 GHz due to the sharp drop in conversion efficiency.)

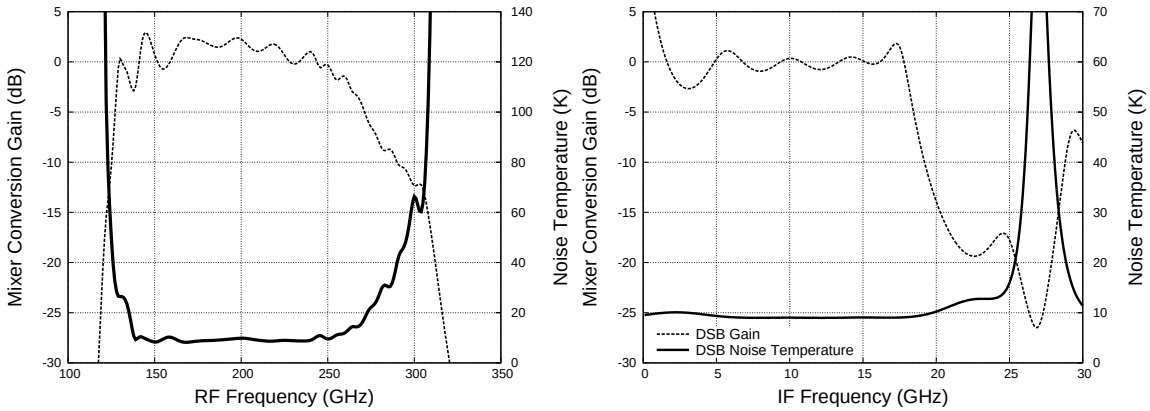

(a) RF performance (b) IF performance

Figure 3.3: Simulated RF and IF performance of the SIS device using SuperMix (taken from [1]).

3.3 Electromagnetic simulations

In order to analyse the RF and IF response, the entire SIS device was simulated using 3D electromagnetic simulation software (ANSYS® HFSS™, Release 15.0). Two different 3D models were used for these simulations: a simplified model (Fig. 3.4a) and a complete model (Fig. 3.4b). The simplified model did not include the serrations, bond pads or waveguide slot, but it was suitable for most analysis and optimisation. The complete model was created in an attempt to capture the entire device, but meshing errors were found at RF frequencies due to the small dimensions of the serrations.

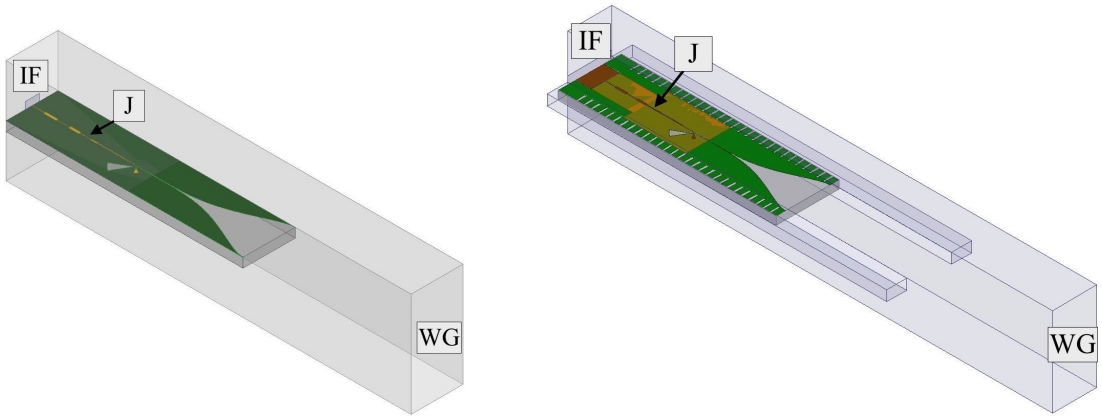

(a) Simplified 3D model (b) Complete 3D model

Figure 3.4: 3D models of the SIS device used in HFSS simulations. The excitation ports are labelled "WG" for the waveguide, "J" for the SIS junction, and "IF" for the IF circuit.

Each 3D model included excitation ports for the waveguide (WG), SIS junction (J) and IF circuit (IF). The scattering parameters[2] (S-parameters) were then simulated to estimate the reflection and transmission coefficients between these ports. Using the terminology from HFSS, the waveguide and microstrip ports are *wave ports*, meaning that the port impedances are calculated based on the geometry of the transmission lines, and the junction port is a *lumped element port*, which required a port impedance to be provided manually. Note that the junction's port impedance is different at RF and IF frequencies. It can either be estimated from Tucker theory, or recovered from experimental results.

[2]Scattering parameters represent the ratio of forward ($a_i = V^+ / \sqrt{Z_0}$) to reverse ($b_i = V^- / \sqrt{Z_0}$) travelling waves between the ports of a microwave network. For example, $S_{11} = b_1 / a_1$ represents the reflection coefficient at port #1, while $S_{21} = b_2 / a_1$ represents the transmission between port #1 and port #2. Here, the ports are identified using descriptive letters instead of numbers. For example, the reflection coefficient seen at the junction port is represented by $S_{\mathrm{J,J}}$, and the transmission between the waveguide port and the junction port is represented by $S_{\mathrm{J,WG}}$.

Surface impedance of superconductors

Surface impedance is an important concept that can be used to simplify electromagnetic simulations and calculations. When electromagnetic radiation is incident upon the surface of a conductor, current is induced along the surface due to the tangential component of the magnetic field. In any real metal, this current will not exist purely on the surface, and will extend into the volume, falling off exponentially with depth. To simulate this current, simulation software can either solve Maxwell's equations inside the conductor, which is computationally expensive, or the net effect can be represented by a sheet resistance on the surface, known as the surface impedance. By using the surface impedance, the interior of 3D conductors can be ignored and planar conductors can be flattened into 2D sheets.

In normal metals, the surface impedance Z_s is related to the metal's conductivity σ through

$$Z_\mathrm{s} = (1+j)\sqrt{\frac{\mu_0\,\omega}{2\,\sigma}} \tag{3.1}$$

where μ_0 is the permeability of freespace and ω is the angular frequency. Superconductors have no DC resistance, but they do have significant AC reactance due to the kinetic energy of Cooper pairs. It is important to include this in electromagnetic simulations, especially when designing tuning structures. Mattis–Bardeen theory [75] provides an approximation of how conductivity and surface impedance change with respect to frequency, temperature and conductor thickness. The conductivity and surface impedance for the wiring layer of the SIS device are plotted in Fig. 3.5b. Note that at high frequencies, far above the gap frequency ν_gap, the surface impedance takes on its normal state value (Fig. 3.5b). Below $\nu_\mathrm{gap}/2$, however, the surface impedance is almost purely reactive. The reactive component is also linear, so it can be approximated by a *surface inductance* [76]:

$$L_\mathrm{s} = \mu_0\lambda \cdot \coth\left(\frac{d}{\lambda}\right), \tag{3.2}$$

where λ is the penetration depth ($\sim$85 nm for niobium) and d is the conductor thickness. This inductance is easily implemented in HFSS. For the wiring and ground layers of the 230 GHz receiver, the surface inductances were set to L_s=116.9 fH/sq. and L_s=117.9 fH/sq., respectively.

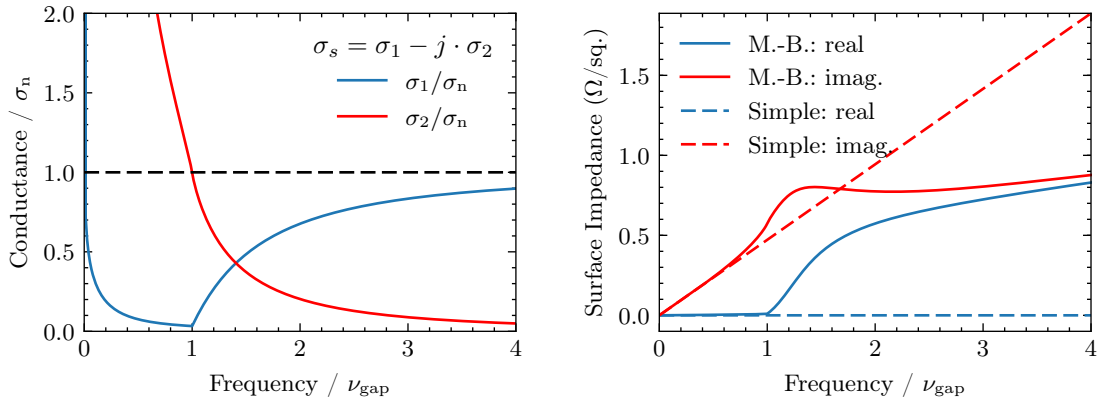

(a) Conductance from Mattis-Bardeen theory

(b) Surface impedance

Figure 3.5: Theoretical properties of the niobium wiring layer (with thickness $d = 400$ nm and temperature $T = T_c/2$). Here "M.-B." represents results from Mattis-Bardeen theory, and "Simple" represents those from Eqn. 3.2.

3.3.1 RF simulation results

The simplified 3D model from Fig. 3.4a was used for the RF frequency simulations because the complete 3D model was prone to numerical errors arising from the serrations around the perimeter of the device. The junction's port impedance was set to $Z_J = 9.5\ \Omega$, which was the average junction impedance found experimentally[3]. In Fig. 3.6, the simulated S-parameters show good coupling between the waveguide and junction ports over a wide RF bandwidth. Two tuning poles are seen at ∼195 and ∼240 GHz, which were set intentionally for broadband operation.

Using the S-parameter results, the embedding impedance[4] seen by the junction was estimated from

$$Z_{emb} = Z_{0,J} \cdot \left[\frac{1 + S_{J,J}}{1 - S_{J,J}}\right] \tag{3.3}$$

where $Z_{0,J} = 9.5\ \Omega$ is the characteristic impedance of the junction port, and $S_{J,J}$ is the complex reflection coefficient. For maximum power transfer, Z_{emb} should be the complex conjugate of the junction impedance, i.e., $Z_J^* = 9.5\ \Omega$. Alternatively, Ke and Feldman [52] define the optimum embedding impedance as

$$R_{opt} = 4R_n \cdot \left(2 + \frac{e\,V_{gap}}{h\,\nu_{LO}}\right)^{-1}, \tag{3.4}$$

[3]These simulations were completed concurrently with the initial tests of the SIS device. The junction's impedance was estimated during impedance recovery and 9.5 Ω was the average value found. Note: the port impedance only influences the S-parameters; not the embedding impedance.

[4]In other words, this is the input impedance seen at the junction port.

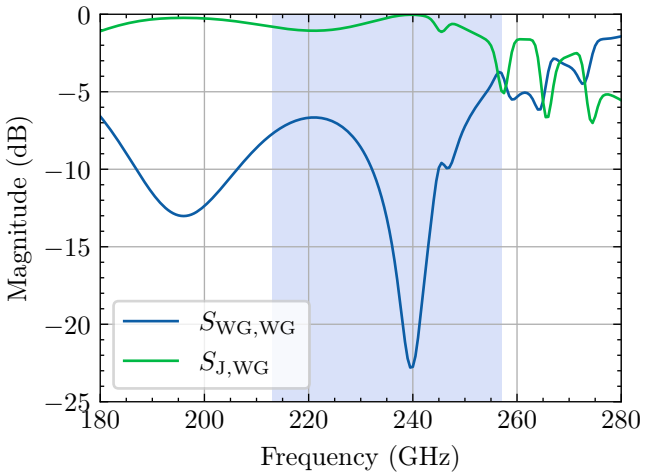

Figure 3.6: Simulated RF performance using the simplified 3D model from Fig. 3.4a. Here, $S_{WG,WG}$ is the reflection coefficient at the waveguide port, and $S_{J,WG}$ is the transmission coefficient between the waveguide and the SIS junction. The pale blue region from 213 – 257 GHz represents the tuning range of the local-oscillator that will be used in the experimental section.

which they calculated by minimising the noise temperature predicted from Tucker theory. In Fig. 3.7a, the simulated embedding resistance is close to $R_J{=}Z_J^*$ and R_{opt} across most of the band, and comes very close around 240 GHz. Ideally, the imaginary component of the embedding impedance should be small, but a capacitive value can help to produce a positive dynamic resistance and stable mixer operation [12].

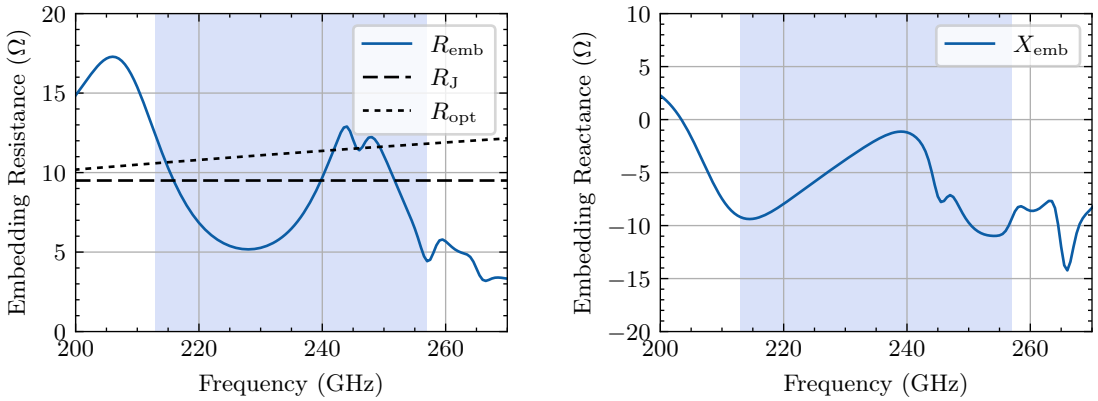

(a) Embedding resistance (R_{emb}). (b) Embedding reactance (X_{emb}).

Figure 3.7: Simulated embedding impedance, $Z_{emb} = R_{emb}+jX_{emb}$, from HFSS. In Fig. 3.7a, R_J is the target value for maximum power transfer, and R_{opt} is the target value for optimum noise properties, according to Ke and Feldman [52]. The pale blue region represents the tuning range of the local-oscillator (213–257 GHz).

Using the simulated embedding impedances from Fig. 3.7, pumped I–V curves

were calculated with the junction drive level set to $\alpha \sim 0.85$. These I–V curves were then used to estimate the dynamic resistance of the first photon step (Fig. 3.8), which sets the output impedance of the SIS junction at IF frequencies [12, 77]. For a good impedance match, this should be equal to the characteristic impedance of the IF measurement chain, $Z_0 = 50\ \Omega$. This is true for part of the tuning range, but the dynamic resistance rises when the embedding impedance is not sufficiently capacitive at frequencies around 240 GHz.

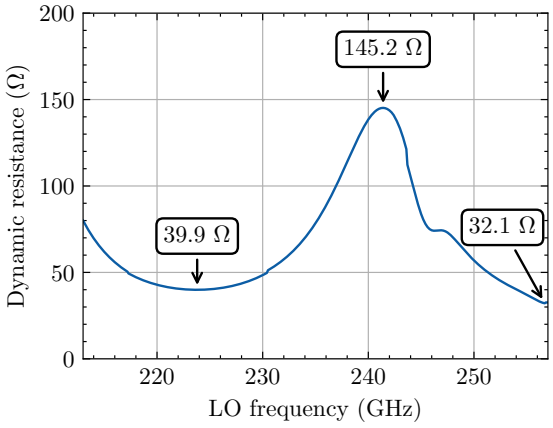

Figure 3.8: Simulated dynamic resistance of the first photon step. The simulated embedding impedances from Fig. 3.7 were used to calculated pumped I–V curves at each LO frequency, from which, the slope of the first photon step was calculated. These results should correspond to the output impedance of the SIS junction at IF frequencies.

3.3.2 IF simulation results

For the IF simulations, the complete 3D model from Fig. 3.4b was used and the junction port impedance was set to $Z_{0,\mathrm{J}} = 50\ \Omega$, which is the dynamic resistance at 230 GHz in Fig. 3.8. From these simulations, the transmission between the junction and IF ports is estimated to be relatively poor above ~6 GHz (Fig. 3.9). This insertion loss is likely due to capacitance from the RF chokes, the RF tuning structures, and the SIS junction. Note that the RF chokes are necessary to prevent the LO signal from leaking into the IF circuit. The effect of this loss is explored in more detail in Sec. 3.8.

Using the simulated reflection coefficient at the IF port $S_{\mathrm{IF,IF}}$, the output impedance from the SIS device was calculated from:

$$Z_{\mathrm{out}} = Z_{0,\mathrm{IF}} \cdot \left[\frac{1 + S_{\mathrm{IF,IF}}}{1 - S_{\mathrm{IF,IF}}}\right] \tag{3.5}$$

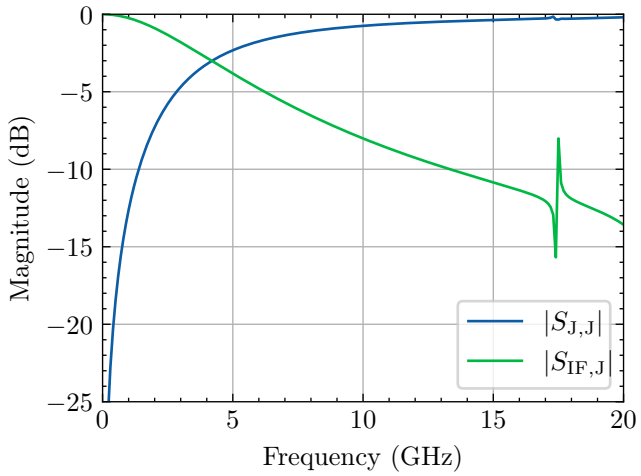

Figure 3.9: Simulated IF performance using the complete 3D model from Fig. 3.4b. Here $S_{J,J}$ is the reflection coefficient at the junction port, and $S_{IF,J}$ is the transmission coefficient between the junction and IF ports (ports labelled in Fig. 3.4b).

where $Z_{0,IF}$ is the characteristic impedance. The results are plotted in Fig. 3.10. The output impedances presents a significant impedance mismatch to the 50 Ω IF circuit for each junction resistance from Fig. 3.8. Based on the results from other finline device (e.g., [63]), these results predict a $0 - 13$ GHz usable IF range; although, the gain will drop off rapidly past ∼5 GHz.

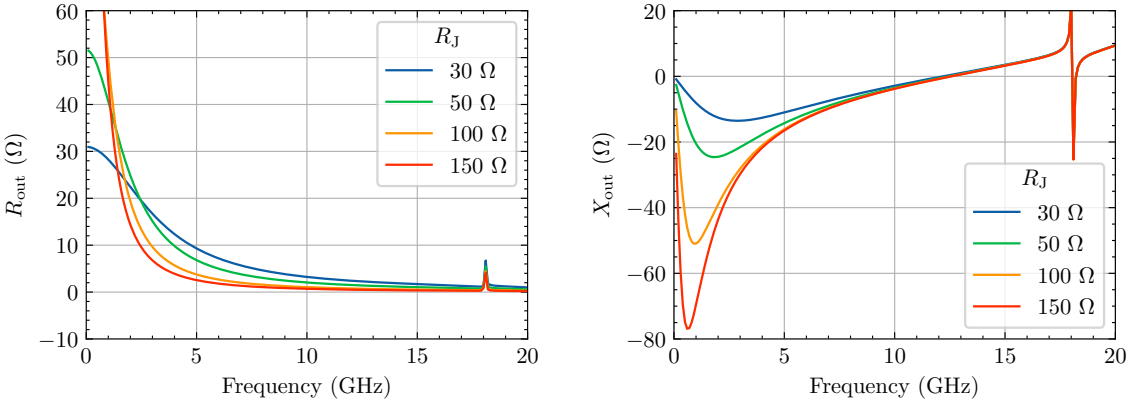

(a) Output resistance (R_{out})

(b) Output reactance (X_{out})

Figure 3.10: Simulated output impedance, $Z_{out} = R_{out} + jX_{out}$, of the SIS device (i.e., the input impedance of the IF port in Fig. 3.4b). This is plotted for several SIS junction resistances R_J, which were previously estimated in Fig. 3.8.

3.4 Fabrication

The SIS devices were fabricated at l'Observatoire de Paris by F. Boussaha and C. Chaumont. To begin, the Nb/AlO_x/Nb trilayer was deposited onto a 300 µm thick quartz substrate using a standard niobium-aluminium fabrication technique [78]. Next, the finline, serrations and slotline structures were defined in the ground plane of the trilayer using ionic etching. The SIS junction was then defined using photolithography and a selective niobium self-aligned etch process. Two layers of SiO were deposited for a total thickness of 490 nm, which was necessary to achieve the desired characteristic impedances for the planar circuit. A 10×10 µm window was left in the second layer of SiO around the SIS junction to improve contact between the wiring layer and the junction. Finally, a 400 nm thick Nb layer was sputtered on top to form the microstrip wiring layer. The final circuit layers are listed in Table 3.2.

Table 3.2: Layers of the planar circuit.

Layer	Thickness	Material	Relative Permittivity
Wiring	400 nm	Nb	–
Dielectric	490 nm	SiO	5.8
Ground	250 nm	Nb	–
Substrate	100 µm	SiO_2/quartz	3.78

The SIS devices were fabricated on a 2" quartz wafer, a sub-sector of which is shown in Fig. 3.11a. A close-up image of one of the devices is shown in Fig. 3.11b and the inset on the bottom shows a magnified view of the junction itself. The yellow square represents the area around the junction where the second layer of SiO was not deposited in order to get better contact between the wiring layer and the junction.

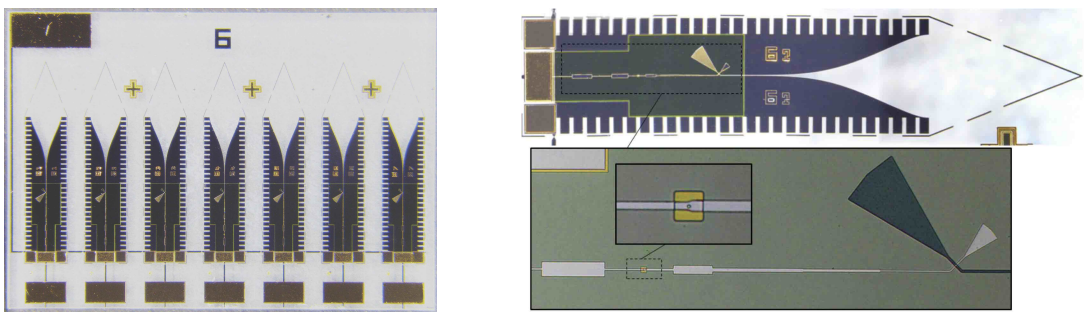

(a) A subsector of the quartz wafer showing 7 SIS devices.

(b) A single device with the area around the junction magnified below

Figure 3.11: Microscope images of the fabricated devices.

3.5 Experimental measurement system

The performance of the new SIS device was characterised by measuring its response to hot and cold black body radiation. To perform these measurements, the SIS device was placed into the experimental system shown in Fig. 3.12. The components of this system are described in the following sub-sections with additional details given in App. B.

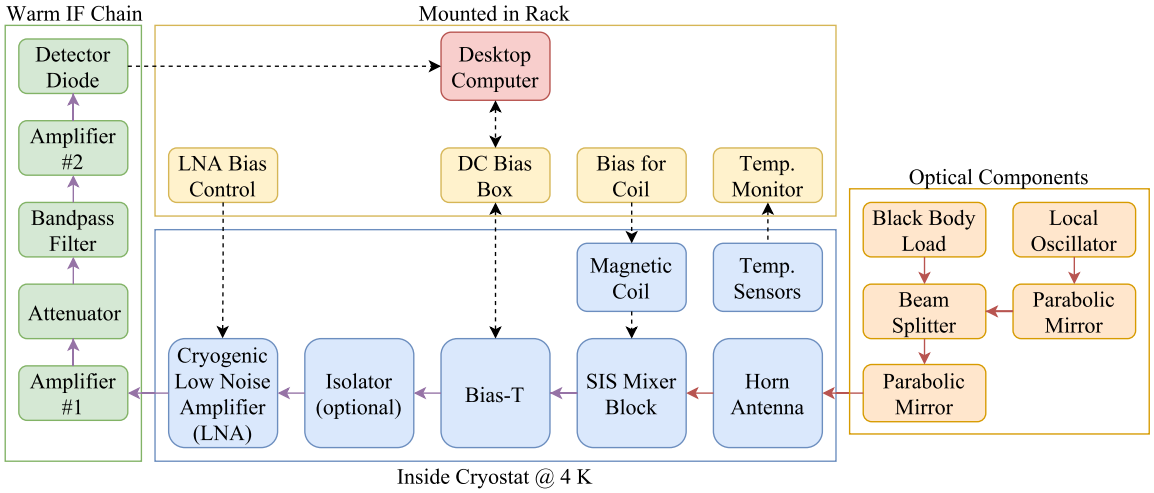

Figure 3.12: The experimental system used to measure the SIS device's response to hot and cold black body radiation. The optical system is shown in orange, the components inside the cryostat are shown in blue, and the warm IF components are shown in green. The SIS device itself is installed in the SIS mixer block, which is inside the cryostat. A desktop computer was used to record all of the experimental data.

The optical components

The optical system (orange in the block diagram) was used to combine the black body and local-oscillator (LO) signals, and then efficiently couple the energy to the mixer horn. The LO signal was generated by a Gunn oscillator in series with a frequency tripler (S/N: 2005 088, Radiometer Physics GmbH). The output of the oscillator could be tuned from 71–86 GHz, resulting in a final tuning range of 213–258 GHz after the multiplier. This LO chain provided +0.5 mW of power over most of the tuning range, and +1.5 mW at the upper frequencies (measured power given in App. B.6 along with a list of the other LOs available in our lab). The LO signal was coupled to the mixer's feed horn using two parabolic mirrors in a *Gaussian beam telescope* configuration (Fig. 3.13). Each mirror had a focal length of $f = 160$ mm. To collimate the LO beam between the mirrors, they were placed at a distance f from the

beam waist of the feed horns. (The LO beam coupling and edge taper are given in App. B.3.)

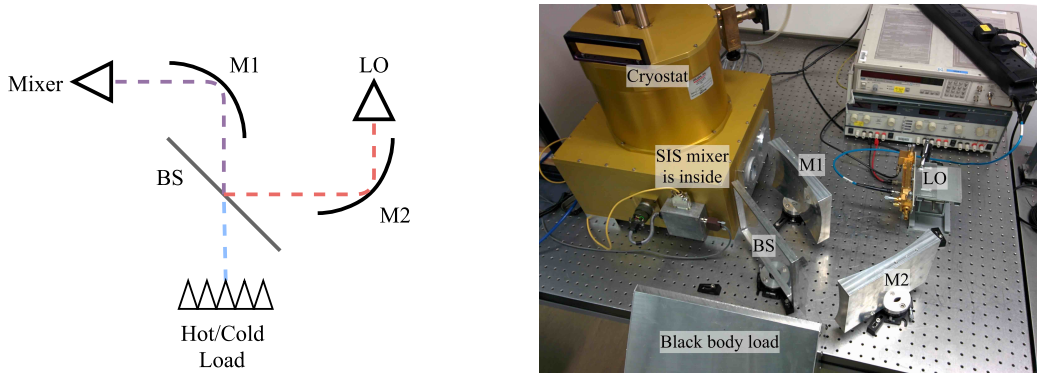

(a) Layout of the optical components

(b) Layout on the optical table

Figure 3.13: A Gaussian beam telescope was used to couple the LO signal to the mixer horn. In these figures, "M1" represents parabolic mirror #1, "BS" represents the beam splitter, and "M2" represents parabolic mirror #2.

For the black body loads, room temperature microwave absorber (Eccosorb®, Emerson & Cuming Microwave Products) was used for the hot load (T_{H}∼295 K), and the same material immersed in liquid nitrogen was used for the cold load (T_{C}∼80 K). These temperatures are both above the Rayleigh-Jeans limit at 230 GHz, meaning that the black body spectral radiance is directly proportional to temperature (see App. B.2). The LO and black body signals were combined using a 12 µm thick Mylar beam splitter. This thickness was a compromise between allowing enough LO power to couple to the mixer while also minimising how much noise is added to the system (reflection and effective noise temperature given in App. B.5).

The cryostat and cryogenic components

The cryostat (blue in the block diagram) was used to cool the SIS devices below the critical temperature of niobium, $T_{\mathrm{c}} = 9.2$ K. Ideally, for good noise performance, the SIS junction temperature should be below $\sim T_{\mathrm{c}}/2$, and fortunately for niobium-based junctions, this approximately corresponds to the boiling point of liquid helium (4.230 K at 1 atm [79]). A simple open-cycle dewar was used for all of the testing in this thesis. The vacuum window on the cryostat was made from a 24 mm thick slab of nitrogen-expanded polypropylene foam (PPA30, Zotefoams PLC). This foam helps to block some infrared light, but it is also nearly transparent below 400 GHz [80]. To further reduce radiative heating, a 1.52 mm thick slab of porous PTFE (ZITEX G-106, Saint-Gobain) was used as an infrared filter on the radiation shield since this

material blocks wavelengths $\lesssim$200 µm [81]. Additional details on the cryostat and cryostat windows are given in App. B.1 and App. B.4, respectively.

Inside the cryostat, the SIS devices were installed in mixer blocks (Fig. 3.14), which couple the RF signals to the device, provide the magnetic field required to suppress Cooper pair tunnelling, and carry the down-converted signal from the device to the rest of the measurement chain. The SIS devices were mounted in the E-plane of the mixer blocks' waveguides using a temporary adhesive (Fig. 3.14c). In most cases, two 1-mil (25.4 µm) diameter aluminium bond wires were connected from the signal bond pad on the device to the IF board, and two other bond wires were connected on either side to ground the device. The IF board could either be a simple 50 Ω microstrip or a tuning circuit used to match the output impedance of the device to the 50 Ω IF circuit (following the work in [63]).

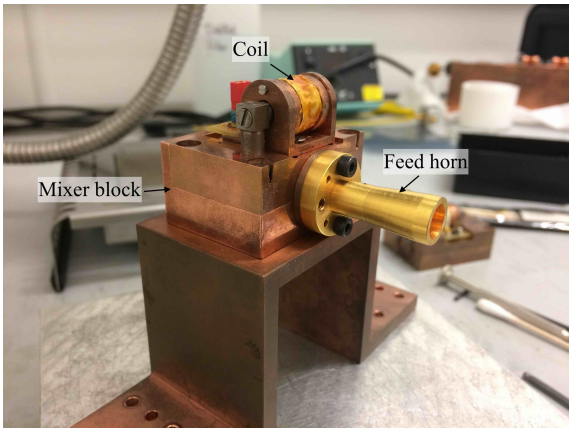

(a) An assembled mixer block

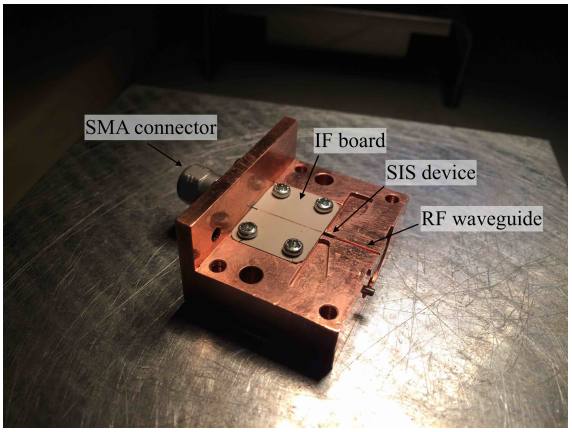

(b) Bottom half of a mixer block

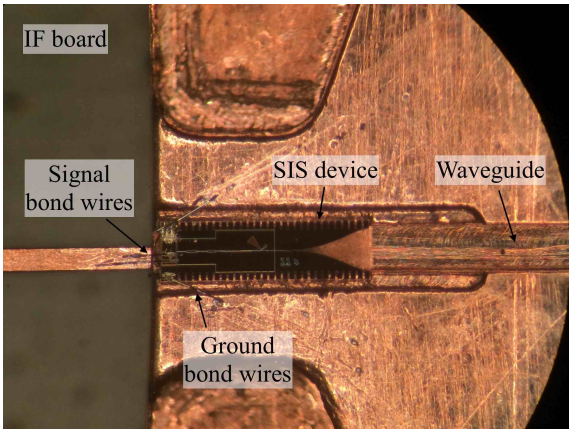

(c) An SIS device mounted inside the bottom half of the mixer block

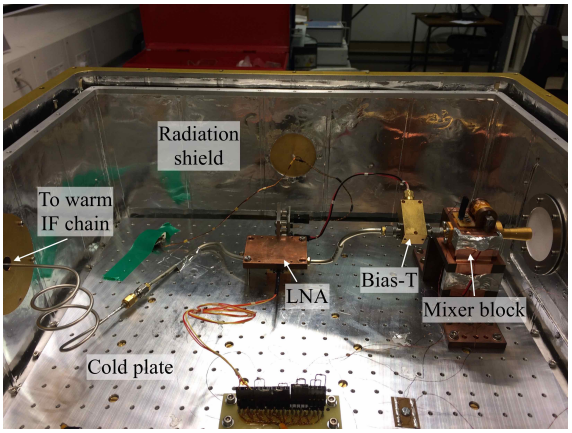

(d) IF components inside the cryostat

Figure 3.14: The mixer block and the cryogenic components.

The mixer block was connected to a bias tee to apply the DC bias voltage (V_0) and measure the resulting DC tunnelling current (I_{dc}). For the down-converted IF signal, a cryogenic low noise amplifier (LNA) was then connected after the bias tee to boost the IF signal to such a level that the warm IF components could measure the signal without contributing too much noise. Four cryogenic LNAs were available in our lab (listed in Table 3.3). Noise and gain properties were provided by the manufacturers for three of the LNAs (Fig. 3.15); although, the tests were performed at different ambient temperatures, making it difficult to directly compare their performance.

Table 3.3: Cryogenic low-noise amplifiers available in our lab.

Manufacturer	Model	Frequency Range (GHz)
CalTech Microwave Research Group†	CITCRYO4–12A‡	4 – 12
Low Noise Factory	LNF–LNC6_20C	6 – 20
Yebes Observatory	Y214G 1011	2 – 14

† This group has closed and support has moved to Cosmic Microwave Technology.
‡ Our group owns two of these LNAs (serial numbers 112D and 495D).

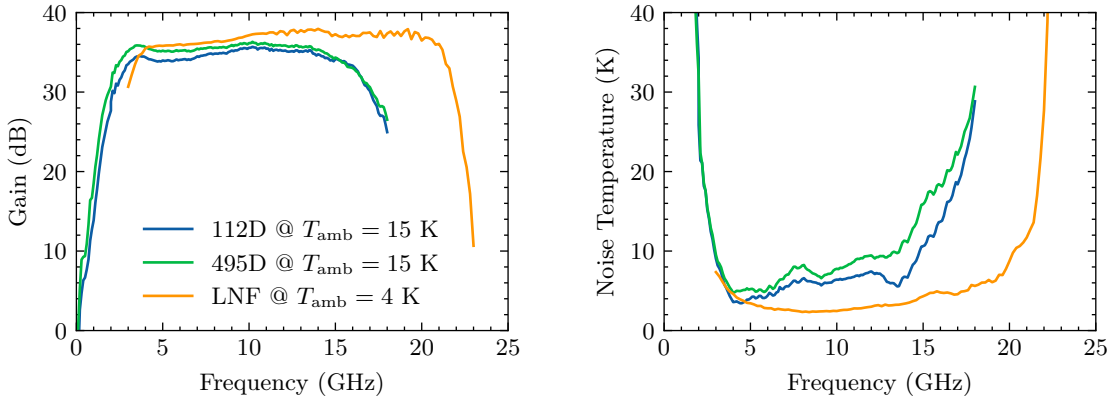

(a) LNA gain

(b) LNA noise temperature

Figure 3.15: Cryogenic LNA performance provided by the manufacturers. "112D" and "495D" correspond to the serial numbers of the two LNAs from CalTech, and "LNF" represents the LNA from Low Noise Factory (see Table 3.3). Note these LNAs were measured at different ambient temperatures T_{amb}.

Warm IF chain

The warm IF chain (green in the block diagram) was used to amplify, filter and measure the down-converted IF signal. It consisted of two 26 dB warm LNAs, a bandpass filter and a detector diode to integrate the IF signal. Attenuators were also

placed throughout the chain to optimise the power entering the LNAs and detector diode, the later of which is only linear around -30 dBm. Alternatively, to measure the IF power as a function of IF frequency, the band pass filter was removed and the detector diode was replaced by a spectrum analyser (MS2665C, Antritsu).

Computer control

All of the experimental data was recorded through a desktop computer connected to a LabView interface. The LabView interface communicated with the DC bias supply (made in-house) and measured the output signal from the detector diode. The DC voltage was typically swept from -7.5 to 7.5 mV with 6000 measurement points per sweep.

3.6 DC junction characteristics

The DC junction properties were measured by cooling the SIS devices to $\sim T_c/2$ and then recording their characteristic current–voltage relationships (i.e., their DC I–V curves). An example DC I–V curve is shown in Fig. 3.16a along with the parameters that can be extracted from the data. Here, the gap voltage V_{gap} was found by locating the minimum dynamic resistance[5], the normal resistance R_n was found by calculating the average dynamic resistance above the transition, and the subgap resistance and leakage current were defined as $R_{sg} \equiv R_{dyn}(2\text{ mV})$ and $I_{leak} \equiv I^0_{dc}(2\text{ mV})$, respectively.

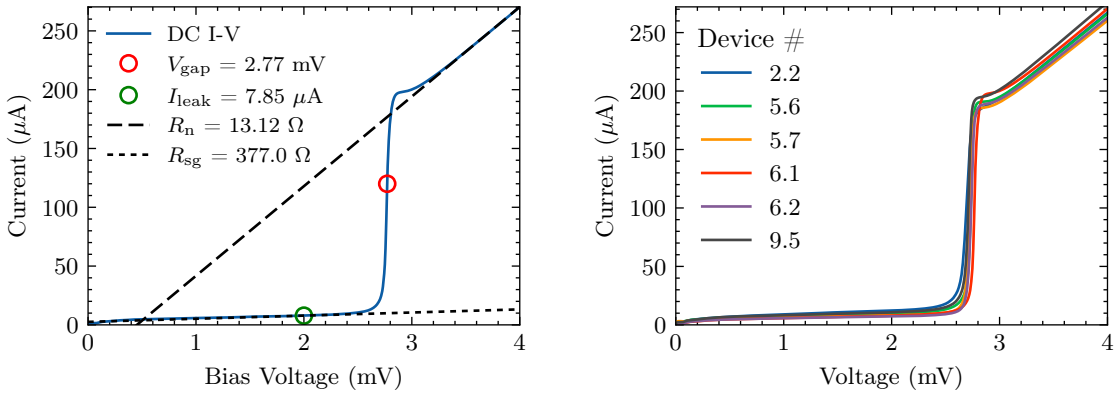

(a) DC I–V curve from device #6.1.

(b) DC I–V curves from 6 different SIS devices (see Table 3.4).

Figure 3.16: Experimental DC I–V curves.

[5]Recall that the dynamic resistance of the DC I–V curve is defined as $R_{dyn}(V_0) \equiv \left(\frac{dI^0_{dc}}{dV_0}\right)^{-1}$ where $I^0_{dc}(V_0)$ is the DC tunnelling current and V_0 is the bias voltage.

This analysis was repeated using six different devices (Fig. 3.16b). The extracted properties are listed in Table 3.4. The temperature T_{block} is the mixer block's temperature, which was measured with a thermal probe. The actual SIS junction temperatures were likely higher than this because quartz substrates provide poor thermal contact between the mixer block and the niobium layers. The temperature of the niobium was estimated by fitting the theoretical subgap leakage current (Eqn. 2.11) to the measured leakage current. The estimated temperatures, listed as T_{leak} in Table 3.4, are all roughly +0.4 K higher than the measured mixer block temperatures. Ideally, niobium-based junctions should be cooled below $T_c/2 \sim 4.6$ K to limit the shot noise, but all of the devices in Table 3.4 are above this temperature, which results in higher noise temperature results. Device #2.2 and #9.5 were especially warm, as evidenced by their high leakage currents. The SIS devices could have been cooled more by connecting a vacuum pump to the liquid helium vessel of the cryostat, but this reduces the hold time and runs the risk of ice forming in the helium vessel tube. This technique was deemed too dangerous for these experiments because this specific dewar does not have an independent pressure relief valve and it has already had issues with ice in the past.

Table 3.4: DC junction properties.

Device #	T^a_{block} (K)	T^b_{leak} (K)	V_{gap} (mV)	R_{n} (Ω)	R_{sg} (Ω)	I_{leak} (μA)	Q^c_{R}	J^d_c (kA/cm^2)	Δ^e_0 (meV)
2.2	4.95	5.43	2.69	13.32	242.5	11.92	18.21	13.48	1.45
5.6	–	5.13	2.73	13.37	344.1	8.77	25.74	13.62	1.45
5.7	–	5.18	2.73	13.62	473.3	8.30	34.75	13.34	1.45
6.1	4.71	5.12	2.77	13.14	395.2	8.70	30.07	14.04	1.47
6.2	4.60	5.01	2.74	13.56	582.3	7.56	42.94	13.46	1.45
9.5	4.94	5.39	2.71	12.83	300.1	10.73	23.38	14.08	1.46

[a] Temperature of the mixer block. Measured using a thermal probe attached to the mixer block.
[b] Temperature of the SIS junction. Estimated by fitting Eqn. 2.11 to the leakage current.
[c] Quality factor: $Q_{\text{R}} = R_{\text{sg}}/R_{\text{n}}$ (defined previously in Eqn. 2.13).
[e] Current density: $J_c = V_{\text{gap}} \,/\, R_{\text{n}} \cdot A_{\text{J}}$ where A_{J} is the area of the junction (defined previously in Eqn. 2.10).
[e] Estimated binding energy at $T = 0$. Calculated by inserting V_{gap} and T_{leak} into Eqn. 2.7.

In addition to high leakage currents, high temperatures also result in lower binding energies and gap voltages. To estimate the binding energy at $T = 0$, the measured gap voltage V_{gap} and niobium temperature T_{leak} were inserted into the self-consistent BCS equation (Eqn. 2.7). The results, listed as Δ_0 in Table 3.4, were found to be very close to the 1.45 meV value that is typical for niobium (e.g., [82–84]).

In Table 3.4, the normal resistance R_n is very consistent between the devices, except for device #6.1, which has a R_n that is ∼7% lower than the other junctions, suggesting a slightly larger junction area. Excluding this device, the average normal resistance in Table 3.4 is 13.40 Ω. With a junction area of 1.5 µm^2 and assuming a specific capacitance of 80 fF/µm^2, this results in an average $\omega R_n C_J$–product of 2.3. This is a good compromise between suppressing the higher-order harmonics and maintaining a low enough capacitance for wide RF and IF bandwidth [85].

3.7 RF performance

The RF performance was characterised by measuring the SIS device's response to hot and cold black body radiation, and then using the Y-factor technique to estimate noise temperature and gain (recall Sec. 2.6). For all of the results below, the IF bandwidth was limited to 4–6 GHz using a bandpass filter and the output power was integrated across this band using a detector diode. As an example of the data analysis, the data from device #5.6 is analysed in Sec. 3.7.1. A summary of results from multiple devices and configurations is then presented in Sec. 3.7.2.

3.7.1 Detailed RF performance of device #5.6

The I–V and IF data collected from device #5.6 at $\nu_{LO} = 230.2$ GHz is shown in Fig. 3.17a. Qualitatively, the I–V data has well defined photon steps and the slope of the first step suggests a capacitive embedding impedance. The IF data on the other hand is mostly clear of Josephson artefacts and there is a large difference between hot and cold load measurements, suggesting a low system noise temperature. By applying the Y-factor technique, the noise temperature and conversion efficiency were found to be 35.7 K and 0.77/-1.1 dB, respectively (Fig. 3.17b).

This process was then repeated across the tuning range of the LO (213–258 GHz). Most of the data was very similar to Fig. 3.17, except for the broken photon steps, which were found consistently between 235 and 250 GHz (e.g., Fig. 3.18). This phenomena is characterised by a large notch in the I–V curve at $V_0 = V_{gap} - V_{ph}/2$ (Fig. 3.18a) and a corresponding dip in IF power (Fig. 3.18b). The broken photon effect was thoroughly studied by A. Ermakov, *et al.* [86] and it does not seem to be due to internal resonances (i.e., Fiske steps) or the Josephson effect (i.e., Shapiro steps). Instead, they suggest that broken photon steps are due to a powerful subharmonic at $\nu_{LO}/2$. This theory is explored through simulations in Chp. 4, and it seems to be correct.

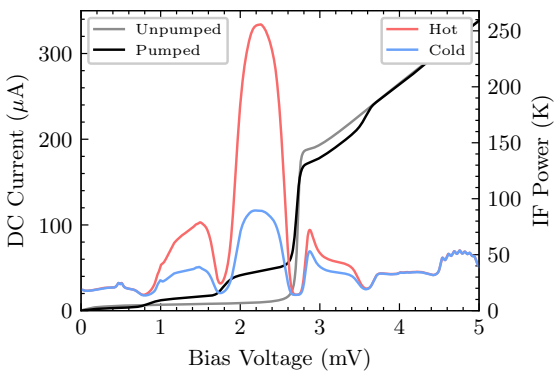

(a) DC tunnelling current and IF power.

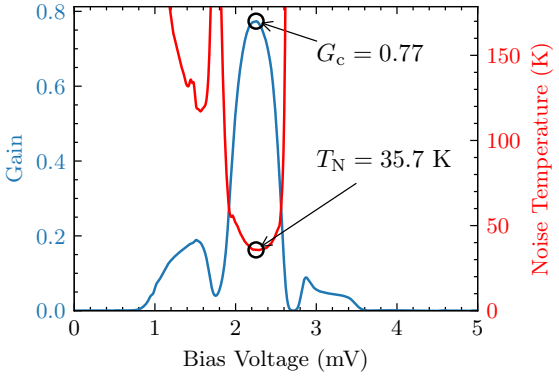

(b) Noise temperature and conversion efficiency estimated from the Y-factor technique.

Figure 3.17: Experimental data from device #5.6 at an LO frequency of $\nu_{LO} = 230$ GHz.

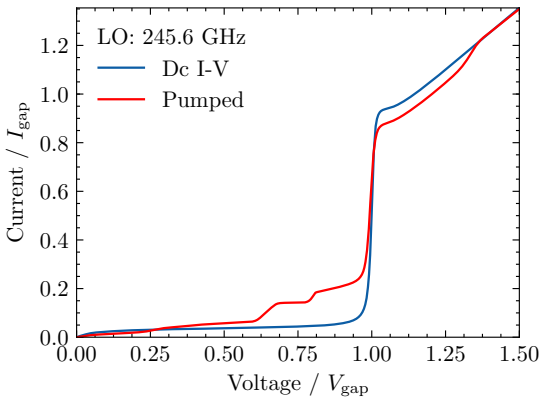

(a) I–V curve

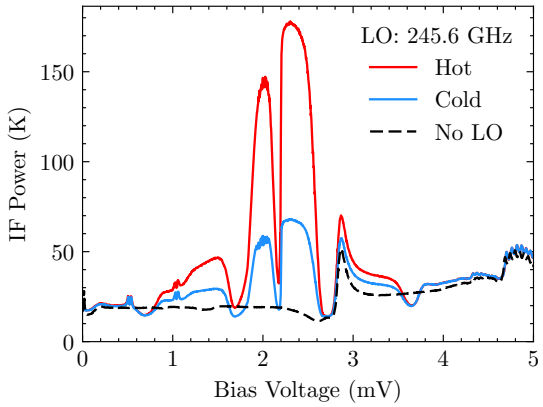

(b) IF data

Figure 3.18: An example of a split photon step found at $\nu_{LO} = 245.6$ GHz.

For device #5.6, the noise temperature was found to be below 50 K from 214–243 GHz (Fig. 3.19) and the best value was 35.7 K at $\nu_{\mathrm{LO}} = 230.2$ GHz. This is 3.2 times the quantum limit $h\nu/k_{\mathrm{B}}$ and close to other state-of-the-art mixers (recall Fig. 1.10). The conversion efficiency over the same frequency range was around -1 dB, which is ideal for good noises properties without experiencing any of the instability issues that coincide with greater than unity gain [12].

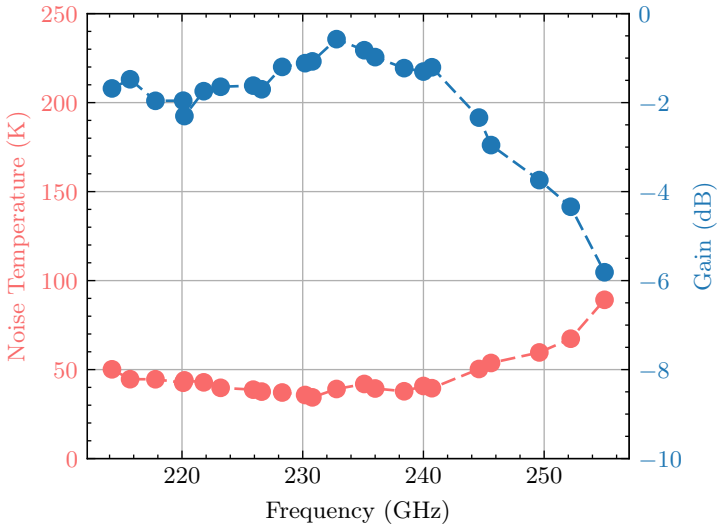

Figure 3.19: Noise temperature and conversion gain from device #5.6.

The RF and IF noise contributions were estimated using the technique of intersecting lines [53] and Woody's method [54], respectively. The IF noise contribution was estimated to be $T_{\mathrm{IF}} = 8.5$ K (Fig. 3.20a), which is independent of the LO frequency. At 230 GHz, the RF noise contribution was estimated to be $T_{\mathrm{RF}} = 12.6$ K (Fig. 3.20b), which does change with LO frequency since the optical components have frequency-dependent properties.

The RF and IF noise contributions cascade within the receiver chain as:

$$T_{\mathrm{N}} = T_{\mathrm{RF}} + \frac{T_{\mathrm{SIS}}}{G_{\mathrm{RF}}} + \frac{T_{\mathrm{IF}}}{G_{\mathrm{RF}}\, G_{\mathrm{SIS}}} \tag{3.6}$$

where T_{N} is the overall system noise temperature (the value measured via the Y-factor technique), T_{SIS} is the noise from the SIS junction, G_{SIS} is the gain from the SIS junction, and G_{RF} is the transmission through the RF components. The three terms on the right-hand side of Eqn. 3.6 are plotted in Fig. 3.21a. The IF and RF noise values were taken from Fig. 3.20, $G_{\mathrm{RF}} \cdot G_{\mathrm{SIS}}$ is equal to the conversion efficiency G_{c} in Fig. 3.19, and the SIS contribution was set as the residual system noise, i.e.,

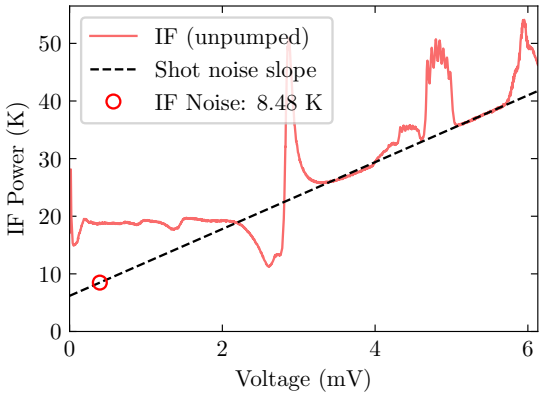

(a) IF noise contribution estimated from the shot noise slope (as described by [54]).

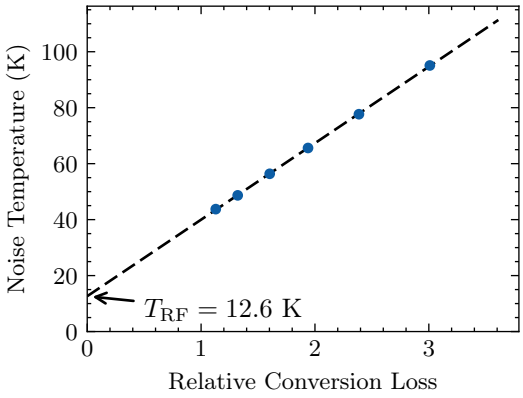

(b) RF noise contribution at 230 GHz estimated by the technique of intersecting lines [53].

Figure 3.20: IF and RF noise contributions from device #5.6.

$T_{SIS}/G_{RF} = T_N - T_{RF} - (T_{IF}/G_{RF}G_{SIS})$. In Fig. 3.21a, the IF noise contribution is $T_{IF}/G_c = 11.0$ K. As described in Appendix A, this IF noise also includes the effect of the impedance mismatch between the SIS junction and the IF circuit. Based on HFSS simulations, we estimate that the true value is $T_{IF} \approx 8.5$ K $\times$ 0.55 = 4.7 K, which is very close to the noise of the LNA ($T_{LNA} \approx 4.5$ K; Fig. 3.15). The noise contribution from the SIS mixer is also reasonable in Fig. 3.21a as it is approximately twice the quantum limit at 230 GHz: $T_Q^{DSB} = \hbar\omega/2k_B \approx 5.5$ K.

The RF noise was decomposed further by estimating the noise contributions from the optical components including the beam splitter (BS), vacuum window (VAC), IR filter (IR) and planar circuit (CCT). These noise contributions cascade as:

$$T_{RF} = T_{BS} + \frac{T_{VAC}}{G_{BS}} + \frac{T_{IR}}{G_{BS}\,G_{VAC}} + \frac{T_{CCT}}{G_{BS}\,G_{VAC}\,G_{IR}} + \ \ldots \tag{3.7}$$

where T and G are the effective noise temperature and transmission coefficient of each component, respectively. The effective noise temperature of the beam splitter and Zotefoam window were calculated from their transmission coefficients[6]. Since these are passive components, their effective noise temperatures are given by:

$$T_{eff} = \left(\frac{1}{G} - 1\right) T_{phys} \tag{3.8}$$

[6]The transmission coefficient for the beam splitter is calculated in App. B.5. The transmission through the Zotefoam window was measured using a vector network analyser, and the results are given in App. B.4

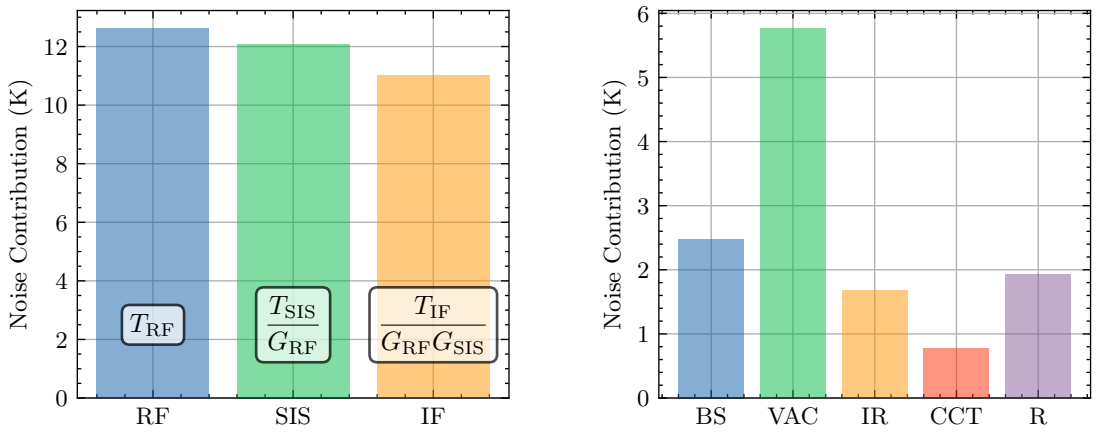

(a) The overall noise composition for device #5.6 broken down into noise from the RF components, noise from the SIS junction, and noise from the IF circuit. These components correspond to the three terms on the right-hand side of Eqn. 3.6.

(b) The RF noise composition. This includes noise contributions from the beam splitter (BS), vacuum window (VAC), infrared filter (IR), and planar circuit (CCT). The remaining RF noise contribution is plotted in the final column (R).

Figure 3.21: Noise composition of device #5.6 at 230 GHz.

where T_{phys} is the physical temperature of the component, equal to 295 K since they are both at room temperature. For the Zitex filter, the RF noise contribution was measured with and without an additional layer of Zitex in the optical path. The difference between these two measurements was found to be 1.63 K at 230 GHz. Finally, the noise from the planar circuit was estimated from the simulated insertion loss (recall Fig. 3.7).

The four terms on the right-hand side of Eqn. 3.7 are plotted in Fig. 3.21b, and the remaining RF noise is plotted in the final column. The remaining RF noise could arise from waveguide losses; although, the mixer block is cryogenic so at most it could add ∼4.7 K. Other potential noise sources include attenuation from water vapour, but this is generally not a problem below ∼400 GHz; noise from the LO; and diffraction in the optical components. Another possibility is that there was an issue with the black body loads. For example, if the cold load was actually warmer than the assumed T_{C} temperature, this would manifest itself as additional RF noise because it would be independent of conversion efficiency. Additional heat in the cold load could have been caused by a layer of vapour forming over the liquid nitrogen (LN), oxygen dissolving into the LN, or the surface of the LN reflecting black body radiation from some where else in the room.

3.7.2 Further investigation of RF performance

Many other SIS devices and configurations were tested using the same technique that was outlined above. These configurations are listed in Table 3.5. The experimental system was setup in the same manner for all of the tests, except for the different vacuum windows, IR filters and LOs listed below.

Table 3.5: Summary of RF performance.

Test #	Dev. #	Vac. Wind.[a]	IR Filt.[b]	LO	T_{block} (K)	T_{leak} (K)	T_{N}^{c} (K)	T_{RF}^{d} (K)	T_{IF} (K)
1	6.1	HDPE	A	Gunn	4.71	5.14	62.2	33.0	13.3
2	6.2	ZF	A	Gunn	4.67	5.22	34.5	15.4	14.0
3	6.2	ZF	B	Gunn	4.77	5.24	34.5	13.3	14.6
4	5.6	ZF	B	Gunn	–	5.13	35.7	12.6	10.3
5	2.2	ZF	B	Gunn*	–	5.46	41.7	13.2	–

[a] Vacuum windows: (HDPE) 553 µm thick HDPE, and (ZF) 24 mm thick Zotefoam. See App. B.4.
[b] Infrared filters: (A) 5 layers of 0.2 mm thick Zitex G-110, and (B) 1 layer of 1.52 mm thick Zitex G-106.
[c] Best noise temperature measured at any frequency.
[d] Measured at $\nu_{\text{LO}} = 230$ GHz.
* The Gunn oscillator was replaced by the GDM-12T oscillator from Millitech.

The noise temperature from most devices was close to 40 K from 225–240 GHz (Fig. 3.22). Test #1 had significantly higher RF noise due to the HDPE vacuum window, which is far more lossy than Zotefoam[7]. Test #5 also had a slightly higher noise temperature because a different LO was used and the mixer block temperature was higher than normal. In tests #2–5, the noise temperature began to deteriorate past 240 GHz, but remained below 100 K up to the highest LO frequency.

The RF and IF noise contributions were estimated in all cases using the technique of intersecting lines [53] and Woody's method [54], respectively. The results, listed in Table 3.5, show that a significant amount of noise came from the RF components (i.e., the beam splitter, vacuum window, IR filter, waveguide and planar circuit). These are all passive components, meaning that they are thermal noise sources where the effective noise temperature is related to the power dissipated in each component (recall Eqn. 3.8). Thermal noise contributions can be reduced by either minimising the power dissipation or lowering the physical temperature of the components. For

[7]This was confirmed by measuring the transmission through both windows using a freespace measurement system connected to a vector network analyser (VNA). The measurement results are presented in App. B.4.

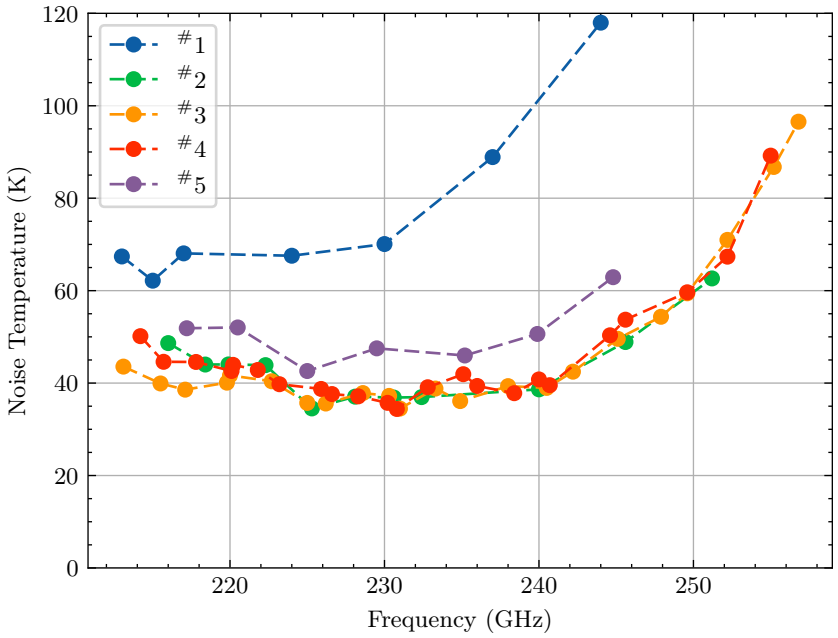

Figure 3.22: Summary of the noise temperature results. The numbers correspond to Table 3.5. Test #1 has a much higher noise temperature because a lossy HDPE window was used for the vacuum window. Test #5 also has a slightly higher noise temperature because the SIS device was relatively warm and a noisy LO was used for the test.

example, based on Table 3.5, switching to a Zotefoam window from HDPE reduced the overall noise temperature by ∼17 K, and switching from 5 layers of 0.2 mm thick Zitex to one layer of 1.52 mm thick Zitex reduced the noise temperature by ∼1 K (although these are all rough estimations because other aspects of the system may have changed between tests). For the most part, all of the RF components were optimised for these experiments (e.g., the thinnest beam splitter was used, and the beam edge tapers were all below -30 dB) and lowering the ambient temperature is not practical. As discussed in the previous subsection, some of the RF noise contribution could come from phase noise from the LO, diffraction in the optics or imperfect black body loads, but so far, there are no techniques to identify or isolate these noise contributions.

Impedance recovery

The embedding impedance refers to the impedance that is seen by the SIS junction. If it presents a poor impedance match to the SIS junction, the conversion efficiency of the mixer will be low and the noise temperature will be high. By recovering the embedding impedance directly from experimental data, it is possible to assess the tuning and to determine the accuracy of the HFSS simulations. The technique used to recover the embedding impedance from experimental data was already described

in Sec. 2.6.2, but a quick example is shown in Fig. 3.23a. The data for this plot was taken from device #6.1 at 230 GHz, and the error surface was calculated using Eqn. 2.60. Based on these results, the embedding impedance is estimated to be $Z_{\text{emb}} = (0.55 - j0.40) \cdot R_{\text{n}}$ at 230 GHz. Then, by using this embedding impedance, a simulated I–V curve was generated[8] , shown in Fig. 3.23b. This simulated I–V curve seems to match the original I–V curve very well even though the fit was only optimised over the first photon step (i.e., the "fit interval" in Fig. 3.23b).

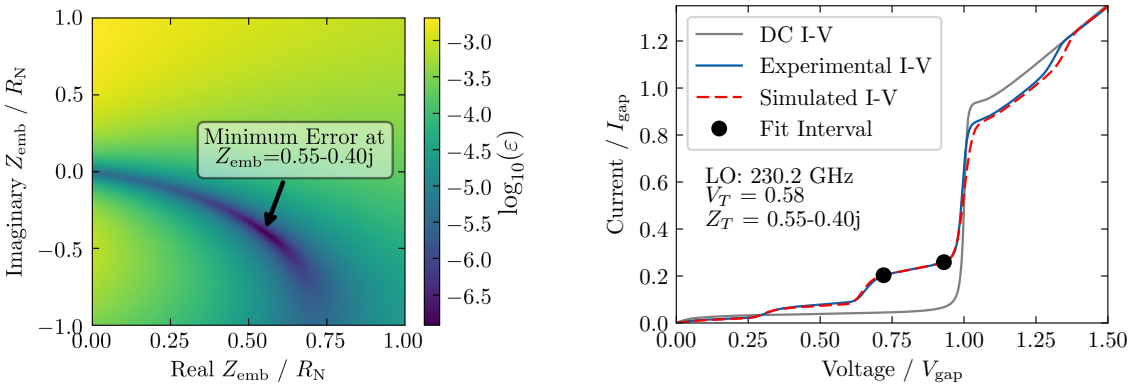

(a) The error surface calculated from Eqn. 2.60. This is used to estimate the embedding impedance.

(b) An I–V curve generated from the recovered embedding impedance (red). It is very close to the experimental I–V curve (blue).

Figure 3.23: An example of impedance recovery. The experimental data was taken from device #6.1 at 230 GHz.

Using the same technique, the embedding impedance was recovered from all of the devices in Table 3.5. As shown in Fig. 3.24, the recovered embedding impedances are very close to the simulated embedding impedance from HFSS, suggesting that the simplified 3D model from Fig. 3.4a was able to capture most of the characteristics of the device. It could be possible to further optimise the HFSS simulations to improve the match; however, there are too many factors that could influence the tuning. This includes the junction size, the specific capacitance, the surface impedance, and any additional loading from the waveguide horn (which was ignored in HFSS).

[8]To generate the response function that was used to simulate the pumped I–V curve, the experimental DC I–V curve was convolved with a Gaussian distribution ($\sigma = 0.02 \cdot V_{\text{gap}}$) in order to match the rounded steps of the experimental data. This issue, where simulated I–V data has sharper steps than experimental data, has also been noticed by other authors including Skalare [55] and could be caused by the RF and IF signals smearing the BCS singularity in the quasiparticle density of states [87] or a heating effect from the LO.

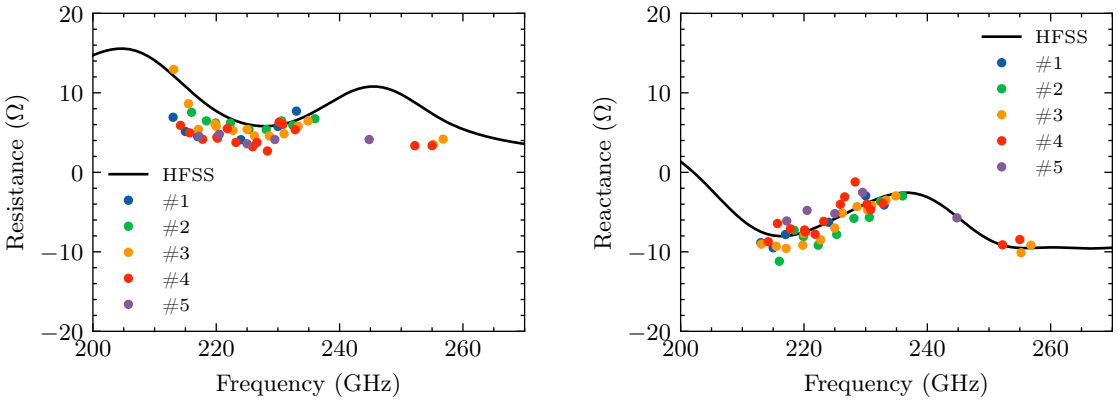

(a) Recovered embedding resistance (R_{emb}) (b) Recovered embedding reactance (X_{emb})

Figure 3.24: The recovered embedding impedances ($Z_{\text{emb}} = R_{\text{emb}} + jX_{\text{emb}}$) for the devices and configurations listed in Table 3.5. For comparison, the embedding impedance from HFSS is also included. Recall that it was not possible to recover the embedding impedance from the broken photon steps between 235 and 250 GHz, which is why there is a gap in the experimental data. Note that the data from HFSS has been smoothed.

Matching notch

In an attempt to lower the insertion loss of the planar circuit and thereby improve the SIS and IF noise contributions, a triangular notch was left in the quartz substrate of several SIS devices (Fig. 3.25a). This notch helps to match the impedance of the unloaded waveguide to that of the loaded waveguide. The notch is triangular because only straight cuts are possible with quartz substrates. The simulated results show much flatter coupling across the entire tuning range of the LO (Fig. 3.25b), and in the experimental results, the matching notch provided a significant noise improvement over a similar device without the matching notch (Fig. 3.25c). Furthermore, the noise improvements were seen predominantly below 235 GHz, as predicted by the simulated results.

3.8 IF performance

Similar to the RF performance, the IF performance was characterised by measuring the SIS device's response to hot and cold black body loads. The main difference was that the output power was instead measured as a function of IF frequency. To accomplish this, the band pass filter was removed from the IF chain and the detector diode was replaced by a spectrum analyser. The Y-factor technique was then applied to estimate the noise temperature and gain. In terms of IF performance, the IF bandwidth is the primary figure of merit, which represents the range of IF frequencies that

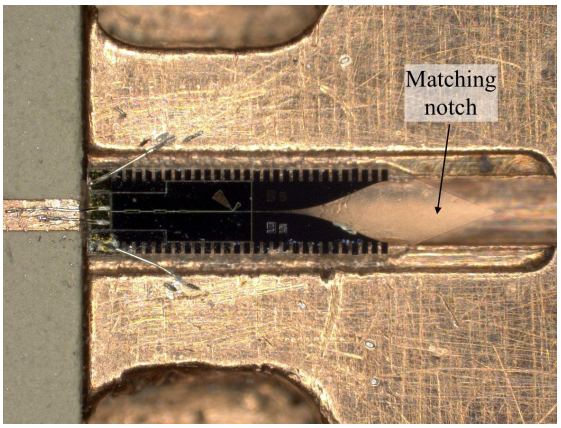

(a) Triangular notch left in the quartz substrate (length ≈ 700 µm).

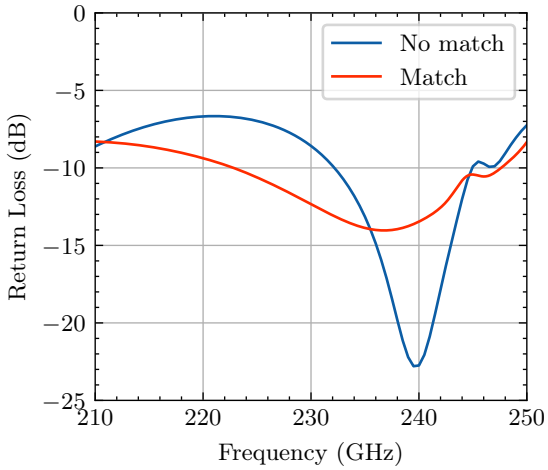

(b) Simulated return loss at the waveguide port (with and without the matching notch).

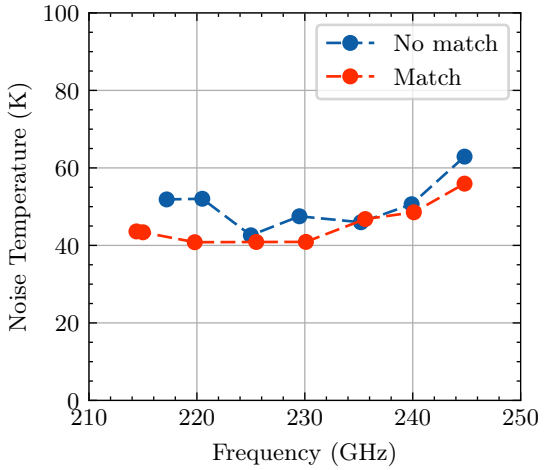

(c) Experimental noise temperature (with and without the matching notch).

Figure 3.25: A triangular notch was added to the quartz substrate to match the impedance of the empty waveguide to that of the loaded waveguide (i.e., with the quartz substrate in the middle). The same LO and IF chain were used for both tests, and the mixer block temperatures were also relatively warm in both tests (close to 4.95 K), resulting in slightly higher noise temperatures.

possess acceptable noise and gain properties.

An example of a typical measurement is shown in Fig. 3.26. This data was measured using device #9.5 in conjunction with a 6–20 GHz LNA. The down-converted IF power from the hot and cold black body loads is shown in red and blue, respectively, and the calculated noise temperature is shown in green. The dashed line represents the noise temperature that was calculated with the detector diode from 4–6 GHz, and it seems to match the results from the spectrum analyser (at least from 4–6 GHz). In these results, the usable IF range spans from approximately 2–9 GHz. The low end of the spectrum is limited by the LNA, which was only intended to operate from 6–20 GHz but has acceptable gain down to 3 GHz, and the high end of the spectrum is limited by two resonance-like structures centred at ∼9.7 and ∼12.7 GHz. These resonances limit the upper IF frequency range; although, the noise temperature drops briefly between 14.5–15 GHz. This IFBW is lower than what was predicted by SuperMix (predicted IF range: 0–17 GHz; recall Fig. 3.3), but it is slightly closer to the results from HFSS (predicted IF range: 0–13 GHz; recall Fig. 3.10).

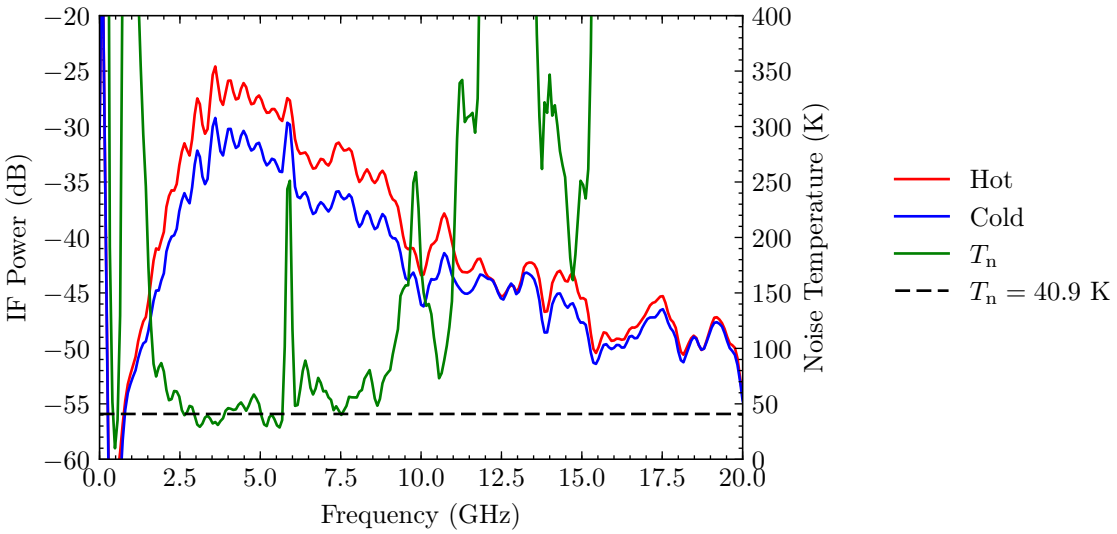

Figure 3.26: Measured IF spectrum from device #9.5 at $\nu_{LO} = 230$ GHz. The down-converted IF power from the hot (red) and cold (blue) black body loads was measured with a spectrum analyser, and the noise temperature (green) was calculated using the Y-factor technique. The dashed line is the noise temperature that was measured between 4 and 6 GHz with the detector diode.

These noise temperature measurements were repeated at different frequencies across the tuning range of the LO (Fig. 3.27), but there were not any significant differences in the IF spectra. The resonant structures stayed centred on the same frequencies except for the peak seen at 6 GHz, which disappeared almost entirely

in some measurements. This narrow peak was likely due to a resonance in the IF measurement chain and only appeared in around 50% of the measurements.

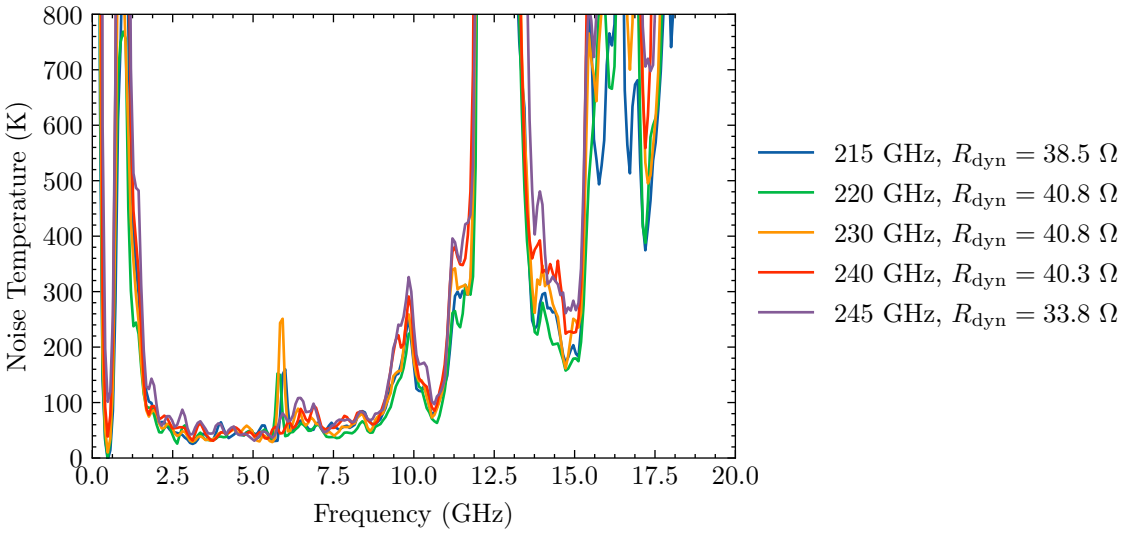

Figure 3.27: Measured IF spectrum from device #9.5 at different LO frequencies. The dynamic resistance R_{dyn} of the first photon step should correspond to the output resistance of the SIS junction. It was calculated from the pumped I–V curves on the first photon step.

The IF spectrum was then measured using multiple different devices and configurations to better understand the resonances in the IF spectrum. The results from four of these devices and configurations are shown in Fig. 3.28, with the details listed in Table 3.6. At the low end of the IF range, ringing was found in all cases below 3 GHz, which corresponds to the lower end of the LNAs' bandwidths. This ringing should mostly disappear if a wideband LNA is used or if an isolator is added between the SIS device and the LNA. At the high end of the IF range, the performance deteriorates past 8–10 GHz and then the IF response vanishes completely around 10–12 GHz. The resonant structure centred on 12.7 GHz did not seem to depend on the device, the LO frequency, the LNA or the number of bond wires.

3.8.1 IF matching circuits

In an attempt to increase the IFBW, several IF tuning boards were designed to match the output impedance of the SIS device to that of the IF circuit ($Z_0 = 50\ \Omega$). These matching circuits can increase the conversion efficiency at the upper IF frequencies, but there are practical limitations: they cannot match the device when the output impedance drops to zero, and they cannot achieve broadband matching when the output reactance exceeds the output resistance (a condition related to the Bode–Fano limit [88–90]).

Table 3.6: Summary of IF testing configurations.

Test #	Device #	No. of B.W.*	ν_{LO} (GHz)	LNA†	LNA BW (GHz)	Vacuum window
1	6.1	1	215	495D	4 – 12	HDPE
2	5.6	2	230	495D	4 – 12	Zotefoam
3	2.2	2	230	LNF	6 – 20	Zotefoam
4	9.5	2	230	LNF	6 – 20	Zotefoam

* The number of bond wires.
† The different LNAs are listed in Table 3.3.

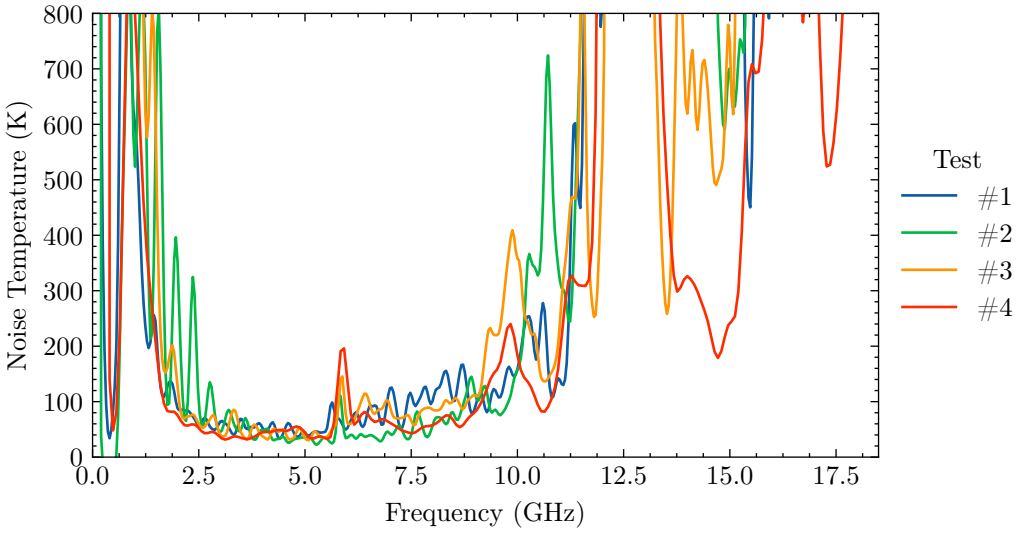

Figure 3.28: Noise temperature for the devices and configurations listed in Table 3.6. The data was convolved with a Gaussian distribution to smooth the data.

To create the matching circuit, the simulated S-parameters from the SIS device were imported into Ansys Designer (ANSYS® Designer™, Release 8.0), 2.5D electromagnetic simulation software. A 6-stage matching circuit was then optimised[9] to match the device to the IF circuit (Fig. 3.29a). The design was verified by simulating the new IF transformer in HFSS and cascading the S-parameters with those from the SIS mixer (Fig. 3.29b). The IF board was optimised for 0–16 GHz and should offer significantly better transmission at the upper IF frequencies (dimensions given in App. D).

[9]The technique that I used is similar to the technique described in [63], except that (a) a full chip simulation was used to generate the S-parameters instead of cascading subsections of the device, (b) the device was simulated as a 1-port network with the waveguide port ignored and the junction port replaced by a load, and (c) the junction impedance was set to R_J=40 Ω instead of R_n=14 Ω since 40 Ω is approximately the dynamic resistance of the first photon step.

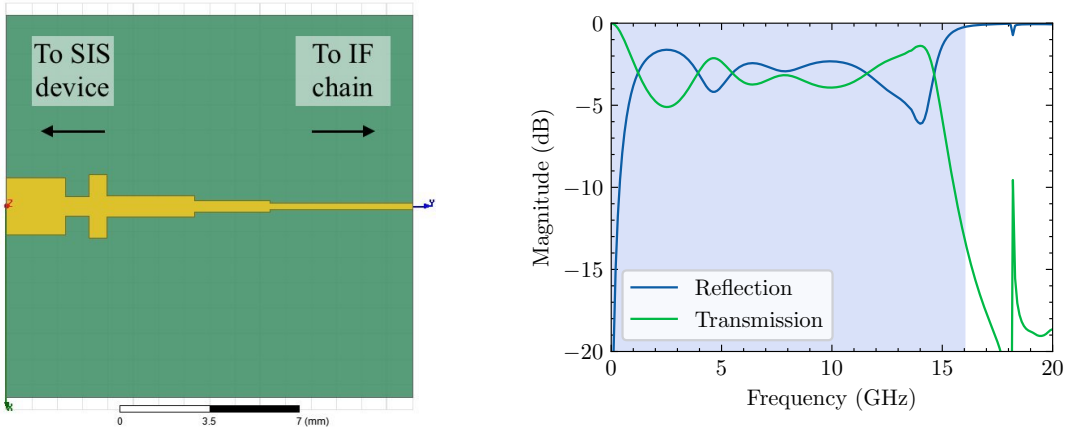

(a) Schematic of the new IF tuning board. The SIS device will be bonded on the left, and the SMA pin will connect on the right.

(b) Simulated performance. For these results, the S-parameters from the SIS device were cascaded with those from the IF board.

Figure 3.29: An IF tuning board optimised for 0–16 GHz.

The IF noise contribution resulting from the new 0–16 GHz IF tuning board is compared to a simple 50 Ω line in Fig. 3.30. (This was isolated from experimental data by using the shot noise. This will be described in more detail in Fig. 3.32.) With the new IF board, the IF noise is marginally flatter and the resonance at 9.7 GHz seems to shift up to ∼10.5 GHz; however, the larger resonance at 12.7 GHz still completely limits the upper IF frequency range to less than 12 GHz.

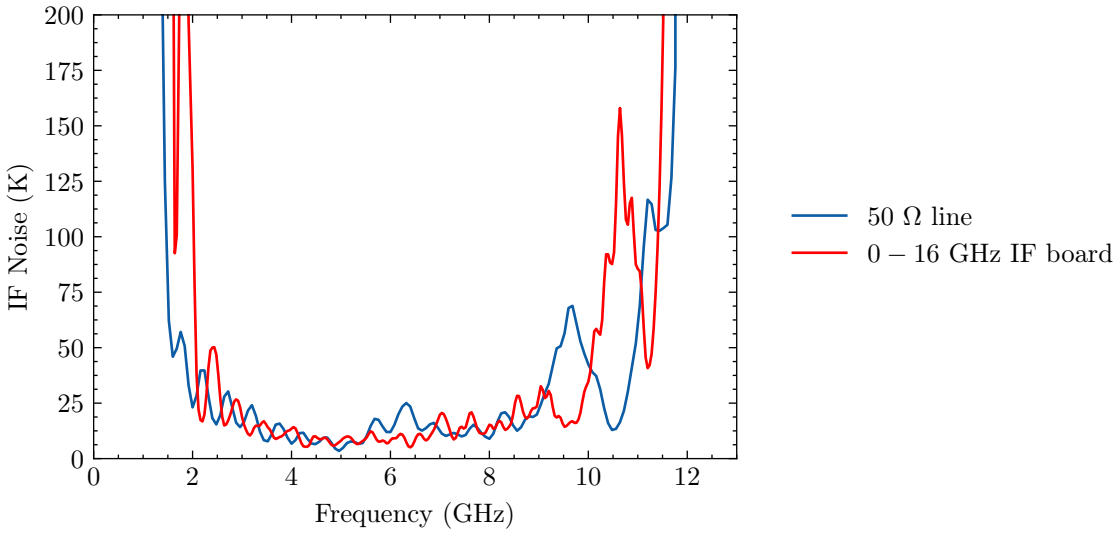

Figure 3.30: The IF noise calculated using different IF tuning boards. Device #9.5 was used for both tests with the same IF chain. The mixer block temperatures were also very similar.

3.8.2 The IF noise contribution

In SIS receivers, the noise component that changes with IF frequency is dominated by noise from the cryogenic LNA (T_{LNA}). When this noise is referred back to the junction, the effect of T_{LNA} is further amplified by the loss of the bias tee, IF board, bond wires and planar circuit. In Fig. 3.31, the noise from the CalTech and Low Noise Factory LNAs is multiplied by the simulated insertion loss of the planar circuit. The results show adequate performance below ∼15 GHz, but they do not explain the large resonance seen in experimental data around 12.7 GHz, suggesting that the resonance is not caused by the planar circuit or the LNA.

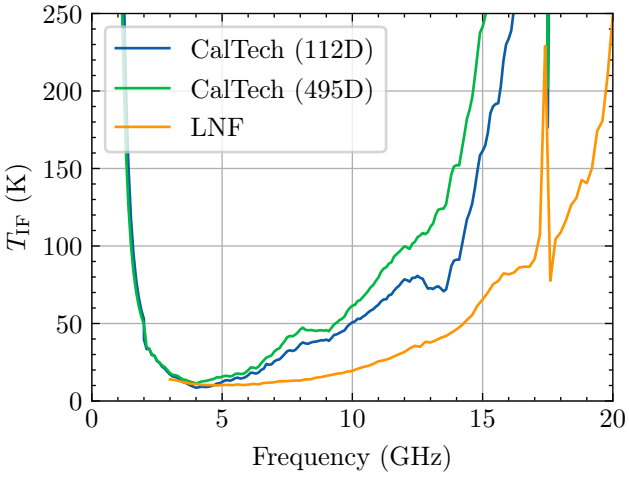

Figure 3.31: Noise from the LNA referred back to the SIS junction. CalTech characterised their LNA noise at 15 K, and Low Noise Factor (LNF) characterised theirs at 4 K.

To recover the IF noise from the experimental system as a function of IF frequency, the LO was turned off and the junction was biased at two different voltages above the gap. By assuming a linear shot noise slope of 5.8 K/mV [54], the IF noise was then estimated using the Y-factor technique. In Fig. 3.32, the estimated IF noise is close to the value that was estimated using the detector diode from 4–6 GHz (dashed line) and close to the noise from the LNA that was estimated in Fig. 3.31 from 3–8 GHz (yellow line). However, the resonances are again present in the experimental data with one centred around 9.7 GHz and another centred around 12.7 GHz. These results support the theory that the resonances are caused by a component in the IF sub-system and not the result of IF frequency dependent noise from the SIS junction. The potentially resonant components include the bond wires, the IF board, the bias tee, the coaxial cables and the LNA. These are investigated in more detail in the following sub-sections.

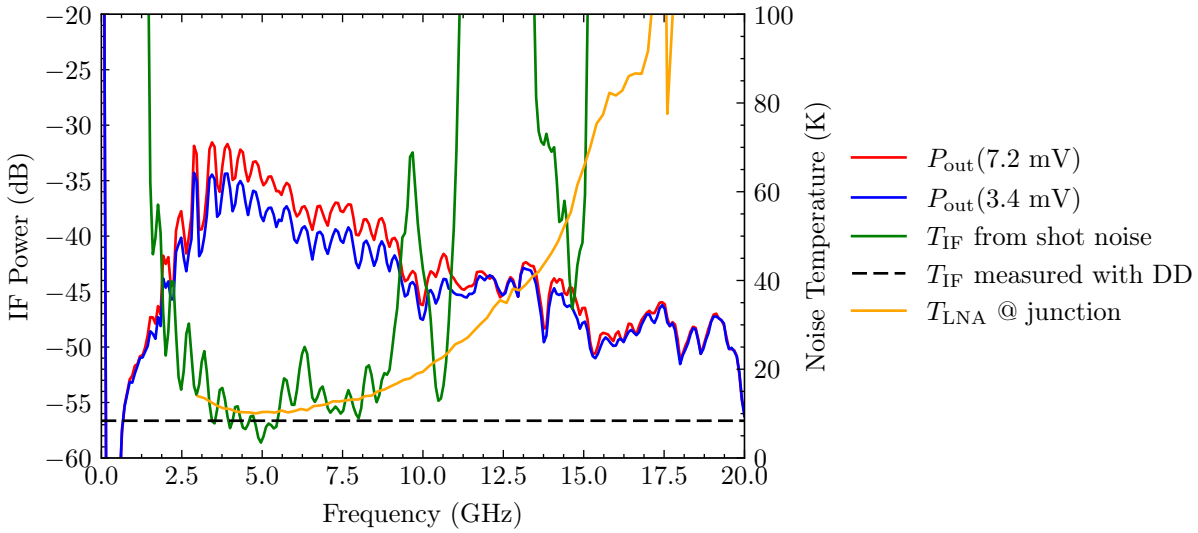

Figure 3.32: Measuring the IF noise as a function of IF frequency. The output power resulting from shot noise at two different bias voltages is shown in blue and red. These voltages correspond to effective temperatures of $T_{\text{shot}}(3.4\text{ mV}) = 16.5$ K and $T_{\text{shot}}(7.2\text{ mV}) = 38.5$ K, respectively. Using the Y-factor technique, the estimated IF noise is then shown in green. This can be compared to the value that was measured using the detector diode and a 4–6 GHz bandpass filter (shown as a dashed black line; from Fig. 3.20a). The noise temperature of the LNA referred to the SIS junction is also plotted in yellow (from Fig. 3.31).

Bond wires

All of the devices that were tested in this thesis were wedge bonded using 1-mil (25.4 µm) diameter aluminium bond wires. One or two short bond wires were used to carry the IF signal from the SIS device to the microstrip on the IF board, and another two were used to ground the device (see App. C). These bond wires present a series inductances to the signal path, which can be problematic at high frequencies.

In Fig. 3.33, the output impedance of the SIS device is plotted for a range of series inductances[10]. The real component R_{out} is not affected by the bond wires, but the imaginary component X_{out} rises considerably. Note that as the output reactance surpasses output resistance, broadband tuning becomes impossible (again, related to the Bode–Fano limit [88–90]). Therefore, the only method to maximise the IFBW is to minimise the bond wire inductance.

The transmission coefficient between the SIS junction and the IF circuit is plotted in Fig. 3.34a. By cascading the LNA noise with these results, the effective IF noise temperature is plotted in Fig. 3.34b. In both plots, the bond wire inductance significantly degrades the IF performance; however, the resonance seen at 12.7 GHz is still

[10]The technique that was used to generate these plots is detailed in App. C.

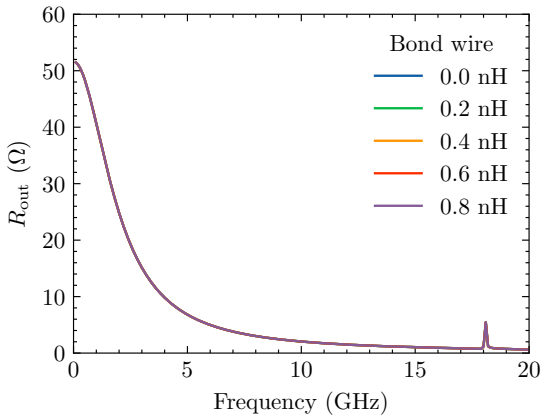

(a) Output resistance (R_{out})

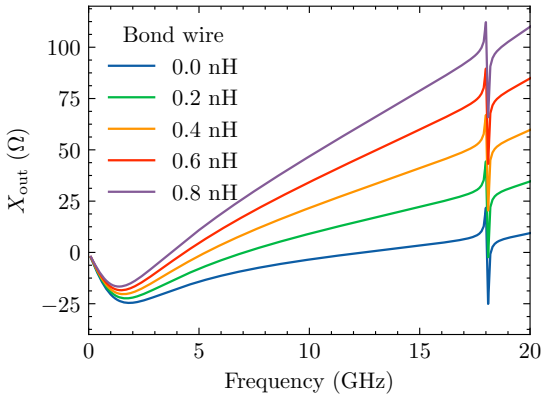

(b) Output reactance (X_{out})

Figure 3.33: The output impedance ($Z_{\text{out}} = R_{\text{out}} + jX_{\text{out}}$) of the mixer chip with a series inductance from a bond wire.

not reproduced, no matter the bond wire inductance, suggesting that there must be another cause for this resonance.

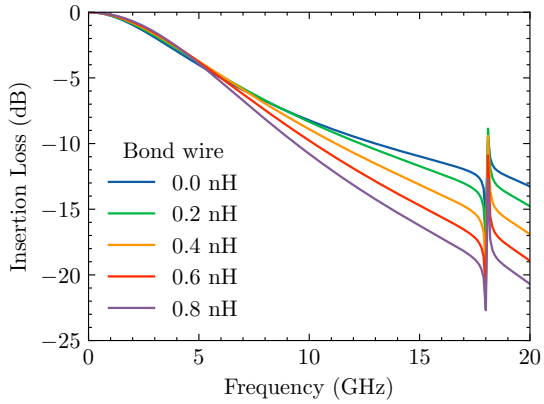

(a) Transmission between the SIS junction and the IF circuit.

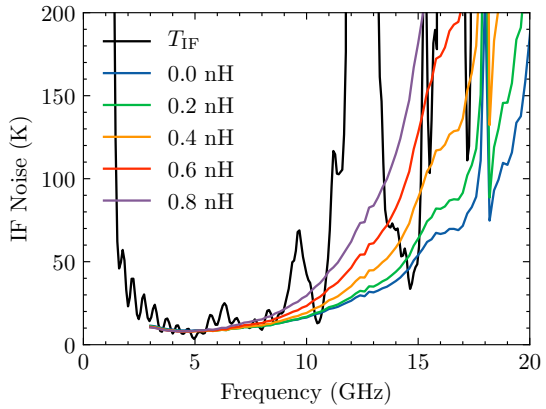

(b) Effective IF noise.

Figure 3.34: The effect of bond wires on transmission and IF noise contribution.

Regardless, the bond wire inductance should be minimised as much as possible by (a) using short, straight bond wires (wedge bonding is good for this), (b) ensuring that the device is as close as possible to the IF board and that it is even with the surface vertically, (c) using large diameter bond wire or ribbon bond, (d) using multiple bond wires, (e) keeping the ground plane close underneath the bond wires, and (f) adding any sort of high permittivity substance under the bond wires to reduce the effective height. In theory, these techniques can be combined to effectively remove the bond

wire inductance.

Cryogenic LNAs

All of the testing configurations so far used either one of the CalTech LNAs or the Low Noise Factor LNA; however, another LNA from the Yebes Observatory was also available. The results from the Yebes LNA are compared to those from the Low Noise Factory LNA in Fig. 3.35. The Yebes LNA was able to extend the IF performance down to ∼0.5 GHz (the lower limit of the bias tee) with significant ringing below 4 GHz. An isolator (QCI-075900XM00, Quinstar) was then added to reduce the ringing, but it limited the IF bandwidth to 3–12 GHz. The Low Noise Factory LNA had slightly better performance than the Yebes LNA at the upper IF frequencies, but neither LNA was able to extend the IF frequency range past 10 GHz.

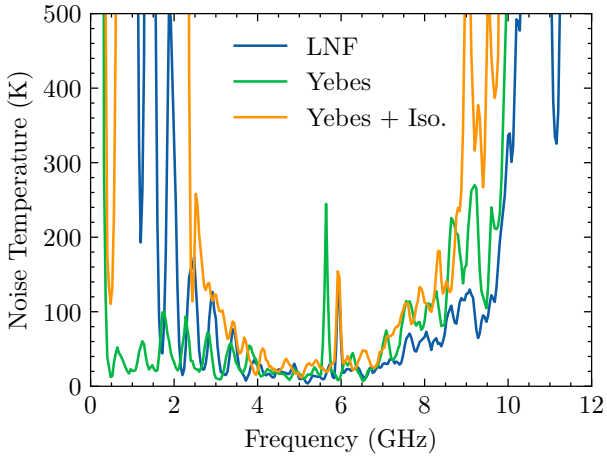

Figure 3.35: The measured IF response from device #5.7 using different LNAs and an optional isolator.

Bias tees

All of the tests so far used a bias tee with a 2–18 GHz operational bandwidth (8810SMF2-18, Inmet Inc.). The bandwidth of this bias tee was confirmed with a vector network analyser (VNA) at room temperature, but the performance could be temperature-dependent. Therefore, the bias tee was placed inside a cryostat, and then the insertion loss was measured with the VNA at three different temperatures: 293 K, 77 K, and 4 K. This bias tee is not rated for cryogenic temperatures, and as seen in Fig. 3.36a, a very pronounced resonance appeared in the transmission results as the bias tee was cooled. If this insertion loss is cascaded to calculate the IF noise temperature, the resultant noise is very close to experimental results (Fig. 3.36b),

strongly suggesting that the bias tee was the cause of the resonance at ∼12.7 GHz. When the IF noise is simulated without the bias tee, the IF response extends well beyond 10 GHz.

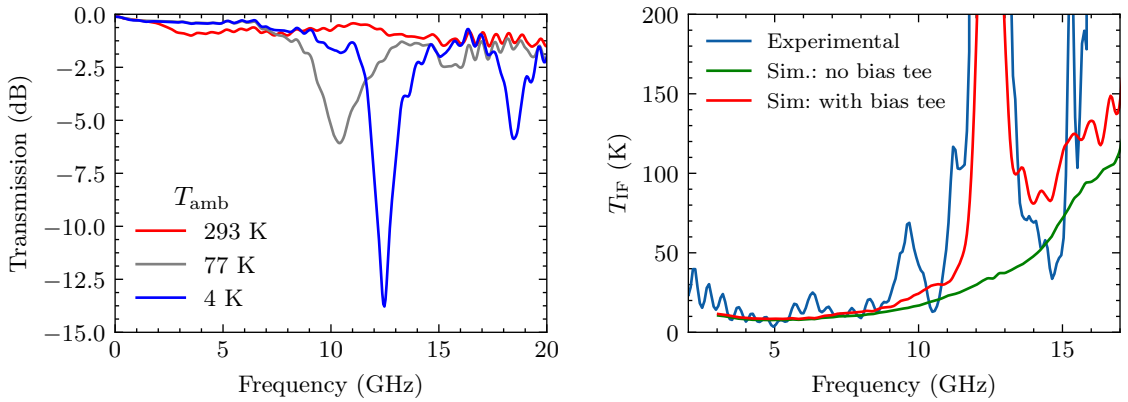

(a) Measured transmission through the bias tee at different temperatures.

(b) Resultant IF noise compared to experimental data.

Figure 3.36: The effect of cooling the bias tee to cryogenic temperatures. The 8810SMF2-18 bias tee from Inmet Inc. was used for this test.

The system was then tested with a different bias tee (8810SMF2-26, Inmet Inc.) that has a 2–26 GHz operational bandwidth. The results, plotted in Fig. 3.37, show that this new bias tee is able to extend the IF response by several gigahertz. The new bias tee, however, is again not rated for cryogenic temperatures and could be causing other resonances. I suspect that the IF response can be extended even further if a cryogenic bias tee is used, but none were available in our lab.

3.9 Future development

Improvements to the experimental measurement system

To improve the high frequency IF response, the measurement chain needs to be upgraded. First, a cryogenic bias tee needs to be installed since the current bias tee is not rated for cryogenic measurements and it is causing a large resonance in the IF response. Second, the LNA should be integrated into the mixer block to reduce the electrical distance to the SIS device, which would help to reduce the ringing in the IF response.

Characterising the IF noise of the measurement system

In Sec. 3.8.2, the IF noise was measured as a function of IF frequency by measuring the shot noise at two different bias voltages. However, this IF noise estimation was

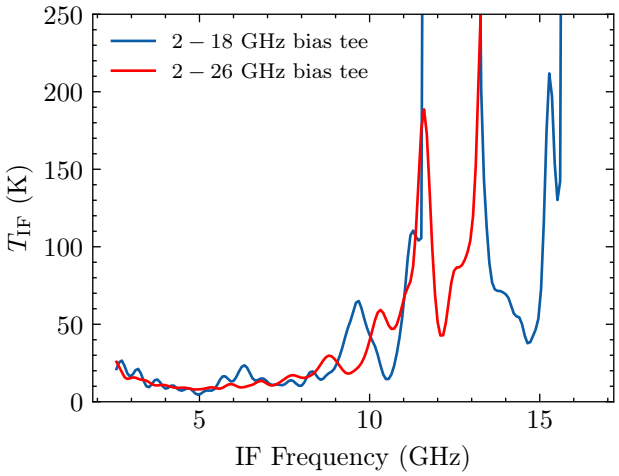

Figure 3.37: The measured IF noise using two different bias tees. Everything else, including the SIS device, was kept the same between the experiments. The 2–18 GHz bias tee (8810SMF2-18, Inmet Inc.) was used for all of the experimental data so far, but the 2–26 GHz bias tee (8810SMF2-26, Inmet Inc.) seems to provide a better IF response.

heavily influenced by the planar circuit of the device. To isolate the noise contribution from the IF measurement chain, a dedicated SIS device could be built to provide a flat shot noise power spectrum from $0 - 30$ GHz (as an example). The device would be very simple: just an SIS junction with minimal tuning and two bond pads. If the device was formed such that it could fit into the waveguide of the mixer block, this would allow the entire IF chain to be characterised in-place, helping to identify the source of any noise contributions (such as faulty bias tees). SIS junctions have been used as shot noise sources in the past (e.g., [91, 92]), but they have not been used in this application.

Y-factor measurements with a shot noise source

One problem with Y-factor measurements (briefly discussed in Sec. 3.7.1) is that the black body loads may be flawed: they may not actually be the correct temperature and their surfaces may be partially reflective. A possible solution is to replace the black body loads with a shot noise source, such as a diode or SIS junction. Then, different effective temperatures could be set by simply changing the bias voltage of the source. The shot noise source would have to be designed to efficiently couple the noise into the mixer block's waveguide, but this can easily be accomplished by using a second SIS device, as demonstrated in Fig. 3.38. In this diagram, device $^{\#}1$ is the device-under-test and device $^{\#}2$ is the noise source. The LO is then injected through a directional coupler.

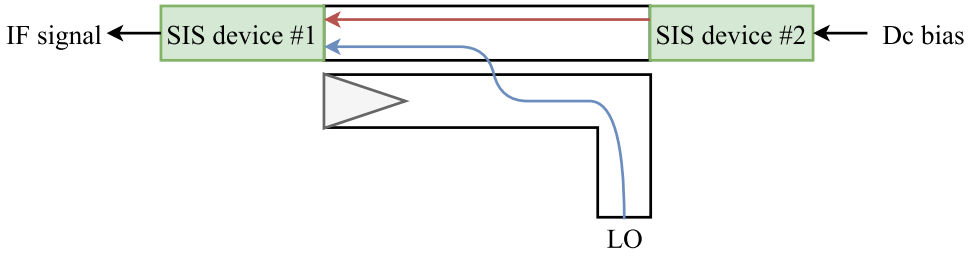

Figure 3.38: Using a second SIS device as a shot noise source for Y-factor measurements. Here, device #1 is the device-under-test, and device #2 is generating shot noise. The effective temperature of device #2 is controlled by a DC bias voltage. The LO signal shown in blue is injected using a waveguide directional coupler.

This configuration would allow for highly accurate input signals with only minimal optical requirements. Additionally, the noise temperature from the device could be isolated from the noise in the RF system, and the conversion efficiency could be easily calibrated by noting the symmetry of the test setup. In the future, this setup could be integrated into receivers or even integrated into SIS devices in order to perform quick noise temperature calibrations between observations. The shot noise source can also be easily modulated, akin to a chopper wheel, in order to analyse gain stability or even to assess direct detection.

3.10 Conclusion

A new 230 GHz SIS device has been presented in this chapter. It was optimised for wide IFBW and it uses a finline transition to couple energy from the waveguide to the planar circuit. The RF performance was measured and multiple devices had noise temperatures of ∼40 K from 215 GHz to 245 GHz, even despite relatively warm cryostat temperatures. The embedding impedance was recovered from the experimental I–V curves and the results were found to be very close to simulation results from HFSS. The IF performance was also characterised and good IF performance was found from approximately $0-10$ GHz. A large resonance was found consistently around 12.7 GHz, which limited the upper IF frequency range. After a long investigation, the source of the resonance was identified as the bias tee. The bias tee was replaced with another model, and then the IF noise contribution was found to be below 200 K from $0-13$ GHz. I suspect that the IF response can be extended even further if the bias tee is replaced with a new bias tee that is rated for cryogenic temperatures.

Chapter 4

SIS Mixer Simulation

4.1 Introduction

In Chapter 2, Tucker's quantum mixer theory [11, 12, 26] was used to describe heterodyne mixing in SIS junctions. To summarise, this approach first calculates the operating point of the SIS junction based on the local-oscillator signal (large-signal analysis) and then the junction is linearised around this point to calculate the noise temperature and conversion gain (small-signal analysis). Tucker theory successfully predicted quantum limited mixing noise (e.g., [93]) and conversion efficiencies above unity (e.g., [94–97]); however, it makes two major assumptions: (1) that the higher-order harmonics are short-circuited by the intrinsic capacitance of the SIS junction, and (2) that the sideband signals are not large enough to affect the operating point of the junction. These assumptions may not hold for the 230 GHz SIS device from Chp. 3 because it has a low $\omega R_{\mathrm{n}} C_{\mathrm{J}}$–product that may not sufficiently short-circuit the higher-order harmonics, and a singular SIS junction, which is prone to power saturation.

To address the first assumption from Tucker theory, Withington and Kollberg [85] calculated the higher-order harmonics of the local-oscillator (LO) using a spectral-domain technique. This was done by noting that the spectrum of the LO's phase factor could be generated by convolving the spectra of the LO's harmonics. Their technique, which they later improved in [98], was then used by researchers at CalTech to create SuperMix [74], an important SIS simulation package. This package still relies on Tucker's perturbation approach, but the higher-order harmonics of the LO are included, which can result in lower conversion gain if the junction's $\omega R_{\mathrm{n}} C_{\mathrm{J}}$–product is small [85, 99].

Kittara, Withington and Yassin [100–102] then addressed the second assumption by extending the *single-tone* analysis to include an arbitrary number of potentially large-signal tones. With *multi-tone* spectral domain analysis (MTSDA), the junction is no longer linearised around an operating point, making it suitable for the analysis of strong sideband signals. With this added capability, the MTSDA technique was used by Withington et al. [101] to analyse SIS mixer saturation and by Kittara et al. [102] to simulate sub-harmonic pumping.

The MTSDA technique is very powerful and could offer much more accurate simulations of the 230 GHz SIS device from Chapter 3. However, the code from [100–102] was never built into a stable release and it was written in what is now an outdated version of C++, making it difficult to read or adapt for a modern computer. There is still more work that can be done with the MTSDA software, but the code needs to be rewritten in a modern, high-level language.

The goal of this chapter is to investigate the operation of the 230 GHz SIS device from Chp. 3 with MTSDA simulations. These simulations can provide more accurate estimations of the IF bandwidth and explain different experimental phenomena, such as the broken photon steps from Sec. 3.7.1. This device has a low $\omega R_{\mathrm{n}} C_{\mathrm{J}}$–product close to 2.3, a wide IFBW and a singular SIS junction, all of which suggest that the mixer's simulated performance could be heavily influenced by the assumptions made by Tucker theory and SuperMix. To begin this chapter, the MTSDA technique is discussed in Sec. 4.2. Next, the harmonic balance procedure that was used to solve for the tunnelling currents in the presence of the embedding network is outlined in Sec. 4.3. A software package was developed to implement these techniques—the details of which are discussed in Sec. 4.4. Basic single-tone simulations are then presented in Sec. 4.5, which help to validate the simulation software and understand how the junction's properties respond to changes in the embedding circuit. Finally, in Sec. 4.6 the 230 GHz SIS device from Chp. 3 is simulated and compared to experimental results.

Note that in this chapter, normalised values are denoted by a tilde placed on top of the variable, e.g., $\widetilde{V} = V \,/\, V_{\mathrm{gap}}$. Voltages are normalised to the gap voltage V_{gap}, impedances are normalised to the normal resistance R_{n}, currents are normalised to $I_{\mathrm{gap}} = V_{\mathrm{gap}}/R_{\mathrm{n}}$, and frequencies are normalised to the gap frequency $\omega_{\mathrm{gap}} = eV_{\mathrm{gap}}/\hbar$.

4.2 Multi-tone spectral domain analysis

In spectral domain analysis[1], the input signals are assumed to be entirely periodic. The combined voltage drop across the junction, for an arbitrary number of frequencies F and harmonics P, can then be written as:

$$V(t) = V_0 + \sum_{f=1}^{F} \sum_{p=1}^{P} |V_p^{(f)}| \, \cos(p\,\omega^{(f)}\,t + \phi_p^{(f)}) \tag{4.1}$$

where $|V_p^{(f)}|$ is the AC voltage amplitude, $\omega^{(f)}$ is the angular frequency, $\phi_p^{(f)}$ is the AC voltage phase, and f and p denote the f^{th} frequency and the p^{th} harmonic, respectively. This voltage modulates the phase factor of the quasiparticles in the ungrounded electrode by[2]:

$$f(t) = \exp\left[-j\,\omega_{\text{gap}} \int_{-\infty}^{t} V(\tau) - V_0 \; \mathrm{d}\tau\right] \tag{4.3}$$

$$= \prod_{f=1}^{F} \prod_{p=1}^{P} \sum_{n=-\infty}^{\infty} A_n^{(f)}(p)\, e^{-jnp\omega^{(f)}t} \tag{4.4}$$

where $\omega_{\text{gap}}{=}eV_{\text{gap}}/\hbar$ is the angular gap frequency and the complex coefficients are given by:

$$A_n^{(f)}(p) = J_n\left(\alpha_p^{(f)}\right)\, e^{-jn\phi_p^{(f)}}\,. \tag{4.5}$$

Here, J_n is the n^{th} order Bessel function of the first kind, and $\alpha_p^{(f)}$ is the junction drive level, defined as:

$$\alpha_p^{(f)} = \frac{e\,|V_p^{(f)}|}{\hbar\, p\, \omega^{(f)}}\,. \tag{4.6}$$

The phase factor $f(t)$ can then be used to calculate the time-averaged tunnelling current from the Werthamer expression [45]:

$$\langle I(t)\rangle = \mathrm{Im} \iint_{-\infty}^{\infty} W(\omega')\, W^*(\omega'')\, e^{-j(\omega'-\omega'')t} \;\cdot\; I_{\text{R}}(V_0 + \hbar\,\omega'/e)\; \mathrm{d}\omega'\, \mathrm{d}\omega'' \tag{4.7}$$

[1] In this section, the description of multi-tone spectral domain analysis is based upon the work found in [100–102], especially P. Kittara's thesis [100]. Also, many of the terms and concepts have already been discussed in Chp. 2, so I will assume that that chapter has already been read.

[2] By applying the Jacobi-Anger expansion:

$$\exp\left\{j \sum_k z_k \,\sin\theta_k\right\} = \prod_k \exp\left\{j\, z_k \,\sin\theta_k\right\} \equiv \prod_k \sum_{n=-\infty}^{\infty} J_n(z_k)\, e^{jn\theta_k} \tag{4.2}$$

where $W(\omega')$ is the Fourier transform of $f(t)$, and I_{R} is the complex response function of the SIS junction[3].

Previously, for the large-signal analysis of the LO in Sec. 2.4, the phase factor $f(t)$ was simply a series of complex exponentials in the time-domain. In the spectral-domain, this manifested as discrete frequency points at all of the harmonics of the LO. Now, due to the products in Eqn. 4.4, $W(\omega')$ has to be generated by convolving the phase factors of the individual tones and harmonics. This can be written as:

$$W(\omega') = W^{(1)}(\omega') * W^{(2)}(\omega') * \ \ldots \ * W^{(F)}(\omega') \tag{4.8}$$

where $W^{(f)}(\omega')$ is the phase factor spectrum of the f^{th} tone, which is itself the convolution product of the phase factor spectra representing the harmonics at this frequency:

$$W^{(f)}(\omega') = W_1^{(f)}(\omega') * W_2^{(f)}(\omega') * \ \ldots \ * W_P^{(f)}(\omega'). \tag{4.9}$$

Since all of the frequency components of $W^{(f)}(\omega')$ are harmonics of $\omega^{(f)}$, $W^{(f)}(\omega')$ can be represented as:

$$W^{(f)}(\omega') = \sum_{k=-\infty}^{\infty} C_k^{(f)} \cdot \delta\left(\omega' - k\,\omega^{(f)}\right), \tag{4.10}$$

where the coefficients are calculated using the recursive formula from [85, 98]:

$$C_k^{(f)}(P) = \sum_{m=-\infty}^{\infty} C_{k-P\,m}^{(f)}(P-1)\, A_m^{(f)}(P). \tag{4.11}$$

The overall phase factor from Eqn. 4.8 can then be written as

$$\begin{aligned} W(\omega') = \sum_{k_1=-\infty}^{\infty} \sum_{k_2=-\infty}^{\infty} \ \ldots \ \sum_{k_F=-\infty}^{\infty} C_{k_1}^{(1)} C_{k_2}^{(2)} \ \ldots \ C_{k_F}^{(F)} \\ \cdot \delta(\omega' - k_1\,\omega^{(1)} - k_2\,\omega^{(2)} - \ \ldots \ - k_F\,\omega^{(F)}). \end{aligned} \tag{4.12}$$

To calculate the tunnelling current from the Werthamer expression, Kittara [100] first combines the coefficients and frequencies as:

$$C_{k_1}^{(1)}\, C_{k_2}^{(2)} \ \ldots \ C_{k_F}^{(F)} \to C_i \tag{4.13}$$

$$k_1\,\omega^{(1)} + k_2\,\omega^{(2)} + \ \ldots \ + k_F\,\omega^{(F)} \to \omega_i\ . \tag{4.14}$$

[3]The response function was previously defined in Sec. 2.4. As a reminder: the imaginary component is the DC I–V curve, and the real component is the Kramers-Kronig transform of the DC I–V curve.

These can then be inserted into Eqn. 4.7 to solve for the time-averaged tunnelling current:

$$\langle I(t)\rangle = \mathrm{Im}\sum_{i,j} e^{j(\omega_j-\omega_i)t}\left(R_{i,j}+jS_{i,j}\right) \tag{4.15}$$

where the coefficients are given by:

$$R_{i,j}+jS_{i,j} = C_i\,C_j^*\cdot I_\mathrm{R}\left(V_0+\frac{\omega_i}{\omega_\mathrm{gap}}\right). \tag{4.16}$$

The tunnelling current at any frequency $\omega_p^{(f)}$ is then:

$$I_p^{(f)} = \sum_{i,j}\left[(S_{i,j}+S_{-i,-j})-j(R_{i,j}-R_{-i,-j})\right] \qquad \forall\,(\omega_j-\omega_i)=\omega_p^{(f)}. \tag{4.17}$$

A much more detailed explanation of the MTSDA technique can be found in [100].

4.3 Harmonic balance

Real SIS junctions exist within complex systems involving freespace components, feed horns, waveguides, and planar circuits. However, if the system only consists of linear components, it can be reduced to a series of Thévenin equivalent circuits, with one for each unique frequency $\omega_p^{(f)}$, as seen in Fig. 4.1. In this diagram, $(V_\mathrm{T})_p^{(f)}$ is the Thévenin voltage, $(Z_\mathrm{T})_p^{(f)}$ is the Thévenin impedance, and $V_p^{(f)}$ and $I_p^{(f)}$ correspond to the junction voltage and current from Eqns. 4.1 and 4.17, respectively. The challenge then is to determine the set of junction voltages $V_p^{(f)}$ that satisfy

$$(V_\mathrm{T})_p^{(f)} - I_p^{(f)}\cdot(Z_\mathrm{T})_p^{(f)} = V_p^{(f)} \tag{4.18}$$

for every Thévenin circuit *simultaneously*. This is difficult because the tunnelling current $I_p^{(f)}$ at one tone f and harmonic p depends on all of the other tones and harmonics, and furthermore, the tunnelling current expression in Eqn. 4.17 is highly non-linear. The process of solving these circuits simultaneously is known as *harmonic balance*.

The harmonic balance procedure from [98, 100] uses Newton's method to solve Eqn. 4.18 in a way that has been adapted for multiple dimensions and complex numbers. To begin, an error function is defined as

$$\mathbf{\Delta}(\mathbf{V}) = \mathbf{V}_\mathrm{T} - \mathbf{Z}_\mathrm{T}\,\mathbf{I}(\mathbf{V}) - \mathbf{V}. \tag{4.19}$$

where $\mathbf{V}$ represents the junction voltages, $\mathbf{I}(\mathbf{V})$ represents the tunnelling currents,

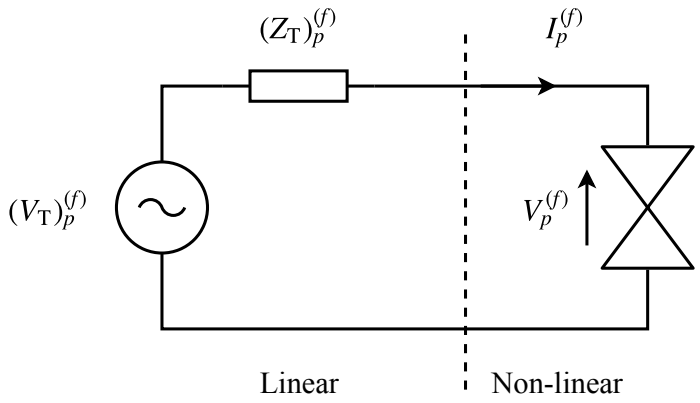

Figure 4.1: The circuit for the p^{th} harmonic of the f^{th} frequency. The Thévenin equivalent circuit is on the left (linear) and the junction is on the right (non-linear). In this diagram, the junction's intrinsic capacitance C_J is included within the embedding circuit.

and $\mathbf{V}_T$ and $\mathbf{Z}_T$ represent the Thévenin voltages and impedances, respectively. In Eqn. 4.19, the current and voltages are column vectors, denoted by bold lettering, while the impedance is a diagonal matrix. The update equation is then given by

$$\mathbf{V}_{k+1} = \mathbf{V}_k - [\mathbf{J}(\mathbf{V}_k)]^{-1} \boldsymbol{\Delta}(\mathbf{V}_k) \tag{4.20}$$

where k is the iteration number, and $\mathbf{J}(\mathbf{V}_k)$ is the Jacobian matrix calculated from the derivatives of $\mathbf{I}(\mathbf{V}_k)$. Provided with an adequate initial guess, Eqn. 4.20 has a quadratic rate of convergence. Practical information on implementing this harmonic balance procedure can be found in [98, 100].

4.4 The QMix software package

A software package named QMix[4], short for Quasiparticle Mixing, was created in order to implement the MTSDA technique and harmonic balance procedure. It was written in Python, which is an interpreted programming language that is easily portable to different machines and operating systems. A linear algebra library (NumPy[5]; based on BLAS and LAPACK) was used extensively to handle the arrays and matrices, and a scientific library (SciPy[6]) was used for general tasks such as generating Bessel functions, performing Hilbert transforms, interpolating and filtering data, and providing scientific constants.

[4]Hosted on https://github.com/garrettj403/QMix.
[5]Online: https://www.numpy.org/
[6]Online: https://www.scipy.org/

The software is easy to use, and several example workflows are provided within the repository. In general, each simulation requires three basic input parameters:

1. General simulation parameters are needed to define such things as the number of tones and the number of harmonics. The summation limits of n in Eqn. 4.4 are also required, which effectively set the number of Bessel functions that are included in the calculation. The value, denoted by N_B, that is required for each simulation depends on the frequency, the number of tones and the junction drive level, with higher drive levels requiring higher summation limits. Kittara [100] suggests $N_\mathrm{B} = 9$ for single-tone simulations and $N_\mathrm{B} = 20$ for heterodyne mixing; although, this is a rough rule-of-thumb.

2. A response function is required in order to characterise the SIS junction. The imaginary component of the response function is simply the DC I–V curve, while the real component is found from the Kramers-Kronig transform (explained previously in Chp. 2). In QMix, the DC I–V curve can either be imported from experimental data or generated from one of several mathematical models. The "ideal" response function is shown in Fig. 4.2, which has an infinitely sharp transition. The response function can also be convolved with a Gaussian distribution to generate a variety of transition linearities.

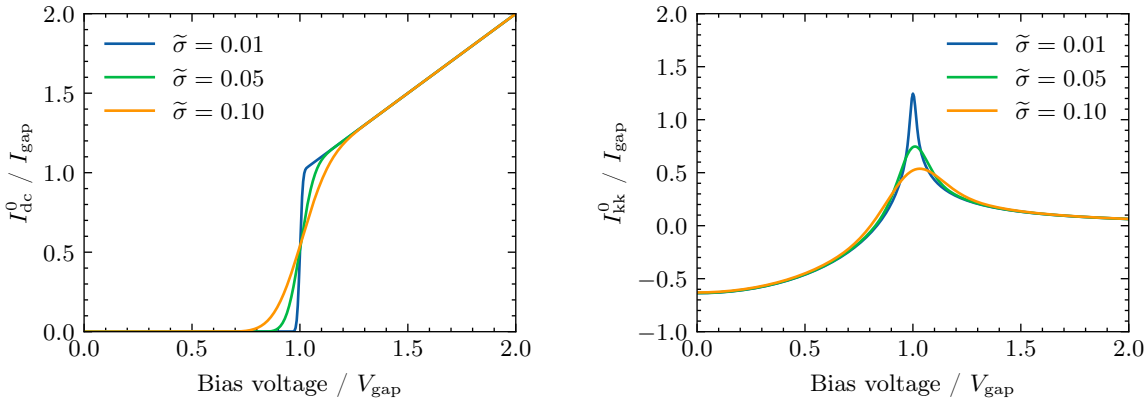

(a) The imaginary component of the response function is the DC I–V curve, represented by $I^0_\mathrm{dc}(V_0)$.

(b) The real component of the response function is the Kramers-Kronig transform of the DC I–V curve, represented by $I^0_\mathrm{kk}(V_0)$.

Figure 4.2: The ideal response function. Here it is convolved with a Gaussian distribution (with standard deviation $\widetilde{\sigma}$) to achieve a range of gap linearities. (Recall that the tildes on top of the variables represent normalised values.)

3. The Thévenin equivalent circuit values are required for each tone and harmonic in order to define the embedding network (i.e., Fig. 4.1). This includes the Thévenin circuits' frequency, voltage and impedance. In QMix, these values are all normalised to the properties of the junction: the voltages are normalised to V_{gap}, the impedances are normalised to R_{n}, the currents are normalised to $I_{\mathrm{gap}} = V_{\mathrm{gap}}/R_{\mathrm{n}}$, and the frequencies are normalised to $\omega_{\mathrm{gap}} = eV_{\mathrm{gap}}/\hbar$.

All of the key functions in this software package have unit tests to ensure that they are operating correctly. Simulated results from this software have also been compared to the results in [100–102] with very good agreement.

4.5 Single-tone simulations

To test the QMix package and investigate simple SIS junction behaviour, a simulation was setup with one tone and one harmonic. For the initial simulations, the embedding circuit was ignored and the junction drive level was set to a constant value of $\alpha = V_1^{(1)}/V_{\mathrm{ph}} = 1$. The normalised frequency was then set to $\omega/\omega_{\mathrm{gap}} = 0.34$, which approximately corresponds to 230 GHz, assuming a gap frequency ~675 GHz. The response function was generated using the polynomial model from [103],

$$\widetilde{I}_{\mathrm{dc}}^{0}(\widetilde{V}_0) = \frac{\widetilde{V}_0^{\,2n+1}}{1+\widetilde{V}_0^{\,2n}}\,, \tag{4.21}$$

with order $n = 30$.

The simulated DC tunnelling current is plotted in Fig. 4.3a. It shows clear photon steps with step widths equal to the photon equivalent voltage, $\widetilde{V}_{\mathrm{ph}} = \omega/\omega_{\mathrm{gap}} = 0.34$. The AC tunnelling current was also simulated, but it was used to calculate the AC junction admittance, $Y_1^{(1)} = I_1^{(1)}/V_1^{(1)}$, where $I_1^{(1)}$ and $V_1^{(1)}$ are the AC current and voltage through the junction, respectively. As seen in Fig. 4.3b, the AC junction admittance changes from capacitive at $\widetilde{V}_0 = 1-\widetilde{V}_{\mathrm{ph}}$ to inductive $\widetilde{V}_0 = 1$, with the admittance becoming purely real in the middle of the first photon step.

Using the same simulation setup, the junction drive level was then swept from $\alpha = 0.5$ to $\alpha = 10$. In Fig. 4.4a, the DC tunnelling current of the first photon step rises with the junction drive level until the current saturates around $\alpha \sim 10$, showing that the probability of a quasiparticle tunnelling through the insulation barrier increases with AC signal power up until a saturation point. The AC junction admittance also approaches the normal-state value as the power is increased (Fig. 4.3b) suggesting

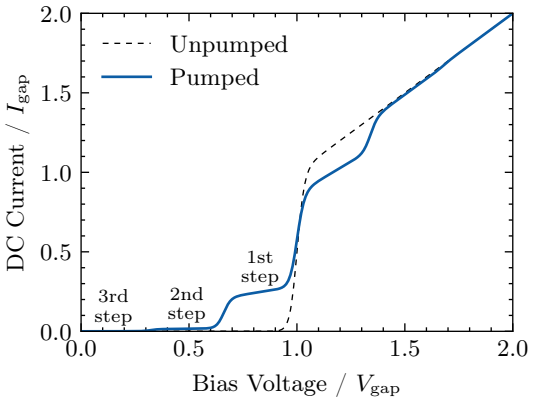

(a) DC tunnelling current. The dashed line represents the DC I–V curve.

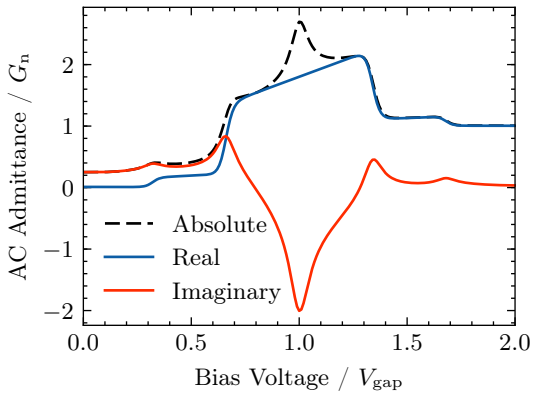

(b) AC junction admittance normalised to the normal-state conductance, $G_n = 1/R_n$.

Figure 4.3: A single tone simulation of an SIS junction with $\omega/\omega_{gap} = 0.34$ and $\alpha = 1$. The polynomial model from [103] was used to generate the DC I–V curve.

that for high signal powers, the junction's electrical properties approach the normal-state values.

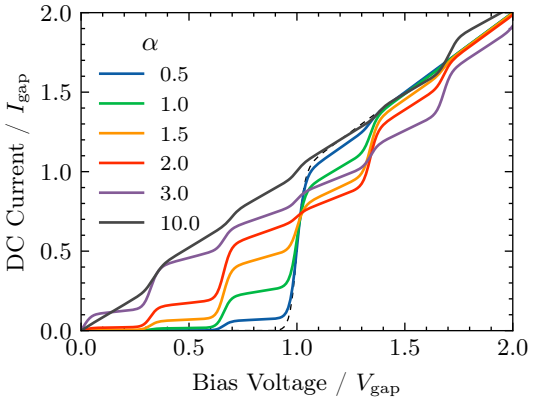

(a) DC tunnelling current. The DC I–V curve is shown as a dotted line.

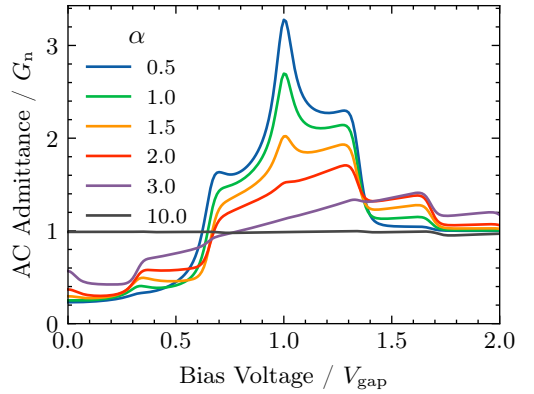

(b) Absolute value of the AC junction admittance (normalised to the normal-state conductance, $G_n = 1/R_n$).

Figure 4.4: A single tone simulation with different junction drive levels, $\alpha = V_1^{(1)}/V_{ph}$. The normalised frequency was kept at $\omega/\omega_{gap} = 0.34$.

Next, the frequency was swept from $\omega = 0.1 \cdot \omega_{gap}$ to $\omega = \omega_{gap}$ with the junction drive level held constant at $\alpha = 1$. As seen in Fig. 4.5a, the photon steps become wider as the frequency increases, and the width of the steps is equal to the photon equivalent voltage, $\widetilde{V}_{ph} = \omega/\omega_{gap}$. At $\omega = \omega_{gap}$, the photon voltage is equal to the gap voltage, so the step extends from $\widetilde{V}_0 = 1$ to $\widetilde{V}_0 = 0$. The AC junction admittance is also plotted for each frequency in Fig. 4.5b. At the lowest frequency, the junction's admittance

approaches the derivative of the DC I–V curve, and at the highest frequency, it approaches the normal-state conductance, $G_n = 1/R_n$.

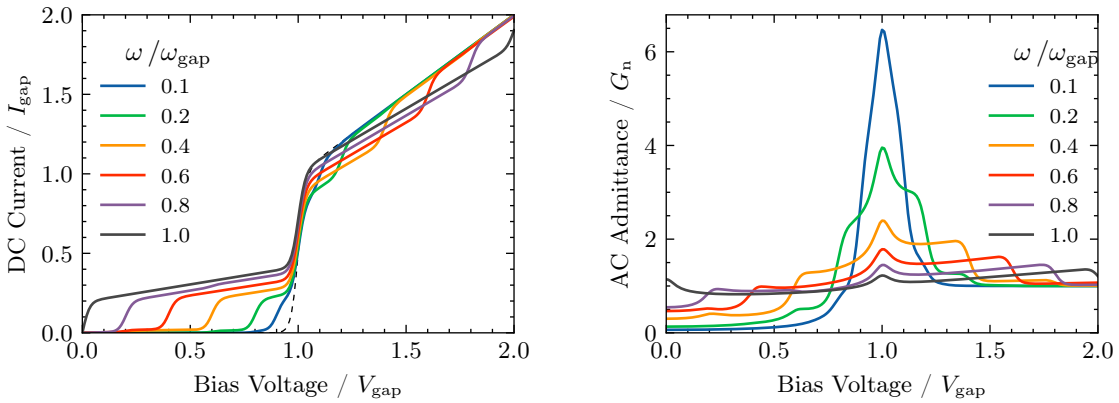

(a) DC tunnelling current. The dashed line represents the DC I–V curve.

(b) Absolute value of the ac junction admittance (normalised to the normal-state conductance, $G_n = 1/R_n$).

Figure 4.5: A single tone simulation at different frequencies. The junction drive level was set to $\alpha = 1$.

The embedding circuit was then incorporated into the simulation (Fig. 4.6). Initially, the embedding impedance was set to $\widetilde{Z}_T^{LO} = 0.3 - j0.3$ and the LO voltage was swept from $\widetilde{V}_T^{LO} = 0.2$ to 1 (the impedance approximately corresponds to the value from the 230 GHz mixer in Chp. 3). The pumped I–V curve was calculated for each voltage level (Fig. 4.7a), from which the dynamic resistance was found from the first photon step (Fig. 4.7b). This dynamic resistance should correspond to the output impedance of the junction at IF frequencies [12, 77].

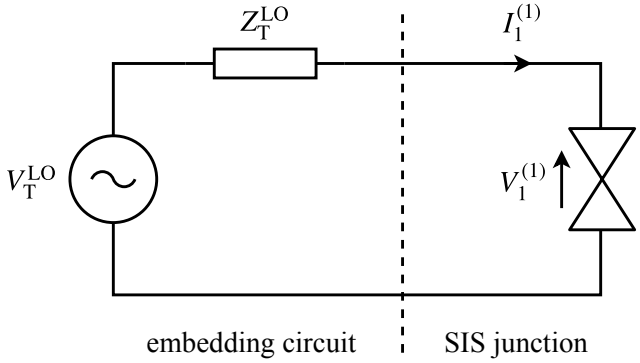

Figure 4.6: The circuit used for single tone simulations. The embedding circuit representing the local-oscillator (LO) is on the left (reduced to a Thévenin circuit), and the junction is on the right.

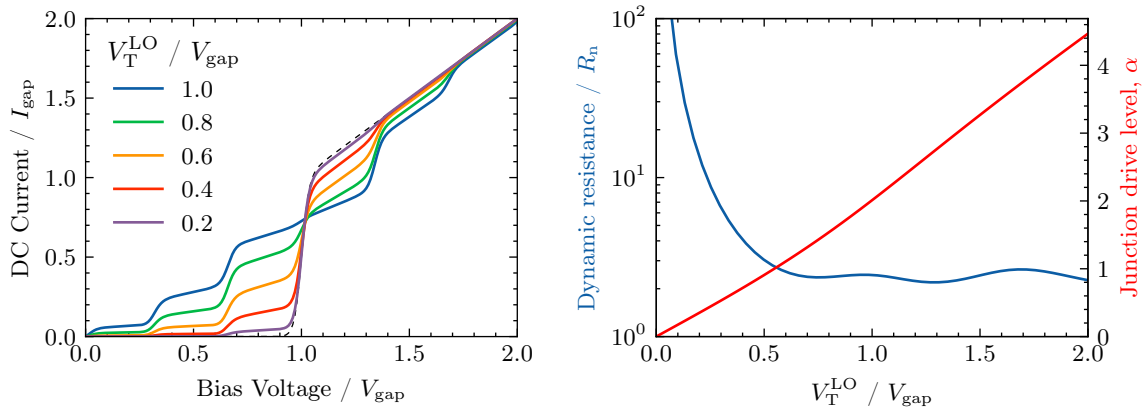

(a) Pumped I–V curves.

(b) Dynamic resistance of the first photon step.

Figure 4.7: A single tone simulation with different LO voltages, $\widetilde{V}_T^{LO}$. The embedding impedance was set to $\widetilde{Z}_T^{LO} = (0.3 - j0.3)$ and the normalised frequency was set to $\omega/\omega_{gap} = 0.34$.

The phase of the embedding impedance was then swept from $\angle Z_T^{LO} = -\pi$ to π, with the magnitude kept at $|\widetilde{Z}_T^{LO}| = 0.4$. The LO voltage for each simulation was set such that the junction drive level would be equal to 1 in the middle of the first photon step (i.e., $\alpha = 1$ at $\widetilde{V}_0 = 1 - \widetilde{V}_{ph}/2$). The pumped I–V curves from this simulation are plotted in Fig. 4.8a. They show that the phase of the embedding impedance has a strong effect on the dynamic resistance R_{dyn} of the first photon step. Generally, capacitive embedding impedances result in positive R_{dyn} values, and inductive embedding impedances result in negative R_{dyn} values. In Fig. 4.8b, the dynamic resistance is plotted for a range of embedding impedances. The phase at which the dynamic resistance goes from positive to negative is 7.6°.

In theory, Fig. 4.8b could be used to match the output impedance of an SIS junction to the intended IF circuit impedance. For example, to design a 40 Ω IF output impedance (i.e., $R_{dyn} = 40\ \Omega$), Fig. 4.8b shows that the embedding impedance should be $\widetilde{Z}_T^{LO} \sim 0.4\angle{-50°}$. This will change with the magnitude of $\widetilde{Z}_T^{LO}$, so a series of these plots could be simulated in order to generate a lookup table. Ideally, the dynamic resistance should remain constant between LO frequencies in order to design a wide IF bandwidth device (e.g., see the recent work on ALMA band-8 [57]).

4.6 Simulating the 230 GHz SIS device

QMix was initially developed to investigate the IF response of the 230 GHz SIS device from Chp. 3. This device has a small $\omega R_n C_J$–product, a wide IFBW and a

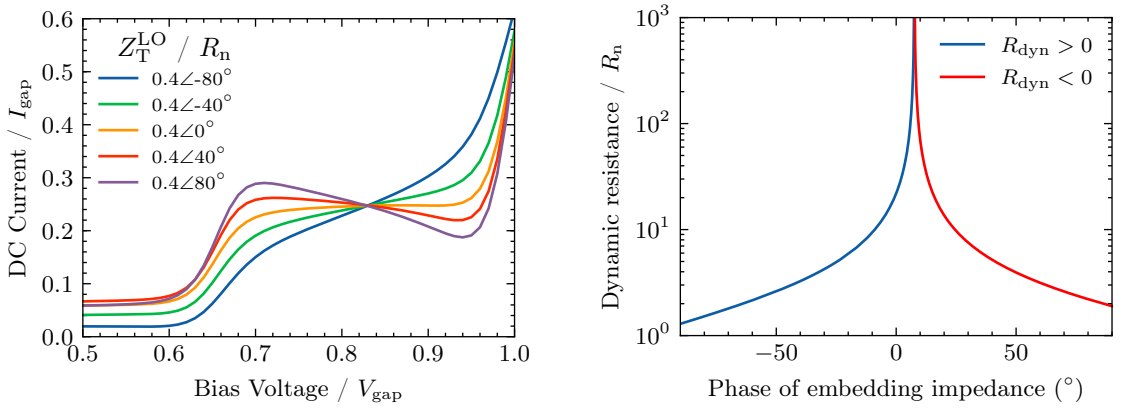

(a) Pumped I–V curves

(b) Dynamic resistance of the first photon step.

Figure 4.8: Sweeping the phase of the embedding impedance (with $|\widetilde{Z}_T^{LO}| = 0.4$ and $\widetilde{V}_{ph}^{LO} = 0.34$). The LO voltage was set such that the junction drive level would be equal to $\alpha = 1$ in the middle of the photon step.

single SIS junction. All of these factors potentially break the assumptions made by Tucker theory and SuperMix. Based on HFSS and SuperMix simulations, the IF range of this device should extend from DC to 17 GHz; however, when the device was measured experimentally in Sec. 3.8, the usable IF range was limited to <10 GHz with a large resonance-like structure centred at 12.7 GHz. The cause of the resonance was later on identified as the bias tee. The MTSDA technique may be able to provide more accurate simulations of the IF response and simulate the broken photon steps that were seen between 235 GHz and 250 GHz (recall Sec. 3.7.1).

With these goals in mind, a 4-tone model was created to simulate dual sideband mixing (Fig. 4.9). This model consists of three input signals: the local-oscillator (LO), the upper sideband (USB) and the lower sideband (LSB); and one output: the intermediate frequency (IF) signal. In Fig. 4.9, each tone is represented by a Thévenin equivalent circuit with voltage V_T, impedance Z_T, and photon voltage V_{ph}. (The IF circuit's voltage is not included because it is a passive port.)

To calculate V_T and Z_T for the RF inputs, simulated results from HFSS were cascaded with the source voltage V_S and impedance Z_S, as shown in Fig. 4.10. The Thévenin impedances were calculated by:

$$Z_T = Z_0 \left(\frac{1 + S_{J,J}^{RF}}{1 - S_{J,J}^{RF}} \right) \tag{4.22}$$

where Z_0 is the characteristic impedance, and $S_{J,J}^{RF}$ the reflection coefficient of the junction port. Next, the Thévenin voltages were calculated by incorporating the loss

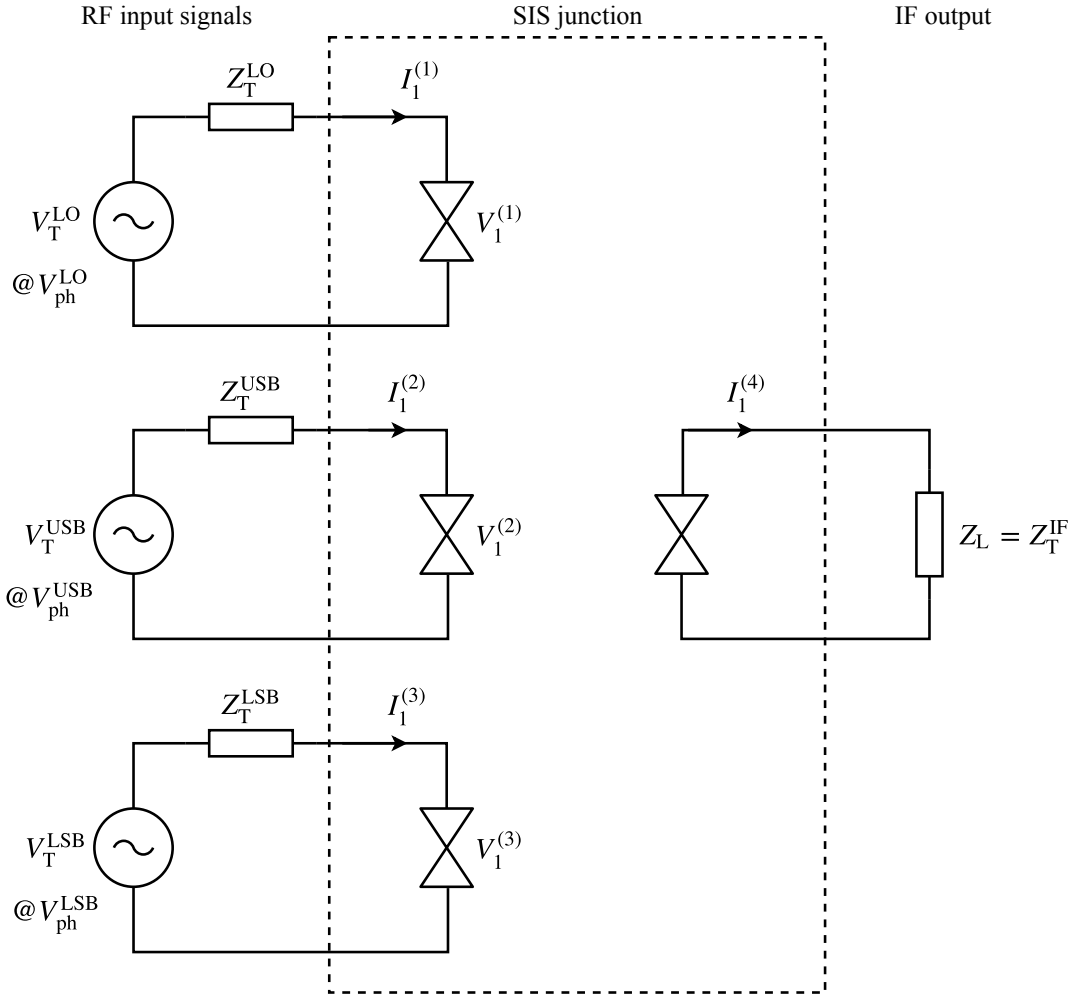

Figure 4.9: 4-port model for a dual sideband (DSB) simulation of the 230 GHz SIS device. Each port is represented by a Thévenin equivalent circuit with voltage V_{emb} and impedance Z_{emb}. The ports on the left are the input ports: the local-oscillator (LO), upper sideband (USB), and lower sideband (LSB). The port on the right is the intermediate frequency (IF) output. The AC voltages and currents induced in the junction are labelled by $V_1^{(f)}$ and $I_1^{(f)}$, respectively, where the superscript identifies the tone.

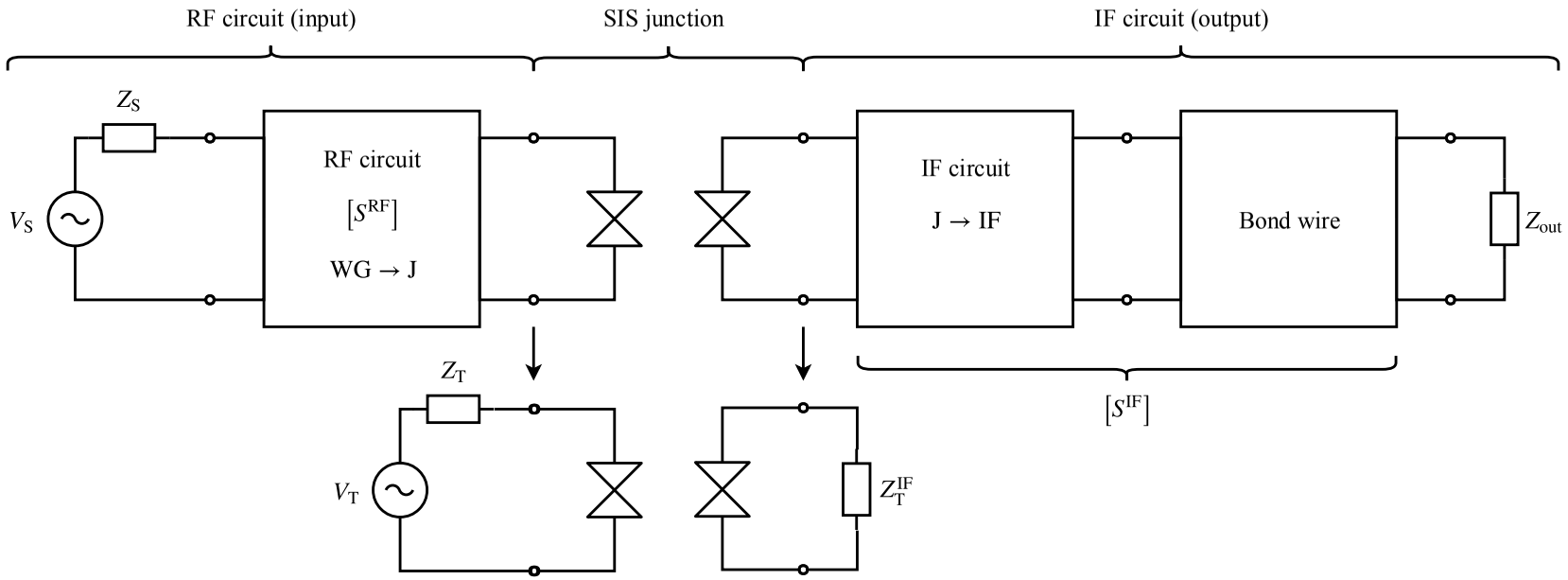

Figure 4.10: Generating the Thévenin circuits from the simulated S-parameters. Both the RF and IF circuit S-parameters were simulated using HFSS (previously shown in Fig. 3.6 and Fig. 3.9, respectively). The bond wire S-parameters were generated using the analytical expression contained within App. C. The RF circuit was reduced to a Thévenin circuit, while the IF circuit was reduced to a simple load impedance since it is entirely passive.

of the RF circuit and change in port impedance:

$$|V_{\mathrm{T}}| = |V_{\mathrm{S}}| \cdot |S^{\mathrm{RF}}_{\mathrm{J,WG}}| \sqrt{\frac{\mathrm{Re}\left\{Z_{\mathrm{T}}\right\}}{\mathrm{Re}\left\{Z_{\mathrm{S}}\right\}}} \tag{4.23}$$

where $|S_{\mathrm{J,WG}}|$ is the transmission coefficient between the RF waveguide and the SIS junction. The available power from the Thévenin circuits is then:

$$\begin{aligned} P_{\mathrm{T}} &= \frac{|V_{\mathrm{T}}|^2}{8 \cdot \mathrm{Re}\left\{Z_{\mathrm{T}}\right\}} \\ &= P_{\mathrm{S}} \cdot |S_{\mathrm{J,WG}}|^2 \end{aligned} \tag{4.24}$$

where P_{S} is the power available from the source circuit.

Since the IF circuit is entirely passive, the Thévenin voltage is ignored. The Thévenin impedance is then calculated by:

$$Z^{\mathrm{IF}}_{\mathrm{T}} = Z_0 \left(\frac{1 + S^{\mathrm{IF}}_{\mathrm{J,J}}}{1 - S^{\mathrm{IF}}_{\mathrm{J,J}}} \right) , \tag{4.25}$$

where $S^{\mathrm{IF}}_{\mathrm{J,J}}$ is again the reflection coefficient at the junction port, except now the S-parameters refer to the IF circuit's simulated results S^{IF}; not the RF circuit's results S^{RF}. (The simulated RF and IF S-parameters were previously presented in Fig. 3.6 and Fig. 3.9, respectively.)

Initial mixer simulations

Before calculating the IF bandwidth, a simple simulation was setup to mimic the measurement of a black body load. The LO frequency was set to the centre frequency of the device ν_{LO}=230 GHz and the IF frequency was set to 5 GHz since most of the experimental measurements were completed with a 4–6 GHz bandpass filter. Then, the LO's source voltage was set such that the junction drive level would be equal to $\alpha = 1$ in the middle of the first photon step (i.e., at $V_0 = V_{\mathrm{gap}} - V_{\mathrm{ph}}/2$), which normally corresponds to the maximum IF output power. The sideband voltages, $V^{\mathrm{USB}}_{\mathrm{T}}$ and $V^{\mathrm{LSB}}_{\mathrm{T}}$, were set to each provide -100 dBm of power in order to simulate a very weak signal. All of the input parameters are listed in Table 4.1.

In Fig 4.11a, the simulated I–V curve shows clear photon steps that are equal in width to the photon voltage of the LO, $\widetilde{V}^{\mathrm{LO}}_{\mathrm{ph}} = 0.3484$. The power delivered to the load was calculated by:

$$P_{\mathrm{L}} = \frac{1}{2} \, |I^{(4)}_1|^2 \cdot \mathrm{Re}\left\{ Z^{\mathrm{IF}}_{\mathrm{T}} \right\} . \tag{4.26}$$

Table 4.1: Input parameters for a 4-tone simulation of the 230 GHz SIS device.

Tone #	Name	Freq. (GHz)	V_S (mV)	Z_S (Ω)	P_S (dBm)	$\widetilde{V}_T$	$\widetilde{Z}_T$	P_T (dBm)	$N_B^\dagger$
1	LO	230	11.61	288.5	-42.33	0.5334	$0.39-j0.28$	-43.2	15
2	USB	235	0.0155	285.2	-99.77	0.0008	$0.48-j0.44$	-100.0	15
3	LSB	225	0.0171	292.0	-99.01	0.0007	$0.40-j0.44$	-100.0	15
4	IF	5	–	–	–	0.0000	$0.60-j1.29$	–	15

Note: The Thévenin circuit parameters are normalised (denoted by the tilde). The voltages are normalised to V_{gap}=2.73 mV and the impedances are normalised to R_n=13.4 Ω.

† N_B represents the truncation limits of n in Eqn. 4.4. This effectively sets the number of Bessel functions that are included.

where $I_1^{(4)}$ is the current that passes through the IF load (see Fig. 4.9). This was then used to calculate the conversion gain[7],

$$G_c = \frac{P_L}{P_S^{USB} + P_S^{LSB}}, \tag{4.27}$$

which is plotted in Fig. 4.11b. The first photon step has the highest conversion gain with a peak slightly above 0.5 or -3 dB. This matches expectations since capacitive embedding impedances typically result in conversion efficiencies below 0 dB. Qualitatively, the gain curve also appears to be very similar to the experimental gain plots from Chp. 3 (e.g., Fig. 3.17b).

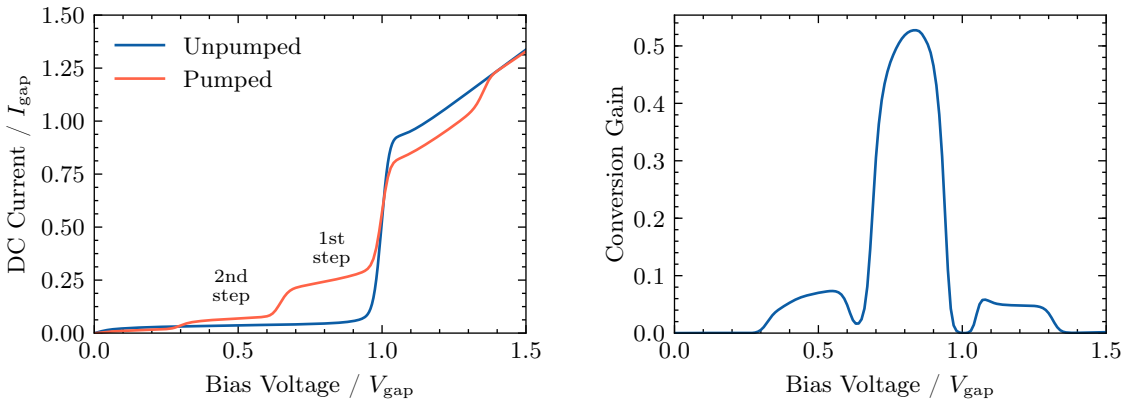

(a) DC tunnelling currents

(b) Conversion gain

Figure 4.11: A 4-tone simulation of the 230 GHz SIS device from Chp. 3. The input parameters are listed in Table 4.1. The embedding impedances were simulated using HFSS (Sec. 3.3).

[7]This is the same definition for conversion gain that was used previously for experimental data in Eqn. 2.54. It includes the RF gain as well as the RF-to-IF conversion loss, i.e., $G_c = G_{RF} \cdot G_{SIS}$.

When SIS devices are tested experimentally, the LO power is typically set to maximise the IF output power of the first photon step. Depending on the device, this power may be lowered slightly to reduce the shot noise resulting from the LO signal. To optimise the LO power for the IFBW simulation, the Thévenin voltage of the LO signal was swept from $\widetilde{V}_{\mathrm{T}}^{\mathrm{LO}} = 0.1$ to 1.0 (Fig. 4.12). In Fig. 4.12b, the simulated IF output power climbs with $\widetilde{V}_{\mathrm{T}}^{\mathrm{LO}}$ until it saturates around $\widetilde{V}_{\mathrm{T}}^{\mathrm{LO}} \sim 0.5$. This corresponds to a junction drive level of $\alpha \sim 1$, as expected. The IF gain response in Fig. 4.12b is also very similar to experimental results: the output power climbs steadily to the saturation point, then the peak becomes very sharp as it begins to descend.

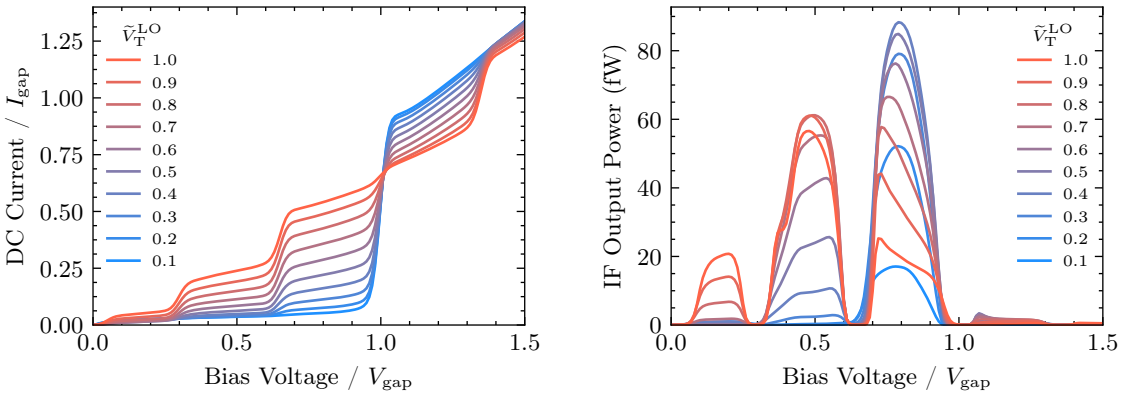

(a) DC tunnelling currents

(b) IF output power

Figure 4.12: Simulated LO power saturation in the 230 GHz SIS device.

Simulated IF response

With the LO power optimised, the IF response was simulated by sweeping the IF frequency from 1 to 20 GHz. The simulated conversion gain is shown in Fig. 4.13a. To estimate the resulting IF noise contribution, the noise temperature from the LNA (specifically, the LNF LNA in Table 3.3) was divided by the simulated conversion gain. The results, shown in Fig. 4.13b, are very close to the experimental IF noise contributions from 4–9 GHz (calculated previously in Sec. 3.8). Above 9 GHz, however, the experimental IF noise contribution is much higher. As discussed in Chp. 3, this is likely due to the bias tee. The simulated results in Fig. 4.13b suggest that if the issue with the bias tee can be resolved, the IF noise contribution should be below 100 K up to 18 GHz.

Another possible IF bandwidth limitation comes from gain compression[8]. If the

[8]Gain compression represents how much the gain drops as the sideband power increases. It is defined as the conversion gain at $P_{\mathrm{in}} = P_{\mathrm{T}}^{\mathrm{SB}}$ divided by the conversion gain at $P_{\mathrm{in}} \to 0$.

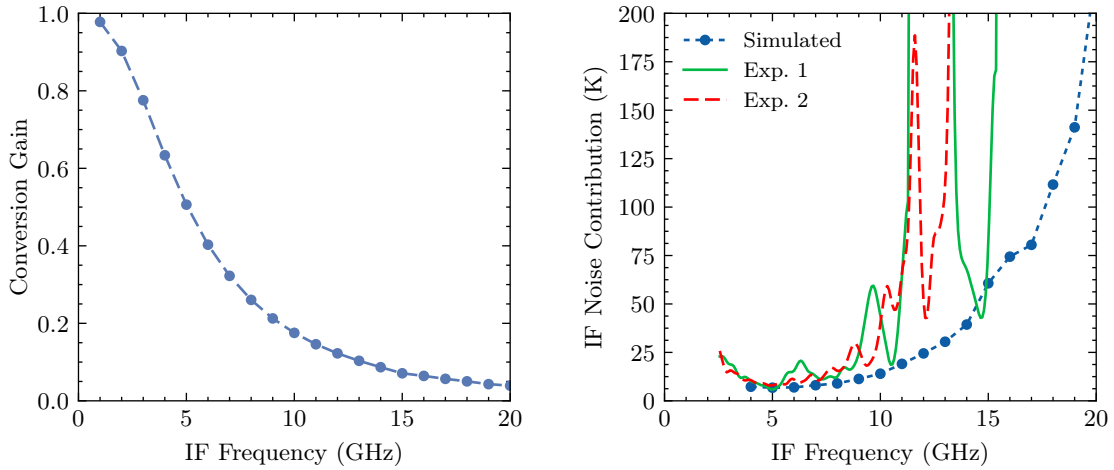

(a) Simulated conversion gain.

(b) Comparing simulated and experimental IF noise contributions. "Exp. 1" and "Exp. 2" were measured with two different bias tees.

Figure 4.13: Simulated IF response of the 230 GHz SIS device.

saturation point of the SIS junction decreases with increasing IF frequency, this could mean that the upper IF frequencies are saturated, resulting in higher noise temperatures from the Y-factor technique. The measured noise temperatures would then have to be corrected using:

$$T_{\mathrm{N}} = \frac{T_{\mathrm{H}} - G_{\mathrm{corr}}\, Y\, T_{\mathrm{C}}}{G_{\mathrm{corr}}\, Y - 1} \tag{4.28}$$

where $G_{\mathrm{corr}} = G_{\mathrm{C}}/G_{\mathrm{H}}$ is the gain correction factor, and G_{C} and G_{H} are the conversion gains for the cold and hot loads, respectively.

To test this idea, the sideband power was swept from -130 to -45 dBm at several different IF frequencies. The gain compression as a function of sideband power is plotted in Fig. 4.14. The point where the gain compression drops to -1 dB is the 1-dB compression point, P1dB, which is traditionally used to mark the end of the linear gain region. The results in Fig. 4.14 suggest that gain compression is not likely the cause of the poor noise temperature results above 10 GHz since the gain compression decreases as the IF frequency increases. This could be verified experimentally by measuring the IF response of the second step since it is able to withstand significantly higher sideband powers and it even experiences gain expansion above $\nu_{\mathrm{IF}} = 7$ GHz. (Note that biasing the SIS junction on the second step could also potentially offer an alternative for measuring strong signals above the compression point of the first step.)

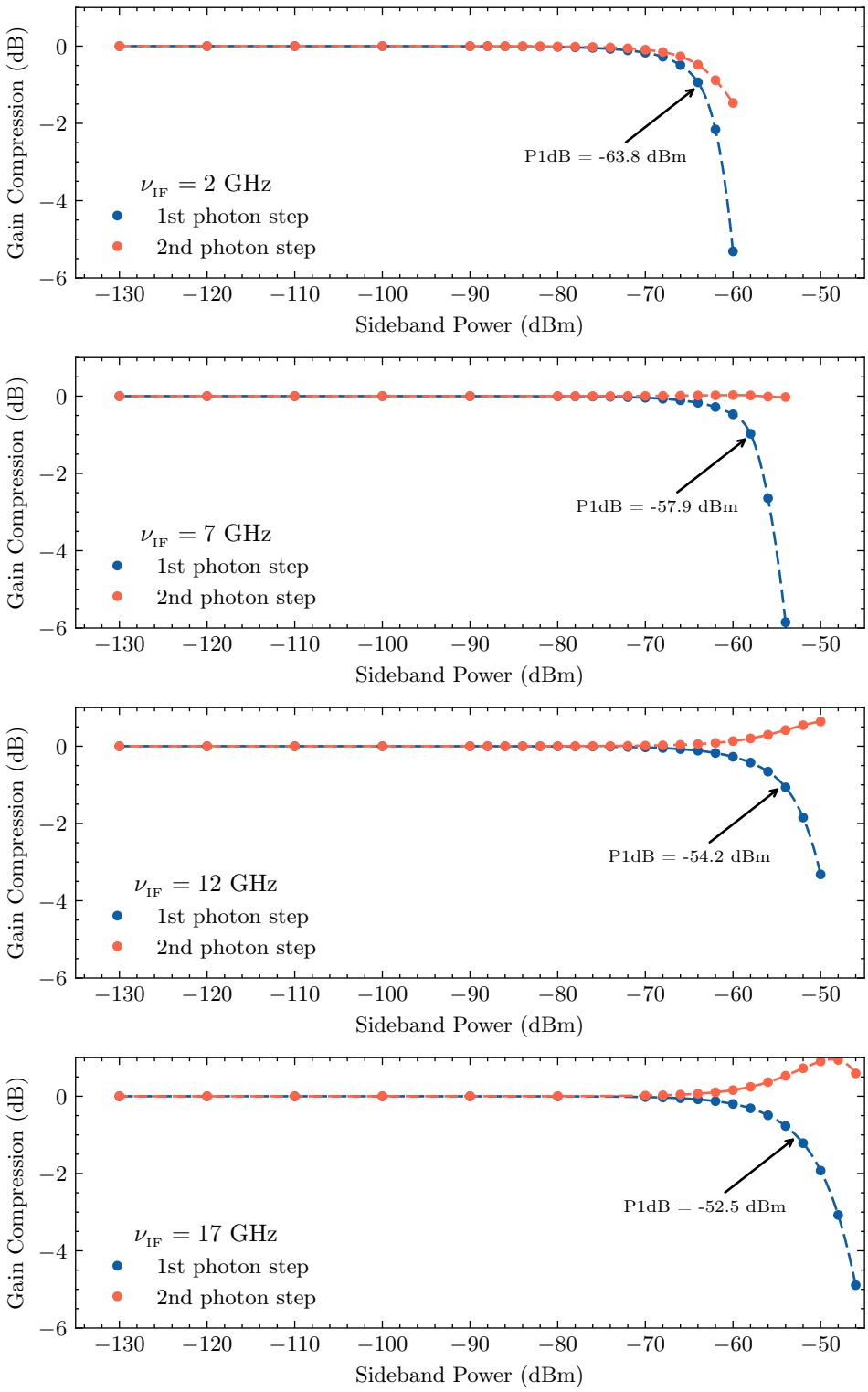

Figure 4.14: Simulated sideband power saturation in the 230 GHz SIS device. The LO voltage was set to optimise the IF power, and the embedding impedances were simulated using HFSS.

Simulating broken photon steps

In addition to simulating the IF response, QMix was also developed to investigate interesting experimental phenomena, such as the broken photon steps[9] that were seen in Sec. 3.7.1. For the analysis shown here, the experimental results from device #5.6 were used as the benchmark since they were the best results from any device tested in Chp. 3. For the first simulation, the Thévenin circuit parameters were again generated from simulated HFSS results (according to Fig. 4.10). The simulated conversion gain is compared to the experimental results in Fig. 4.15. When the broken photon step is not present, the shape of the simulated gain curve is very close to the experimental results, and the peak simulated gain is slightly higher than the peak experimental gain (i.e., $G_{\rm sim}$>$G_{\rm exp}$). The first photon step has by far the highest conversion gain, and nulls are seen at $V_0 = V_{\rm gap} - V_{\rm ph}$ and $V_0 = V_{\rm gap}$. However, the broken photon steps between 245 GHz and 250 GHz were not recreated at any frequency.

Since these simulations are very sensitive to the Thévenin impedance, I then simulated the conversion gain using the embedding impedances recovered from experimental data (Fig. 4.16). These impedances are compared to the values from HFSS in Fig. 4.17, and although they are very close, the real component of the recovered embedding impedances are consistently ∼40% lower than the HFSS results. Using the new impedance values, the simulated gain is compared to the experimental results in Fig. 4.16. These simulated gains are again very close to the experimental results, but the broken photon steps were still not recreated at any frequency, suggesting that this effect was not due to the fundamental tone of the local-oscillator.

A. Ermakov, *et al.* [86] suggest that the broken photon step effect is caused by powerful sub-harmonics from the LO. To test this theory, a sub-harmonic at $\nu_{\rm LO}/2$ was added to the simulation. Since the embedding impedance of the sub-harmonic was not known, a range of Thévenin voltages and impedances were tested, and inductive embedding impedances were found to have the most noticeable effects on the gain curves. One of the split photon steps is simulated in Fig. 4.18. In this case, the embedding circuit of the sub-harmonic was estimated by fitting the gain curve by hand. This sub-harmonic is able to recreate the experimental results very well, supporting the theory that sub-harmonics cause broken photon steps.

[9]Recall that at certain frequencies there were notches in the experimental I–V curves that always occurred exactly in the middle of the first photon step. This effect also manifested as large clefts in the IF output power (e.g., Fig. 3.18).

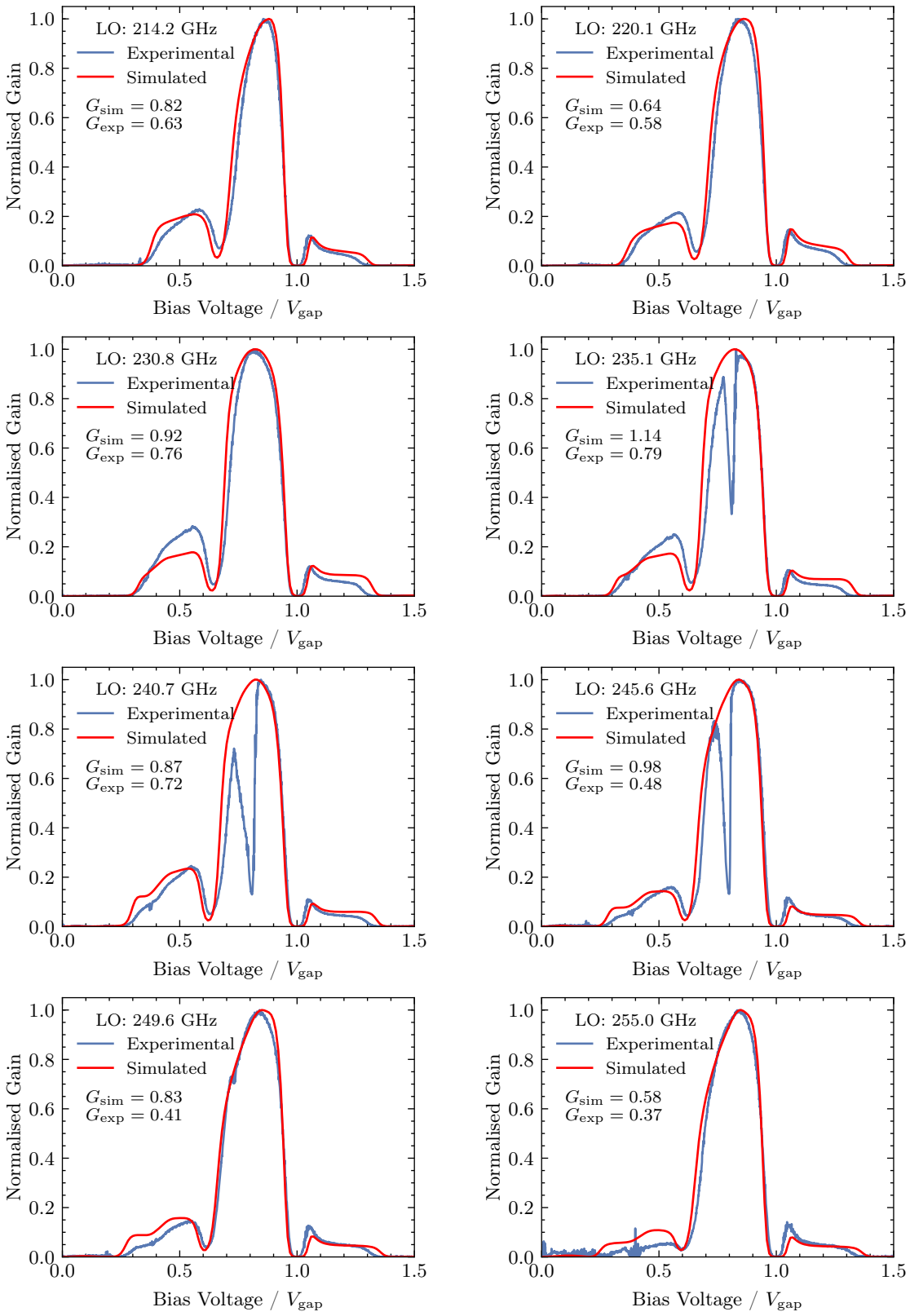

Figure 4.15: Simulated DSB conversion gain compared to experimental data from device #5.6. For this simulation, the Thévenin impedances were generated from HFSS results (according to Fig. 4.10). The gains are normalised to the values listed in the legends. Notice that in all cases $G_{sim} > G_{exp}$ and the dip in gain has not been successfully recovered.

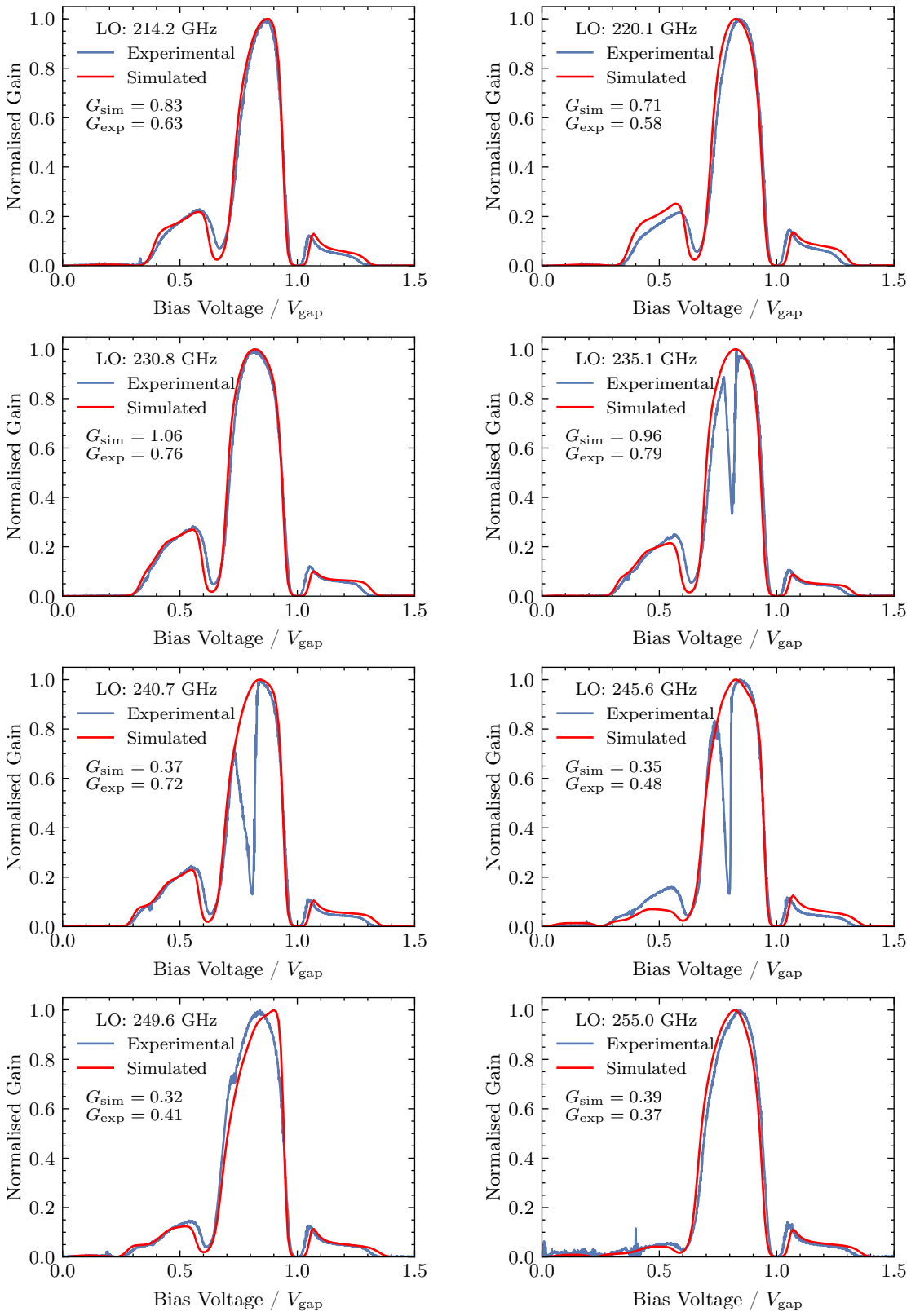

Figure 4.16: Simulated DSB conversion gain compared to experimental data from device #5.6. For this simulation, the Thévenin impedances were generated from the embedding impedances recovered from experimental data. Again, the dip in gain has not been successfully recovered.

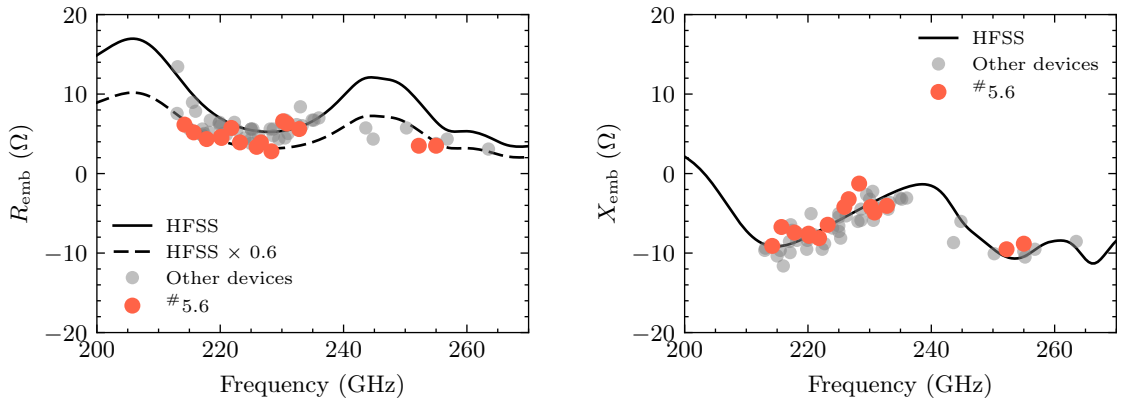

Figure 4.17: Embedding impedances recovered from device #5.6. The grey circles represent values from all of the other devices previously presented in Chp. 3.

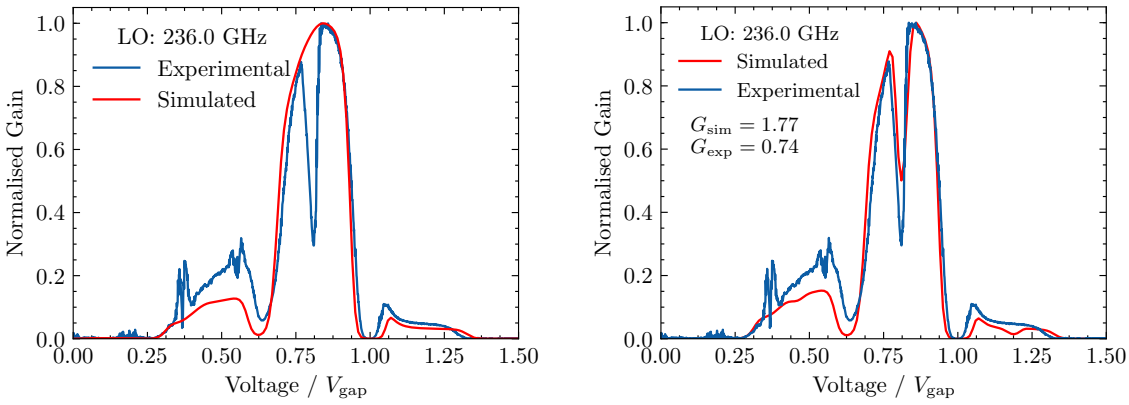

(a) Simulating only the fundamental tone of the LO.

(b) Including a sub-harmonic (SH) at $\nu_{\mathrm{LO}}/2$. ($\widetilde{V}_{\mathrm{T}}^{\mathrm{SH}} = 0.07$ and $\widetilde{Z}_{\mathrm{T}}^{\mathrm{SH}} = 0.4 + j\,0.35$.)

Figure 4.18: Recreating the broken photon step at ν_{LO}=230.6 GHz by adding a sub-harmonic at $\nu_{\mathrm{LO}}/2$.

In the experimental data from the 230 GHz receiver (Chp. 3), all of the split photon steps occurred between $\nu_{\text{LO}} = 235$ GHz and $\nu_{\text{LO}} = 250$ GHz. Therefore, the sub-harmonics would have to occur between 117.5 GHz and 125 GHz. At these frequencies, all of the sub-harmonics are below the waveguide cutoff of the input waveguide ($\nu_{\text{cutoff}} = 136.3$ GHz for TE_{10} in WR4.3) meaning that the sub-harmonics should be evanescent and should attenuate exponentially with distance. However, since they are relatively close to the cutoff frequency, these evanescent waves have long decay lengths equal to $1/\alpha$ where $\alpha = \text{Im}\{\beta\}$ and β is the phase constant. This allows them to reach far down the RF waveguide despite being below the cutoff frequency. A. Ermakov, *et al.* [86] found similar results. They reported broken photon steps in the ALMA band-5 receiver at frequencies above 180 GHz. This corresponds to sub-harmonics at +90 GHz. They do not list the waveguide size that they use, but it is likely WR5.1, which has a cutoff frequency of 116 GHz. Therefore, their broken photon steps are also caused by evanescent sub-harmonics just below the cutoff frequency, suggesting that this phenomena is related to the evanescent behaviour of the sub-harmonics.

4.7 Conclusion

Multi-tone spectral domain analysis (MTSDA) is a powerful simulation technique for calculating quasiparticle tunnelling currents in SIS junctions. Unlike other simulation techniques, MTSDA can include multiple strong signals and an arbitrary number of higher-order harmonics for each tone. A software package named QMix was created to implement MTSDA and a harmonic balance procedure. QMix can also utilise experimental DC I–V curves to generate the response function and import embedding impedances directly from simulated results, allowing QMix to perform highly accurate simulations of SIS device behaviour. Initially, a simple one-tone simulation was created to test and validate the software package. Different frequencies, drive levels and embedding circuits were all tested to validate the software and to learn how these parameters influence the AC and DC properties of the junction. Then, the 230 GHz SIS device from Chp. 3 was simulated using a 4-tone dual sideband simulation. This simulation was setup to recreate a black body load measurement. The simulated IF response was close to the experimental results below ~11 GHz, but the experimental results contain a large resonance due to the bias tee. The simulated results suggest that the IF noise contribution can be below 100 K up to 18 GHz if the resonance from the bias tee is removed. The results from QMix were then compared to experimental gain curves (as a function of bias voltage) with very good agreement. By adding

a subharmonic at half the LO frequency, the broken photon steps were recreated, supporting a previous theory. Overall, QMix presents a new tool to analyse the performance of SIS devices, and given it's success, it can be used to design new devices in the future.

Chapter 5

A 1×4 Focal Plane Array

5.1 Introduction

Millimetre-wave heterodyne receivers are commonly used to observe spectral lines in both galactic and extra-galactic star forming regions. We would like to map these regions to understand their physical and chemical properties; however, from our perspective, some of these regions are distributed over large solid angles. For example, the nearby Whirlpool Galaxy[1] is 11.2×6.9 arcmin (Fig. 5.1), the Orion Nebula is approximately $1^\circ \times 1^\circ$, and the Large Magellanic Cloud[1] is $10.75^\circ \times 9.17^\circ$. Large surveys are slow using single dish antennas and even more difficult with interferometers due to their inherently narrow beam widths. Unfortunately, it is not possible to significantly increase the mapping speed of the heterodyne receivers around 230 GHz because the current state-of-the-art SIS mixers are already close the quantum limit of sensitivity. This means that any further improvements to sensitivity (and therefore mapping speed) will be modest using single pixel receivers.

An alternative technique to improve the mapping speed is to increase the number of receivers (i.e., pixels) in the focal plane. The mapping speed of such an array is proportional to

$$\frac{N_{\text{pixels}}}{(T_{\text{sys}})^2} \tag{5.1}$$

where N_{pixels} is the number of pixels in the array, and T_{sys} is the system noise temperature. Based on the above equation, if the number of pixels is increased by a factor of 4, the observating time will also drop by a factor of 4. If however the noise temperature of each receiver is twice as high, the effective sensitivity will be the same as the

[1] From the NASA/IPAC Extragalactic Database.

(a) An optical image of M51 taken by the *Hubble Space Telescope*. (Credit in footnote[2]).

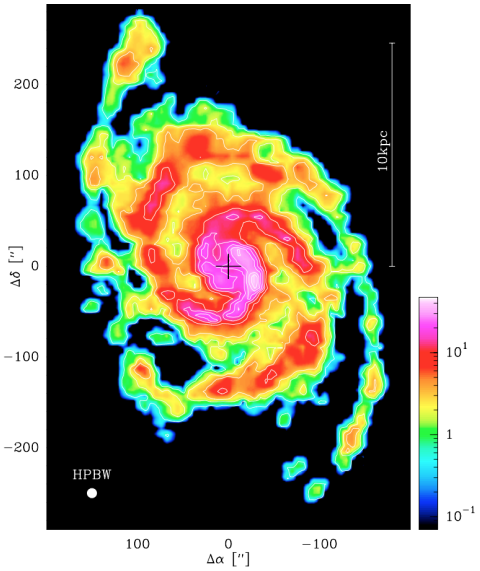

(b) A CO(J=2→1) map taken by the HERA focal plane array on the IRAM 30 m telescope. The half power beam width (HPBW) is shown in the bottom left corner. (Credit: K. Schuster, *et al.* [104].)

Figure 5.1: Images of the nearby spiral galaxy M51, also known as the Whirlpool Galaxy. It is interacting with a dwarf galaxy (NGC 5195), seen in the top left in both figures above. The CO emission in (b) traces the cold molecular gas that fuels star formation. By comparing these two figures, we can see that the molecular gas is mostly contained in the central bulge and the spiral arms of the galaxy.

original receiver. Therefore, the challenge is to add more pixels without significantly increasing the noise temperature.

Perhaps the most obvious challenge in creating a focal plane array is the complexity: more pixels require more feed horns, low noise amplifiers (LNAs), magnetic coils, bias wires, etc. All of these components are required to fit into a compact space, and for older telescopes, this often means fitting into a space that was only ever intended for a single pixel receiver. Out of these, the bulkiest components in the focal plane are the magnetic coils that are required to suppress Cooper pair tunnelling in SIS junctions. One solution is to replace the coils with permanent magnets, which is done in the proposed KAPPa design [105]. Alternatively, if the frequency is low enough and SIS junction size is large enough, it is also possible to remove the magnetic coils since the junctions' capacitance should short-circuit the high-frequency oscillations (e.g., HERA [106]). A side-effect of the complexity is also the added thermal load due to the extra wiring, coaxial cables, LNAs, windows, etc. It can be difficult to properly

[2]Credit: NASA, ESA, S. Beckwith (STScI), and The Hubble Heritage Team (STScI/AURA).

cool focal plane arrays, especially if any active components are in close proximity to the SIS devices.

Another major challenge comes from efficiently pumping all of the SIS devices. The LO signal is required to be divided uniformly between the pixels (i.e., multiplexed) and then injected into each device (i.e., diplexed) without interfering with the astronomical signals. SIS mixers are relatively insensitive to LO power compared to hot electron bolometers (HEBs), but it is important to keep Eqn. 5.1 in mind in order to balance the pros and cons of adding more pixels. The different LO injection techniques are listed in Table 5.1 for all of the focal plane arrays that use SIS mixers. Out of these arrays, six are within the range of 200–400 GHz: NRAO 8-Beam, HERA, DesertStar, HARP, SuperCam, LAsMA and SHERA. Since these designs are the most similar to the array presented in this chapter, they are discussed in more detail below (except for LAsMA because there has not yet been very much information published about this array):

NRAO 8-beam was the first heterodyne receiver array every built. Originally commissioned using Shottky mixers in 1988 [107], it was later upgraded to SIS mixers in 1996 [108]. The array was split into two 1×4 pixel sub-arrays, with each sub-array in a separate cryostat, to form a 2×4 beam pattern on the sky. Inside each sub-array, the LO power was divided between the pixels using cascaded wire grids, and then combined with the RF signals using Martin-Puplett interferometers[3] (MPIs). The MPIs were originally required for the Shottky mixers since they require strong LO signals, but MPIs are bulky and susceptible to beam walk off as the tuning frequency changes and they could be difficult to implement in a large array. (For example, PoleStar also used an MPI to inject the LO signal, and they found a 3 dB loss in LO coupling when the beam was misaligned by only 0.5° [135].)

HERA (*Heterodyne Receiver Array*) is a 3×3 array installed on the IRAM 30 m telescope [106, 113, 114]. The first 3×3 array was installed in 2001 and then another array was added in 2004 to provide the second polarisation. In each 3×3 array, the LO power is divided between the three rows using a 3-way waveguide power splitter. Each row has an attenuator to balance the LO power, and then the LO power is combined with the RF signals using -15 dB waveguide

[3]Martin-Puplett interferometers use wire polarising grids and rooftop mirrors to combine RF and LO signals. They are useful when LO power is limited, which is often the case at high frequencies.

Table 5.1: Focal plane arrays using SIS receivers.

Array name	Telescope	Frequency (GHz)	N_{pixels}	Array format	Pol.	Mixing type	SSB filter[a]	LO division[b]	LO injection[c]	IFBW[d] (GHz)	Ref.
8-Beam	NRAO 12 m	∼230	8	2 × 4	1	DSB		PG	MPI	0.3	107, 108
BEARS	Nobeyama 45 m	82–116	25	5 × 5	1	DSB		WgPS	WgDC	0.5	109, 110
CHAMP	APEX & CSO	460–490	8+8	2-4-2	1/2	SSB	MPI	FG	MPI	2	111
PoleStar	AST/RO	807.5	4	2 × 2	1	DSB		QBS	MPI	1	112
HERA	IRAM 30 m	220–260	9	3 × 3	2	SSB	BT	WgPS	WgDC	1	106, 113, 114
SMART	NANTEN2	460–490/800–880	8/8	2 × 4	1	DSB		CFG	MPI	1	115–117
DesertStar	HHT	320–370	7	hex.[e]	1	DSB		CFG	BS	0.25	118, 119
HARP	JCMT	325–375	16	4 × 4	1	SSB	MZI	ML	BS	1.9	120
CHAMP$^+$	CSO & APEX	620–720/780–950	7/7	hex.[e]	1	SSB	MPI	CFG	MPI	2.8	121
SuperCam	HHT & APEX	329–360	64	8 × 8	1	DSB		WgPS	BS	0.25	122
FOREST	Nobeyama 45 m	80–116	4	2 × 2	2	2SB		WgPS	HC	4/8	123, 124
LAsMA†	APEX	270–370	7	hex.[e]	1	2SB		–	–	4	125, 126
SHERA†	IRAM 30 m	200–280	49	7 × 7	2	2SB		WgPS	WgDC	–	127, 128
CHAI[f]†	CCAT-p	455–490/800–835	64/64	8 × 8	1	–		–	–	–	129, 130
SSAR†	Delinha 13.7 m	85–115.6	9	3 × 3	1	–		WgPS	WgDC	1	131

This table builds upon reviews found in [132–134]. The entries are sorted by the date that they were commissioned.

† Currently under development.

Notes:

[a] SSB filtering: backshort tuning (BT), Martin-Puplett interferometer (MPI), Mach-Zender interferometer (MZI)

[b] LO division: collimating Fourier grating (CFG), Fourier grating (FG), 90° hybrid coupler (HC), freespace meander line (ML), polarising/wire grid (PG), crystalline quartz beam splitter (QBS), waveguide power splitter (WgPS)

[c] LO injection: Mylar beam splitter (BS), 90° hybrid coupler (HC), Martin-Puplett interferometer (MPI), waveguide directional coupler (WgDC)

[d] This is the processed IFBW, which is usually limited by the backend of the receiver (not by the SIS device).

[e] Arranged into a hexagonal pattern with one pixel in the centre and six around the outside (for a total of 7 pixels).

[f] The SMAI (SMART+CHAI) array will act as a proof of concept for CHAI. SMAI will be 4 × 4 and installed on the NANTEN2 telescope.

couplers. To isolate one of the sidebands, HERA tunes the waveguide backshorts to suppress the image sideband by ∼10 dB.

DesertStar was a 7 pixel array that was installed on the Heinrich Hertz Telescope[4] (HHT) in 2003 [118, 135]. The pixels were constructed individually in "rocket" shaped mixer blocks, and then packed into a hexagonal pattern in the focal plane. Unlike the other arrays around this frequency range, this array used a reflective Fourier grating to divide the LO signal. The Fourier grating was superimposed onto a parabolic mirror to simultaneously multiplex and collimate the LO beam, and it achieved an 80% beam efficiency. The LO beams were then injected into the RF feed horns using a Mylar beam splitter. The Fourier grating, however, limited the RF bandwidth to ∼10% since gratings are inherently frequency-dependent (i.e., the beam pattern is a function of wavelength divided by the periodic spacing).

HARP-B (*Heterodyne Array Receiver Program*) is a 4×4 focal plane array that was installed on the James Clerk Maxwell Telescope (JCMT) in 2005. Using a unique technique, the LO signal passes back and forth in front of each feed horn in a freespace meander line (Fig. 5.2, [136]). A series of Mylar beam splitters, with one in front of each horn, are then used to inject a small fraction of the LO signal into each pixel. Since the meander line is attached to the inside the cryostat window, this design requires a large cryostat and it would be difficult to implement the meander line in an array any larger than 4×4 pixels. HARP-B achieves sideband separation using a Mach-Zehnder interferometer to reject the image sideband. It is still operational today with 14 out of 16 pixels active.

SuperCam is the largest SIS array ever built [122]. The array is constructed from 1×8 linear modules that are stacked to form an 8×8 array. Each linear module contains integrated diagonal feed horns, electromagnets, and LNAs. In a separate block, the LO power is divided using cascaded waveguide power splitters, and then optically injected into the array using a Gaussian beam telescope and a 25.4 µm thick Mylar beam splitter. SuperCam was originally tested on the Submillimeter Telescope (SMT) in 2012, and more recently trialed in the Southern Hemisphere on APEX in 2014.

SHERA (*Super Heterodyne Receiver Array*) is a 7×7 array that is currently in development to replace HERA on the IRAM 30 m telescope [127, 128]. Similar

[4]Now known as the Submillimeter Telescope (SMT).

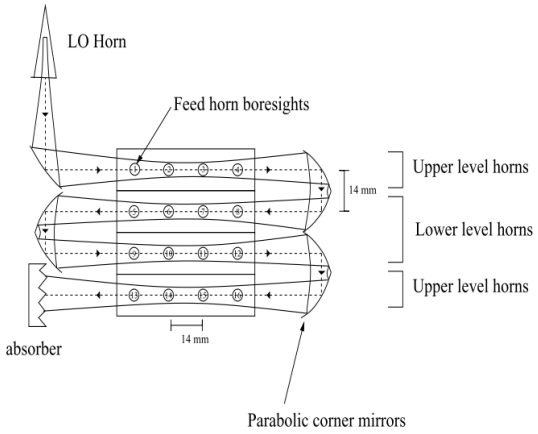

(a) Diagram of the meander line. Parabolic mirrors refocus the LO beam after each row.

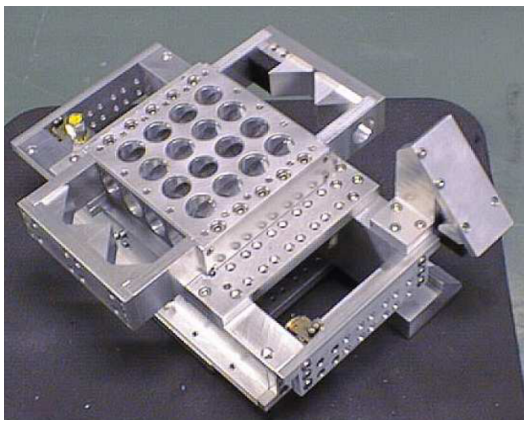

(b) Photograph of the finished unit. This fits onto the inside of the cryostat window.

Figure 5.2: The meander line used by HARP to deliver the LO signal to each SIS device. (Credit: Leech [136]).

to HERA, there will be two sub-arrays with one for each polarisation, and similar to SuperCam, the sub-arrays will be assembled from linear strips that are stacked to form a 7×7 square grid. Each 1×7 linear strip is constructed from three split-block components: the bottom and middle split-blocks form a sideband separating waveguide circuit, and the middle and top split-blocks handle the LO distribution. The LO power is divided between the pixels using a series of branchline couplers, and then the LO power passes through the middle split-block to couple to each pixel through another branchline coupler. This design is very intricate, and it will require extremely precise machining, especially for the branchline couplers.

In this chapter, a new 1×4 focal plane array is presented for operation around 230 GHz. The array was designed to test new array technology that can be used to create larger arrays in the future. To begin, the design of the array and electromagnetic simulations of the waveguide components are described in Sec. 5.2. Practical details on fabricating the array are then given in Sec. 5.3, including several challenges that were encountered during the assembly. Finally, the performance of the demonstrator array is presented in Sec. 5.4 with suggestions on how to improve future designs in Sec. 5.5.

5.2 Design

The design of the new 1×4 array block[5] is shown in Fig. 5.3. This initial array was limited to a linear strip of 4 pixels due to the size of the test cryostat, but the architecture can be extended in the future into a larger $1 \times N$ strip and then stacked to form a $N \times N$ square array, similar to SuperCam and SHERA.

In Fig. 5.3a, the waveguide flanges for the four pixels are seen on the front of the array block and one flange is visible on the side for the LO signal. Astronomical signals will enter the pixels through feed horns mounted to the front of the array block (not shown in Fig. 5.3a). On the other hand, the LO signal can either enter through freespace coupling (i.e., through another feed horn) or the LO multipliers can be connected directly to the array block (similar to HERA). Spindles for the superconducting magnetic coils are also visible in Fig. 5.3a, with one for each pixel and soft iron pole pieces to focus the magnetic field across the SIS junctions.

The waveguides were designed for split-block fabrication[6]. In Fig. 5.3b, the top half of the array block is removed to expose the waveguide circuit. As the LO signal enters the array block from the left-hand side, it is first divided in four using cascaded E-plane power splitters. Then, the LO signal is injected into the RF waveguides using -17 dB directional couplers. The remaining LO power is absorbed by a load placed at the end of the waveguide. Fig. 5.3b only shows the first pixel, but all of the RF waveguides are identical (Fig. 5.3c). After the LO signal is injected using a cross-guide coupler, the combined RF+LO signal then couples to an SIS mixer mounted in the E-plane of the RF waveguides. (This will be the device that was presented in Chp. 3.) Since the LO and RF waveguides are created by the same split-block interface, the down-converted IF signal is routed downwards in Fig. 5.3b to avoid any cross-over. The pockets for the IF tuning circuits are visible in Fig. 5.3d including holes pre-drilled for the SMA connectors. Once installed, the IF tuning circuits will be connected to the SIS devices by bond wires that arch over the 90° corner. At the other end, they will be soldered to the pin of an SMA connector.

[5]The array block was designed by Dr. Jamie Leech [3].

[6]Split-block fabrication involves machining the waveguides in two separate halves. The split runs through the E-plane of the waveguide, which is the minor axis of the waveguide's cross-section. In this way, the surface currents should not be affected by the split. Since most waveguides have dimensions $a \times b$ where $a = 2b$, split-block fabrication results in two channels, each with dimensions $b \times b$. One channel is machined in the top half of the block, and a matching channel is machined in the bottom half.

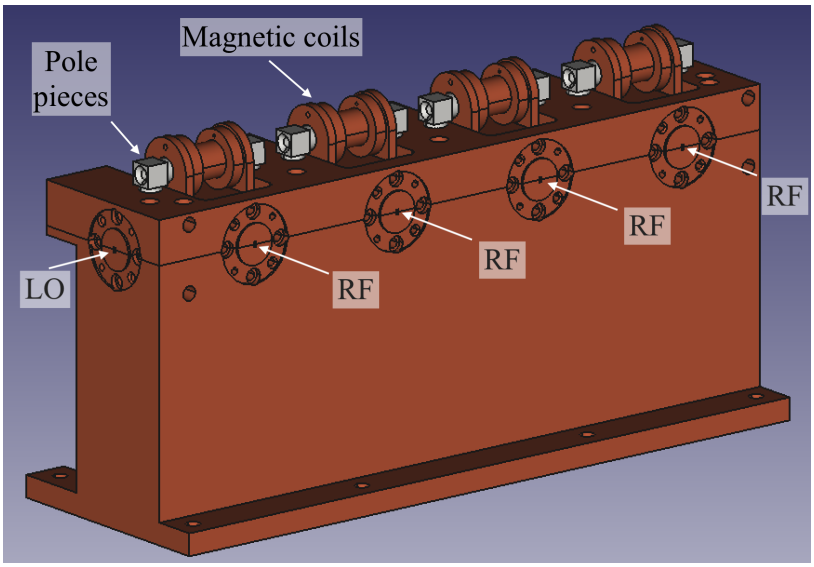

(a) The entire array block. There are four waveguide flanges on the front of the block for the RF signals and one on the side for the LO signal. There are also 4 spindles for the magnetic coils on top of the block, with soft-iron pole pieces to focus the magnetic field across the SIS junctions.

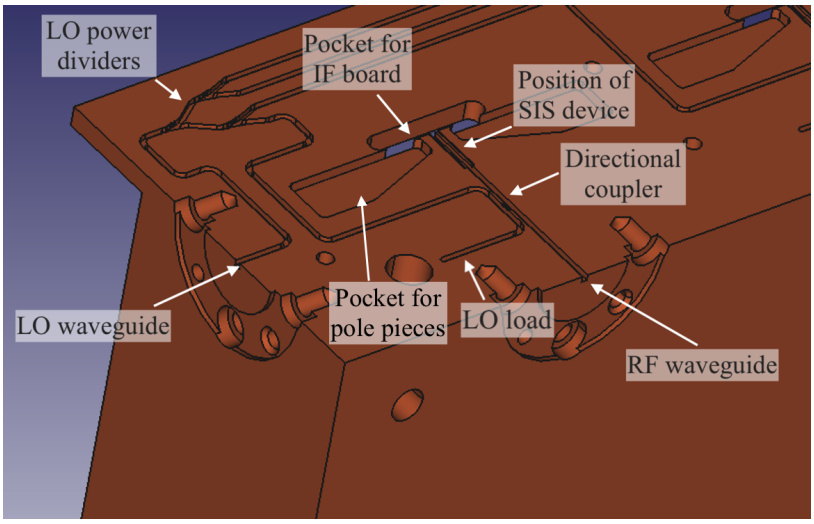

(b) Here, the top half of the array block is removed to expose the split-block waveguides. The LO power is divided using cascaded -3 dB power splitters and then injected into the RF waveguides using directional couplers. Note that the directional couplers are shown here in the wrong orientation. This error will be discussed in Sec. 5.3.1.

Figure 5.3: The design of the new 1 × 4 array block.

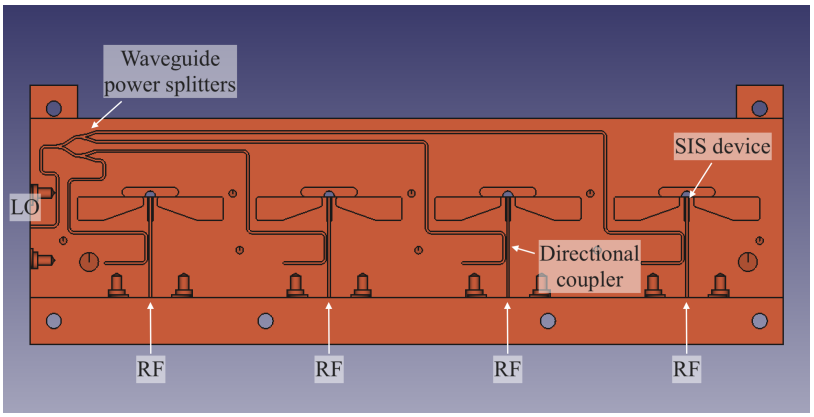

(c) The entire bottom half of the array block (with the top half removed). The four RF signals arrive from the front, while the LO signal is injected from the side of the block. Each RF waveguide is identical.

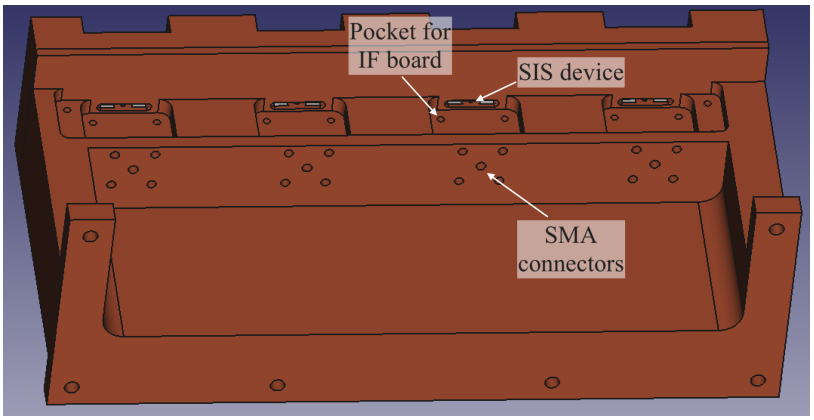

(d) Back of the array block. Since the LO and RF waveguides are in the same plane, the IF signal has to be routed downwards to avoid any cross-over. The IF tuning boards sit in small pockets (labelled) to connect the SIS devices to the SMA connectors (not shown).

Figure 5.3: The design of the new 1×4 array block *(continued)*.

The waveguide power splitters

The array block design uses cascaded -3 dB E-plane power splitters to divide the LO signal between the pixels. The 3D model for one of these power splitters is shown in Fig. 5.4a. As the LO signal enters from the left, the waveguide expands in 4 stages to match to the input impedance of the splitter. This was optimised using High Frequency Structural Simulation software (ANSYS® HFSS™, Release 15.0) to provide more than 15 dB of return loss from 200 GHz to 280 GHz (Fig. 5.4b). Note that it was designed assuming that the cutting tool will be the diameter of the waveguide's minor axis, so all of the matching stages use rounded fillets instead of sharp inside corners[7]. The point that splits the waveguides was also set to a realistic sharpness that should be feasible to machine with a high quality milling machine. The point has a chisel shape with an angle of 24° and a flat section across the tip that is 20 µm wide.

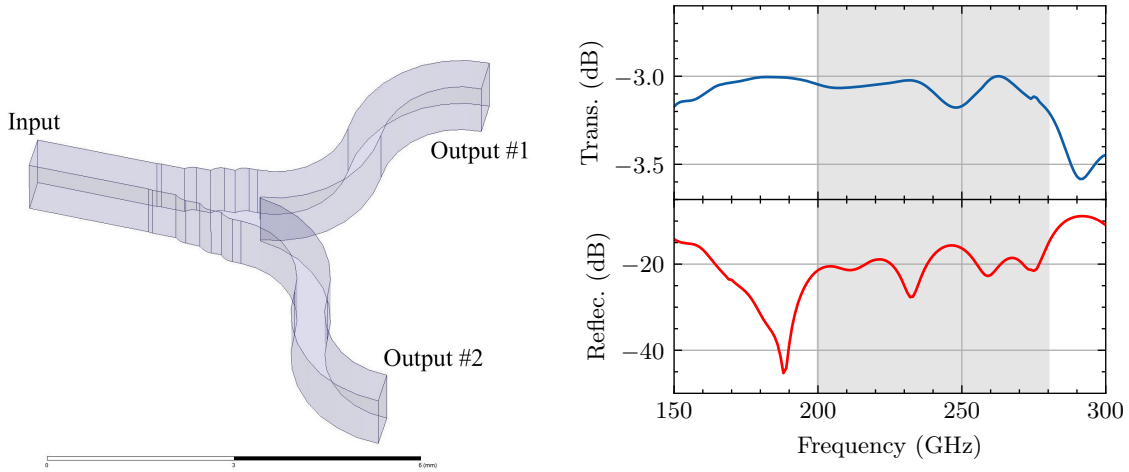

(a) 3D render of the waveguide power splitter. The input port is on the left, and the two output ports are on the right. The scale at the bottom of the figure is 6 mm long.

(b) Simulated performance from HFSS. The reflection is measured at the input port, and the transmission is measured between the input and one of the output ports. Ideally, this should be -3 dB since the power is divided in half.

Figure 5.4: Simulation of the -3 dB E-plane waveguide power splitter.

Above ∼250 GHz, the performance of the power splitter is heavily dependent on the sharpness of the point that splits the waveguides (labelled in Fig. 5.5a). In Fig 5.5, the reflection is simulated for different tip widths. Even for relatively wide

[7]The waveguides are machined using a cylindrical cutting tool. Due to its shape, it cannot cut a sharp 90° into the outside edge of the corner. Instead, a cylindrical fillet is left-over.

points around ∼150 µm, the reflection is still below -10 dB, suggesting that this design should be feasible even if the tip is more rounded than intended. (Note that waveguide power splitters generally are not used above 400 GHz. Part of the reason is that this tip cannot be machined to an acceptable tolerance. Another reason is that quasi-optical components are preferred since the waveguide losses increase rapidly with frequency.)

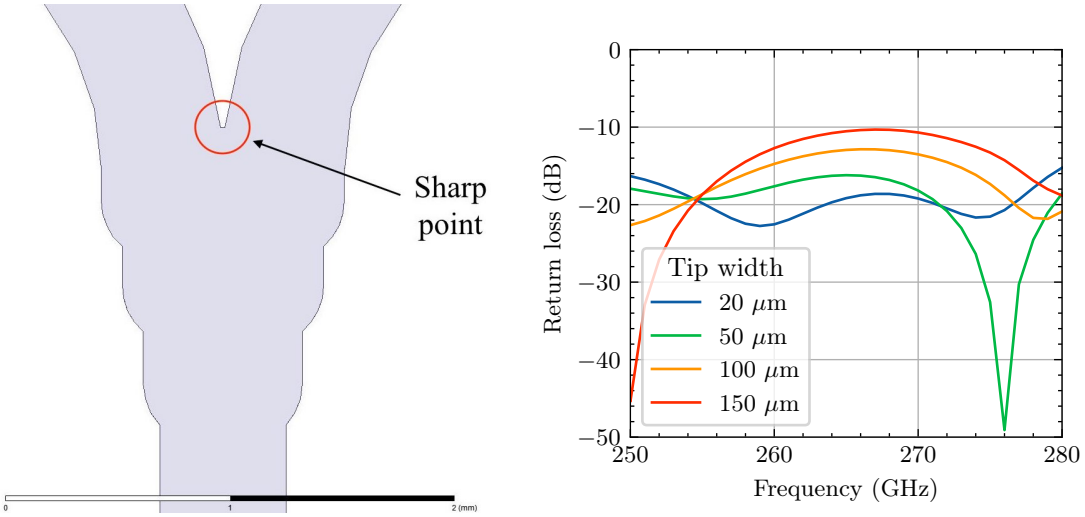

(a) A cross-section of the waveguide power splitter. The sharp point that is required for good performance at high frequencies is labelled. The scale at the bottom is 2 mm.

(b) Simulated performance from HFSS. The 'tip width' is the width of the flat section at the tip of the waveguide split.

Figure 5.5: Simulating the machining tolerance for the waveguide power splitter.

The directional couplers

The array uses directional couplers to inject the LO signal into the RF waveguides. Each of these couplers consist of 3 bow-tie probes made from two radial stubs connected by a stripline (Fig. 5.6a). The probes are a quarter-wavelength long, and they sit in cross-guide slots between the RF and LO waveguides. The radial stubs on the middle coupler are larger than the two outer couplers. This design was originally used by the GUBBINS system, outlined in [137].

Using HFSS, the radial stubs were optimised to provide approximately -17 dB of coupling at 230 GHz (Fig. 5.6b); although, past experience from the GUBBINS systems suggests that the actual coupling could be closer to -13 dB. Higher coupling will result in higher noise temperatures, but for the initial experiments, I favoured high LO coupling to ensure that the devices would be pumped to an adequate level.

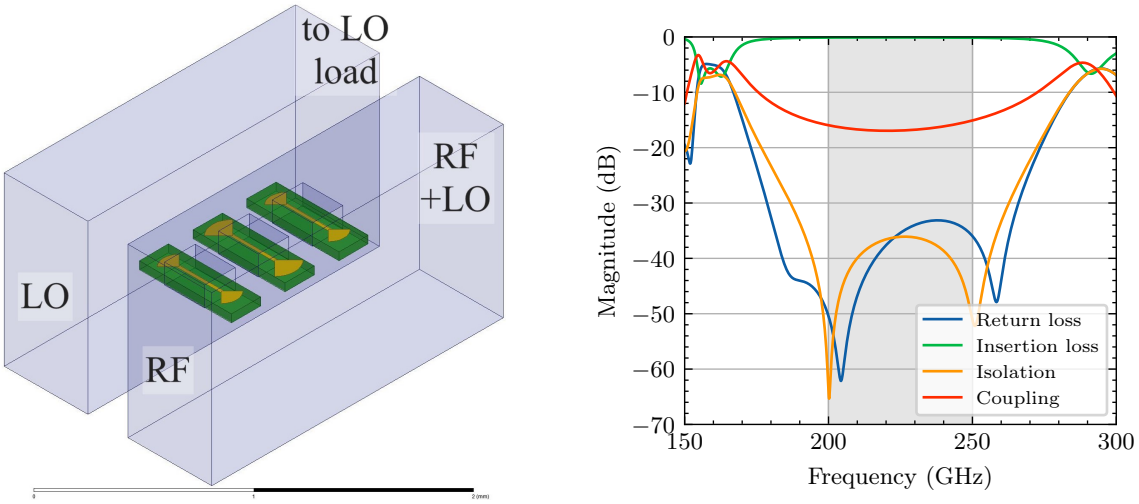

(a) 3D render of the directional coupler.

(b) Simulated performance from HFSS.

Figure 5.6: Waveguide directional coupler employing 3 bow-tie probes.

If the coupling is too high, the bow-ties can be replaced in the future with smaller radial probes. This is a major advantage over the branchline couplers used by other arrays. The dimensions of the optimised design are listed in Table 5.2.

Table 5.2: Dimensions of the bow-tie waveguide directional couplers.

Dimension	Size (µm)
Coupler spacing	350
Waveguide slot width	200
Waveguide slot height	130
Coupler chip thickness	50
Coupler chip width	190
Coupler chip length	600
Stripline width	20
Stripline length	275
Outer probe radius	100
Inner probe radius	130

Note: These are the same dimensions that were used by GUBBINS [137].

The bow-tie probes are placed manually into the cross-guide slots. In one axis, they are held by the slots, but in the other horizontal axis their position between the LO and RF waveguides is set by hand. To assess the sensitivity to this placement, the coupler was simulated with the bow-tie probes displaced by different offsets (Fig. 5.7a). According to the results shown in Fig. 5.7b, the outer bow-tie is the most sensitive.

It can only be offset by 60 µm before the coupling drops by more than 1 dB. The bow-tie positioning should be better than this in the actual array, but the bow-ties can also be offset in the vertical direction (e.g., if too much glue is used) or they can be twisted in their slots, so careful placement is still required.

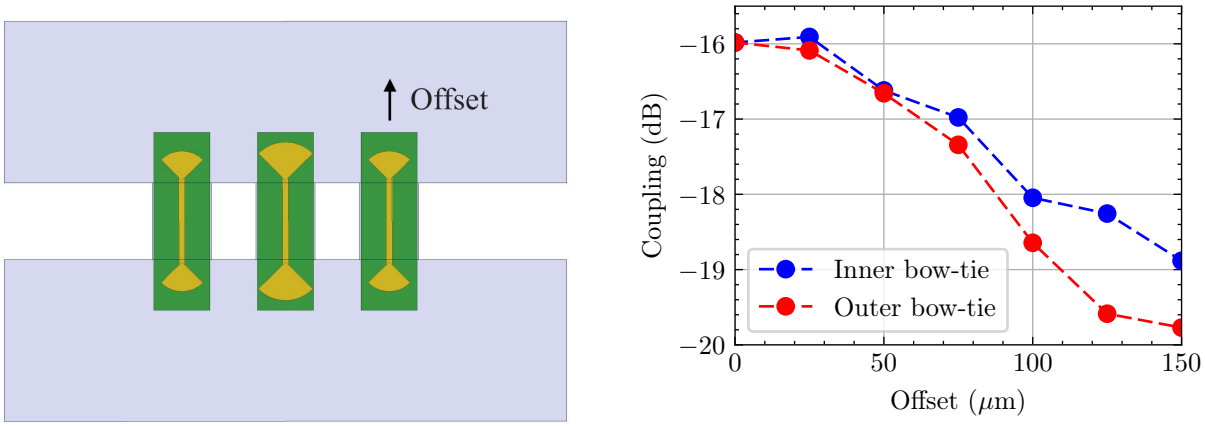

(a) Offset of the bow-tie probes.

(b) Loss in coupling due to probe offset.

Figure 5.7: Sensitivity of the bow-tie probe placement.

5.3 Fabrication and assembly

The array block was fabricated at the Rutherford Appleton Laboratory (RAL) Space Precision Design Facility by Mat Beardsley. The block was machined from high quality copper using a CNC milling machine, and the magnetic pole pieces were machined from soft iron. Photos of the finished array block are shown in Fig. 5.8. Details on assembling the array are discussed below.

The directional couplers

The bow-tie probes were fabricated by Dr. Byron Alderman and then installed by Nick Brewster at RAL. An image of one of the directional couplers is shown in Fig. 5.9. The probes sit in small cross-guide slots and they are held in place with a wax adhesive. Although they were installed by hand, it is possible to see that the neck of each bow-tie is aligned with the sidewall of the waveguide. When they are observed through a stereo microscope, it is also possible to tell that they are lying flat (i.e., they are not twisted in their slots).

The IF tuning circuits

In the original design, the IF tuning circuits were meant to be installed vertically with bond wires arcing over a 90° corner to attach to the SIS device (see Fig. 5.10a).

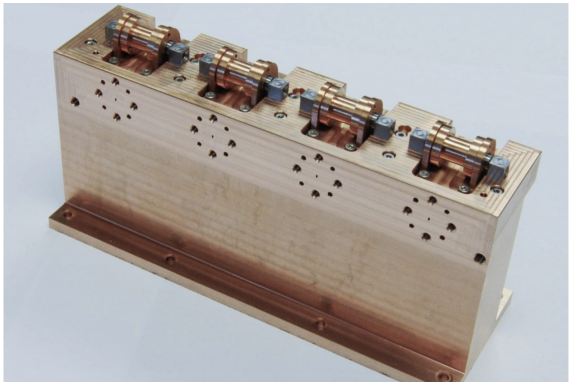

(a) Front

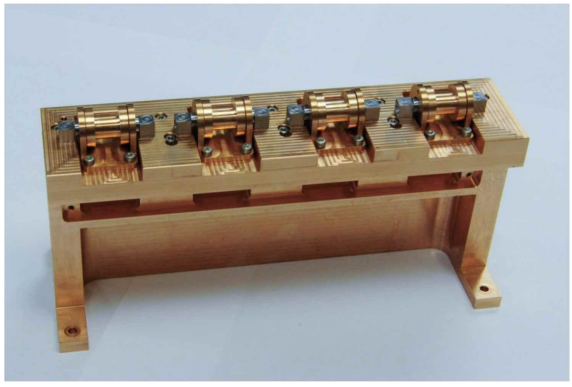

(b) Back

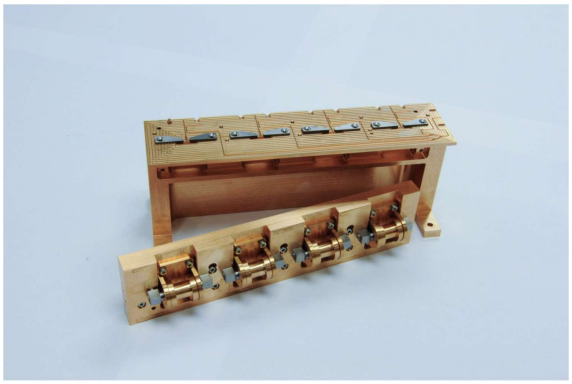

(c) With the top half removed.

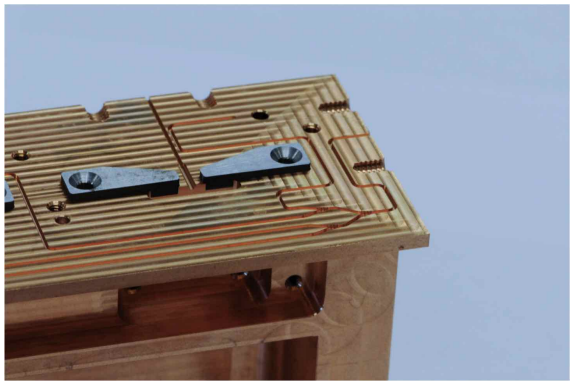

(d) Bottom half of the array block. Here, the soft iron pole pieces are shown placed in their pockets. Normally they are attached to the upper half of the block.

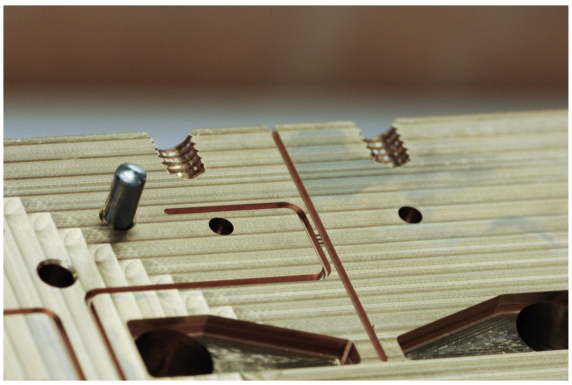

(e) A waveguide direction coupler.

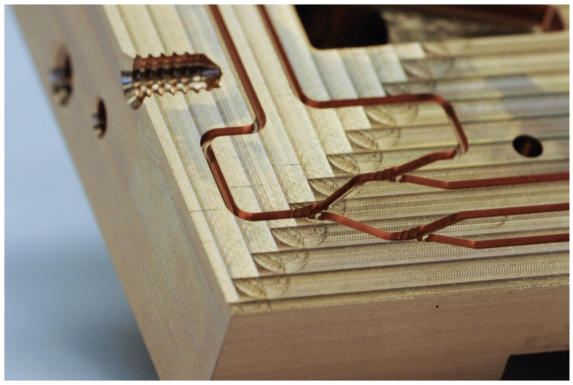

(f) Cascaded waveguide power splitters.

Figure 5.8: Photos of the finished array block.

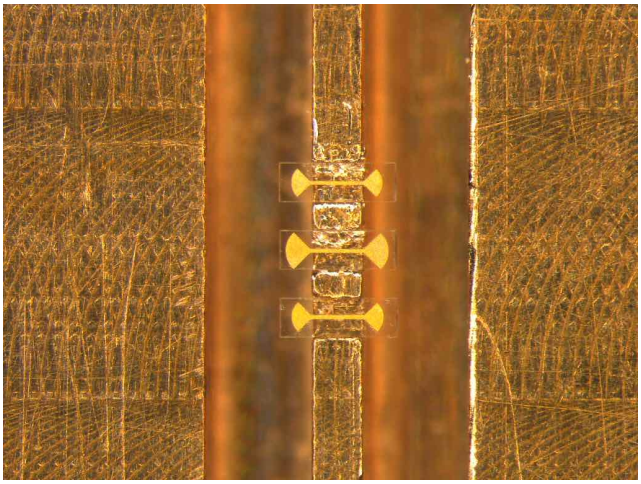

Figure 5.9: Bow-tie probes installed in array block.

In practice, however, it was too difficult to attach the bond wires. To adapt the design, the IF tuning circuits were instead printed on a flexible substrate (Duroid™ Pyralux® TK1810018R). This allowed the IF boards to bend onto the top of the array block such that one end of the board is in the same plane as the SIS device (Fig. 5.10b). It was then simple to attach the bond wires.

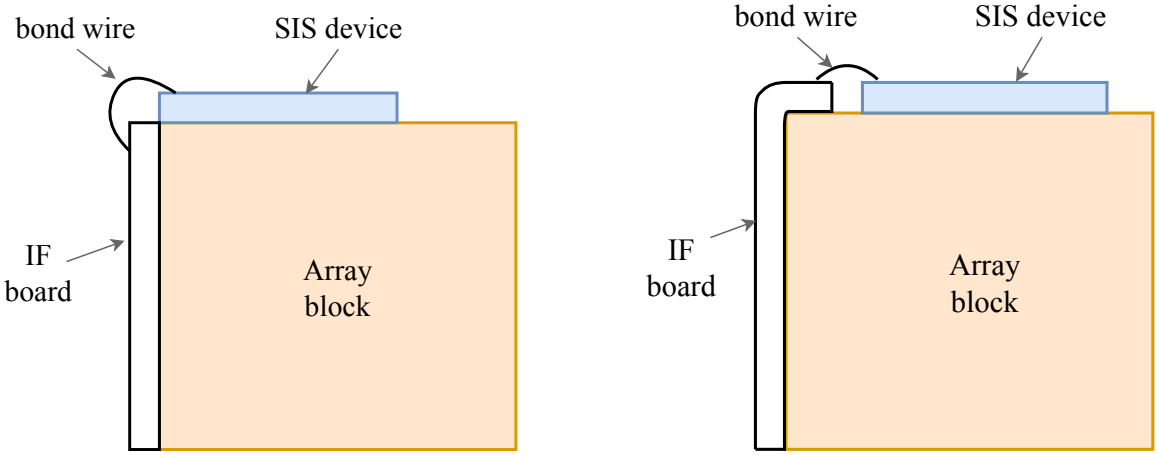

(a) The original design with the IF tuning circuit printed on a rigid substrate.

(b) The new solution with the IF tuning circuit printed on a flexible substrate.

Figure 5.10: Cross-section of the IF tuning boards mounted in the array block.

One concern with the flexible substrate was that it might present a higher insertion loss than the rigid substrate. To quantify the loss, a 50 Ω microstrip was printed onto the flexible substrate, and then the microstrip was measured on a probe station connected to a vector network analyser (VNA). For a 2.5 cm long section, the measured transmission was -0.4 dB at 10 GHz (Fig. 5.11), which is very similar

to the transmission through the rigid substrate that was used in Chp. 3. Assuming an ambient temperature of 5 K, this insertion loss corresponds to an effective noise temperature of 0.5 K.

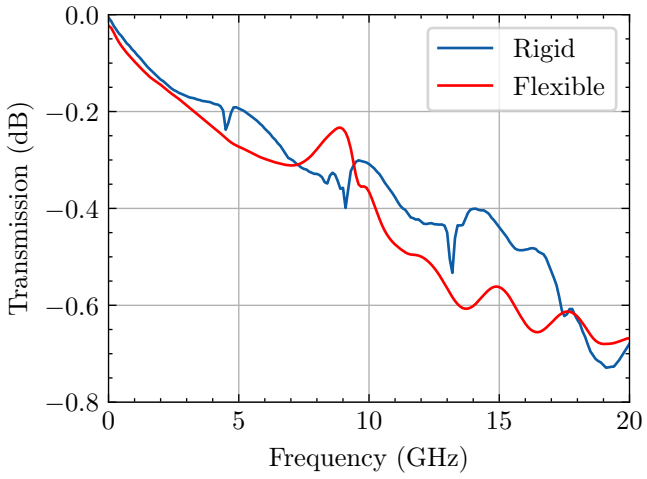

Figure 5.11: Measured transmission through 50 Ω microstrips printed on different substrates. The rigid IF board was 1.6 cm long and printed on 254 µm thick RT/duroid® 6010 ($\epsilon_r = 10.2$, $\tan\delta = 0.002$), and the flexible IF board was 2.5 cm long and printed on 100 µm thick Duroid™ Pyralux® TK1810018R ($\epsilon_r = 2.5$, $\tan\delta = 0.002$). The transmission was measured using a probe station connected to a VNA. Note that the VNA was calibrated, but the probe station itself was not de-embeded from these results. The actual transmission will be slightly higher.

LO loads

The array design requires waveguide loads to terminate the portion of the LO signal that is not coupled into the RF waveguide. These were made from Eccosorb® MF-116, which is a hard microwave absorbing material. Wedges of this material were placed at the end of the LO waveguides to terminate the LO signals. A picture of one of the LO loads installed in the array block is shown in Fig. 5.12. Based on HFSS simulations, the return loss from this wedge should be higher than 35 dB.

5.3.1 Modifications to the LO couplers

When the array block was initially fabricated, the LO couplers were implemented in the wrong orientation. (This is visible in Fig. 5.8e. Note that these couplers have forward coupling.) To fix this error, the old waveguides were drilled out and then filled back in with copper slugs, which allowed the waveguides to be completely re-machined in the correct orientation. Unfortunately, at the time that these corrections were made, only non-computer controlled milling machines were available at RAL.

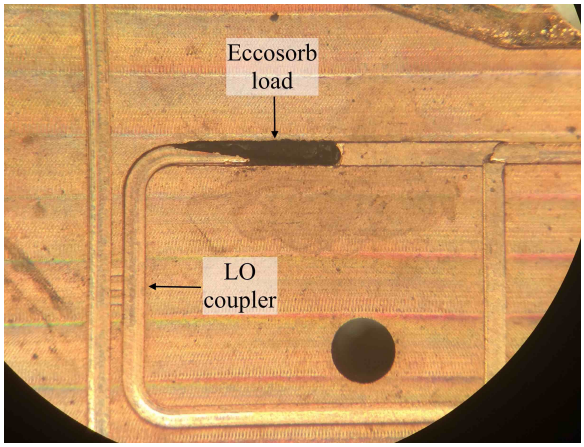

Figure 5.12: An LO load installed in the array block.

These milling machines are still very precise, but smooth waveguide bends are not possible without computer control. A new technique was needed to create waveguide bends using only linear passes with the cutting tool. The solution, shown in Fig. 5.13, leaves a notch in the outside corner. Note that this design assumes that the cutting tool is the diameter of the waveguide's minor axis, $b = 0.55$ mm, which is often the case at millimetre wavelengths.

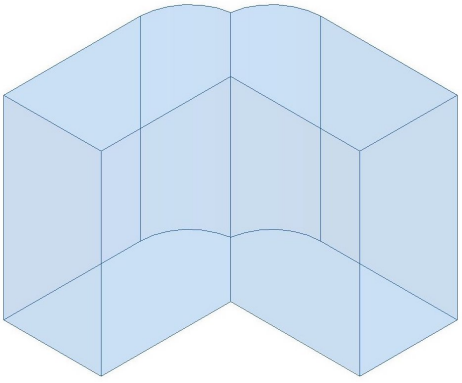

(a) 3D model of the waveguide bend.

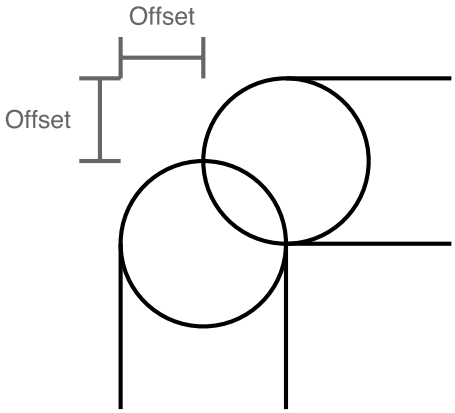

(b) Cross-section of the bend. The circles represent the diameter of the cutting tool.

Figure 5.13: The new 90° waveguide bend that does not require a computer controlled milling machine. Instead of running the cutting tool all the way into the corner, a notch of material is left in the outside corner. This design was optimised assuming that the cutting tool would be the diameter of the waveguide's minor axis, so the notch in the corner has fillets on either side.

The design was simulated with HFSS. The "offset" dimension that is labelled in Fig. 5.13b was optimised to provide the best insertion loss. The simulated scattering

parameters are plotted in Fig. 5.14 for an offset equal to 43.6% of the width of the minor axis (i.e., offset $= 0.436 \cdot b$). The results are also compared to a 90° waveguide bend with no notch (i.e., offset $= 0$).

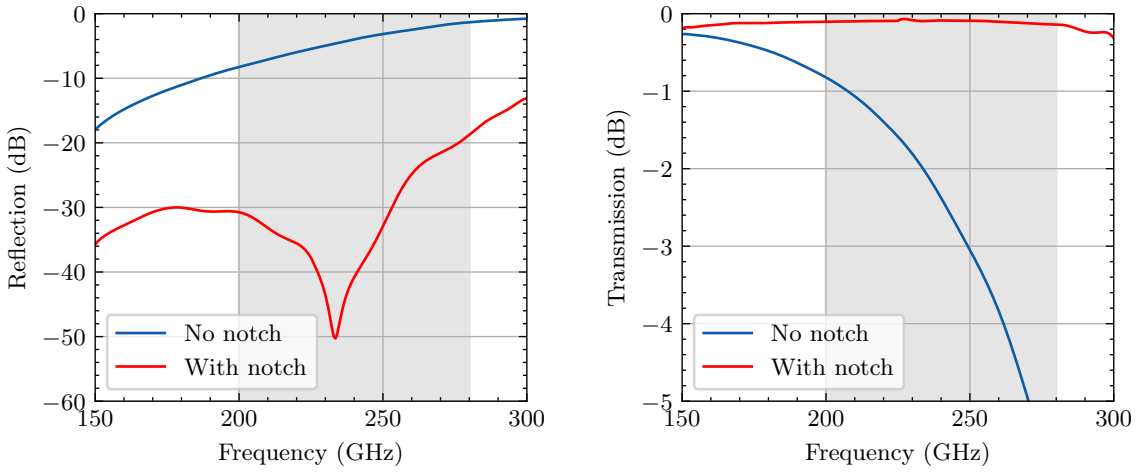

(a) Reflection (b) Transmission

Figure 5.14: Simulated performance of the new 90° waveguide bend. The performance is also compared to a 90° waveguide bend with no notch in the outside corner.

To validate this design, the waveguide bend was scaled to the Ku-band (frequency: 12.4−18.0 GHz, waveguide dimensions: 620×310 mil/15.80×7.90 mm). The physical model is shown in Fig.5.15a, and the measured results are compared to simulated results in Fig. 5.15b. The measured insertion loss is approximately 0.1 dB across the entire band, which corresponds to 97.7% power transmission in linear units. (Note that part of this loss is due to the conduction loss of the aluminium waveguide walls.)

Once the waveguide bend was validated with the scale model, it was implemented in the array block (Fig. 5.16). It was not possible to test the waveguide bend in this configuration, but the scale model at Ku-band suggests that these waveguide bends should function as intended.

5.4 Experimental performance

To test the performance of the array, it was installed into the open-cycle cryostat shown in Fig. 5.17. This is the same cryostat that was used in Chp. 3, except that additional wiring was added to accommodate the new pixels. Since this cryostat had had difficulties cooling in the past, only two windows were installed on the front of the cryostat to limit the infrared heat load. This allowed for freespace coupling for the LO signal and one RF pixel (i.e., pixel #3 if they are counted left to right).

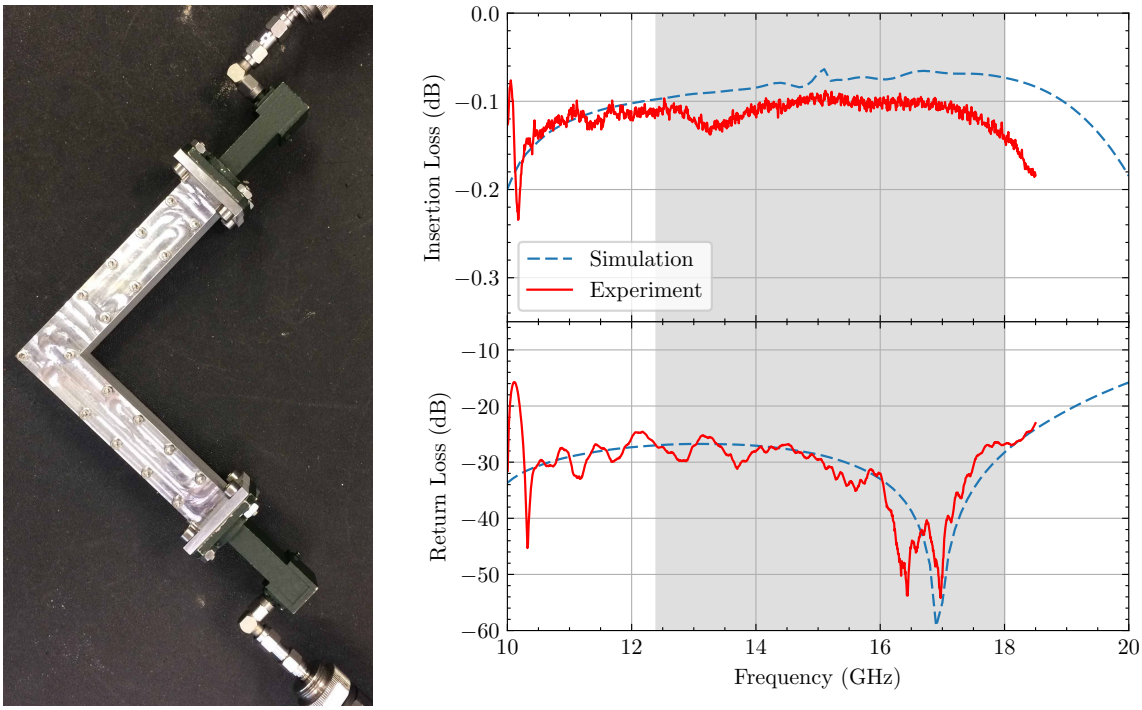

(a) Photo of the waveguide bend connected to a VNA.

(b) Scattering parameters of the waveguide bend. The shaded area is the Ku-band (12.4–18 GHz).

Figure 5.15: The new waveguide bend scaled to Ku-band.

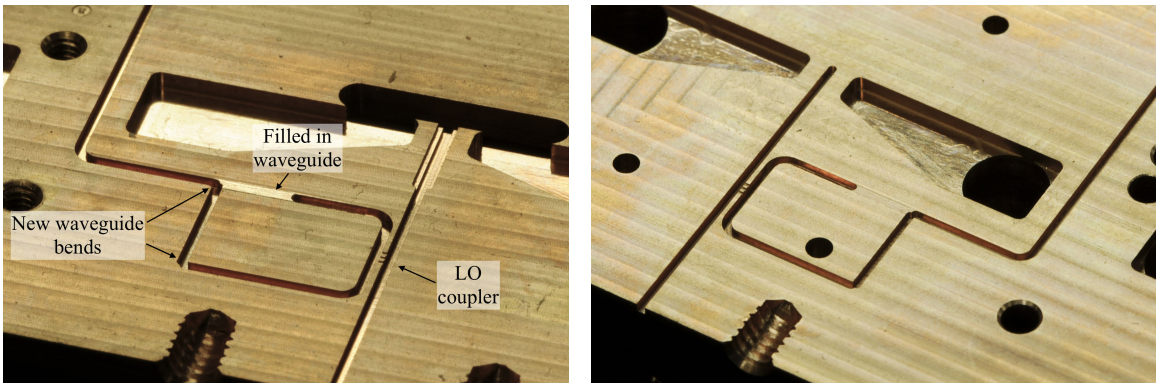

(a) Bottom half of the array block.

(b) Top half of the array block.

Figure 5.16: Photos of the new 90° waveguide bends implemented in the array block. These changes were made to fix the orientation of the directional couplers.

Since each pixel is identical, each pixel should also have the same noise properties, provided that the LO distribution is homogeneous. Therefore, pixel #3 should be able to represent the noise properties of the other pixels. Even though only pixel #3 was setup for RF measurements, all of the other pixels were still connected to DC bias supplies and current sources for the magnetic coils. This allowed all of the I–V curves to be measured, from which the junction drive levels can be recovered to assess LO distribution and isolation.

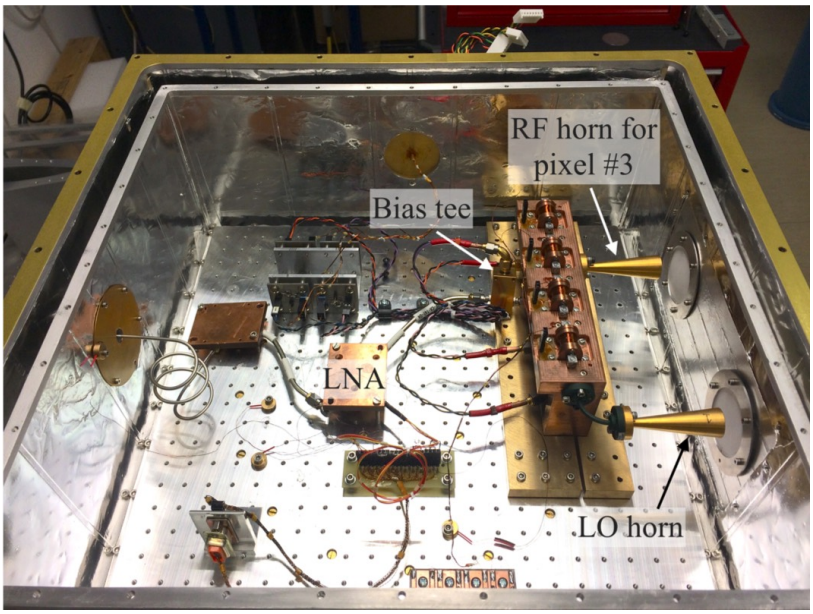

(a) The array installed inside the cryostat.

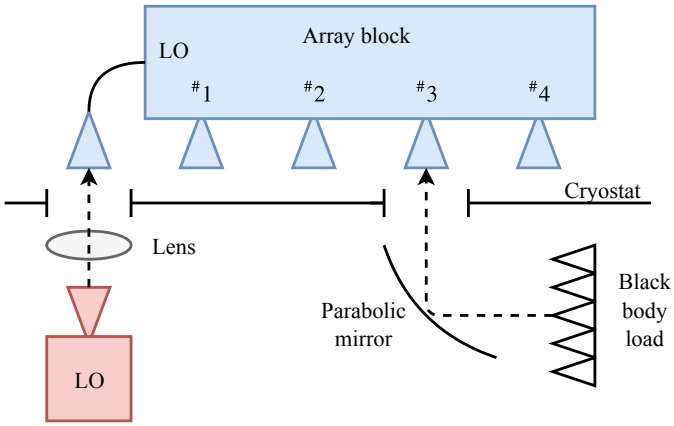

(b) Layout of the optical components.

Figure 5.17: Experimental setup for testing the focal plane array. All of the pixels are connected to DC bias supplies and current sources for the magnetic coils, but only pixel #3 is setup for black body load measurements.

5.4.1 DC properties

To begin, the array was cooled down and the DC I–V curves were measured from each SIS device. The I–V curves are shown in Fig. 5.18, and the extracted properties are listed in Table 5.3. During this test, the temperature of the array block was measured using a thermal probe to be 5.416 K, and the temperature of the cold plate was measured to be 5.229 K (placed next to the array block). This is not cold enough for optimum SIS performance. We typically aim for temperatures below $T_c/2$, which is ∼4.6 K for niobium, to limit the leakage current and the associated shot noise. Since the block temperature is very close to the temperature of the cold plate, there is likely an issue with the cryostat (i.e., the problem does not seem to be due to poor thermal contact with the cold plate). The temperature of the SIS devices was estimated by fitting the theoretical leakage current to the measured leakage current. This is listed as T_{leak} in Table 5.3. Again, it is above the temperature that is typically desired for SIS devices. This also manifests as low gap voltages in Table 5.3.

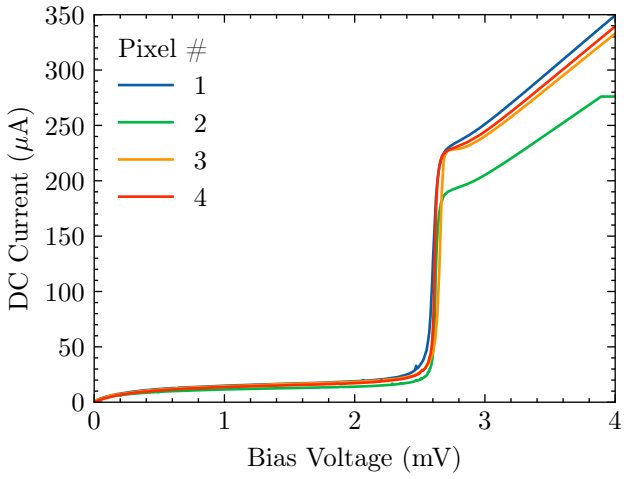

Figure 5.18: DC I–V curves measured from the pixels in the focal plane array. Note that pixel #2 has a higher normal resistance. This plot has been corrected for a series resistance of 3.2 Ω.

In order to have consistent noise properties and LO pumping requirements, the DC properties of the pixels should be similar. Unfortunately, the normal resistance of pixel #2 was about 20% higher than the other pixels. The normal resistance of this pixel was also higher at room temperature (R_{warm} in Table 5.3). Ideally, it should have been exchanged with another device, but at the time of this test, there were no spare devices available.

Table 5.3: DC properties of the pixels extracted from the I–V curves in Fig. 5.18.

Pixel #	R^a_{warm} (Ω)	V_{gap} (mV)	R_{n} (Ω)	R_{sg} (Ω)	T^b_{leak} (K)
1	93.0	2.59	10.08	141.8	5.85
2	100.6	2.62	12.30	268.9	5.79
3	89.9	2.64	10.59	187.5	5.97
4	92.5	2.61	10.38	181.7	5.70

[a] Normal resistance at room temperature.
[b] The temperature of the SIS junction. Estimated by fitting Eqn. 2.11 to the leakage current.

5.4.2 RF performance

The RF performance of the array block was characterised by measuring pixel #3's response to hot and cold black body radiation (see diagram in Fig. 5.17b). The Y-factor technique was then applied to estimate noise temperature and gain (results in Fig. 5.19). The lowest noise temperature was 87.8 K at 222.2 GHz, but above 225 GHz, the noise temperature climbed steadily with frequency up to 230 K at 255 GHz. Conversely, the measured conversion efficiency was very low with all measured values below -3.5 dB or 45%.

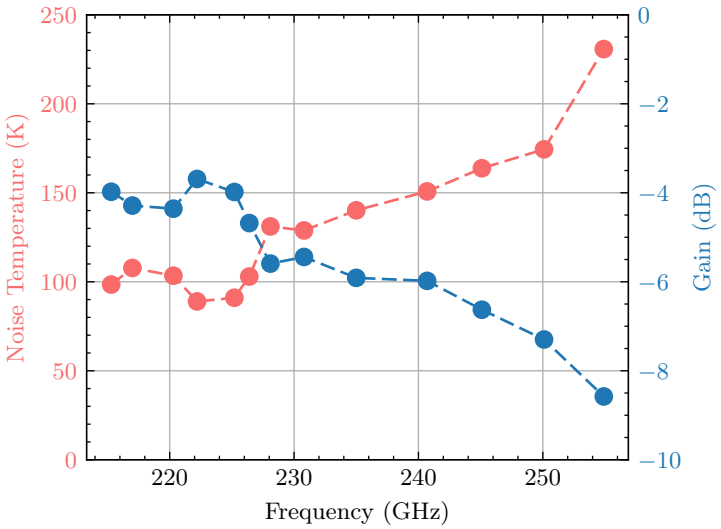

Figure 5.19: Experimental noise temperature and conversion efficiency/gain using pixel #3 on the focal plane array.

The noise temperatures in Fig. 5.19 are much higher than the values that were previously measured with the single block in Chp. 3 (e.g., the noise temperature with

the single block was $T_{\mathrm{N}}\sim$40 K from $215-245$ GHz in Fig. 3.22). To find the source of the additional noise, the IF and RF noise contributions were estimated using Woody's method [54] and the technique of intersecting lines [53], respectively. In Fig. 5.20a, the IF noise is estimated to be 18.5 K, and in Fig. 5.20b, the RF noise is estimated to be 15.8 K at 230 GHz. These values are compared to the values from the single block in Table 5.4.

As seen in Table 5.4, the RF noise from the single block and RF noise from the array block are relatively similar. The IF noise, on the other hand, is significantly higher with the array block. Since the same IF chain was used for both experiments, the extra noise must come from additional loss between the SIS junction and the bias tee. We can cascade the noise properties from the single block system to estimate the gain G of the lossy component[8]:

$$T_{\mathrm{IF,array}} \approx \left(\frac{1}{G}-1\right) T_{\mathrm{phys}} + \frac{T_{\mathrm{IF,single}}}{G} \tag{5.2}$$

where $T_{\mathrm{IF,array}}$ is the IF noise with the array block, $T_{\mathrm{IF,single}}$ is the IF noise with the single block, and T_{phys} is the temperature of the lossy component. By assuming a physical temperature of 5.3 K and then rearranging Eqn. 5.2, the estimated gain of the lossy component is 66.5%. One possibility is that this could come from the flexible IF board. Back in Fig. 5.11, the transmission through the flexible IF board was found to be very similar to the transmission through the rigid IF board, but this did not take into account that the insertion loss may be much higher when the flexible IF board is bent at a sharp angle, such as it is in the array block (see Fig. 5.10b). If the IF noise of the array block could be lowered to the value of the single block, I estimate that the system noise temperature would be:

$$T'_{\mathrm{N}} = T_{\mathrm{N,array}} - \frac{T_{\mathrm{IF,array}}}{G_{\mathrm{c,array}}} + \frac{T_{\mathrm{IF,single}}}{G_{\mathrm{c,array}}} = 93.5 \text{ K} \tag{5.3}$$

at 230 GHz. Therefore, out of total noise temperature at 230 GHz ($T_{\mathrm{N}} = 127.8$ K), 27% of the noise is caused by additional loss in the IF chain, likely due to the bend in the flexible IF board.

Since the RF and IF noise cannot account for all of the additional noise of the array block, the noise from the SIS junction is likely very high. By subtracting the RF and IF noise contributions, the noise contribution from the SIS junction can be

[8]Recall that the effective noise temperature of a lossy component is: $T_{\mathrm{eff}} = (1/G - 1)\ T_{\mathrm{phys}}$ where G is the gain/transmission, and T_{phys} is the physical temperature.

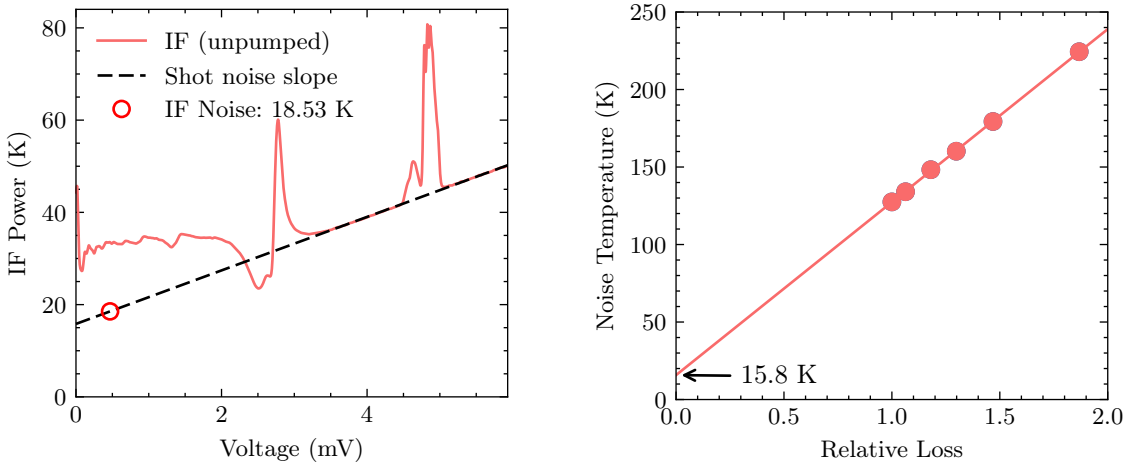

(a) The IF noise calculated using Woody's method [54].

(b) The RF noise calculated using the technique of intersecting lines [53].

Figure 5.20: Noise contributions measured from the focal plane array.

Table 5.4: Measured performance with the single block and with the array block at 230 GHz.

Parameter	Symbol	Value	
		Single block	Array block
Receiver noise temperature	T_{N}	35.7 K	127.8 K
Conversion gain/efficiency	G_{c}	77.0%	29.2%
RF noise	T_{RF}	12.6 K	15.8 K
IF noise	T_{IF}	8.5 K	18.5 K

isolated by:

$$\frac{T_{\rm SIS}}{G_{\rm RF}} = T_{\rm N} - T_{\rm RF} - \frac{T_{\rm IF}}{G_{\rm RF}\,G_{\rm SIS}} \tag{5.4}$$

where $T_{\rm SIS}$ is the noise from the SIS junction, and $G_{\rm RF}$ and $G_{\rm SIS}$ are the gain of the RF components and the SIS junction, respectively. Recall that the conversion efficiency is equal to $G_{\rm c}$=$G_{\rm RF}$·$G_{\rm SIS}$. To isolate $T_{\rm SIS}$ and $G_{\rm SIS}$, we need to know $G_{\rm RF}$. In Table 5.5, the gain G and effective noise temperature T of each component in the RF chain is estimated. By cascading all of the RF components, the RF gain is estimated to be $G_{\rm RF}$=79.1%, resulting in an SIS gain of $G_{\rm SIS}$=36.9% and an SIS noise of $T_{\rm SIS}$=38.2 K. The noise and gain properties of the SIS junction in the array block are therefore much worse than the junction properties in the single block (see Table 5.5). This is likely the result of a very high array block temperature, which results in higher leakage current, higher shot noise, a smeared DC I–V curve, and lower gain. If the SIS junction in the array block could be cooled to the temperature that it was in the single mixer block, the estimated system noise temperature is:

$$\begin{aligned} T'_{\rm N} &= T_{\rm N,array} - \left(\frac{T_{\rm SIS,array} - T_{\rm SIS,single}}{G_{\rm RF,array}}\right) - \left[\frac{T_{\rm IF,array}}{G_{\rm RF,array}}\left(\frac{1}{G_{\rm SIS,array}} - \frac{1}{G_{\rm SIS,single}}\right)\right] \\ &= 55.5\ K \end{aligned} \tag{5.5}$$

at 230 GHz. Therefore, the warm SIS junction is likely causing 57% of the array block's current noise temperature. If the SIS junctions in the array block can be cooled to the level of the single block, the system noise temperature should be close to 55.5 K.

5.4.3 LO distribution

In a focal plane array, it is important that the LO power is distributed evenly between the pixels in order to pump each SIS device to the optimum drive level. Otherwise, if the pump level of some pixels is lower than others, the conversion gain of those pixels will be lower, resulting in higher IF noise contributions. To test the LO distribution, the LO was injected into the LO port of the array block (Fig. 5.21a) and then the pumped and unpumped I–V curves were measured from each pixel (Fig. 5.21b). These I–V curves were used to recover the junction drive levels, listed in Table. 5.6.

Based on these results, the LO distribution is relatively uneven. Pixel #3 receives by far the most power, while pixel #4 receives 72% less power. Several possible reasons

Table 5.5: Noise composition of the SIS receivers.

	Component	T_{phys} (K)	Single block		Array block		Ref.
			G (%)	T (K)	G (%)	T (K)	
RF comp.	12 µm beam splitter	295	99.2^{c}	2.48	–	–	App. B.5
	Zotefoam vacuum window	295	98.1^{m}	5.71	98.1^{m}	5.71	App. B.4.2
	Zitex IR filter	90	98.0	1.63^{m}	98.0	1.63^{m}	Sec. 3.7.1
	Directional coupler	5.3	–	–	95.0^{e}	0.28	Fig. 5.6b
	Planar circuit (WG→J)	4.7/5.3	86.6^{s}	0.73	86.6^{s}	0.82	Sec. 3.7
	SIS junction	–	93.2^{r}	11.3^{r}	36.9^{r}	38.2^{r}	
IF comp.	Planar circuit (J→IF)	4.7/5.3	52.3^{s}	3.6	52.3^{s}	3.6	Sec. 3.8
	IF board	4.7/5.3	95.9^{m}	0.20	94.8^{m}	0.29	Fig. 5.11
	LNA	–	–	4.0^{m}	–	4.0^{m}	Fig. 3.15

This table is listed in order from input to output (i.e., from the black body load to the detector diode). They are also grouped by sub-system: RF components, SIS junction and IF components. The single block refers to Sec. 3.7.1, and the array block refers to Sec. 5.4.
Legend: (*c*) calculated from theory, (*e*) estimated, (*m*) measured directly, (*r*) recovered, (*s*) simulated results from HFSS

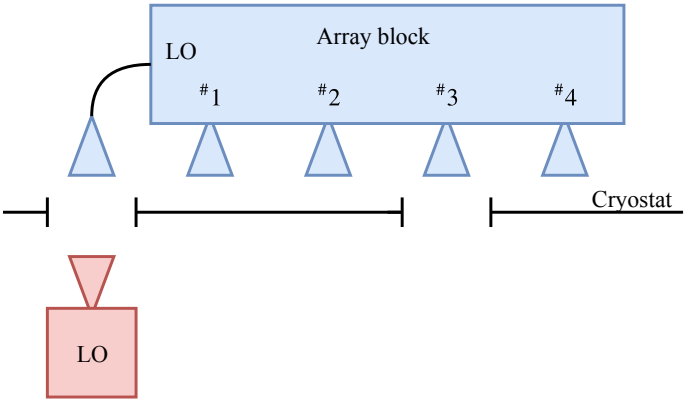

(a) The LO was injected into the LO port of the array block.

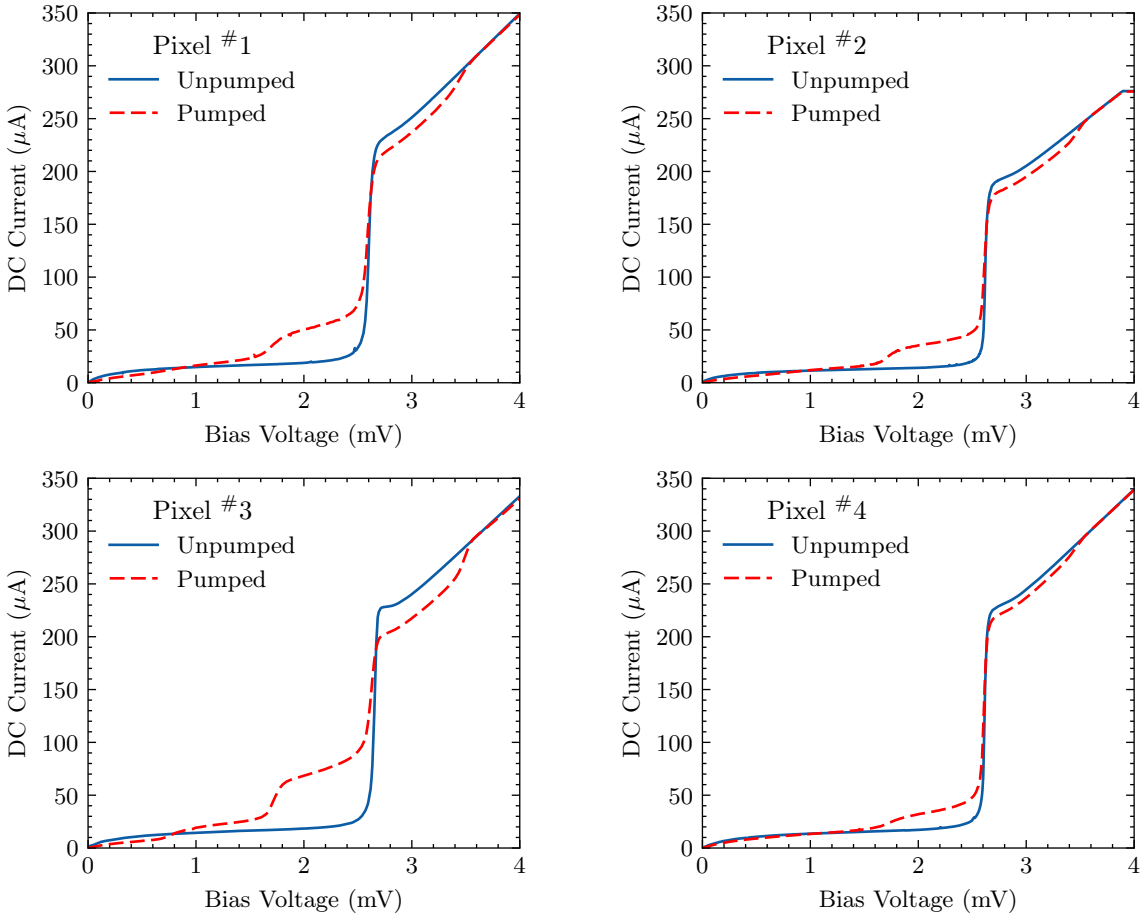

(b) The I–V curves measured from the four pixels.

Figure 5.21: Distribution of the local-oscillator signal between the pixels.

Table 5.6: LO distribution in the array block at 230 GHz.

Pixel	Embedding circuit			Junction properties		
#	V_{LO} (mV)	Z_{LO} (Ω)	P_{avail} (dBm)	α	Z_{J} (Ω)	P_{deliv} (dBm)
1	1.38	$5.14 - j7.06$	-43.35	0.80	$8.22 + j0.55$	-44.48
2	1.18	$6.27 - j6.40$	-45.60	0.72	$9.82 + j1.07$	-46.23
3	1.28	$2.12 - j2.22$	-40.13	1.07	$8.73 + j0.70$	-42.21
4	0.78	$3.53 - j4.67$	-46.62	0.55	$8.15 + j0.66$	-47.77

for this include: (a) the power splitters may divide the power unevenly, (b) some of the bow-ties couplers may have higher coupling than others, (c) dirt and grime in the waveguides may attenuate some of the signals, or (d) different LO waveguide lengths may result in different attenuation levels. Another possibility is that the freespace LO signal is leaking into the RF waveguide horn on pixel #3. Since the LO signal is much more powerful, even a small amount of leakage could result in pixel #3 pumping to a higher level.

Using the single pixel block from Chp. 3, the noise temperature and gain were measured as a function of drive level (Fig. 5.22). Assuming that the noise temperature of the array block is similar to the single block (once it is properly cooled), this allows the drive levels α to be mapped to receiver noise temperatures T_{N}. The junction drive levels listed in Table 5.6 then correspond to noise temperatures of $T_{\mathrm{N},1} = 43.1$ K, $T_{\mathrm{N},2} = 46.2$ K, $T_{\mathrm{N},3} = 40.2$ K, and $T_{\mathrm{N},4} = 57.4$ K. Therefore, even though the LO distribution is uneven, the resulting noise temperatures should be relatively consistent. This is especially true once other noise contributions are taken into account, such as atmospheric transmission. Also, when the power LO was set for Fig. 5.21, the power level was set according to pixel #3. Since this pixel receives the most power, in practice, the LO power level should be set higher in order to optimise the noise temperature of the other pixels (such that some will be over-saturated and some will be under-saturated).

5.4.4 RF signal isolation

One concern with focal plane arrays is that RF signals may couple between adjacent pixels, resulting in cross-talk and artefacts in the final image. The RF signal isolation is a measure of this leakage. To measure isolation, a strong signal is normally injected into one of the pixels, and then the IF output powers of the surrounding pixels are compared to quantify the power leakage. Unfortunately, with the array in its

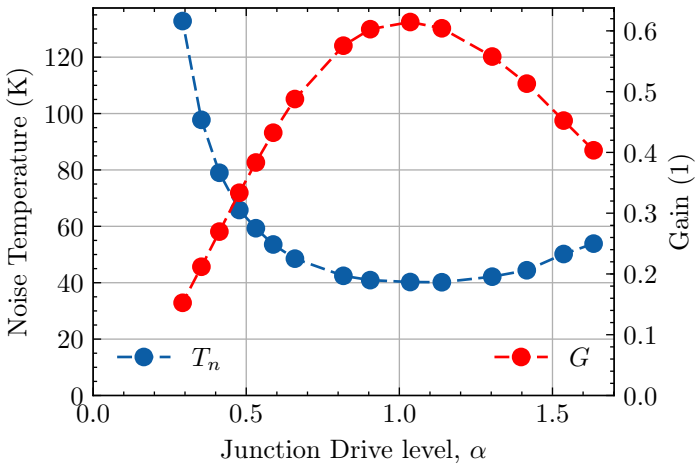

Figure 5.22: Gain and noise temperature as a function of drive level. This was measured using the single mixer block from Chp. 3. The drive level is defined as $\alpha \equiv V_\omega/V_{\text{ph}}$ where V_ω is the voltage across the junction due to the LO and $V_{\text{ph}} = h\nu/e$ is the photon equivalent voltage.

current configuration (Fig. 5.17), the IF output is only measured from one pixel. To measure the isolation with this test setup, the LO signal was injected directly into pixel $^{\#}3$ (Fig. 5.23a), and then the I–V curves from the surrounding pixels were measured (Fig. 5.23b). If there is any leakage, it should manifest as photon steps in the I–V data.

The measured I–V data from the isolation test is shown in Fig. 5.23b. Pixel$^{\#}3$ was pumped nearly to saturation. For the other pixels, the difference between pumped and unpumped current is very small, suggesting good isolation. The recovered drive levels for these pixels are: $\alpha_1 = 0.045$, $\alpha_2 = 0.048$, $\alpha_3 = 1.624$, and $\alpha_4 = 0.046$. In terms of isolation, calculated as $I_i = 20 \cdot \log_{10}(\alpha_i/\alpha_3)$, these junction drive levels correspond to $I_1 = -31.1$ dB, $I_2 = -30.6$ dB, and $I_4 = -31.0$ dB. This means that less than $1/1000^{\text{th}}$ of the signal power leaks into the surrounding pixels, which is a good level of isolation.

5.5 Future work

The 1×4 focal plane array was built as a demonstrator to test a new array architecture that can then be expanded into a larger array in the future. As expected with any new design, several issues were found during testing. Several improvements are suggested below:

- The first issue is that the array was not able to be cooled to an adequate

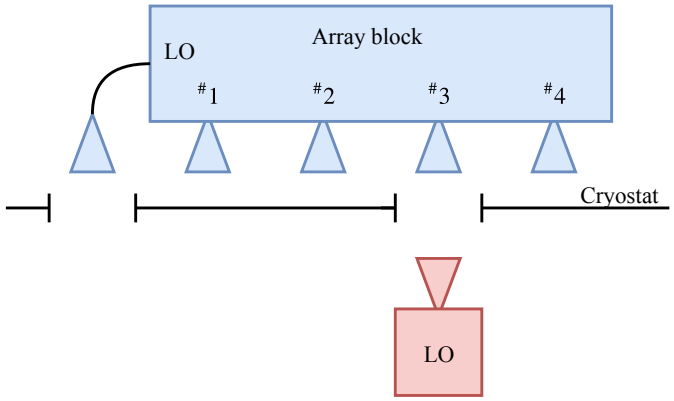

(a) The LO was injected directly into pixel #3.

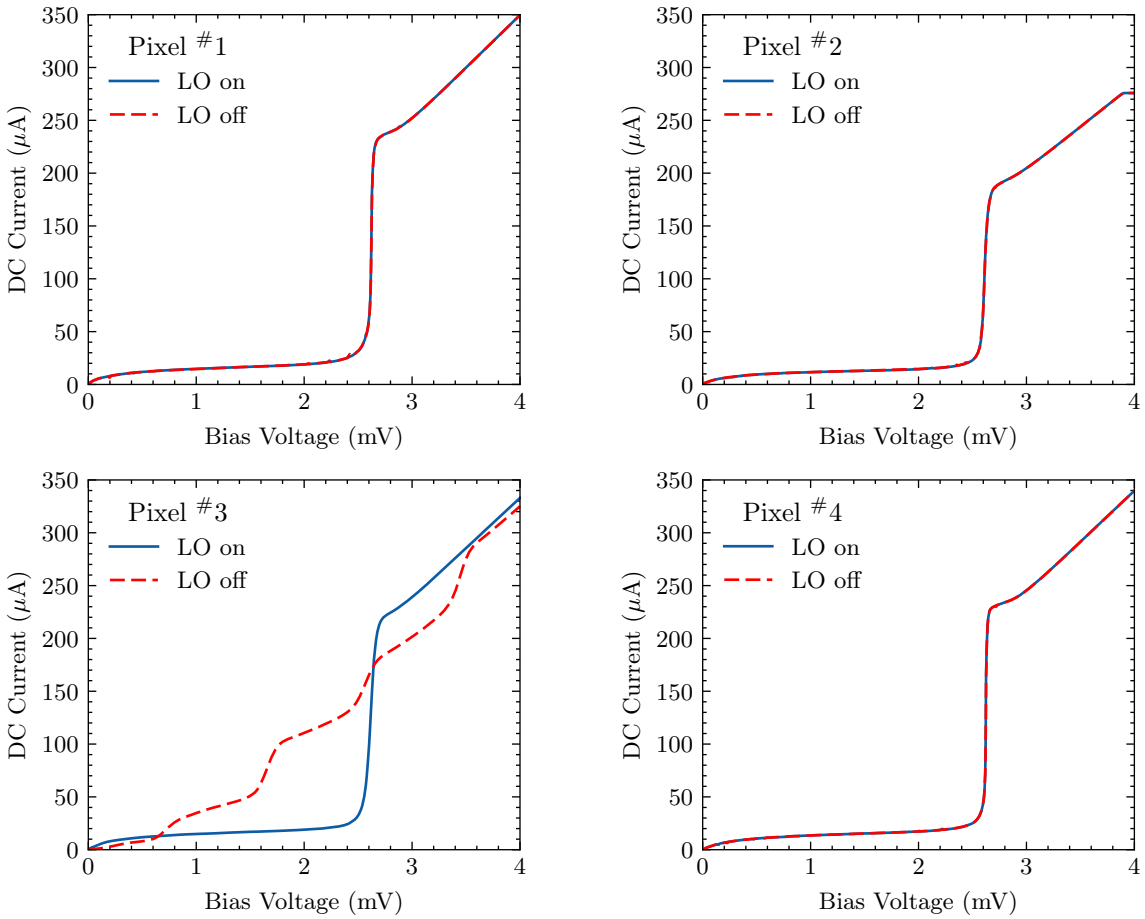

(b) The measured I–V curves. Only pixel #3 should be pumped.

Figure 5.23: Signal isolation in the focal plane array. The LO was injected directly into pixel #3. Ideally, very little pumping should be seen at the other pixels.

temperature. This is more to do with the cryostat since it even had difficulties cooling the single mixer block in Chp. 3. One solution is to use better infrared filters on the radiation shield. Currently, the cryostat uses Zitex filters (the same ones that were used in Chp. 3), but more selective multi-mesh filters may be required. Also, the cold plate seems to have poor thermal contact with the liquid helium vessel. A new cold plate contoured to the liquid helium veseel could be machined from a metal with higher thermal conductivity, such as cooper or brass.

- The second issue is that the LO distribution is relatively uneven. Even though this should not affect the noise temperatures too much, it would still help improve the overall sensitivity of the array. The LO distribution could be improved by repositioning the bow-ties or perhaps cleaning the LO waveguides. In any future array design, the LO waveguides should all be the same length to have the same conduction loss between the pixels. Also, the array could be gold plated to help reduce corrosion.
- The last issue that I encountered with the array was the flexible IF boards. Although they worked for the testing in this thesis, they likely have significant insertion loss and they were difficult to install in the array block. In future designs of the array block, non-flexible IF boards should be designed to meet the SIS device at a 45° angle. This would still allow the IF signal to be routed down below the LO and RF waveguides, but it would also allow the bond wires to be attached without the need for flexible substrates.

5.6 Conclusion

In this chapter, a new 1×4 focal plane array at 230 GHz was presented. The array block has waveguide flanges for 4 pixels on the front and another for the LO signal on the side. Inside the array block, the LO power is divided using cascaded E-plane power splitters and then injected into the RF waveguides using directional couplers. After the directional coupler, the combined RF+LO signals are coupled to SIS devices. (The same SIS devices that were presented in Chp. 3.) The down-converted IF signals are then coupled to an IF tuning board that is mounted vertically to avoid any cross-over with the RF and LO waveguides. When the array was tested experimentally, it was difficult to cool the block to an adequate temperature. This resulted in high leakage currents and noise temperatures. Most of the added noise temperature is likely caused by the high temperature (not due to the array architecture), so the noise temperature

should decrease significantly once the array is cooled to a lower temperature. The LO distribution was characterised by comparing the pumped and unpumped I–V curves measured from each pixel. Although the distribution was not as uniform as expected, it should theoretically result in relatively consistent noise temperatures between 40 K and 57 K. The RF signal isolation was also measured by injecting the LO directly into one of the RF pixels and then again comparing the pumped and unpumped I–V curves that were measured from each pixel. This test showed that the isolation is below -30 dB, meaning that less than $1/1000^{\text{th}}$ of the power from one pixel leaks into the surrounding pixels. Overall, the new focal plane array has demonstrated promising initial results. To improve upon these results, the array should be cooled to a lower temperature and some of the bow-ties should be repositioned.

Chapter 6

Tracers of Star Formation Activity at Intermediate Redshift

6.1 Introduction

Stars form in dense clouds of molecular gas and dust, known as *giant molecular clouds* or GMCs. As the name suggests, these are massive clouds that can extend up to 100 pc in diameter[1], with masses of $M{\sim}10^{5-6.5}\,\mathrm{M}_{\odot}$ and average densities of $n(\mathrm{H}_2){\sim}10^2$ cm^{-3}. The internal structure of GMCs is highly irregular, including filaments and sheets of higher density gas. Through local gravitational collapse, these regions first compress into *clumps* ($d{\sim}1$ pc, $M{\sim}10^3\,\mathrm{M}_{\odot}$, $n(\mathrm{H}_2){\sim}10^3$ cm^{-3}) that later go on to form stellar clusters, and then the clumps further fragment and condense into *molecular cores* ($d{\sim}0.1$ pc, $M{\sim}\mathrm{M}_{\odot}$, $n(\mathrm{H}_2){\sim}10^4$ cm^{-3}) that form individual and binary stars (McKee and Ostriker [138]). GMCs have been thoroughly studied within the Milky Way and several nearby galaxies (e.g., Kennicutt and Evans [139]); however, they become unresolved beyond a redshift of $z \sim 0.01$. Instead, the metrics that trace the chemical and physical properties of the interstellar medium (ISM) are integrated over entire GMCs or even entire galaxies. Empirical relationships, known as scaling laws, are then used to interrelate the global properties, such as the star formation rate, the mass of the molecular gas reservoir, and the star formation efficiency. In this

The work in this chapter was completed under the supervision of Dimitra Rigopoulou and in collaboration with Isabella Cortzen and Georgios Magdis from the University of Copenhagen. The work that we completed together been submitted for publication in [5]. In this chapter, I focus on the CO observations; not on the PAH or IR data. I also include the metallicity of the sample galaxies, which was not included in [5]. Note that the CO data from September 2016 was collected by Isabella and I, but I completed all of the data analysis by myself.

[1]In this chapter, distances are typically measured in parsecs (pc) where 1 pc $\sim$ 3.26 light-years (ly) $\sim 3.09 \times 10^{16}$ m, masses are measured in solar masses ($\mathrm{M}_{\odot}$) where 1 $\mathrm{M}_{\odot} \sim 2 \times 10^{30}$ kg, and luminosities are measured in solar luminosities ($\mathrm{L}_{\odot}$) where 1 $\mathrm{L}_{\odot} = 3.828 \times 10^{26}$ W.

chapter, three different tracers are discussed: two tracers of the star formation rate (infrared luminosity and emission from polycyclic aromatic hydrocarbons) and one tracer of the molecular gas reservoir (emission from carbon monoxide).

The infrared (IR) luminosity $L_{\rm IR}$ traces the ultraviolet (UV) light from young O/B stars that has been absorbed by grains of dust and then reradiated in the IR spectrum. In dusty star-forming galaxies, $L_{\rm IR}$ is an ideal tracer of the star formation rate (SFR) because the dust absorbs almost all of the UV light that is emitted by the young O/B stars. Examples of dusty star-forming galaxies include Luminous Infrared Galaxies (LIRGs; defined as $L_{\rm IR} = 10^{11} - 10^{12}\ L_{\odot}$) and Ultra Luminous Infrared Galaxies (ULIRGs; defined as $L_{\rm IR} > 10^{12}\ L_{\odot}$), which dominated the star formation activity between $z \sim 1 - 3$ (Madau and Dickinson [140]). Some of the ULIRGs, however, have active galactic nuclei (AGN) at their cores that can contribute >50% of the total infrared luminosity (e.g., J. Smith, *et al.* [141], G. Magdis, *et al.* [142], Y. Wu, *et al.* [25]). This results in an over-estimated star formation rate and scatter between $L_{\rm IR}$ and the other global SF properties.

To measure the true SFR, a possible alternative to $L_{\rm IR}$ is the emission from polycyclic aromatic hydrocarbons (PAHs; Tielens [143] and references therein). These are large organic molecules formed from a honeycomb structure of carbon atoms, with hydrogen atoms bonded around the perimeter. They absorb optical and UV photons from young O/B stars, and then re-emit the energy as spectral features between 3–17 µm. The PAH molecules are thought to be found in the photodissociation region (PDR; Hollenbach and Tielens [144], Hollenbach and Tielens [145]), which is a shell-like structure that surrounds all dense molecular gas. In this region, UV photons from young stars and the interstellar radiation field (ISRF) play an important role by photodissociating molecules, ionising atomic gas, and exciting PAHs. G. Bendo, *et al.* [146] found that PAH emission is spatially correlated with cold dust emission (as traced by 160 µm), suggesting that it could be used to trace cold molecular gas. PAHs also seem to be destroyed by the hard radiation from AGN (F. Boulanger, *et al.* [147], F. Boulanger, *et al.* [148], Helou et al. [149], J. Pety, *et al.* [150]), which could make PAH emission more selective of star formation than $L_{\rm IR}$ (although, recent studies have challenged this view on PAH destruction, e.g., J. Jensen, *et al.* [151]).

The final tracer that will discussed in this chapter is emission from molecular gas. This traces the amount of fuel that is available for forming new stars. Most of the gas in GMCs is molecular hydrogen (H_2); however, H_2 lacks a permanent dipole moment and it is a very light molecule, meaning that it requires a very high excitation

temperature. Typically, only 1–30% of the H_2 gas is hot enough to emit spectral lines (e.g., H. Roussel, *et al.* [152]), and even when H_2 is excited, most of the lines are emitted in the mid-IR and UV bands, which cannot be observed from the ground. Instead, carbon monoxide (CO) is used to trace H_2 since CO is both abundant and it has rotational lines that are easily excited at cold temperatures. The well-known *X-factor* is then used to estimate the H_2 concentration from the CO emission (Bolatto et al. [153]):

$$X_{\rm CO} \equiv N({\rm H_2})/I_{\rm CO} \tag{6.1}$$

where $N(H_2)$ is the column density of H_2 gas, and $I_{\rm CO}$ is the integrated intensity of CO. At higher redshifts, when the surface density is not resolved, the total CO luminosity[2] $L'_{\rm CO}$ is instead used relate to the total H_2 mass through (Solomon and Vanden Bout [155], Carilli and Walter [154]):

$$\alpha_{\rm CO} \equiv M_{\rm H_2}/L'_{\rm CO}\,. \tag{6.2}$$

The scaling relationships between ISM tracers have been studied in both nearby and high-z galaxies (e.g., A. Kirkpatrick, *et al.* [156], A. Pope, *et al.* [157], D. Calzetti, *et al.* [158], J. Smith, *et al.* [141], G. Bendo, *et al.* [146]). The most well-established relationship for cold gas is the Schmidt-Kennicutt law (SK law; Schmidt [159], Kennicutt [160], Kennicutt and Evans [139]):

$$\dot{\Sigma}_* \propto \Sigma_{\rm gas}^{1.4\pm0.15} \tag{6.3}$$

where $\dot{\Sigma}_*$ is the surface density of star formation rate, and $\Sigma_{\rm gas}$ is the surface density of the molecular and H I gas. Since $\dot{\Sigma}_*$ is traced by $L_{\rm IR}$ and $\Sigma_{\rm gas}$ is traced by $L'_{\rm CO}$, this also suggests strong $L_{\rm IR} - L'_{\rm CO}$ correlation. There is however considerable scatter in this relationship, with some galaxies exhibiting far higher $L_{\rm IR}$ for a given $L'_{\rm CO}$. These *starburst* galaxies are likely experiencing a short-lived period of increased star formation due to a recent merger event. The merger results in denser star forming regions which artificially boosts the star formation efficiency[3], defined as SFE $\equiv$

[2] In this chapter, all CO luminosities are quoted as $L'_{\rm CO}$ in units of K km s^{-1} pc^2 (versus $L_{\rm CO}$ in units L$_\odot$ or another similar unit). The definition of $L'_{\rm CO}$ takes into account the redshift of the galaxy (Eqn. 6.15), and it is directly proportional to the brightness temperature $T_{\rm B}$. Note that $L'_{\rm CO}$ can be converted to $L_{\rm CO}$ using: $L_{\rm CO} = 3\times10^{-11}\,\nu_{\rm rest}^3\,L'_{\rm CO}$, where $\nu_{\rm rest}$ is the rest frequency of the CO transition. More information can be found in [154].

[3] A more direct definition of star formation efficiency is SFE $\equiv \dot{M}_*/M_{\rm gas}$ where $\dot{M}_*$ is the star formation rate and $M_{\rm gas}$ is the total mass of molecular gas. This definition, however, requires estimating $\dot{M}_*$ from $L_{\rm IR}$ and $M_{\rm gas}$ from $L'_{\rm CO}$. I avoid these conversions by working directly with $L_{\rm IR}$ and $L'_{\rm CO}$.

$L_{\rm IR}/L'_{\rm CO}$ (R. Genzel, *et al.* [161], E. Daddi, *et al.* [162], E. Daddi, *et al.* [163], L. Tacconi, *et al.* [164]). Additional scatter can also result from AGN activity, which heats the dust and results in high IR luminosities and star formation efficiencies.

An alternative to $L_{\rm IR} - L'_{\rm CO}$ would be to formulate a $L_{6.2} - L'_{\rm CO}$ relationship. PAH emission should be more specific to new star formation since PAHs are likely destroyed by the intense radiation in starburst and AGN-dominated galaxies. In nearby spiral galaxies, PAH has been found to spatially correlate with FIR emission (G. Bendo, *et al.* [146]) and CO emission (M. Regan, *et al.* [165], G. Bendo, *et al.* [166]). These findings suggest that PAH emission could provide an alternative means to estimate the $L'_{\rm CO}$ with potentially less scatter.

In this chapter, CO(J=1→0) measurements are presented for 34 intermediate redshift galaxies selected from the 5 mJy Unbiased *Spitzer* Extragalactic Survey (5MUSES, Y. Wu, *et al.* [25]). The CO data was collected with the IRAM 30 m telescope, while the IR and PAH luminosities were available in the literature. These results are combined with additional data from nearby and high redshift galaxies to formulate scaling laws that span a large fraction of cosmic time. In the following sections, the sample galaxies are discussed in Sec. 6.2, the CO observations and data analysis procedure are described in Sec. 6.3, the additional SF studies are described in Sec. 6.4, and then the CO measurements are correlated with the other SF tracers in Sec. 6.5.

To be consistent with the 5MUSES data from Y. Wu, *et al.* [25], I used a flat ΛCDM model for all of the analysis in this chapter with $H_0 = 70$ km s^{-1} MPc^{-1}, $\Omega_\Lambda = 0.73$, and $\Omega_{\rm m} = 0.27$.

6.2 Sample galaxies

For our sample galaxies, we selected 34 sources from the 5 mJy Unbiased *Spitzer* Extragalactic Survey (5MUSES, Y. Wu, *et al.* [25]). 5MUSES was a spectroscopic survey of 330 galaxies from the SWIRE (SIRTF Wide-area InfraRed Extragalactic survey, C. Lonsdale, *et al.* [167]) and XFLS (*Spitzer* Extragalactic First Look Survey, D. Fadda, *et al.* [168]) fields with the selection criteria that $f_{24\mu{\rm m}} > 5$ mJy. The sample mostly contains galaxies with IR luminosities of 10^9 L$_\odot$ $< L_{\rm IR} <$ $10^{13.5}$ L$_\odot$ and redshifts of $0.008 < z < 4.27$. The subset of galaxies selected for our CO(J=1→0) observations are listed in Table 6.1. These galaxies were selected to sample a broad range of IR luminosities, dust temperature, PAH properties and star formation activity. Specifically, they were selected to cover a range of PAH equivalent widths (EW$_{6.2}$),

which has been proposed as a technique to identify AGN activity. The redshift of the sample galaxies ranges from $0.025 < z < 0.277$ with an average of $\langle z \rangle = 0.097$.

Additional CO(J=1→0) data is also included in this chapter from A. Kirkpatrick, *et al.* [156] (hereafter K14). This study measured the CO(J=1→0) emission line from 24 galaxies in the 5MUSES sample using the Redshift Search Receiver (RSR) on the Large Millimetre Telescope (LMT). The LMT is a relatively new telescope located in Volcan Sierra Negra, Mexico. It has a 50 m dish, but only a 32.5 m subsection was operational during the early science phase. Their sample was selected based on the infrared luminosity such that the integration time for the CO(J=1→0) emission line would be less than 90 min. Out of the 24 galaxies, 17 had detections above $3\,\sigma$. The properties of these galaxies are given in Appendix E.3.

The distribution of the general 5MUSES sample is compared to our sample galaxies and those from K14 in Fig. 6.1. Since K14 selected their sample for short integration times, their sample is biased towards sources with high $L_{\rm IR}$. Our samples complement those from K14 since they tend to have lower $L_{\rm IR}$ and z. Together, the combined distribution is similar to the original 5MUSES sample, except that no ULIRGs were selected since our focus was on main-sequence galaxies.

IR data from *Spitzer*

Infrared photometry data was available for the entire sample since 5MUSES lies within the SWIRE and XFLS fields. This data was collected with the Infrared Array Camera (IRAC, 3.6–8.0 µm) on the *Spitzer Space Telescope*. In addition, Y. Wu, *et al.* [25] (hereafter W10) measured photometry data with the Multiband Imaging Photometer for *Spitzer* (MIPS) at 24 µm, 70 µm and 160 µm for 100%, 90% and 54% of the sources, respectively, and low resolution spectra from 5.5–35 µm using the Infrared Spectrograph (IRS). W10 then measured the properties of the PAH emission using two different methods: by fitting a spline to the plateaus between the PAH features to isolate the PAH emission and by using the PAHFIT software package (J. Smith, *et al.* [141]). They found similar results using both techniques, but the values listed in Table 6.1 were calculated using PAHFIT. W10 also fit spectral energy density (SED) models to the mid-IR spectra from IRAC and MIPS to estimate the infrared luminosity ($L_{\rm IR}$). The infrared luminosity and the equivalent width of the 6.2 µm PAH feature from W10 are also listed in Table 6.1.

Using the data from W10, the star formation rate (SFR) was calculated from the

Table 6.1: Sample galaxies.

ID[a] #	RA (J2000)	DEC (J2000)	$z_{\rm IR}^{b,c}$	$\rm EW_{6.2}{}^{c}$ (µm)	$\log_{10}\left(\frac{L_{\rm IR}}{\rm L_\odot}\right)^{c,d}$
20	02h19'09.6"	−05°25'12.9"	0.098[b]	< 0.194	10.74 ± 0.02
22	02h19'16.1"	−05°57'27.0"	0.103[b]	0.198 ± 0.027	10.71 ± 0.05
28	02h19'53.0"	−05°18'24.2"	0.072[b]	0.781 ± 0.019	10.93 ± 0.03
36	02h21'47.9"	−04°46'13.5"	0.025[b]	0.809 ± 0.035	9.15 ± 0.02
64	02h25'48.2"	−05°00'51.5"	0.150[a]	0.297 ± 0.051	11.19 ± 0.04
66	02h26'00.0"	−05°01'45.3"	0.205[b]	0.916 ± 0.027	11.39 ± 0.04
75	02h27'41.6"	−04°56'50.6"	0.055[b]	0.627 ± 0.004	10.53 ± 0.03
86	10h36'46.4"	+58°43'30.6"	0.140[b]	0.549 ± 0.020	10.94 ± 0.03
106	10h44'38.2"	+56°22'10.8"	0.025[a]	0.509 ± 0.027	10.49 ± 0.05
107	10h44'54.1"	+57°44'25.8"	0.118[a]	0.585 ± 0.096	10.99 ± 0.02
118	10h49'07.2"	+56°57'15.4"	0.072[a]	0.805 ± 0.014	10.65 ± 0.03
123	10h50'06.0"	+56°15'00.0"	0.119[b]	0.714 ± 0.097	11.14 ± 0.04
146	10h59'03.5"	+57°21'55.1"	0.119[b]	< 0.261	10.87 ± 0.05
152	11h01'33.8"	+57°52'06.6"	0.277[b]	0.509 ± 0.057	11.84 ± 0.04
185	16h08'58.4"	+55°30'10.3"	0.066[a]	0.586 ± 0.104	10.34 ± 0.02
187	16h09'07.6"	+55°24'28.4"	0.065[a]	0.670 ± 0.003	10.54 ± 0.03
188	16h09'08.3"	+55°22'41.5"	0.084[a]	0.824 ± 0.056	10.65 ± 0.02
191	16h09'31.6"	+54°18'27.4"	0.082[a]	0.497 ± 0.033	10.61 ± 0.04
192	16h09'37.5"	+54°12'59.3"	0.086[a]	0.681 ± 0.018	10.66 ± 0.02
196	16h12'23.4"	+54°03'39.2"	0.138[b]	0.839 ± 0.136	11.07 ± 0.03
197	16h12'33.4"	+54°56'30.5"	0.083[a]	0.560 ± 0.083	10.66 ± 0.04
198	16h12'41.1"	+54°39'56.8"	0.035[b]	0.841 ± 0.078	9.51 ± 0.03
200	16h12'50.9"	+53°23'05.0"	0.048[b]	0.405 ± 0.074	10.40 ± 0.05
202	16h12'54.2"	+54°55'25.4"	0.065[b]	0.624 ± 0.015	10.59 ± 0.01
294	17h12'32.4"	+59°21'26.2"	0.210[b]	0.507 ± 0.006	11.59 ± 0.04
297	17h13'16.6"	+58°32'34.9"	0.079[b]	0.780 ± 0.020	10.34 ± 0.04
302	17h14'46.4"	+59°33'59.8"	0.129[a]	0.637 ± 0.002	11.11 ± 0.02
310	17h17'11.1"	+60°27'10.0"	0.110[a]	0.488 ± 0.053	10.78 ± 0.06
315	17h19'33.3"	+59°27'42.7"	0.139[b]	0.495 ± 0.005	11.28 ± 0.07
316	17h19'44.9"	+59°57'07.1"	0.069[b]	0.753 ± 0.005	10.73 ± 0.05
317	17h20'43.3"	+58°40'26.9"	0.125[b]	0.498 ± 0.006	11.14 ± 0.03
319	17h21'59.3"	+59°50'34.2"	0.028[b]	0.387 ± 0.031	9.78 ± 0.03
328	17h25'46.8"	+59°36'55.3"	0.035[b]	0.554 ± 0.041	10.49 ± 0.04
329	17h25'51.3"	+60°11'38.9"	0.029[a]	0.454 ± 0.005	10.25 ± 0.03

Note: The values for the galaxies from A. Kirkpatrick, *et al.* [156] are given in Table E.1.

[a] The identification number from 5MUSES.

[b] Redshifts from either (a) NASA/IPAC Extragalactic Database, or (b) the IRS spectra.

[c] Values from Y. Wu, *et al.* [25].

[d] Integrated from 5–1000 µm.

Sample galaxies (*continued*).

ID #	$\log_{10}\left(\frac{\mathrm{SFR}}{\mathrm{M}_\odot\,\mathrm{yr}^{-1}}\right)^e$	$\log_{10}\left(\frac{M_*}{\mathrm{M}_\odot}\right)^f$	$\log_{10}\left(\frac{\mathrm{sSFR}}{\mathrm{Gyr}^{-1}}\right)^g$	$\log_{10}\left(\frac{\mathrm{sSFR_{MS}}}{\mathrm{Gyr}^{-1}}\right)^h$
20	0.90 ± 0.02	10.37 ± 0.12	-0.47 ± 0.13	-0.85
22	0.87 ± 0.05	10.98 ± 0.20	-1.11 ± 0.21	-0.84
28	1.09 ± 0.03	10.71 ± 0.16	-0.63 ± 0.16	-0.87
36	-0.69 ± 0.02	8.93 ± 0.11	-0.63 ± 0.11	-0.92
64	1.35 ± 0.04	10.70 ± 0.18	-0.36 ± 0.18	-0.80
66	1.55 ± 0.04	10.98 ± 0.09	-0.44 ± 0.10	-0.75
75	0.69 ± 0.03	10.22 ± 0.20	-0.53 ± 0.20	-0.89
86	1.10 ± 0.03	10.67 ± 0.09	-0.57 ± 0.10	-0.81
106	0.65 ± 0.05	10.74 ± 0.15	-1.10 ± 0.16	-0.92
107	1.15 ± 0.02	11.03 ± 0.07	-0.89 ± 0.08	-0.83
118	0.81 ± 0.03	10.10 ± 0.11	-0.30 ± 0.12	-0.87
123	1.30 ± 0.04	11.12 ± 0.09	-0.83 ± 0.10	-0.83
146	1.03 ± 0.05	10.73 ± 0.02	-0.71 ± 0.05	-0.83
152	2.00 ± 0.04	11.41 ± 0.15	-0.41 ± 0.16	-0.69
185	0.50 ± 0.02	10.68 ± 0.08	-1.19 ± 0.08	-0.88
187	0.70 ± 0.03	10.29 ± 0.10	-0.59 ± 0.10	-0.88
188	0.81 ± 0.02	10.59 ± 0.08	-0.78 ± 0.08	-0.86
191	0.77 ± 0.04	10.62 ± 0.16	-0.86 ± 0.16	-0.86
192	0.82 ± 0.02	10.80 ± 0.09	-0.99 ± 0.09	-0.86
196	1.23 ± 0.03	10.60 ± 0.08	-0.38 ± 0.09	-0.81
197	0.82 ± 0.04	10.99 ± 0.10	-1.17 ± 0.11	-0.86
198	-0.33 ± 0.03	9.30 ± 0.20	-0.64 ± 0.20	-0.91
200	0.56 ± 0.05	10.48 ± 0.16	-0.92 ± 0.17	-0.89
202	0.75 ± 0.01	11.22 ± 0.10	-1.47 ± 0.10	-0.88
294	1.75 ± 0.04	11.49 ± 0.10	-0.75 ± 0.11	-0.75
297	0.50 ± 0.04	10.88 ± 0.08	-1.38 ± 0.09	-0.87
302	1.27 ± 0.02	11.16 ± 0.06	-0.90 ± 0.06	-0.82
310	0.94 ± 0.06	10.65 ± 0.13	-0.72 ± 0.14	-0.84
315	1.44 ± 0.07	10.96 ± 0.14	-0.52 ± 0.16	-0.81
316	0.89 ± 0.05	10.55 ± 0.08	-0.66 ± 0.09	-0.87
317	1.30 ± 0.03	10.91 ± 0.06	-0.62 ± 0.06	-0.82
319	-0.06 ± 0.03	9.93 ± 0.06	-0.99 ± 0.07	-0.91
328	0.65 ± 0.04	10.96 ± 0.08	-1.31 ± 0.09	-0.91
329	0.41 ± 0.03	10.67 ± 0.05	-1.26 ± 0.06	-0.91

[e] Star formation rate. Derived from L_{IR} in Eqn. 6.4.
[f] Stellar masses from Y. Shi, *et al.* [169].
[g] Specific star formation rate. Derived from SFR and M_* in Eqn. 6.5.
[h] Main sequence star formation rate. Derived from redshift in Eqn. 6.6.

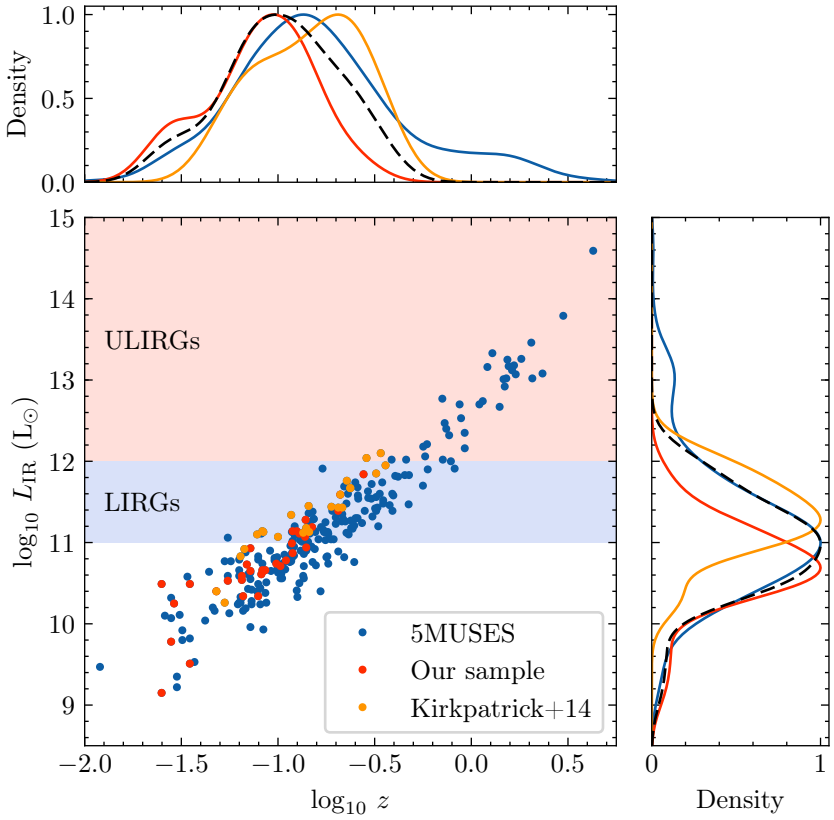

Figure 6.1: Distribution of our sample galaxies galaxies compared to the general 5MUSES sample and those selected by A. Kirkpatrick, *et al.* [156]. Here, $L_{\rm IR}$ is the IR luminosity integrated from 5–1000 µm and z is redshift (both from Y. Wu, *et al.* [25]). The density plots on the top and right-hand side were generated by a kernel density estimation (KDE) and they represent the normalised probability density function of z and $L_{\rm IR}$, respectively. The dashed black line represents the combined distribution.

infrared luminosity using:

$$\left(\frac{\mathrm{SFR}}{\mathrm{M}_\odot\ \mathrm{yr}^{-1}}\right) = 1.509 \times 10^{-10} \left(\frac{L_{\mathrm{IR}}}{L_\odot}\right) . \tag{6.4}$$

Eqn. 6.4 was taken from K14 who adopted this ratio by assuming a Kroupa initial mass function (IMF) and a constant star formation rate for the past 100 Myr (E. Murphy, *et al.* [170]). The specific star formation rate (sSFR) was then found by dividing this value by the stellar mass (M_*) of the galaxy:

$$\mathrm{sSFR} = \frac{\mathrm{SFR}}{M_*} . \tag{6.5}$$

The masses were calculated by Y. Shi, *et al.* [169], who estimated M_* by fitting a population synthesis model to the SED, assuming a Charbrier IMF. This was then compared to the main-sequence[4] specific star formation rate ($\mathrm{sSFR_{MS}}$),

$$\mathrm{sSFR_{MS}} = 38 \times \left(\frac{t_{\mathrm{cosmic}}}{\mathrm{Gyr}^{-1}}\right)^{-1} , \tag{6.6}$$

to get the relative star formation rate, $\mathrm{sSFR/sSFR_{MS}}$, which can be used to identify starbursting galaxies. Eqn. 6.6 was taken from K14 who derived this ratio by altering the relationship between sSFR and redshift from D. Elbaz, *et al.* [172] to use a Kroupa IMF instead of a Salpeter IMF. The stellar masses, SFR, sSFR and $\mathrm{sSFR_{MS}}$ are all listed in Table 6.1.

Galaxy classification

The classification of the sample galaxies was initially taken from the Sloan Digital Sky Survey (SDSS), which automatically classifies the galaxies based on their optical spectra. However, SDSS classifications were not available for 11 of the 34 sample galaxies. For these galaxies, the AGN-dominated galaxies were first identified based on the equivalent width of the 6.2 µm PAH feature ($\mathrm{EW_{6.2}}$). G. Magdis, *et al.* [142] found that the L_{IR} from sources with $\mathrm{EW_{6.2}} \leq 0.2$ µm is typically dominated by AGN activity, while at least 50% of the L_{IR} is due to star formation for sources with $\mathrm{EW_{6.2}} > 0.2$ µm. To be on the safe side, all of the 5MUSES galaxies with $\mathrm{EW_{6.2}} \leq 0.4$ were classified as AGN-dominated. From the remaining non-AGN dominated galaxies, the starburst galaxies were separated from the regular star-forming

[4]There is a strong correlation between sSFR and stellar mass in star-forming galaxies from $0 < z < 2$ (e.g., E. Daddi, *et al.* [171]). Galaxies on this trend line are known as *main-sequence* galaxies, while galaxies above and below are known as *starburst* and *quiescent*, respectively.

galaxies based on the specific star formation rate. They were classified as starburst if $\mathrm{sSFR}/\mathrm{sSFR}_{\mathrm{MS}} > 2$. The classification results are listed in Table 6.2 and the classification metrics are compared in Fig. 6.2. Based on Fig. 6.2, the classification metrics seem to be consistent, with only a few inconsistent galaxies that are very close to the threshold values.

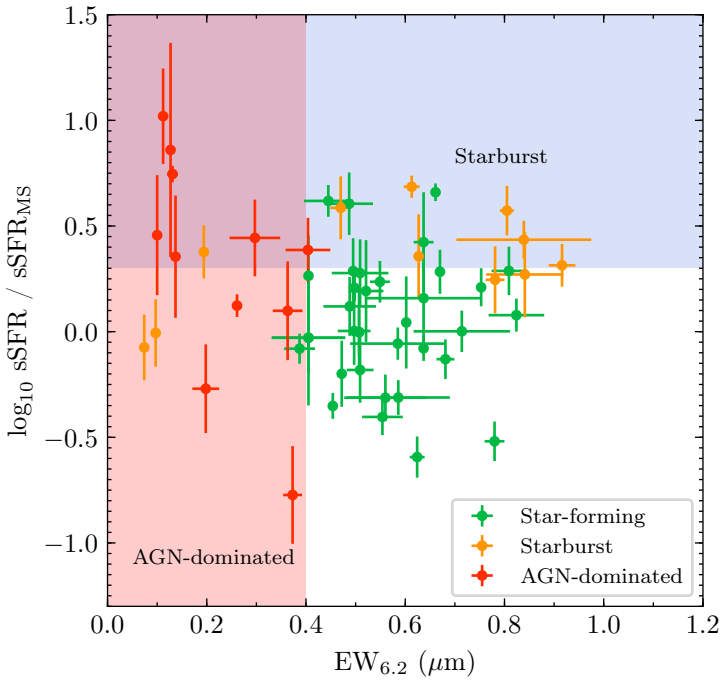

Figure 6.2: Galaxy classification compared to the relative star formation rate and the equivalent width of the 6.2 µm PAH feature.

Optical data from SDSS

Optical spectra from SDSS was available for 23 of the 34 sample galaxies. This was used to estimate the metallicity. For 5 of the sample galaxies, $12 + \log_{10}(\mathrm{O/H})$ metallicity values were available from C. Tremonti, *et al.* [173][5], but this study only covered up to SDSS digital release #7 (DR7). For the rest of the galaxies, the optical spectra were downloaded from SDSS DR13 and then two different metallicity metrics were calculated:

$$\log_{10}\left(\frac{[\mathrm{N\,II}]\,\lambda6583}{\mathrm{H}\alpha}\right) \tag{6.7}$$

and

$$\log_{10}\left(\frac{[\mathrm{O\,III}]\,\lambda5007}{\mathrm{H}\beta}\right). \tag{6.8}$$

[5]Data from: https://wwwmpa.mpa-garching.mpg.de/SDSS/DR7/oh.html

Table 6.2: Galaxy classification.

ID	Classification† from			Combined
#	SDSS	$EW^{\ddagger}_{6.2}$	$sSFR/sSFR_{MS}{}^{*}$	Classification
20	SB	→	→	SB
22	AGN	→	→	AGN
28	SB	→	→	SB
36	–	SF	SF	SF
64	–	AGN	→	AGN
66	–	SF	SB	SB
75	–	SF	SB	SB
86	–	SF	SF	SF
106	SF	→	→	SF
107	SF	→	→	SF
118	SB	→	→	SB
123	SF	→	→	SF
146	AGN	→	→	AGN
152	–	SF	SF	SF
185	–	SF	SF	SF
187	SF	→	→	SF
188	SF	→	→	SF
191	G	→	→	SF
192	SF	→	→	SF
196	SB	→	→	SB
197	SF	→	→	SF
198	SB	→	→	SB
200	SF	→	→	SF
202	SF	→	→	SF
294	–	SF	SF	SF
297	SF	→	→	SF
302	–	SF	SF	SF
310	–	SF	SF	SF
315	–	SF	SF	SF
316	SF	→	→	SF
317	SF	→	→	SF
319	SF	→	→	SF
328	SF	→	→	SF
329	SF	→	→	SF

† Classified as star-forming (SF), starburst (SB), or AGN-dominated (AGN).

‡ Identified as AGN dominated if $EW_{6.2} \leq 0.4$ µm, following G. Magdis, *et al.* [142].

* Identified as starburst if $sSFR/sSFR_{MS} > 2$.

An example spectrum from M028 is shown in Fig. 6.3. The baseline continuum spectrum was removed by windowing the spectral lines and fitting a 1st order polynomial. The integrated flux was then calculated by fitting a Gaussian distribution to the data.

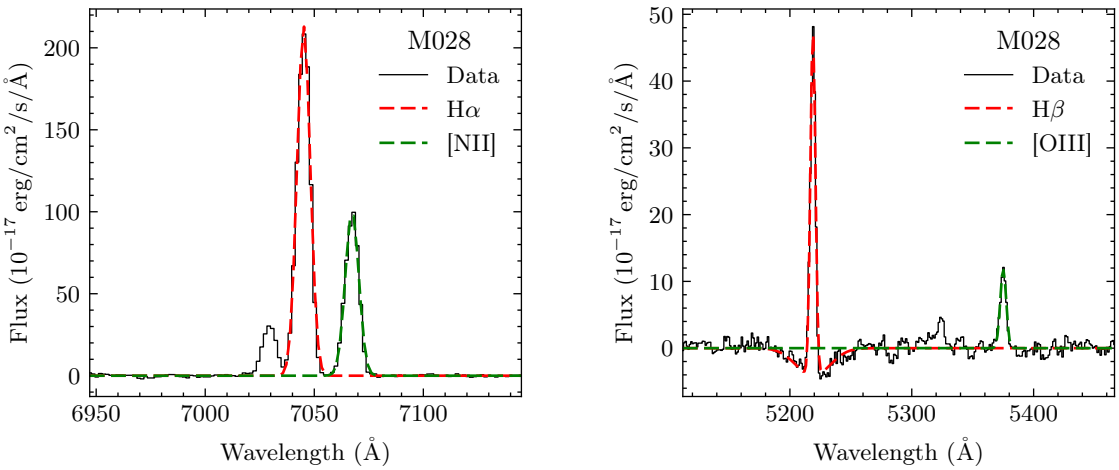

(a) [N II] λ6583 vs. Hα (b) [O III] λ5007 vs. Hβ

Figure 6.3: Metallicity metrics derived from the optical spectra of M028. The baseline continuum was removed in both plots and Gaussian distributions were fit to the data to estimate the integrated flux.

Using these two metallicity metrics, the $O3N2$ index was calculated:

$$O3N2 \equiv \log_{10}\left(\frac{[\mathrm{O\,III}]\,\lambda5007/\mathrm{H}\beta}{[\mathrm{N\,II}]\,\lambda6583/\mathrm{H}\alpha}\right). \tag{6.9}$$

This was then used to estimate the 12+log(O/H) metallicity value using the empirical formula from Pettini and Pagel [174]:

$$12 + \log \mathrm{O/H} = 8.73 - 0.32 \times O3N2\,. \tag{6.10}$$

These values are listed alongside those from C. Tremonti, *et al.* [173] in Table 6.3. Note that this was only applied to the star-forming galaxies because AGN activity renders Eqn. 6.10 unreliable.

In Fig. 6.4, the galaxy classifications are compared to the two metallicity metrics from Table 6.3 (i.e., log([O III]/Hβ) and log([N II]/Hα)). The classifications mostly agree with the empirical results from Veilleux and Osterbrock [175].

Table 6.3: Metallicity of the sample galaxies.

ID #	$\log_{10}\left(\frac{[\mathrm{N\,II}]\,\lambda6583}{\mathrm{H}\alpha}\right)$	$\log_{10}\left(\frac{[\mathrm{O\,III}]\,\lambda5007}{\mathrm{H}\beta}\right)$	$12+\log_{10}(\mathrm{O/H})$	
			from $O3N2^{*}$	from Tremonti†
20	-0.501 ± 0.005	0.544 ± 0.011	8.395 ± 0.250	–
28	-0.318 ± 0.001	-0.569 ± 0.028	8.811 ± 0.250	–
36	–	–	–	–
64	–	–	–	–
66	–	–	–	–
22	-0.111 ± 0.003	0.898 ± 0.006	~~8.407~~ ± ~~0.250~~§	–
75	–	–	–	–
86	–	–	–	–
106	-0.204 ± 0.002	-0.493 ± 0.028	8.822 ± 0.250	–
107	-0.376 ± 0.019	–	–	–
118	-0.381 ± 0.004	-0.372 ± 0.032	8.727 ± 0.250	9.039
123	-0.135 ± 0.009	–	–	–
146	0.052 ± 0.009	0.934 ± 0.016	~~8.448~~ ± ~~0.250~~§	–
152	–	–	–	–
185	–	–	–	–
187	-0.289 ± 0.005	-0.539 ± 0.057	8.810 ± 0.250	–
188	-0.417 ± 0.005	-0.608 ± 0.038	8.791 ± 0.250	–
191	–	–	–	–
192	-0.331 ± 0.007	-0.291 ± 0.059	8.717 ± 0.250	–
196	-0.356 ± 0.003	-0.217 ± 0.029	8.685 ± 0.250	–
197	-0.322 ± 0.006	-0.581 ± 0.083	8.813 ± 0.250	–
198	-0.703 ± 0.002	0.163 ± 0.003	8.453 ± 0.250	–
200	–	–	–	–
202	–	–	–	–
294	–	–	–	–
297	-0.259 ± 0.007	-0.518 ± 0.093	8.813 ± 0.250	9.143
302	–	–	–	–
310	–	–	–	–
315	–	–	–	–
316	-0.308 ± 0.008	-0.176 ± 0.045	8.688 ± 0.250	–
317	-0.306 ± 0.006	–	–	–
319	-0.408 ± 0.005	-0.094 ± 0.037	8.629 ± 0.250	8.920
328	-0.269 ± 0.005	-0.623 ± 0.091	8.843 ± 0.250	9.213
329	-0.279 ± 0.005	–	–	9.091

Note: The values for the galaxies from A. Kirkpatrick, *et al.* [156] are given in Table E.2.

* Calculated from the $O3N2$ index (Eqn. 6.10).

† Values from C. Tremonti, *et al.* [173]. Only includes galaxies contained within SDSS DR7.

§ These galaxies are dominated by AGN activity, making the metallicity estimation unreliable.

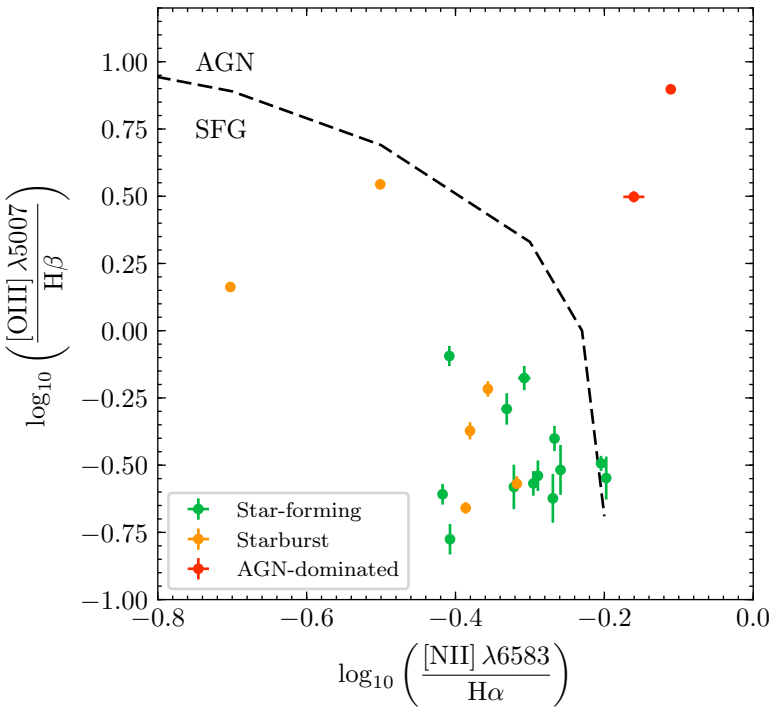

Figure 6.4: Galaxy classification compared to the metallicity metrics that were derived from optical SDSS data. The dashed line represents the empirical division between AGN-dominated galaxies and star-forming galaxies from Veilleux and Osterbrock [175].

6.3 CO(J=1→0) observations with IRAM 30 m

The CO(J=1→0) emission line[6] was observed using the IRAM 30 m telescope on Pico Veleta, Spain. The EMIR E090 frontend receiver (M. Carter, *et al.* [69]) was used for all of the measurements, which is a sideband separating (2SB) receiver with a 73–117 GHz RF tuning range, a 4 GHz IFBW for each sideband, and an average SSB noise temperature of 50 K. The down-converted signals were measured using the WILMA backend, an autocorrelator with 2 MHz resolution. For our sample galaxies, the redshifted CO(J=1→0) emission line ranged from 90–112 GHz. The integration time required for a detection above $\sim 3\,\sigma$ was estimated using IRAM's online time estimator[7] and ranged between 1 and 8 hours, with the average galaxy requiring 3.5 hrs[8].

Prior to observing each galaxy, the telescope was calibrated using a strong radio source, such as a planet, to set the focus of the secondary mirror and the pointing

[6] CO(J=1→0) has a rest frequency of $\nu_{\rm rest} = 115.271$ GHz.
[7] Online: http://www.iram.es/nte/
[8] This is much longer than K14 who only observed galaxies that required less than 90 min with a similar telescope.

of the dish. This was then repeated with another bright source closer to the target galaxy and again every 2 hours during long integrations. (The shortest observation time was 45 minutes, while the longest took over 7 hours.) All of the sample galaxies were observed using the wobbler-switching mode, where the secondary mirror chops between the target and empty sky in order to calibrate for atmospheric effects.

The CO observations were carried out in three runs: 7 nights in 2015, 3 days in June 2016, and 7 nights September 2016[9].

Data analysis

All of the measurement data was analysed using IRAM's CLASS/GILDAS software[10]. To begin, corrupted scans were identified from the spectral data and dropped. The average was then taken of the remaining data with a weighting factor of $\Delta t \Delta\nu / T_{\rm sys}^2$ and the resulting spectrum was smoothed by combining the frequency bins in a 16:1 ratio. This resulted in an average channel width of ∼70 km/s. The baseline continuum was then removed by fitting and subtracting a 1$^{\rm st}$ order polynomial. The residual error from this fitting was calculated as the baseline root-mean-square (RMS) error $\sigma_{\rm base}$ in units K.

A Gaussian curve was fit to the spectral data to identify the CO(J=1→0) emission line (e.g., Fig. 6.5). The area of this curve is the integrated line intensity $S'_{\rm CO}\Delta v$ in units K km/s. This value was converted into the integrated line flux $S_{\rm CO}\Delta v$ in units Jy km/s by multiplying $S'_{\rm CO}\Delta v$ by the sensitivity of the telescope: $S/T_{\rm A}^* = 6.2$ Jy/K at 100 GHz [176]. The measurement error was estimated by

$$\epsilon_{\rm obs}\Delta v = \frac{\sigma_{\rm base}\, W_{\rm FWHM}}{\sqrt{W_{\rm FWHM}/\Delta\omega_{\rm ch}}} \tag{6.11}$$

where $\Delta\omega_{\rm ch}$ is the width of each channel and $W_{\rm FWHM}$ is the full width at half maximum (FWHM) of the Gaussian curve. The signal-to-noise ratio[11] was then calculated by:

$$\mathrm{S/N} = \frac{S'_{\rm CO}\Delta v}{\epsilon_{\rm obs}\Delta v}\,. \tag{6.12}$$

If no obvious peak was found or if S/N < 5, the source was classified as a non-detection. To set an upper limit on these non-detections, the baseline error was used

[9] I only took part in the September 2016 observing run.

[10] Online: https://www.iram.fr/IRAMFR/GILDAS/

[11] There are two different ways that the measurement error for emission lines is typically defined: (1) as it is here, and (2) by dividing the peak of the emission line by $\sigma_{\rm base}$. The first technique is more accurate since it takes into account the width of the emission line; however, it results in a S/N that is approximately 1.5 times higher than the second technique.

to set $S'_{\rm CO}\Delta v = 5 \times \epsilon_{\rm obs}\Delta v$ (assuming an average width of $W_{\rm FWHM} = 400$ km s^{-1}).

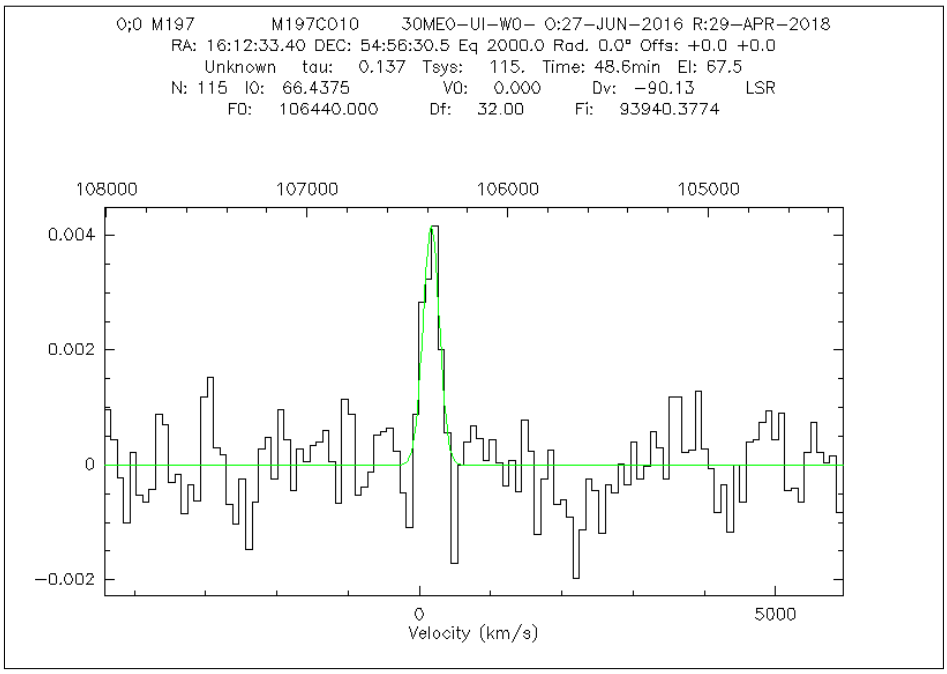

Figure 6.5: Output from the CLASS software for M197. In this figure, the baseline continuum has already been removed and a Gaussian distribution (green) has been fit to the data. The y-axis is flux in units of mK, and the top x-axis is frequency in units of MHz.

The redshift was also calculated from the peak of the CO(J=1→0) emission line by:

$$z_{\rm obs} = \frac{\nu_{\rm rest}}{\nu_{\rm obs}} - 1 \tag{6.13}$$

where $\nu_{\rm rest} = 115.271$ GHz is the CO(J=1→0) rest frequency. The discrepancy between this value and the value found from the IR measurements was then defined as:

$$\epsilon_z = \frac{|z_{\rm obs} - z_{\rm IR}|}{1 + z_{\rm IR}}\,. \tag{6.14}$$

Similar to K14, sources with $\epsilon_z \geq 0.15$ % were classified non-detections.

Derived quantities

The CO line luminosity, in units K km s^{-1} pc^2, was calculated from the integrated line flux using (Solomon and Vanden Bout [155]):

$$L'_{\rm CO} = 3.25 \times 10^7 \cdot S_{\rm CO}\Delta v \cdot \frac{D_{\rm L}^2}{\nu_{\rm obs}^2 (1+z)^3} \tag{6.15}$$

where $D_{\rm L}$ is the luminosity distance[12] in units of MPc, $\nu_{\rm obs}$ is the observed frequency in units of GHz, and z is redshift. Aperture corrections were not required for most of the sample galaxies since the sources were smaller than the main beam of the telescope (approximately 22" at 115 GHz). This can be seen in the SDSS images of the sample galaxies that are provided in Appendix E.2.

The CO luminosity was then combined with the IR luminosity to calculate the star formation efficiency (SFE), defined here as:

$$\mathrm{SFE} \equiv \frac{L_{\rm IR}}{L'_{\rm CO}}\,. \tag{6.16}$$

Note that SFE is typically defined as the ratio of new stars to the molecular gas reservoir: $\mathrm{SFE} \equiv \mathrm{SFR}/M(\mathrm{H_2})$. The definition in Eqn. 6.16 represents the same ratio, but it avoids any issues with converting $L'_{\rm CO}$ to $M(\mathrm{H_2})$ or $L_{\rm IR}$ to SFR.

6.4 Additional SF studies

The intermediate redshift galaxies from 5MUSES were supplemented with nearby spiral galaxies from SINGS and NGLS as well as local and high-z ULIRGs. These are described below.

SINGS + NGLS

The SIRTF Nearby Galaxy Survey (SINGS, R. Kennicutt, *et al.* [177]) observed the mid-IR (MIR) spectra of 75 galaxies using *Spitzer Space Telescope*[13]. The observations included imaging and low-resolution spectroscopy of each galaxy as well as high-resolution spectroscopy of the galactic centres and a few extranuclear infrared emitting regions. The sample included galaxies at distances less than 30 MPc, with an average of ∼9.5 Mpc. None of the galaxies were very bright ($L_{\rm IR} < 3 \times 10^{11}\,\mathrm{L_\odot}$) and none showed signs of AGN activity within the IR data. J. Smith, *et al.* [141] presented the low-resolution *Spitzer* IRS spectra (5–38 µm) for a subset of 59 galaxies (targeting PAH emission) and D. Dale, *et al.* [178] presented far-IR spectra using *Herschel* for a subset of 57 galaxies (KINGFISH). C. Wilson, *et al.* [179] measured the CO(J=3→2) emission line from 155 galaxies with the HARP-B receiver on the James Clerk Maxwell Telescope as a part of the Nearby Galaxies Legacy Survey (NGLS). 47 of these galaxies overlap with SINGS. As suggested by C. Wilson, *et al.* [179], we

[12]The luminosity distance was calculated from the redshift using a flat ΛCDM model with $H_0 = 70$ km s^{-1} MPc^{-1}, $\Omega_\Lambda = 0.73$, and $\Omega_{\rm m} = 0.27$.

[13]The *Spitzer Space Telescope* was originally named the *Space Infrared Telescope Facility (SIRTF).*

used the line ratio $r_{32/10} = 0.18$ to convert these results to CO(J=1→0). The aperture of the $L'_{\rm CO}$ data was also corrected to match the aperture used to collect the PAH data[14].

High-z ULIRGs

A. Pope, *et al.* [157] measured the CO(J=2→1) emission line from three z∼1 ULIRGs using the IRAM Plateau de Bure Interferometer (PdBI). Two out of the three galaxies were detected, and a line ratio of $r_{21/10} = 0.8 \pm 0.1$ (M. Aravena, *et al.* [180], D. Frayer, *et al.* [181]) was used to convert to CO(J=1→0). A. Pope, *et al.* [157] also measured the mid-IR emission from 6 other ULIRGs to characterise the PAH emission. They combined their new CO and PAH emission data with other studies (B. Magnelli, *et al.* [182], D. Frayer, *et al.* [183], A. Pope, *et al.* [184], C. Casey, *et al.* [185], M. Aravena, *et al.* [180], M. Bothwell, *et al.* [186], R. Ivison, *et al.* [187], C. Carilli, *et al.* [188], D. Riechers, *et al.* [189]) to create a sample of 12 ULIRGs around z∼1, all of which have $L'_{\rm CO}$, $L_{\rm IR}$ and $L_{6.2}$ measurement data. Similar to A. Pope, *et al.* [157], I also include 14 local ULIRGs with CO and PAH observations from L. Armus, *et al.* [190] and V. Desai, *et al.* [191]. Many of these local ULIRGs, however, have strong AGN contributions.

6.5 Results and discussion

CO(J=1→0) observation results

Out of the 34 sample galaxies, there were 9 non-detections: 3 where no emission line was found and 6 with S/N < 5. Two additional sources were classified as non-detections because the measured CO(J=1→0) line was detected at the wrong frequency, i.e., $|z_{\rm CO} - z_{\rm IR}|/(1+z_{\rm IR}) > 0.15\%$. This left 23 positive detections from our sample and 40 positive detections when combined with A. Kirkpatrick, *et al.* [156]. Overall, the combined sample contains 27 star-forming galaxies, 7 starburst, and 6 AGN-dominated sources. All of the observation results are listed in Table 6.4, the measured CO spectra from each sample galaxy are plotted in Appendix E.1, and the CO results from A. Kirkpatrick, *et al.* [156] are given in Appendix E.3.

Correlations between molecular gas and dust

The CO(J=1→0) luminosity is compared to $L_{\rm IR}$ in Fig. 6.6a. Since $L'_{\rm CO}$ traces the molecular gas and $L_{\rm IR}$ traces the star formation rate, the relationship found in

[14] Values from I. Cortzen, *et al.* [5].

Table 6.4: CO(J=1→0) observation results.

5MUSES ID	$S_{\mathrm{CO}}\Delta v$ (Jy km s^{-1})	S/N	$\log_{10}\left(\frac{L'_{\mathrm{CO}}}{\mathrm{K\,km\,s^{-1}pc^2}}\right)$	$\log_{10}\left(\frac{\mathrm{SFE}}{\mathrm{L_\odot/K\,km\,s^{-1}pc^2}}\right)$
M020	< 1.45	3.7	< 8.82	< 1.90
M022	1.46 ± 0.27	5.4	8.86 ± 0.08	1.82 ± 0.09
M028	6.68 ± 0.98	6.8	9.21 ± 0.06	1.70 ± 0.07
M036	< 2.78	–	< 7.90	< 1.23
M064	< 1.37	–	< 9.18	< 1.99
M066	2.56 ± 0.32	8.1	9.73 ± 0.05	1.64 ± 0.07
M075	3.18 ± 0.55	5.7	8.65 ± 0.08	1.86 ± 0.08
M086	2.11 ± 0.32	6.5	9.30 ± 0.07	1.62 ± 0.07
M106	14.55 ± 1.41	10.3	8.62 ± 0.04	1.85 ± 0.07
M107	3.74 ± 0.55	6.8	9.40 ± 0.06	1.57 ± 0.07
M118	< 4.45	4.8	< 9.03	< 1.60
M123	2.53 ± 0.41	6.2	9.23 ± 0.07	1.88 ± 0.08
M146	< 1.40	5.6	< 8.98	< 1.87
M152	< 4.59	4.3	< 10.25	< 1.57
M185	3.26 ± 0.42	7.8	8.82 ± 0.06	1.50 ± 0.06
M187	< 4.79	4.7	< 8.97	< 1.54
M188	4.49 ± 0.56	8.0	9.17 ± 0.05	1.45 ± 0.06
M191	< 4.82	6.6	< 9.19	< 1.40
M192	3.97 ± 0.66	6.0	9.14 ± 0.07	1.50 ± 0.08
M196	2.08 ± 0.39	5.3	9.28 ± 0.08	1.77 ± 0.09
M197	7.47 ± 0.69	10.8	9.38 ± 0.04	1.25 ± 0.06
M198	< 2.23	–	< 8.10	< 1.39
M200	5.56 ± 0.86	6.4	8.77 ± 0.07	1.61 ± 0.08
M202	6.64 ± 1.12	6.0	9.12 ± 0.07	1.45 ± 0.07
M294	< 2.14	4.8	< 9.67	< 1.90
M297	3.46 ± 0.66	5.3	9.00 ± 0.08	1.31 ± 0.09
M302	7.71 ± 1.24	6.2	9.79 ± 0.07	1.30 ± 0.07
M310	3.33 ± 0.49	6.8	9.28 ± 0.06	1.47 ± 0.09
M315	3.90 ± 0.71	5.5	9.56 ± 0.08	1.70 ± 0.11
M316	< 5.97	3.7	< 9.12	< 1.58
M317	2.54 ± 0.42	6.1	9.28 ± 0.07	1.84 ± 0.08
M319	8.24 ± 1.29	6.4	8.47 ± 0.07	1.29 ± 0.07
M328	14.61 ± 1.92	7.6	8.91 ± 0.06	1.55 ± 0.07
M329	9.60 ± 1.09	8.8	8.57 ± 0.05	1.66 ± 0.06

Note: The values for the galaxies from A. Kirkpatrick, *et al.* [156] are given in Table E.3.

Fig. 6.6a acts as a proxy for the SK law. Orthogonal Distance Regression[15] (ODR) was used to fit a linear trend to this data:

$$\log_{10}\left(\frac{L'_{\rm CO}}{\rm K\ km\ s^{-1}\ pc^2}\right) = \alpha_1 + \beta_1 \cdot \log_{10}\left(\frac{L_{\rm IR}}{\rm L_\odot}\right) \tag{6.17}$$

with $(\alpha_1;\ \beta_1) = (1.44 \pm 0.78;\ 0.73 \pm 0.07)$ and a scatter[16] of $\sigma_1 = 0.19$ dex. Several of the outliers in Fig. 6.6a are marked with their 5MUSES ID number. This includes two star-forming galaxies that are below the trend line with lower than expected $L'_{\rm CO}$: M106 and M329. SDSS images (Appendix E.2) suggest that the CO emission from these two galaxies may have extended beyond the beam of the IRAM 30 m telescope. Instead of applying an aperture correction, which typically adds a very high level of uncertainty, these two galaxies were simply dropped and not used for the linear regression in Eqn. 6.17. Interestingly, M179, M225 and M275 all have higher than expected $L'_{\rm CO}$ despite being classified as AGN. Normally, we would expect a higher $L_{\rm IR}/L'_{\rm CO}$ ratio for these galaxies due to extra heat from the AGN. The AGNs in these galaxies could be quenching star formation and transitioning to a more quiescent phase. However, all of the starburst galaxies, are below the trend line, as expected. The $L_{\rm IR}-L'_{\rm CO}$ trend from M. Sargent, *et al.* [192] is also plotted in Fig. 6.6a: $(\alpha_1;\ \beta_1) = (0.54 \pm 0.02;\ 0.81 \pm 0.03)$. M. Sargent, *et al.* [192] calculated this value by fitting 52 main-sequence galaxies: 20 from the HERACLES (A. Leroy, *et al.* [193], A. Leroy, *et al.* [194], A. Leroy, *et al.* [195]) and 32 from COLD GASS (A. Saintonge, *et al.* [196]). The 5MUSES star-forming galaxies fit this trend with a scatter of $\sigma = 0.17$ dex, and the entire 5MUSES sample fits this trend with scatter of $\sigma = 0.20$ dex.

$L'_{\rm CO}$ is compared to PAH emission ($L_{6.2}$) in Fig. 6.6b. Again, this can act as a proxy for the SK law; although, it should be more robust since PAHs are likely destroyed by AGN activity. ODR was again used to fit a linear trend to this data:

$$\log_{10}\left(\frac{L'_{\rm CO}}{\rm K\ km\ s^{-1}\ pc^2}\right) = \alpha_2 + \beta_2 \cdot \log_{10}\left(\frac{L_{6.2}}{\rm L_\odot}\right). \tag{6.18}$$

with $(\alpha_2;\ \beta_2) = (-1.50 \pm 1.43;\ 1.24 \pm 0.16)$ and a scatter of $\sigma_2 = 0.31$ dex. This scatter is slightly higher than the scatter from the $L_{\rm IR} \rightarrow L'_{\rm CO}$ correlation, suggesting

[15] Orthogonal Distance Regression (ODR) attempts to minimise the orthogonal distance between each data point and the line of best fit. It was used because ODR can take into account errors in both x and y.

[16] The scatter is defined here as the root-mean-square error (RMSE) between the linear regression and the CO luminosity: $\sigma_1 = \sqrt{\left\langle [L'_{\rm CO} - (\alpha_1 + \beta_1\ \log_{10} L_{\rm IR})]^2 \right\rangle}$.

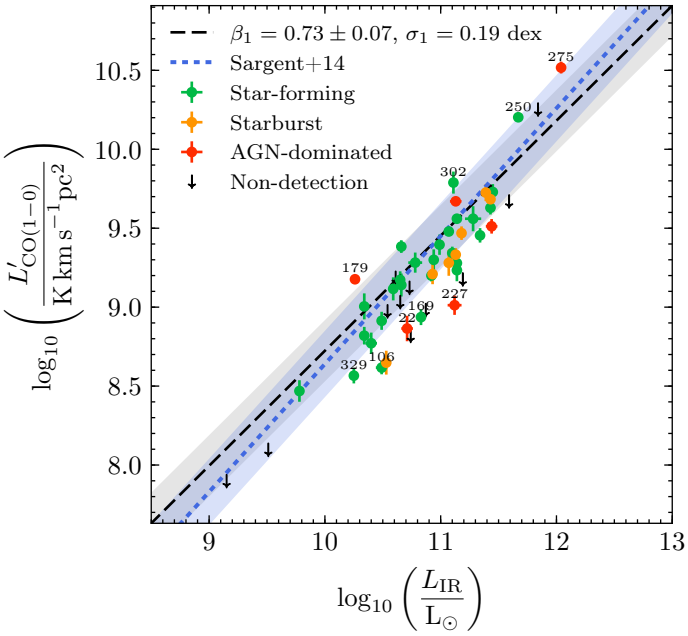

(a) L_{IR} as a tracer of L'_{CO}.

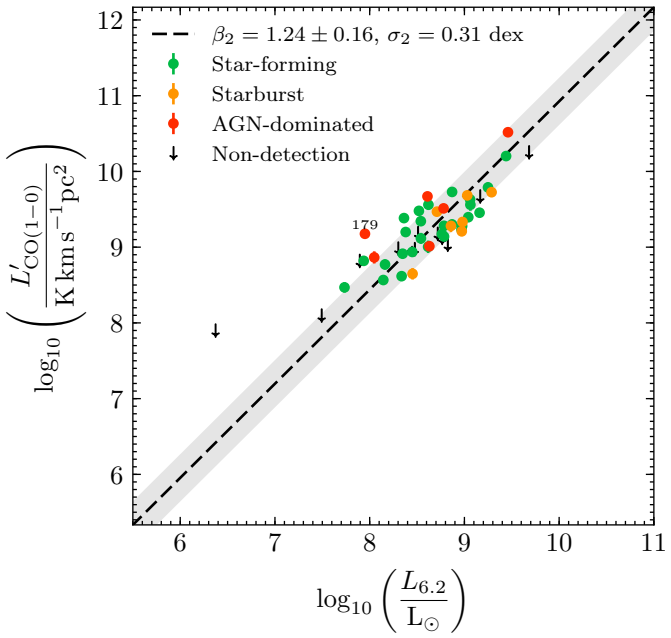

(b) $L_{6.2}$ as a tracer of L'_{CO}.

Figure 6.6: CO luminosity compared to dust emission. In both cases, the linear relationships were calculated using Orthogonal Distance Regression (ODR). The slopes β and scatters σ are listed in the legends. The grey regions represent one standard deviation above and below the linear regression. Several of the outliers are labelled with their 5MUSES ID numbers.

that $L_{\rm IR}$ is a better tracer of $L'_{\rm CO}$ than $L_{6.2}$ (at least for this sample). However, the scatter could also be higher due to the larger uncertainties on the $L_{6.2}$ values.

Five additional parameters were then added to see if they could improve either the $L_{\rm IR}$→$L'_{\rm CO}$ or the $L_{6.2}$→$L'_{\rm CO}$ estimation. These parameters were: metallicity, the relative PAH emission, the equivalent width of the 6.2 µm PAH feature, the $O3N2$ index, and the $O3N2'$ index, defined as:

$$O3N2' \equiv \log_{10}\left(\frac{[\mathrm{O\,III}]\,\lambda5007 \cdot [\mathrm{N\,II}]\,\lambda6583}{\mathrm{H}\alpha \cdot \mathrm{H}\beta}\right). \tag{6.19}$$

(Note that $O3N2'$ is not a conventional parameter; however, based on the shape of the empirical line that separates AGN and star-forming galaxies in Fig. 6.4, it might be able to loosely trace AGN activity.) In Fig. 6.7, the error from the previous two fittings is plotted against these additional parameters. The $O3N2'$ index was found to provide the largest improvement upon the $L'_{\rm CO}$ estimation (Fig. 6.7i and Fig. 6.7j). The linear regressions in these plots are:

$$\log_{10}\left(\frac{L'_{\rm CO}}{\mathrm{K\ km\ s^{-1}\ pc^2}}\right) = \alpha_1 + \beta_1 \cdot \log_{10}\left(\frac{L_{\rm IR}}{\mathrm{L_\odot}}\right) + \alpha_{11} + \beta_{11} \cdot O3N2' \tag{6.20}$$

with $(\alpha_{11};\ \beta_{11}) = (-0.22 \pm 0.07;\ -0.11 \pm 0.09)$ and

$$\log_{10}\left(\frac{L'_{\rm CO}}{\mathrm{K\ km\ s^{-1}\ pc^2}}\right) = \alpha_2 + \beta_2 \cdot \log_{10}\left(\frac{L_{6.2}}{\mathrm{L_\odot}}\right) + \alpha_{12} + \beta_{12} \cdot O3N2' \tag{6.21}$$

with $(\alpha_{12};\ \beta_{12}) = (0.15 \pm 0.15;\ 0.29 \pm 0.12)$. By including the $O3N2'$ index, the RMSE errors dropped by $\Delta\sigma_1 = -0.010$ and $\Delta\sigma_2 = -0.035$, which is only a modest improvement, especially considering only 16 galaxies had both $L'_{\rm CO}$ and $O3N2'$ values. Interestingly, the metallicity values did not improve the $L'_{\rm CO}$ estimation in either case (Fig. 6.7a and Fig. 6.7b), but only a very narrow range of metallicity values is contained with our sample since they are all dusty galaxies.

Compared to other SF studies

The nearby star-forming galaxies from SINGS+NGLS (R. Kennicutt, *et al.* [177], J. Smith, *et al.* [141], C. Wilson, *et al.* [179]) and the ULIRGs from A. Pope, *et al.* [157] were then added to the 5MUSES galaxies to form scaling laws over a wide range of galaxy sizes, luminosities and redshifts. In Fig. 6.8, $L'_{\rm CO}$ is again compared to $L_{\rm IR}$ and $L_{6.2}$, now with the larger sample. Using the same definitions as Eqn. 6.17 and Eqn. 6.18, the linear relations were found to be $(\alpha_1;\ \beta_1) = (0.81 \pm 0.40;\ 0.77 \pm 0.04)$ and $(\alpha_2;\ \beta_2) = (0.53 \pm 0.49;\ 1.00 \pm 0.06)$ with scatters of $\sigma_1 = 0.27$ dex and $\sigma_2 =$

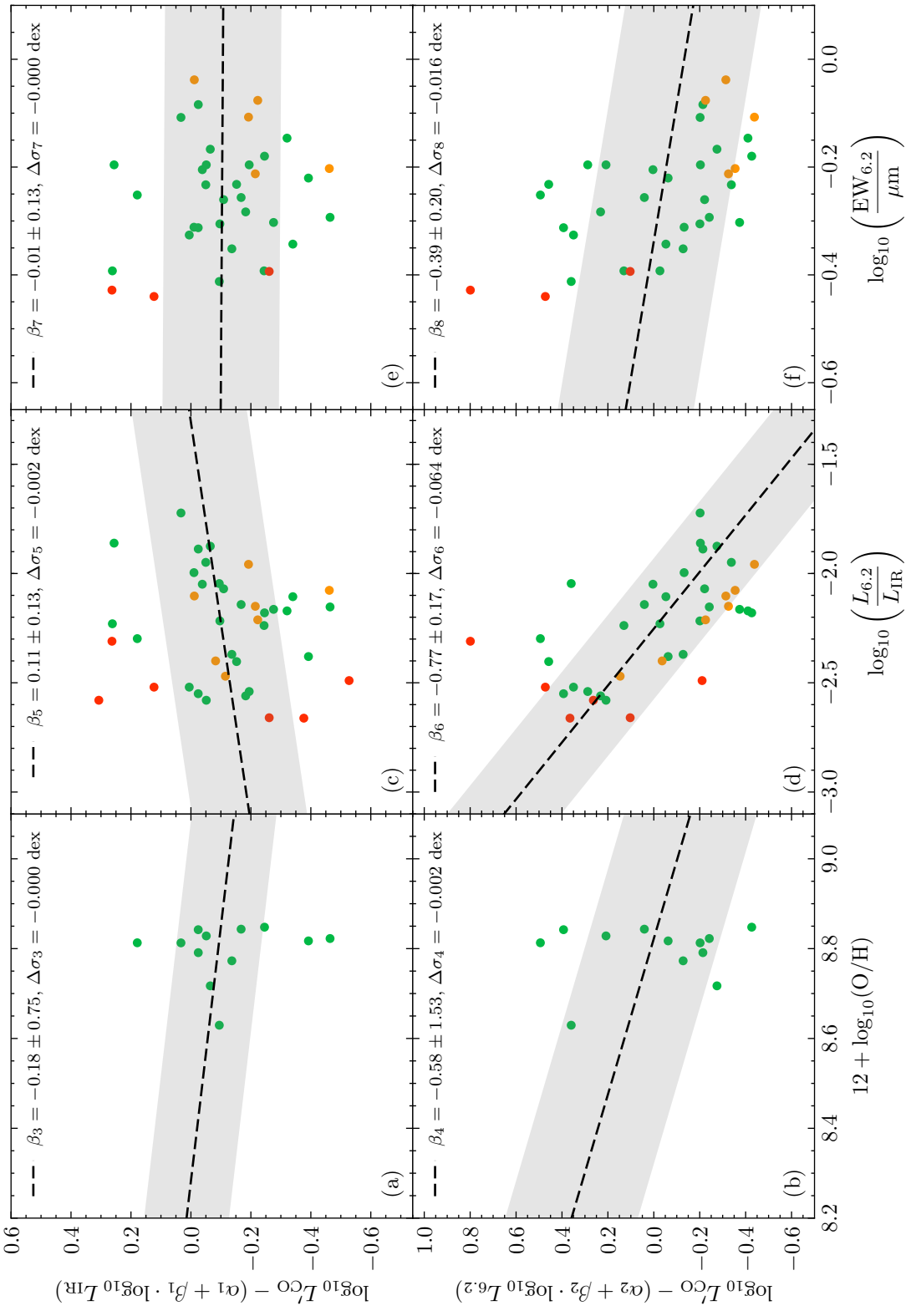

Figure 6.7: Additional metrics for estimating the CO(J=1→0) luminosity. ODR was used to fit a linear trend to each plot. The slope of this trend (β) is listed in the legend along with the change in scatter ($\Delta\sigma$). Similar to Fig. 6.6, green represents star-forming galaxies, yellow represents starburst galaxies, and red represents AGN-dominated galaxies. The grey regions represent one standard deviation above and below the trend line.

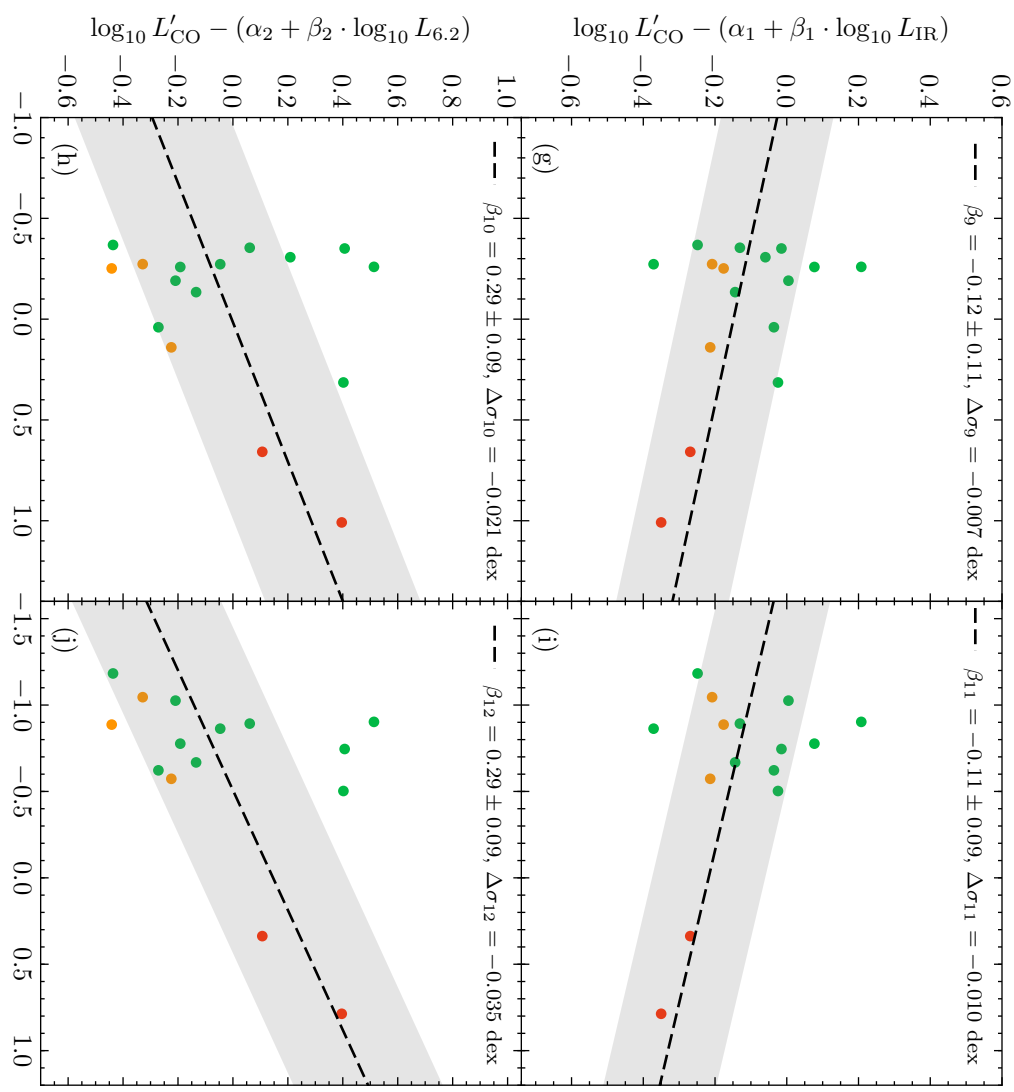

Figure 6.7: Additional metrics for estimating the CO(J=1→0) luminosity *(continued)*.

0.31 dex, respectively. The average difference between the measured $L'_{\rm CO}$ value and the linear regression is listed in Table 6.5. Based on these results, both correlations seem to be reasonably robust, except that the $L_{6.2}$→$L'_{\rm CO}$ estimation is more accurate for the local ULIRGs (many of which are AGN-dominated) and the $L'_{\rm CO} \rightarrow L'_{\rm CO}$ estimation is more accurate for the 5MUSES AGN-dominated galaxies (however, there are only 6 of these galaxies and some of the AGN in these galaxies may be quenching star formation). Since the $L_{6.2} \rightarrow L'_{\rm CO}$ relationship is linear (i.e., $\beta \sim 1$), it can also be written as:

$$L'_{\rm CO} = (3.39 \pm 0.72) \cdot L_{6.2} \tag{6.22}$$

where $L_{6.2}$ is in units of $L_\odot$ and $L'_{\rm CO}$ is in units of K km s^{-1} pc^2.

Table 6.5: Average difference between the measured $L'_{\rm CO}$ value and the linear regression (LR).

Data sample	$\langle \log L'_{\rm CO} - {\rm LR} \rangle$ (dex)	
	$L_{\rm IR} \rightarrow L'_{\rm CO}$ (Fig. 6.8a)	$L_{6.2} \rightarrow L'_{\rm CO}$ (Fig. 6.8b)
5MUSES: SFG	-0.0295	0.0486
5MUSES: SB	-0.1241	-0.0731
5MUSES: AGN	-0.0186	0.3428
Local ULIRGs	-0.4778	0.0162
High-z ULIRGs	0.0659	-0.0380
SINGS+NGLS	-0.0027	-0.1059

Finally, as a means of plotting all 3 tracers in one figure, PAH suppression is plotted against star formation efficiency in Fig. 6.9. Here, SFE decreases with rising PAH strength, suggesting that PAH emission is suppressed in luminous galaxies, whether by AGN or stellar activity. The linear regression was found to be:

$$\log_{10}\left(\frac{L_{\rm IR}}{L'_{\rm CO}}\right) = \alpha + \beta \cdot \log_{10}\left(\frac{L_{6.2}}{L_{\rm IR}}\right) . \tag{6.23}$$

with $(\alpha;\ \beta) = (0.08 \pm 0.19;\ -0.72 \pm 0.08)$ and a scatter of $\sigma_9 = 0.29$ dex.

6.6 Conclusion

In this chapter, new CO(J=1→0) measurements were presented for 34 intermediate redshift galaxies. These galaxies were selected from the 5 mJy Unbiased *Spitzer* Extragalactic Survey (5MUSES), and as such, infrared luminosity and PAH emission

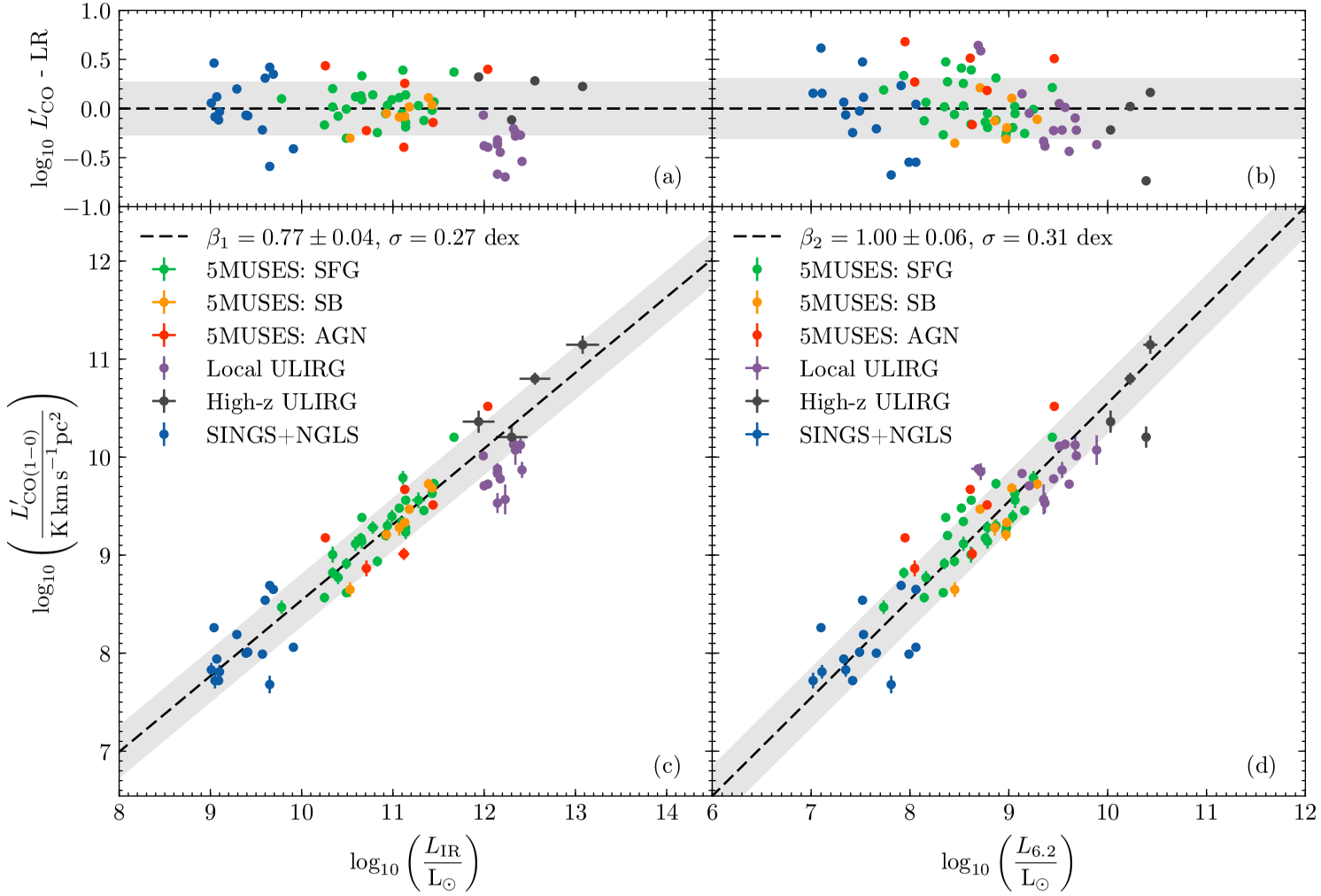

Figure 6.8: CO luminosity compared to dust emission. The dashed lines were fit to the entire sample using Orthogonal Distance Regression (ODR), and the grey region represents one standard deviation above and below the linear regression (LR). The plots on top ((a) and (b)) represent the difference between the measured $L'_{\rm CO}$ value and the linear regression (LR).

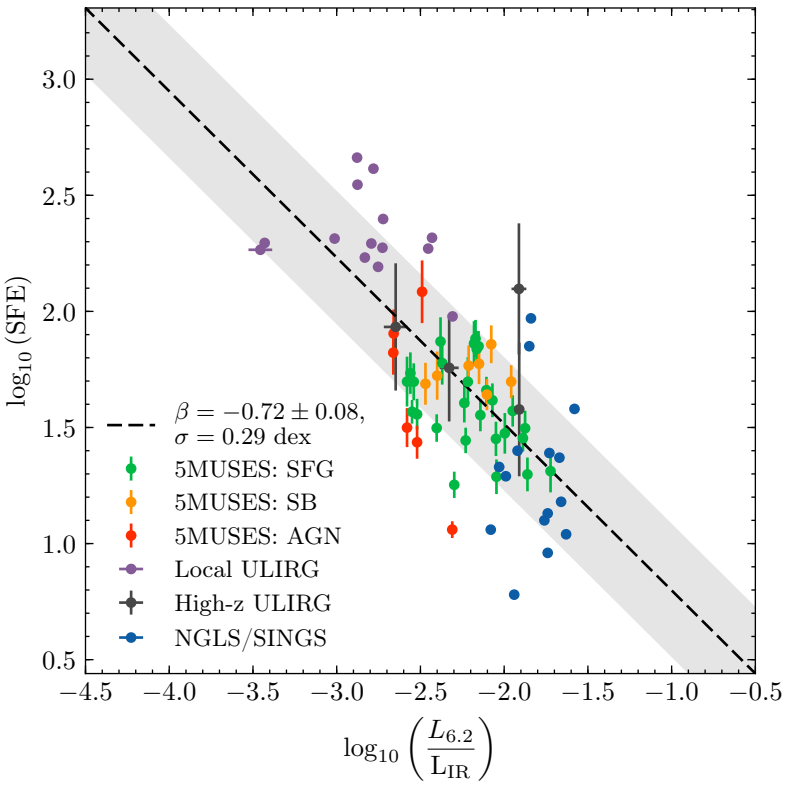

Figure 6.9: The correlation between PAH suppression and star formation efficiency (SFE). Here, SFE $\equiv L_{\mathrm{IR}}/L'_{\mathrm{CO}}$ in units of $\mathrm{K\,km\,s^{-1}\,pc^2\,L_\odot^{-1}}$. The dashed line was fit to the entire sample using Orthogonal Distance Regression (ODR), and the grey region represents one standard deviation above and below the linear regression.

data was available in the literature. The sample galaxies were observed with the IRAM 30 m telescope, and positive detections were found from 23 out of 34 target galaxies. These detections were combined with the 17 positive detections from A. Kirkpatrick, *et al.* [156], for a total of 40 intermediate redshift galaxies: 23 star-forming galaxies, 7 starburst galaxies, and 6 with AGN-dominated sources. The CO(J=1→0) measurements were compared to infrared and PAH luminosities to derive scaling relations: $L_{\mathrm{IR}} - L'_{\mathrm{CO}}$ and $L_{6.2} - L'_{\mathrm{CO}}$. Between these two relationships, the infrared luminosity was found to have a tighter correlation with L'_{CO}. Other parameters (such as metallicity and PAH suppression) were also added to see if they could improve either of the correlations, but only a very modest improvement was found with $O3N2'$ (defined in Eqn. 6.19). Metallicity likely does have an effect, but only a very narrow range of values was contained within our sample since they are all dusty galaxies.

Additional star formation studies were then added to extend our sample. This included several nearby galaxies from SIGNS+NGLS (R. Kennicutt, *et al.* [177], J.

Smith, *et al.* [141], C. Wilson, *et al.* [179]) as well as several local and high-z ULIRGs (compiled by A. Pope, *et al.* [157]). Both trend lines resulted in similar dispersions, but the $L_{6.2} - L'_{\rm CO}$ relationship was found to be more robust with the local ULIRGs and it resulted in a linear correlation: $L'_{\rm CO} = (3.39 \pm 0.72) \cdot L_{6.2}$. The relative PAH emission was also compared to star formation efficiency and a strong anti-correlation was found. This suggests that PAH emission is suppressed by the hard radiation that is present in both starburst and AGN-dominated galaxies.

Chapter 7

Summary and Future Work

The noise properties of modern Superconductor/Insulator/Superconductor (SIS) mixers are now $\sim$3 times the quantum limit of sensitivity. It is therefore becoming increasingly difficult to reduce the noise properties any further, and we have to look to new techniques to improve the capability of these mixers. In this thesis, we investigated two such techniques: increasing the instantaneous bandwidth of the SIS mixers, and increasing the number of pixels in the focal plane. To support this work, we presented new simulation software to help characterise SIS mixers that have wide bandwidths, strong sideband signals, or higher-order harmonics from local-oscillator. In Chapter 6, we also presented CO(J=1$\rightarrow$0) emission results from distant galaxies. This was part of an an effort to study star formation across cosmic time.

I began this thesis by providing the theory behind SIS mixers in Chapter 2. Each subsequent chapter is summarised below along with suggestions for future work:

- In Chapter 3, a new SIS mixer was presented for operation around 230 GHz. It is a single-ended design that uses a finline transition to couple the astronomical and local-oscillator (LO) signals from the waveguide to the planar circuit. By minimising the surface area of the planar circuit, the device was designed to have a wide instantaneous bandwidth, which is also known as the intermediate frequency bandwidth or IFBW. Wide IFBW provides higher sensitivity for continuum sources and greater survey depth for emission line sources by allowing multiple lines to be observed simultaneously. Extensive electromagnetic simulations of this device predicted excellent RF performance from 180$-$255 GHz and an IF response extending from 0$-$13 GHz. The SIS device was fabricated at l'Observatoire de Paris with a 1.5 μm^2 niobium/aluminium-oxide/niobium junction. The performance of the SIS device was then characterised by comparing

its response to hot and cold black body radiation. In terms of RF performance, the noise temperature was found to be ∼40 K from 220−245 GHz, and below 100 K across the entire tuning range of the LO (213−257 GHz). Simulations of the RF performance suggest that the noise temperature should be very low down to at least 180 GHz, but no LOs were available at those frequencies. The IF response was also assessed, and initial experiments found very good noise properties from 0.5−10 GHz. After extensive testing, it was discovered that the bias tee was limiting the IF bandwidth. When it was replaced with another model, the IF response then extended up to 12 or 13 GHz; although, there were still some resonance features in the IF spectrum. Overall, this device provides very good noise properties that are only 3.3 times the quantum limit, and a wide IF bandwidth from approximately 0.5−12 GHz. To further optimise the test system and measure the full extent of the IF response, the current bias tee needs to be replaced with a model that is rated for cryogenic temperatures. Another suggestion would be to integrate the LNA into the mixer block to reduce the electrical distance between the SIS device and the LNA, which should help to reduce ringing in the IF spectrum. Finally, it would also be beneficial to test this device at colder temperatures. Many of the device were tested at ∼5.0 K, but better performance would be found if the devices could be cooled to ∼4.4 K.

- In Chapter 4, the design of the 230 GHz mixer was further investigated using simulation software based on multi-tone spectral domain analysis (MTSDA). Compared to Tucker theory, the MTSDA technique provides more accurate simulation results because the junction is not linearised around an operating point, allowing MTSDA to simulate strong sideband signals and high-order harmonics. To implement this technique, an extensive software package was developed, called QMix. It uses a harmonic balance procedure to reconcile the voltages in the embedding circuit and the MTSDA technique to calculate the tunnelling currents. Simulation results from this software were compared to experimental results, and in many cases the results were found to be very consistent:
  - First, the IF responses were compared (i.e., gain and noise versus IF frequency). The simulated IF response was very close to the experimental values from 4–9 GHz, but above 9 GHz, the experimental noise properties were much higher. As discussed previously, this was likely due to the bias tee, and not due to the SIS mixer itself. If the bias tee can be replaced, the

simulated results suggest that this device should have a noise temperature below 100 K up to ∼15 GHz.

- Next, the IF data was compared (i.e., IF power versus bias voltage). When the broken photon steps were not present, the shapes of the IF data was very similar. The only difference was that the simulated gain was slightly higher, likely because the simulated results did not take into account the losses in the optical path. The broken photon steps were then recreated by adding a sub-harmonic to the LO signal, supporting the theory from [86].

Based on this success, QMix has shown that it can be very useful for simulating SIS mixers and recreating different phenomena seen in experimental data. It can also be applied to simulating other non-linear tasks, such as frequency multiplication (e.g., [197]). QMix was written entirely in Python and makes use of many of the standard libraries. This should hopefully make the code easy to understand and expand in the future for new applications.

- In Chapter 5, a new 1×4 focal plane array was presented. This was built to act as a demonstrator for a new array architecture, with the aim to expand the design in the future into a much large format. The array block was fabricated at the Rutherford Appleton Laboratory using split-block fabrication. It features 4 waveguide flanges on the front of the block for the RF signals and one flange on the side for the LO signal. As the LO enters the block, it is first divided in four using cascaded -3 dB waveguide power splitters, and then it is injected into each RF waveguide using a directional coupler. We chose to only use waveguide components for the LO because it simplifies the optics of the array. The finished array block was tested in an open-cycle cryostat with two vacuum windows on the front: one window was used for the LO signal and the other was used to couple black body radiation to one of the pixels. Using this one pixel, the noise temperature was measured to be 87.8 K at 222.2 GHz, but the noise temperature steadily increased past this frequency, up to 230 K at 255 GHz. By analysing the noise contributions, we discovered that (a) one of the IF components was more lossy than we expected, and (b) the SIS junction had higher noise and lower gain than the previous experiments with the single block in Chp. 3. We expect that the first issue was likely due to the IF boards. The IF boards were printed on a flexible substrate, and then, when they were installed inside the array block, they were bent around a sharp corner. This sharp bend could be causing the higher loss. We need to be careful in future designs to avoid these

sharp bends or to only use rigid substrates. The second issue was likely because the array was too warm. The array block temperature was measured at 5.3 K and the devices were around 5.8 K. Warm temperatures cause much higher noise temperatures in SIS junctions and poor conversion efficiencies. For any future testing, we will need to make an effort to get the array block much colder. This could be done by either using better infrared filters on the radiation shield or by remachining the cryostat's cold plate, which seems to have poor thermal contact with the liquid helium vessel. Despite these issues, the LO distribution and RF signal isolation were still measured. The LO distribution was found to be relatively uneven; although, based on the results from the single block, the pixels should still have consistent noise temperatures. The RF signal isolation was found to be around -30 dB, meaning that less than $1/1000^{\text{th}}$ of the power from one pixel leaks into the surrounding pixels.

- In Chapter 6, 34 galaxies from the 5 mJy Unbiased *Spitzer* Extragalactic Survey (5MUSES) were observed using the IRAM 30 m telescope in Pico Veleta, Spain. The observations targeted the CO(J=1→0) emission line ($\nu_{\text{rest}} = 115.271$ GHz), which can be used to trace the mass of the cold molecular gas and therefore the amount of fuel available for forming new stars. These measurements were then compared to tracers of the star formation rate (i.e., the infrared luminosity L_{IR} and the emission from polycyclic aromatic hydrocarbons $L_{6.2}$) to form empirical relationships between the global quantities, known as scaling laws. For the 5MUSES galaxies, the CO luminosity (L'_{CO}) was found to have a tighter correlation with L_{IR} than with $L_{6.2}$. Other star formation studies were then added to extend our sample. This included nearby galaxies from the SIRTF Nearby Galaxy Survey (SINGS) and Nearby Galaxies Legacy Survey (NGLS), as well as several ultraluminous infrared galaxies (ULIRGs). With these additional galaxies, we found a similar correlation between $L'_{\text{CO}} - L_{\text{IR}}$ and $L'_{\text{CO}} - L_{6.2}$; however, the latter was more robust with ULIRGs, which may have large active galactic nuclei (AGN). We also found that $L_{6.2}/L_{\text{IR}}$ decreases with star formation efficiency, suggesting that PAH is suppressed in the presence of either strong stellar or AGN radiation.

Appendix A

Shot Noise From an SIS Junction

As described previously in Chp. 2, the shot noise from an SIS junction can be used to: (a) calibrate the IF output power, and (b) estimate the IF noise contribution. The circuit diagram for this process is shown in Fig. A.1a, and the shot noise produced by the junction is given by:

$$T_{\rm in}^{\rm shot}(V_0) = \frac{e}{2\,k_{\rm B}}\, I_{\rm dc}^{0}(V_0)\, R_{\rm dyn} \coth\left(\frac{e\,V_0}{2\,k_{\rm B}T_{\rm amb}}\right) \tag{A.1}$$

where e is the charge of an electron, $k_{\rm B}$ is the Boltzmann constant, $I_{\rm dc}^{0}(V_0)$ is the DC tunnelling current, $R_{\rm dyn} = (\mathrm{d}I_{\rm dc}^{0}/\mathrm{d}V_0)^{-1}$ is the dynamic resistance, and $T_{\rm amb}$ is the ambient temperature of the SIS junction. When the junction is biased at a voltage above the gap, i.e., $|V_0| > V_{\rm gap}$, the shot noise in Eqn. A.1 rises at a constant rate of $\Delta T_{\rm in}^{\rm shot}/\Delta V_0 = e/2\,k_{\rm B} \approx 5.8$ K/mV.

The gain of the IF circuit

In Fig. A.1a, the gain of the entire IF chain is represented by $G_{\rm IF}$. This combines everything between the SIS junction and the IF power detector including the planar circuit, bond wires, IF tuning board, coaxial cables, LNAs and bandpass filters. The measured output temperature is then given by:

$$T_{\rm out}^{\rm shot} = G_{\rm IF} \cdot T_{\rm in}^{\rm shot} \cdot (1 - |\Gamma_{\rm shot}|^2) \tag{A.2}$$

where $(1 - |\Gamma_{\rm shot}|^2)$ represents the impedance mismatch between the junction and the IF circuit. The reflection coefficient $\Gamma_{\rm shot}$ is given by:

$$\Gamma_{\rm shot} = \frac{Z_{\rm IF} - Z_{\rm J}}{Z_{\rm IF} + Z_{\rm J}} \tag{A.3}$$

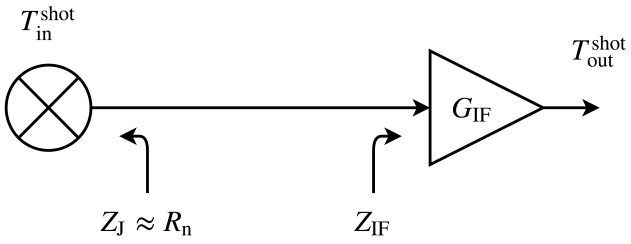

(a) When an SIS junction is not exposed to any AC input signals (i.e., with no LO pumping), the junction produces a well-defined shot noise, given by Eqn. A.1. This fact can be used to de-embed the IF chain, represented here as G_{IF}. There is, however, an impedance mismatch between the output impedance of the junction Z_{J} and the input impedance of the IF circuit Z_{IF}, which has to be taken into account. In this scenario, the output impedance of the SIS junction Z_{J} is approximately equal to R_{n} when the junction is biased above the gap, but the input impedance of the IF chain Z_{IF} is unknown.

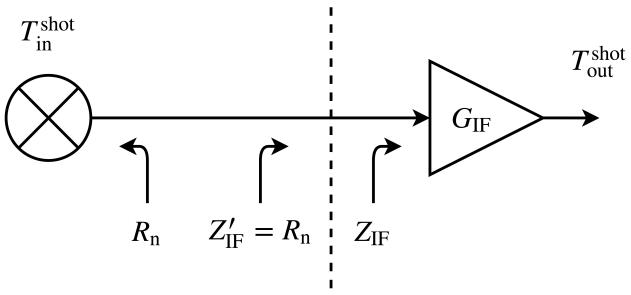

(b) Since the input impedance of the IF chain is unknown in Fig. A.1a, we can instead set it to a constant value as shown above. To simplify Eqn. A.2, here we set $Z'_{\text{IF}} = R_{\text{n}}$. This has the effect of setting a reference plane between the SIS junction and the IF circuit, shown here as a dashed line.

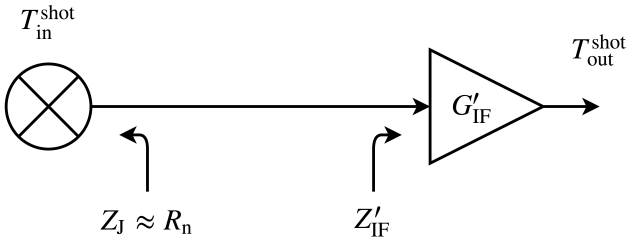

(c) Here the effect of the reference plane is incorporated into the gain of the IF circuit. The gain is now equal to $G'_{\text{IF}} = G_{\text{IF}} \cdot (1 - |\Gamma|^2)$ where $\Gamma = (Z_{\text{IF}} - Z'_{\text{IF}})/(Z_{\text{IF}} + Z'_{\text{IF}})$.

Figure A.1: Calibrating an SIS junction using the shot noise.

where $Z_{\rm IF}$ is the input impedance of the IF chain (looking in from the point of view of the junction) and $Z_{\rm J}$ is the output impedance of the SIS junction. When the junction is biased above the gap, the output impedance is $Z_{\rm J} \approx R_{\rm n}$ where $R_{\rm n}$ is the normal resistance of the SIS junction. The input impedance of the IF chain ($Z_{\rm IF}$) on the other hand is a complex value that changes with IF frequency. For example, from HFSS simulations of the planar circuit, $Z_{\rm IF} \approx 50\ \Omega$ at 0 Hz, but this value changes to $Z_{\rm IF} \approx 7.44 - j\,17.06\ \Omega$ at 5 GHz. These simulations, however, ignore the components that come after the planar circuit, such as the bond wires and IF tuning circuit. Since the actual value for $Z_{\rm IF}$ is unknown, we can instead set $Z'_{\rm IF} = R_{\rm n}$ (Fig. A.1b), which in turn sets $\Gamma_{\rm shot} = 0$. Then by comparing the slope of the measured output power ($\Delta T^{\rm shot}_{\rm out}/\Delta V_0$) to the theoretical value for the shot noise ($\Delta T^{\rm shot}_{\rm in}/\Delta V_0 \approx 5.8$ K/mV; Eqn. A.1), we are then able to solve for the gain of IF chain ($G'_{\rm IF}$ in Fig. A.1c).

Estimating the IF noise

In Sec. 2.6.1, the IF noise was calculated using Woody's method [54]. This technique again relies on the fact that the shot noise from an SIS junction rises at a rate of 5.8 K/mV (when biased above the gap). If the IF noise is estimated using the reference plane shown in Fig. A.1b, the measured IF noise $T'_{\rm IF}$ will include the effect of the impedance mismatch:

$$T'_{\rm IF} = \frac{T_{\rm IF}}{G_{\rm mismatch}} \tag{A.4}$$

where $G_{\rm mismatch} = (1 - |\Gamma_{\rm shot}|^2)$. To recover the actual IF noise contribution $T_{\rm IF}$, the effect of the mismatch can be de-embedded by: $T_{\rm IF} = T'_{\rm IF} \cdot (1 - |\Gamma_{\rm shot}|^2)$. Again, this requires the knowledge of the input impedance of the IF chain $Z_{\rm IF}$, which changes with IF frequency.

In this thesis, most of the experimental results were measured with a 4–6 GHz bandpass filter. Therefore, we can compromise on $Z_{\rm IF}$ by estimating its value at 5 GHz. Based on HFSS simulations, the input impedance of the IF chain (from the point of view of the junction) is $Z_{\rm IF} \approx 7.44 - j\,17.06\ \Omega$ at 5 GHz, but this does not include any of the components that follow the SIS device. For example, if we cascade a 0.2 nH bond wire (see App. C), the value of the input impedance changes to $Z_{\rm IF} \approx 7.95 - j\,17.87\ \Omega$. Ignoring these components for now, the mismatch factor is equal to $G_{\rm mismatch} = 0.55$.

Calibrating the IF output power

Fig. A.2a depicts an SIS junction being operated as a heterodyne mixer. The gain of the IF chain G'_{IF} is the same as it was in Fig. A.1c, but now the output impedance of the junction $Z_{\mathrm{J}}^{\mathrm{IF}}$ is no longer equal to the normal resistance. This leads to an impedance mismatch. The output power can be calculated by:

$$T_{\mathrm{out}}^{\mathrm{IF}} = G_{\mathrm{IF}} \cdot T_{\mathrm{in}}^{\mathrm{IF}} \cdot (1 - |\Gamma_{\mathrm{IF}}|^2) \tag{A.5}$$

where

$$\Gamma_{\mathrm{IF}} = \frac{Z'_{\mathrm{IF}} - Z_{\mathrm{J}}^{\mathrm{IF}}}{Z'_{\mathrm{IF}} + Z_{\mathrm{J}}^{\mathrm{IF}}} \,. \tag{A.6}$$

To a rough approximation, the output impedance of the junction is equal to the dynamic resistance of the pumped I–V curve [12, 77], i.e., $Z_{\mathrm{J}}^{\mathrm{IF}} \approx (\mathrm{d}I_{\mathrm{dc}}^0/\mathrm{d}V_0)^{-1}$, which changes with respect to the DC bias voltage, LO frequency and LO pump level. This complicates the calibration, and makes it very difficult to de-embed the actual IF output power from the junction ($T_{\mathrm{in}}^{\mathrm{IF}}$ in Fig. A.2a). Similar to the case with the shot noise (Fig. A.1b), a reference plane is set according to an arbitrary input impedance, as depicted in Fig. A.2b. Here, we set $Z_{\mathrm{J}}'^{\mathrm{IF}} = R_{\mathrm{n}}$ to ignore the impedance mismatch between the junction and the IF circuit. We can then recover the IF power from the junction by:

$$T'_{\mathrm{in}}{}^{\mathrm{IF}} = \frac{T_{\mathrm{out}}^{\mathrm{IF}}}{G'_{\mathrm{IF}}} \,. \tag{A.7}$$

Note that this IF output power includes the impedance mismatch between the junction and the IF circuit. This definition is used throughout this thesis.

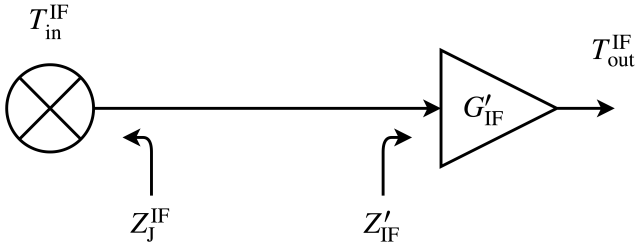

(a) This figure depicts an SIS junction being operated as a heterodyne mixer. $T_{\text{in}}^{\text{IF}}$ represents the down-converted IF power. This signal is then amplified by the IF chain (G'_{IF}) before the output power ($T_{\text{out}}^{\text{IF}}$) is measured by the power detector. The impedance mismatch between the output impedance of the SIS junction Z_{J}^{IF} and the input impedance of the IF chain Z'_{IF} results in reflections and a loss in power transmission.

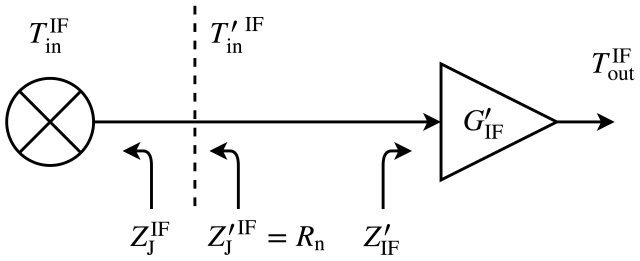

(b) Since the output impedance of the SIS junction is unknown, we can set a reference plane as shown above. If we then de-embed the IF circuit (by dividing $T_{\text{out}}^{\text{IF}}$ by G'_{IF}), we can then recover $T'_{\text{in}}{}^{\text{IF}}$ from experimental data.

Figure A.2: Calibrating the IF output power from an SIS junction.

Appendix B

The Experimental Test System

The experimental system that was used to characterise the 230 GHz SIS receiver and focal plane array was described briefly in Sec. 3.5. This appendix contains additional information including part numbers, dimensions and specifications.

B.1 Cryostat

An open-cycle dewar (HDL–10 with a custom 13.5"×13.5" cold plate, Infrared Laboratories, Inc.) was used for all of the tests in this thesis. This dewar contains two internal vessels for the cryogenic liquids: one that is attached directly to the cold plate, and one attached to an intermediate radiation shield. Typically, the dewar was pre-cooled with liquid nitrogen for +12 hours before running an experiment (Fig. B.1a). The vessel attached to the cold plate was then purged with nitrogen gas and filled with liquid helium (Fig. B.1b). The aluminium cold plate was typically cooled to ∼4.4 K; although, this temperature was often much higher next to the mixer block, since aluminium does not provide very good thermal conductivity and the contact between the cold plate and the helium vessel was relatively poor. The hold time varied between 2 and 8 hours depending on how much liquid helium was transferred.

B.2 Black body loads

The Y-factor technique requires black body loads at two different temperatures in order to estimate the system's noise temperature and gain. For the testing in this thesis, room temperature microwave absorber (Eccosorb®, Emerson & Cuming Microwave Products) was used as the hot load ($T_{\mathrm{H}} \sim 295$ K), while the same material immersed in liquid nitrogen was used as the cold load ($T_{\mathrm{C}} \sim 78.5$). Both of these temperatures are above the Rayleigh-Jeans limit at 230 GHz (Fig. B.2), meaning

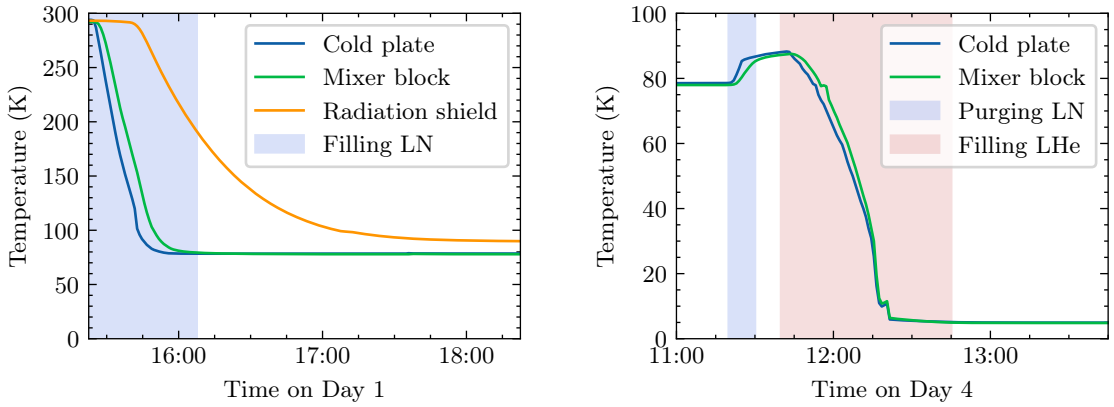

(a) Pre-cooling with liquid nitrogen (LN). (b) Cooling with liquid helium (LHe).

Figure B.1: Cooling the open-cycle dewar with liquid nitrogen and liquid helium. In this case, the dewar was pre-cooled over the weekend.

that the spectral energy density of the loads was proportional to temperature. At 230 GHz, the equivalent temperatures from the Callen-Welton equations [49] are $T_{\mathrm{H}} = 295.03$ K and $T_{\mathrm{C}} = 78.63$ K, respectively.

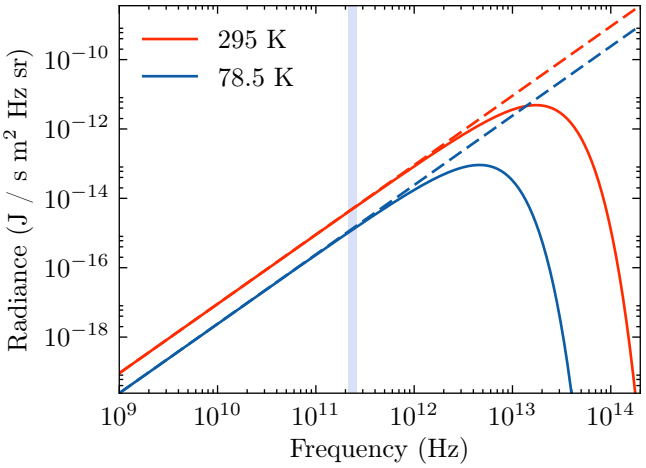

Figure B.2: Theoretical black body radiation from the test loads: room temperature Eccosorb ($T_{\mathrm{H}} \approx 295$ K), and Eccosorb immersed in liquid nitrogen ($T_{\mathrm{C}} \approx 78.5$ K). The solid lines are the Planck distributions, and the dashed lines are the Rayleigh-Jeans approximations. The pale blue bar represents the tuning range of the LO (213–257 GHz).

B.3 Optics

The LO signal was coupled to the mixer's horn using a Gaussian beam telescope. Gaussian beam telescopes should provide frequency-independent coupling; however, the beam waists of feed horns move with frequency, resulting in the marginal loss of

coupling seen in Fig. B.3a. Additionally, the distance between the mirrors was slightly higher than the ideal $2{\cdot}f$ (where f is the focal length of the mirrors), which is why the optimum coupling frequency moved from 230 GHz to 240 GHz.

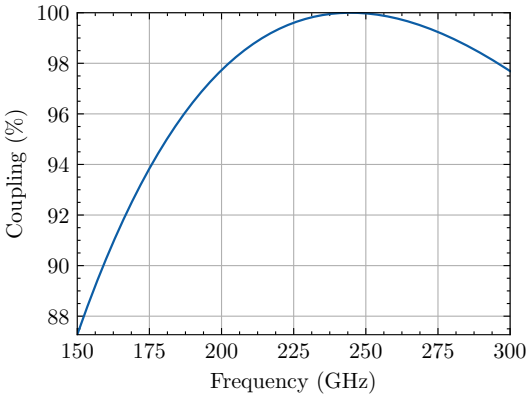

(a) Theoretical coupling between the LO and mixer horns (ignoring losses from the beam splitter and vacuum window). Perfect coupling is found at 244.5 GHz.

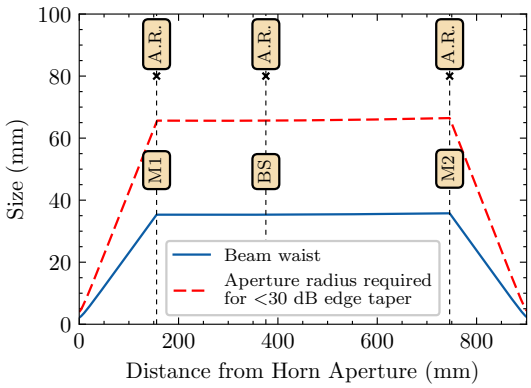

(b) Beam waist as it travels through the optical system. The aperture radii (A.R.) are also included for the beam splitter and two mirrors.

Figure B.3: Theoretical beam properties for the Gaussian beam telescope in Fig. 3.13.

The beam waist was also calculated along the entire LO path and the edge taper was analysed[1] at each aperture (this is the ratio of power at the aperture to the power in the centre of the beam). All of the edge tapers were found to be far below -30 dB (Fig. B.3b), which helps to prevent extra thermal noise from entering the system.

B.4 Vacuum windows

Vacuum windows are required to be both mechanically strong and relatively transparent over the intended RF bandwidth. In most cases, vacuum windows can be modelled as simple lossless dielectric slabs. For a plane wave normal to the surface of a dielectric slab of thickness d and index of refraction n, the reflection coefficient is given by:

$$\Gamma = \frac{\rho \cdot (1 - e^{-j\omega T})}{1 - \rho^2 \, e^{-j\omega T}} \tag{B.1}$$

where ω is the angular frequency, $T = 2dn/c$, and c is the speed of light. Here, the ρ coefficient represents the reflection at the air/dielectric interface, and is given by:

$$\rho = \frac{\eta_d - \eta_0}{\eta_d + \eta_0} \tag{B.2}$$

[1]Fig. B.3a and B.3b were generated using the GaussOpt software package that I developed to do basic Gaussian beam analysis. Hosted at: https://github.com/garrettj403/GaussOpt

where η_0 is the impedance of freespace and η_d is the impedance inside the dielectric slab. The transmitted power is then given by:

$$|T|^2 = 1 - |\Gamma|^2. \tag{B.3}$$

B.4.1 HDPE windows

The cheapest and most readily available material is high density polyethylene (HDPE). Initially, an HDPE window leftover from an experiment at 650 GHz was used for the experiments at 230 GHz. To assess the unknown window, the power transmission was measured using a freespace measurement system[2] and poor transmission was found at 255 GHz (Fig. B.4a). By fitting Eqns. B.1-B.3 to the measured data, the thickness and index of refraction were estimated to be 553 µm and 1.57, respectively. (This index of refraction is within 3% of the value given for HDPE by Lamb *et al.* [198].) I then designed a new HDPE window to be one wavelength thick at 220 GHz: a thickness of 894 µm assuming a refractive index of $n = 1.525$ [198]. The power transmission of this window was also measured, but unfortunately HDPE is difficult to machine accurately and the window came out too thick (Fig. B.4b).

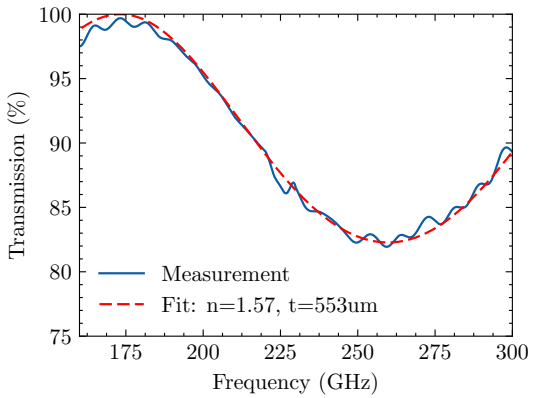

(a) Transmission through an old HDPE window left over from an experiment at 650 GHz.

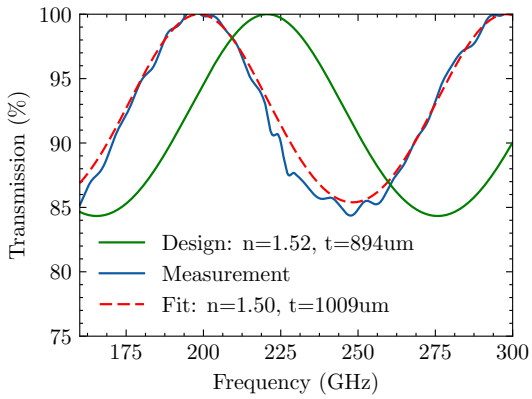

(b) Transmission through a new window designed to be one wavelength thick at 230 GHz.

Figure B.4: Transmission through HDPE vacuum windows.

[2]The freespace measurement system consisted of a VNA connected to two waveguide horns with a sample holder in the middle. The data was measured at the Rutherford Appleton Laboratory (RAL) with help from Dr. Manju Henry.

B.4.2 Zotefoam window

A new window was then created from a 24 mm thick slab of nitrogen-expanded polypropylene foam (PPA30, Zotefoams PLC, Croydon, UK), which has excellent transmission below 400 GHz [80]. This was confirmed by measurements with the freespace measurement system (Fig. B.5). The simple linear trend in Fig. B.5 is:

$$\text{Transmission } [\%] = -0.01724 \times \text{Frequency } [\text{GHz}] + 102.1\,. \tag{B.4}$$

The transmission at 230 GHz is 98.1%, and assuming a physical temperature of 295 K, this leads to an effective noise temperature of 5.71 K. Note that Zotefoam is used for the vacuum windows on PoleStar [135], BICEP2/Keck [199] and the South Pole Telescope [200].

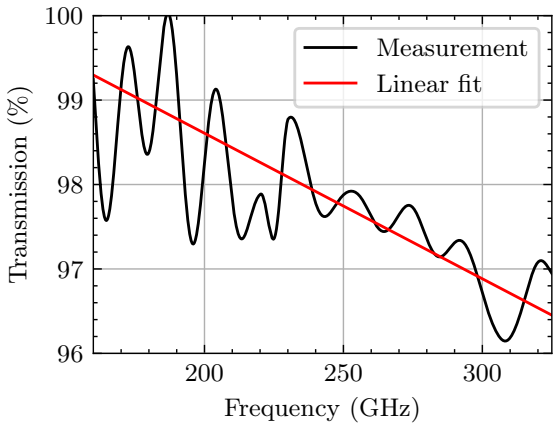

Figure B.5: Transmission through a 24 mm slab of Zotefoam.

B.5 Beam splitters

The beam splitter were made from sheets of Mylar film, and they were kept as thin as possible to reduce the noise contribution to system. The reflection coefficient from Mylar aligned at 45° with parallel polarisation is plotted in Fig. B.6a, and the resulting the effective noise temperature is plotted in Fig. B.6b.

To confirm the properties of the Mylar material, a 75 µm thick Mylar beam splitter was measured with a freespace measurement system and compared to the theoretical transmission (Fig. B.7).

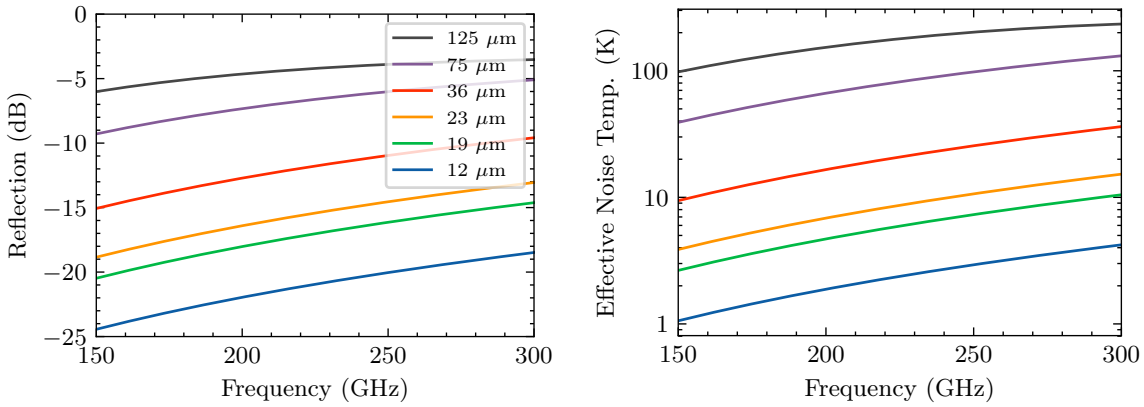

(a) Reflection coefficient

(b) Effective noise temperature

Figure B.6: A Mylar beam splitter at 45° with parallel polarisation.

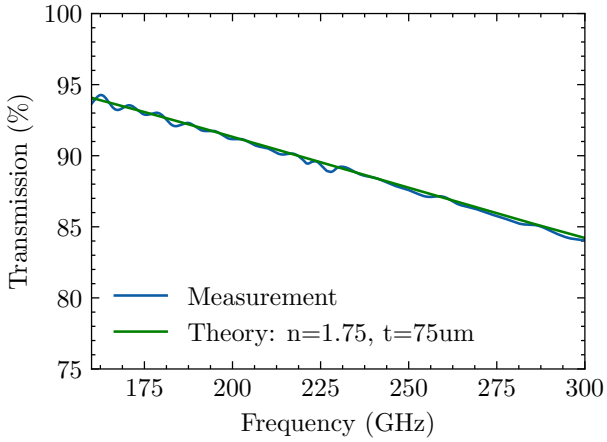

Figure B.7: Transmission through a 75 µm thick beam splitter (at a 0° angle).

B.6 Local-oscillators

Three different local-oscillators (LOs) were available in our lab (Table B.1). The source based on a Gunn oscillator was used for most of the testing because the synthetic sources were found to contain very powerful harmonics (see [201]).

Table B.1: Available local-oscillators.

Model	Manufacturer	Signal source	Multiplier	Tuning range (GHz)
2005 088	RPG	Gunn osc.	×3	213–258
2008 004b	RPG	Synthetic	×18	195–260
AFM6-90	RPG	Synthetic	×18	195–260

Unfortunately, the original Gunn oscillator was damaged during the time that the 230 GHz receiver was being tested and it was replaced temporarily by the Millitech oscillator in Table B.2. And then, in March 2018, another Gunn oscillator was purchased from LinWave to replace the original oscillator from RPG.

Table B.2: Available Gunn oscillators.

Model	Manufacturer	Tuning Range (GHz)	Average Power (dBm)	Tuneable backshort
2005 088	RPG	71.0 – 86.0	16	Yes
GDM-12T	Millitech	73.3 – 81.6	16	No
	LinWave	73.3 – 81.6	16	Yes

The output power of the Gunn-based LO was measured using a power meter and it was found to be very close to the values provided by the manufacturer (Fig. B.8).

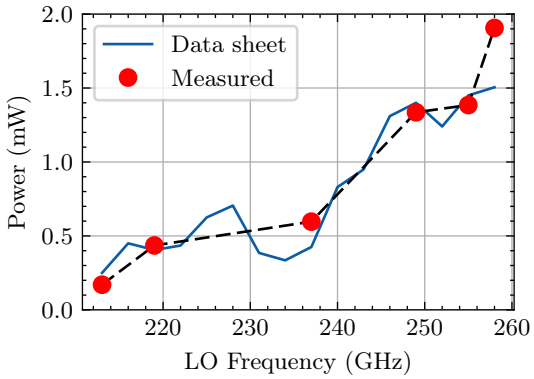

Figure B.8: Measured power from the Gunn-based local oscillator.

Appendix C

The Influence of Bond Wires on the IF Response

Bond wires were used to connect the SIS devices to the IF tuning boards. These bond wires influence the IF response of the SIS device due to the added inductance. This inductance can be estimated using the empirical formula from [202]:

$$L_{\mathrm{bw}} \approx \frac{\mu_0\, l}{2\,\pi}\left[\ln\left(\frac{2\,l}{r}\right) - 0.75\right] \tag{C.1}$$

where l and r are the wire's length and radius, respectively. For a typical bond wire in this thesis (∼0.3 mm long and 25.4 µm in diameter, example in Fig. C.1) this expression estimates $L_{\mathrm{bw}} = 0.19$ nH. However, Eqn. C.1 is only for straight wires. According to [203], the bond wire inductance will be overestimated by 10–50% since the curvature is ignored in Eqn. C.1.

For two bond wires in parallel, the inductance should drop by an additional 50%, but if they are close together, there is a small amount of additional mutual inductance [202]:

$$M \approx \frac{\mu_0\, l}{2\,\pi}\left[\ln\left(\frac{2\,l}{d}\right) - 1 + \frac{d}{l}\right] \tag{C.2}$$

where d is the distance between the two wires. The overall inductance is then:

$$L_{\mathrm{2bw}} = \frac{L_{\mathrm{bw}} + M}{2}\,. \tag{C.3}$$

For two bond wires separated by 0.15 mm, Eqns. C.1–C.3 estimate $L_{\mathrm{2bw}} = 0.12$ nH (again assuming $l = 0.3$ mm and $r = 0.5$ mil, and ignoring curvature).

The bond wires' inductance (L_{2bw}) can then be converted to an S-parameter

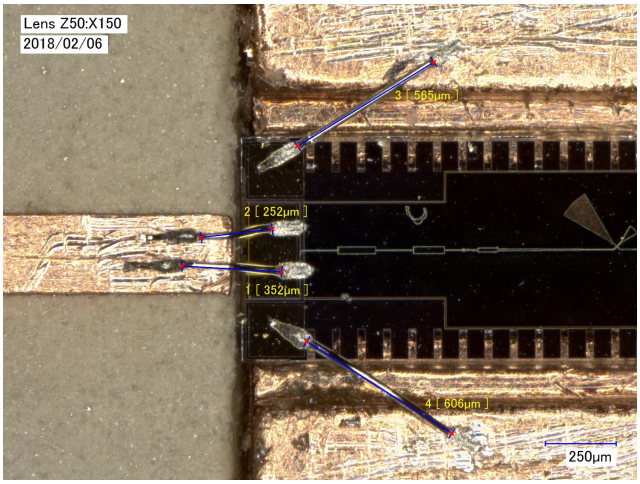

Figure C.1: Bond wires attached to device #2.2. The distances marked on the image are distances in the plane of the device; they do not take into account the curvature of the bond wires.

matrix by:

$$S = \begin{bmatrix} S_{11} & S_{12} \\ S_{21} & S_{22} \end{bmatrix} = \frac{1}{j\omega L_{2\text{bw}} + 2Z_0} \begin{bmatrix} j\omega L_{2\text{bw}} & 2Z_0 \\ 2Z_0 & j\omega L_{2\text{bw}} \end{bmatrix} \tag{C.4}$$

where Z_0 is the characteristic impedance of the transmission line. To combine the bond wires with the S-parameters of the planar circuit (i.e., the simulated results from Sec. 3.3.1), the S-parameters were cascaded as seen in Fig. C.2a. To isolate transmission, the S-parameter diagram was reduced to the signal flow diagram in Fig. C.2b. By applying the rule for self-loops [204], the transmission was found to be:

$$T = \frac{b_2}{a_1} = \frac{S_{a21}\ S_{b21}}{1 - S_{a22} \cdot S_{b11}}\,. \tag{C.5}$$

A similar process was used to isolate the reflection coefficient seen looking back into the IF port:

$$\Gamma_{\text{out}} = \frac{b_2}{a_2} = S_{b22} + \frac{S_{b12}\ S_{b21}\ \Gamma_{\text{out,device}}}{1 - S_{b22}\ \Gamma_{\text{out,device}}} \tag{C.6}$$

where $\Gamma_{\text{out,device}}$ is the reflection coefficient at the output port of the device (without any bond wires):

$$\Gamma_{\text{out,device}} = S_{a22} + \frac{S_{a12}\ S_{a21}\ \Gamma_{\text{SIS}}}{1 - S_{a22}\ \Gamma_{\text{SIS}}} \tag{C.7}$$

and Γ_{SIS} is the reflection coefficient seen at the junction:

$$\Gamma_{\text{SIS}} = \frac{Z_{\text{SIS}} - Z_0}{Z_{\text{SIS}} + Z_0}\,. \tag{C.8}$$

If the SIS junction impedance is matched to the characteristic impedance, $\Gamma_{\text{SIS}} = 0$

and the output reflection coefficient reduces to

$$\Gamma_{\text{out}} = S_{b22} + \frac{S_{b12}\, S_{b21}\, S_{a22}}{1 - S_{b22}\, S_{a22}}\,. \tag{C.9}$$

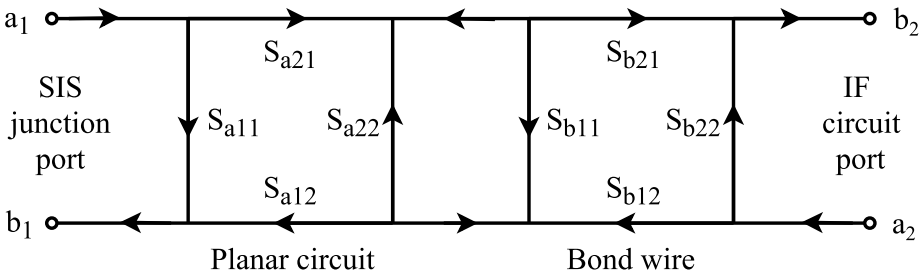

(a) The S-parameters of the planar circuit $[S_a]$ cascaded with the S-parameters for the bond wires $[S_b]$.

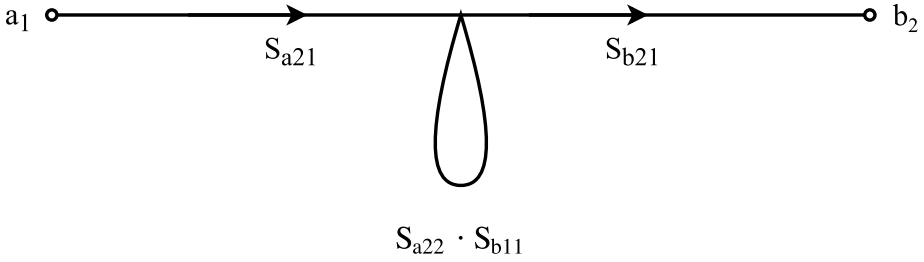

(b) The signal flow diagram used to isolate the transmission coefficient.

Figure C.2: Cascading the planar circuit with the bond wire inductance to determine the overall transmission and reflection coefficients.

Appendix D

IF matching circuits

IF tuning boards were designed to match the output impedance of the SIS devices to the IF chain ($Z_0 = 50\ \Omega$) using the technique described in [63]. A brief description of the design process was already covered in Sec. 3.8.1. Three different IF boards were designed: one optimised for 0–16 GHz, another for 5–16 GHz, and another for 0–13 GHz with partial compensation for a bond wire. The dimensions of the 6 stage transformers (Fig.D.1) are given in Table D.1. They were fabricated on 10 mil/254 µm thick RT/duroid® 6010 from Rogers Corp. The width of a 50 Ω transmission line on this substrate is 227 µm. A triangle was added on the right-hand side in Fig. D.1 to bond to the pin of the SMA connector.

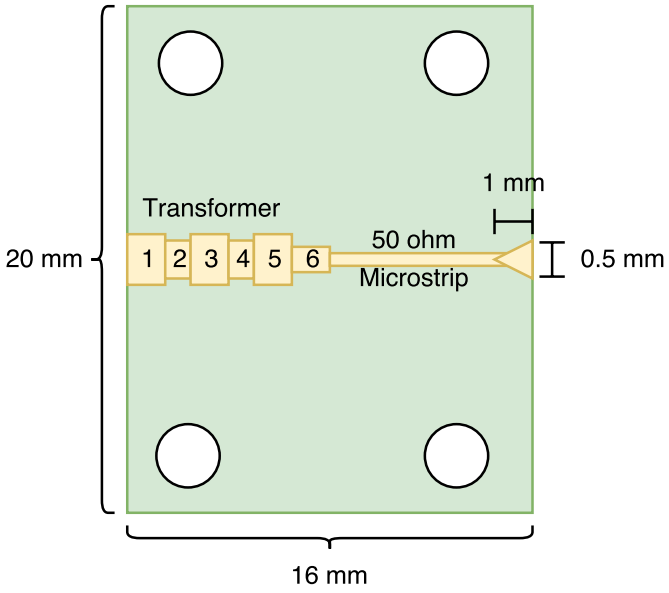

Figure D.1: 6-stage IF board layout. The SIS device is connected on the left-hand side, and the pin for a coaxial connector is connected on the right.

Table D.1: IF board dimensions (in mm).

Dimension	IF board name		
	"0–16ghz"	"5–16ghz"	"0–13ghz–bw"
W1	2.266	4.893	4.205
W2	1.613	4.120	0.497
W3	0.888	4.994	1.276
W4	1.656	2.714	0.777
W5	0.778	0.995	0.559
W6	0.413	0.732	0.339
L1	1.959	1.915	0.805
L2	0.502	0.524	1.116
L3	0.781	2.415	1.294
L4	1.222	2.449	1.469
L5	3.231	2.552	3.483
L6	2.975	2.693	3.813

Note: "W" represents the width of the microstrip, and "L" represents the length.

The 0–16 GHz IF board was already presented in Fig. 3.29. The 5–16 GHz IF board is shown in Fig. D.2a with the simulated performance in Fig. D.2b. By limiting the IF range to 5–16 GHz, the transmission can be optimised to be much flatter than the 0–16 GHz case (recall Fig. 3.29).

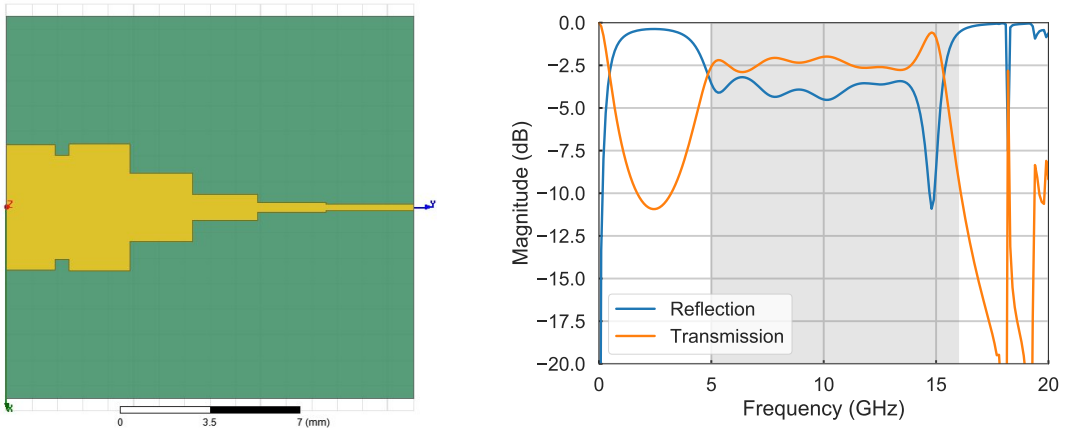

(a) Layout (b) Simulated performance

Figure D.2: Matching circuit optimised for 5–16 GHz.

Compensating for bond wire inductance

As explained in Sec. **??**, bond wires can severely limit the performance at upper IF frequencies. As an example, the performance of the 0–16 GHz IF board is plotted in Fig. D.3 with and without a 0.2 nH bond wire.

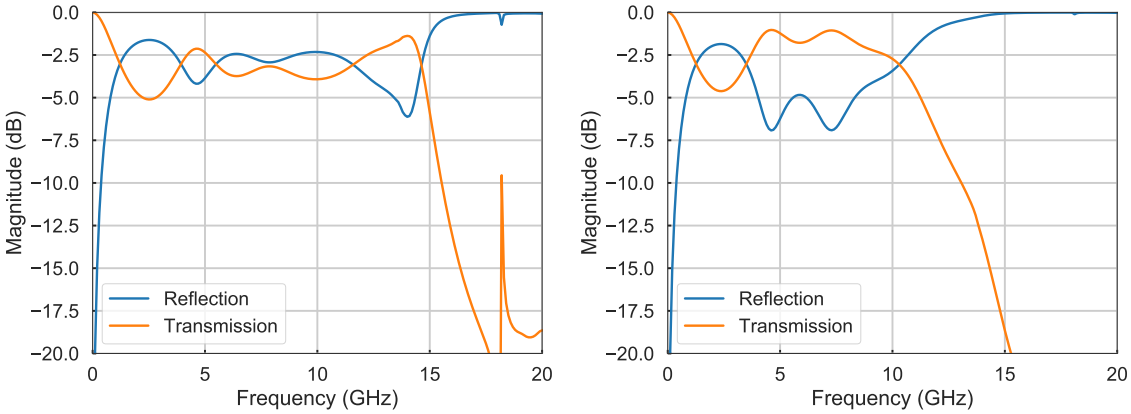

(a) No series inductance (b) 0.2 nH series inductance

Figure D.3: The effect of a series inductance on the 0–16 GHz IF board.

An IF board was designed to partially compensate for a 0.2 nH series inductance (Fig. D.4); although, the simulated performance is worse than the case with no added inductance (Fig. D.4).

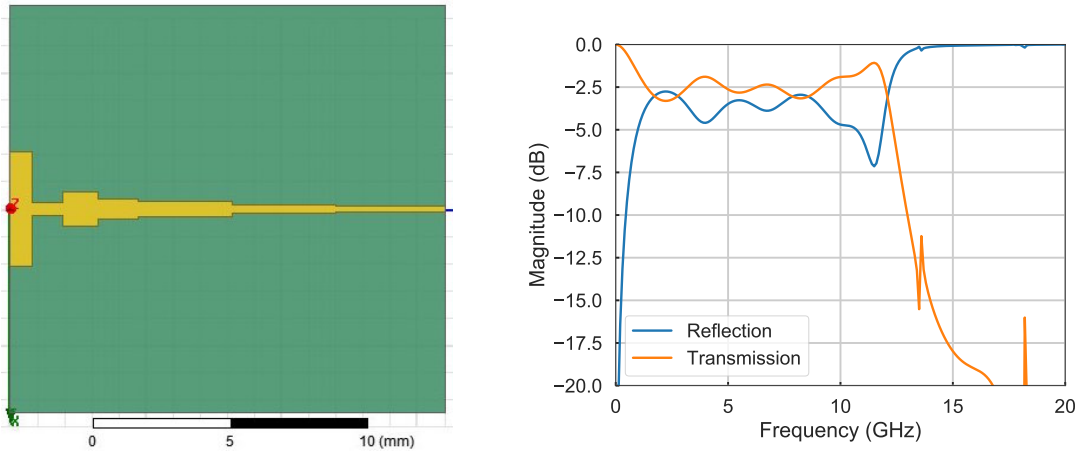

(a) IF board layout (b) Simulated performance

Figure D.4: IF board designed to compensate for a 0.2 nH series inductance.

Appendix E

Additional Star Formation Data

This appendix contains additional data relating to Chapter 6: "Tracers of Star Formation Activity". This includes all of the measured CO(J=1→0) spectra from the observing run in September 2016 (Sec. E.1), SDSS images of the target galaxies (Sec. E.2), and data relating to the additional sources added from [156] (Sec. E.3).

E.1 Measured CO(J=1→0) spectra

The measured CO(J=1→0) spectra from the 5MUSES galaxies are shown in Fig. E.1. This data was measured with the IRAM 30 m telescope and analysed with IRAM's CLASS/GILDAS software package (see Sec. 6.3 for more details).

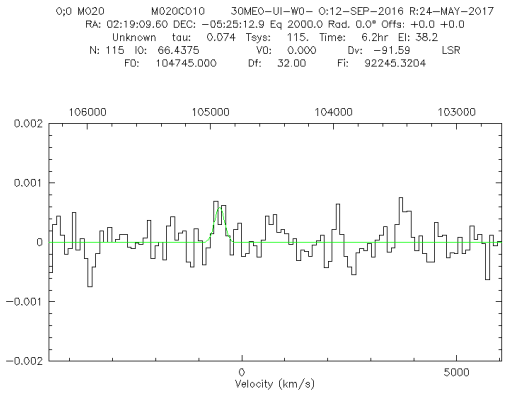

M020

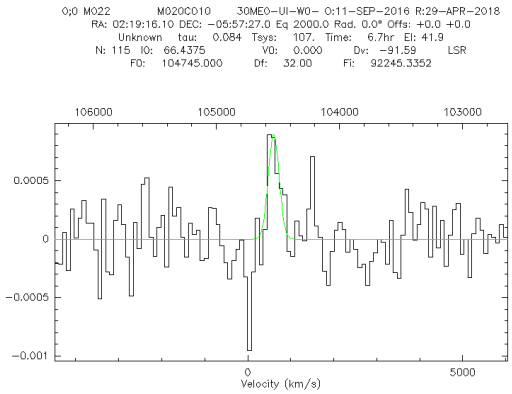

M022

Figure E.1: Measured CO(J=1→0) spectra from the 5MUSES galaxies. These plots were generated with IRAM's CLASS/GILDAS software package. Only the galaxies that were observed in September 2016 are included in this figure. Note that some of these were classified as non-detections.

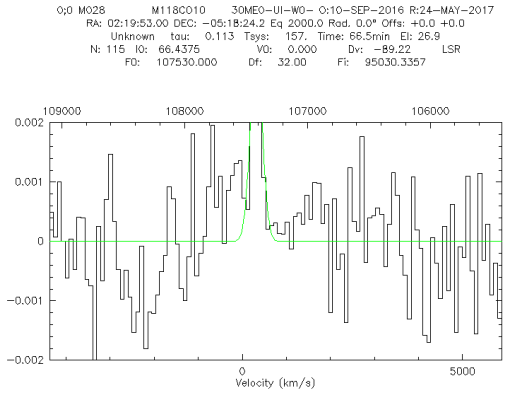

M028

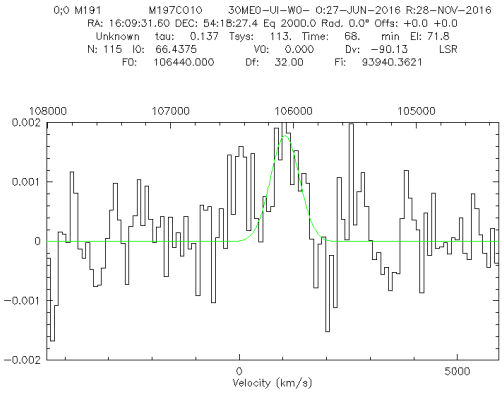

M036

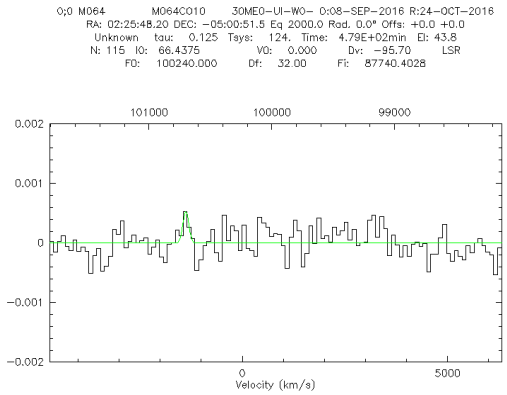

M064

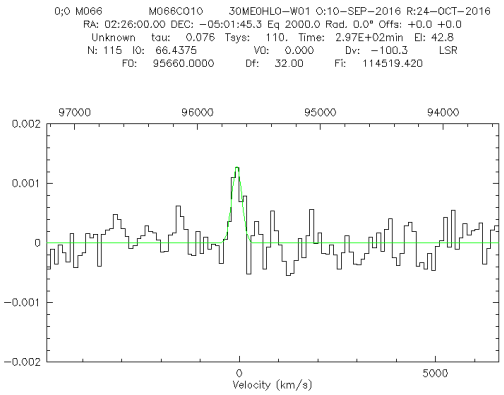

M066

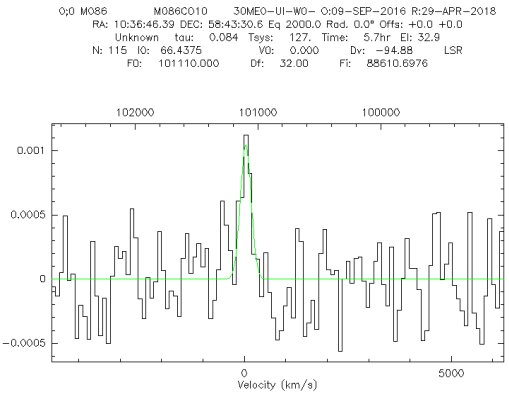

M086

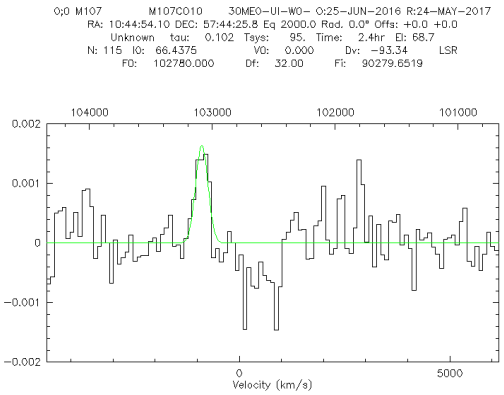

M107

Figure E.1: Measured CO(J=1→0) spectra for the 5MUSES galaxies *(continued)*.

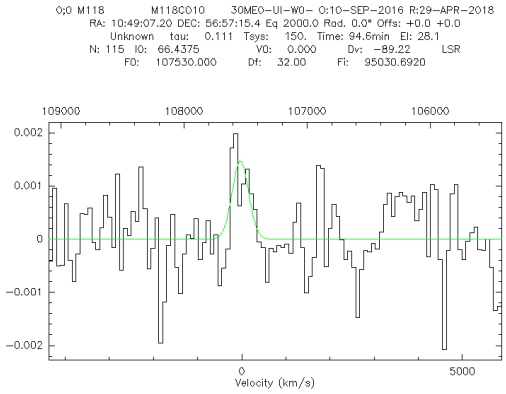

M118

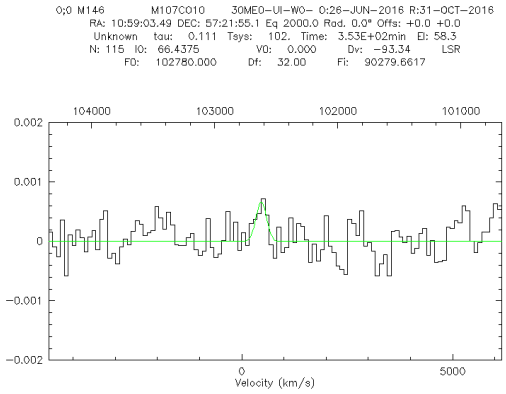

M146

M185

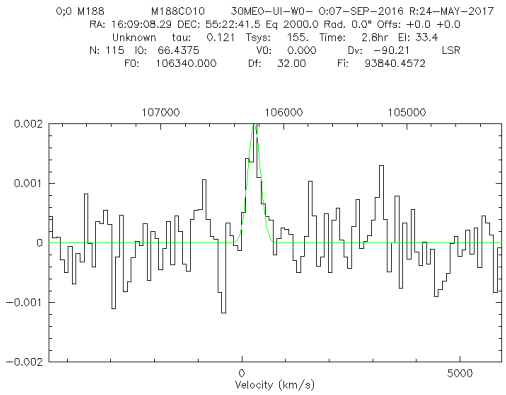

M188

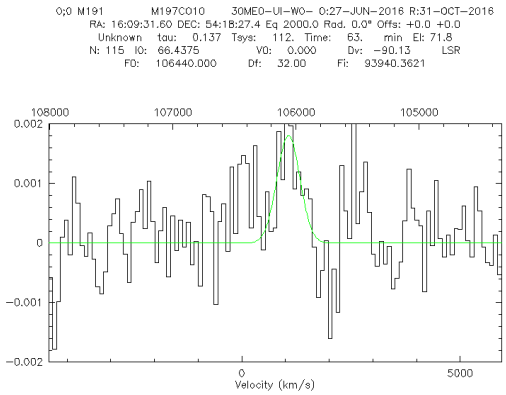

M191

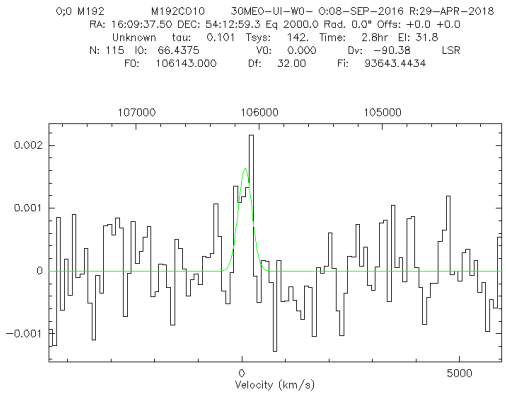

M192

Figure E.1: Measured CO(J=1→0) spectra for the 5MUSES galaxies *(continued)*.

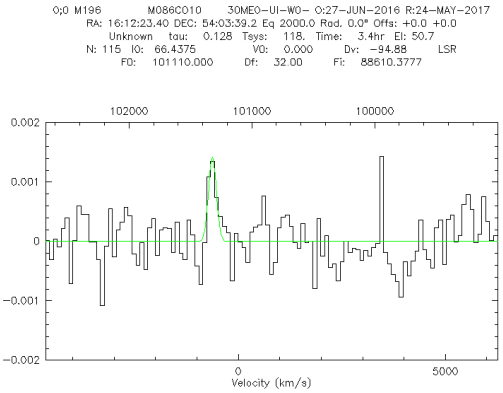

M196

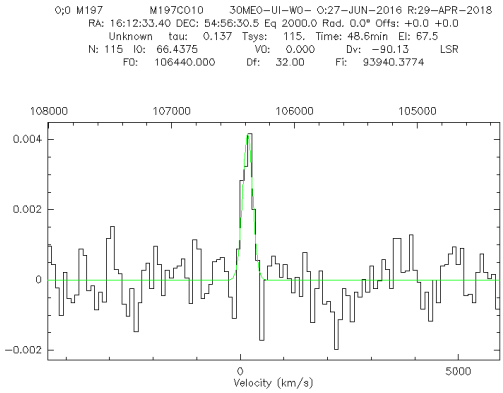

M197

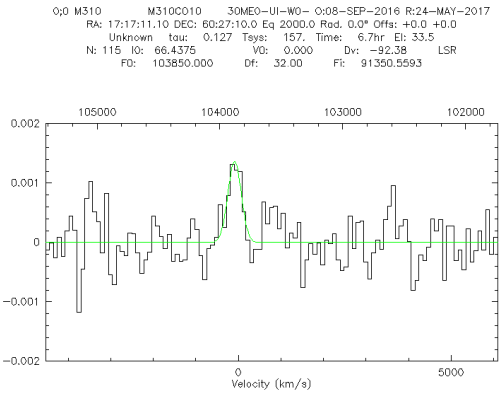

M310

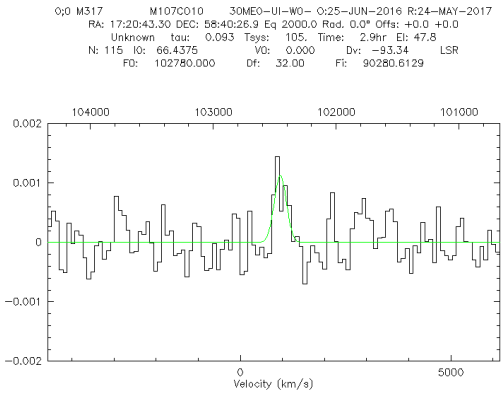

M317

Figure E.1: Measured CO(J=1→0) spectra for the 5MUSES galaxies *(continued)*.

E.2 Images from SDSS

Images from the Sloan Digital Sky Survey[1] (SDSS) were available for all of our target galaxies as well as all of the galaxies included from A. Kirkpatrick, *et al.* [156]. These are shown in Fig. E.2. Note that the full width half maximum (FWHM) beamwidth of both the IRAM 30 m telescope and the LMT (in the early science phase) is ∼22" at 110 GHz. Galaxies M106 and M329 may require an aperture correction for the CO data.

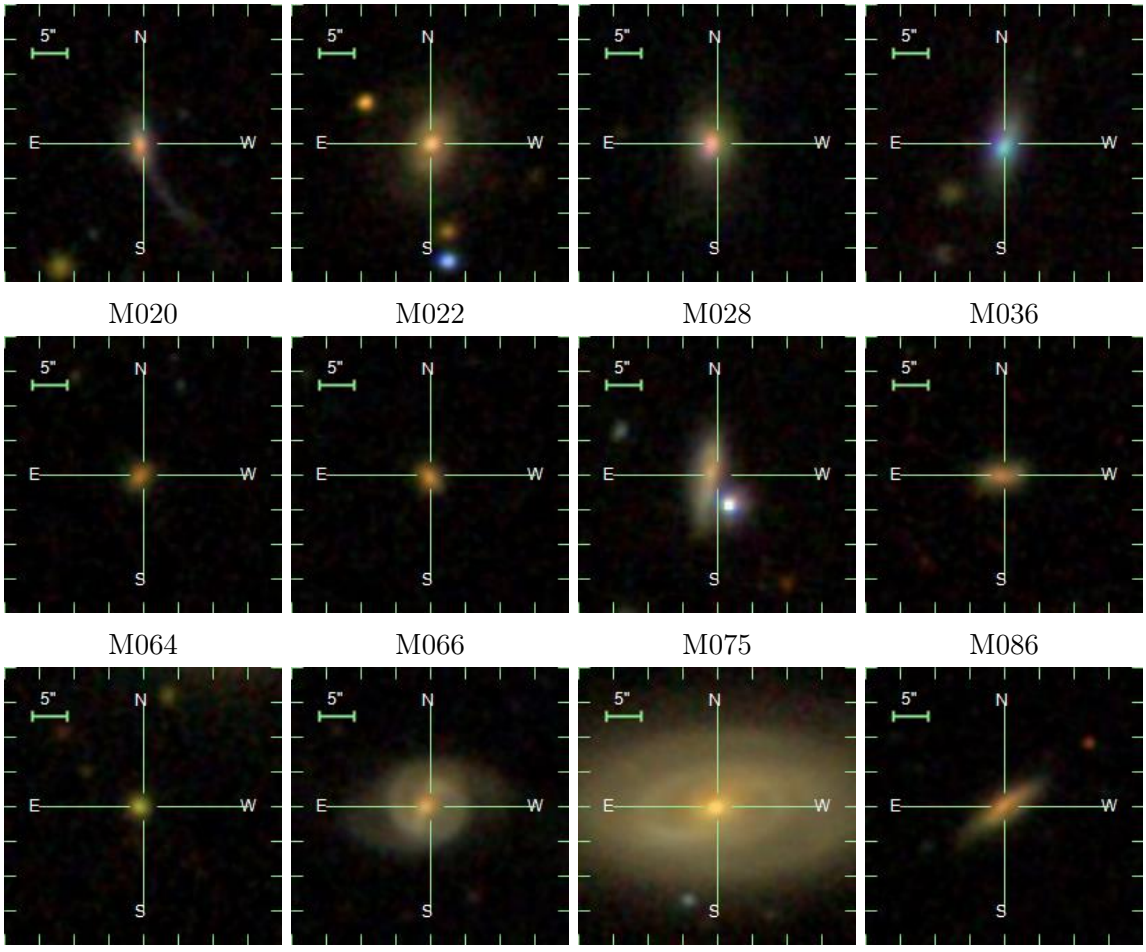

Figure E.2: Images of the target galaxies from the Sloan Digital Sky Survey (SDSS).

[1]Online: http://skyserver.sdss.org/dr13/

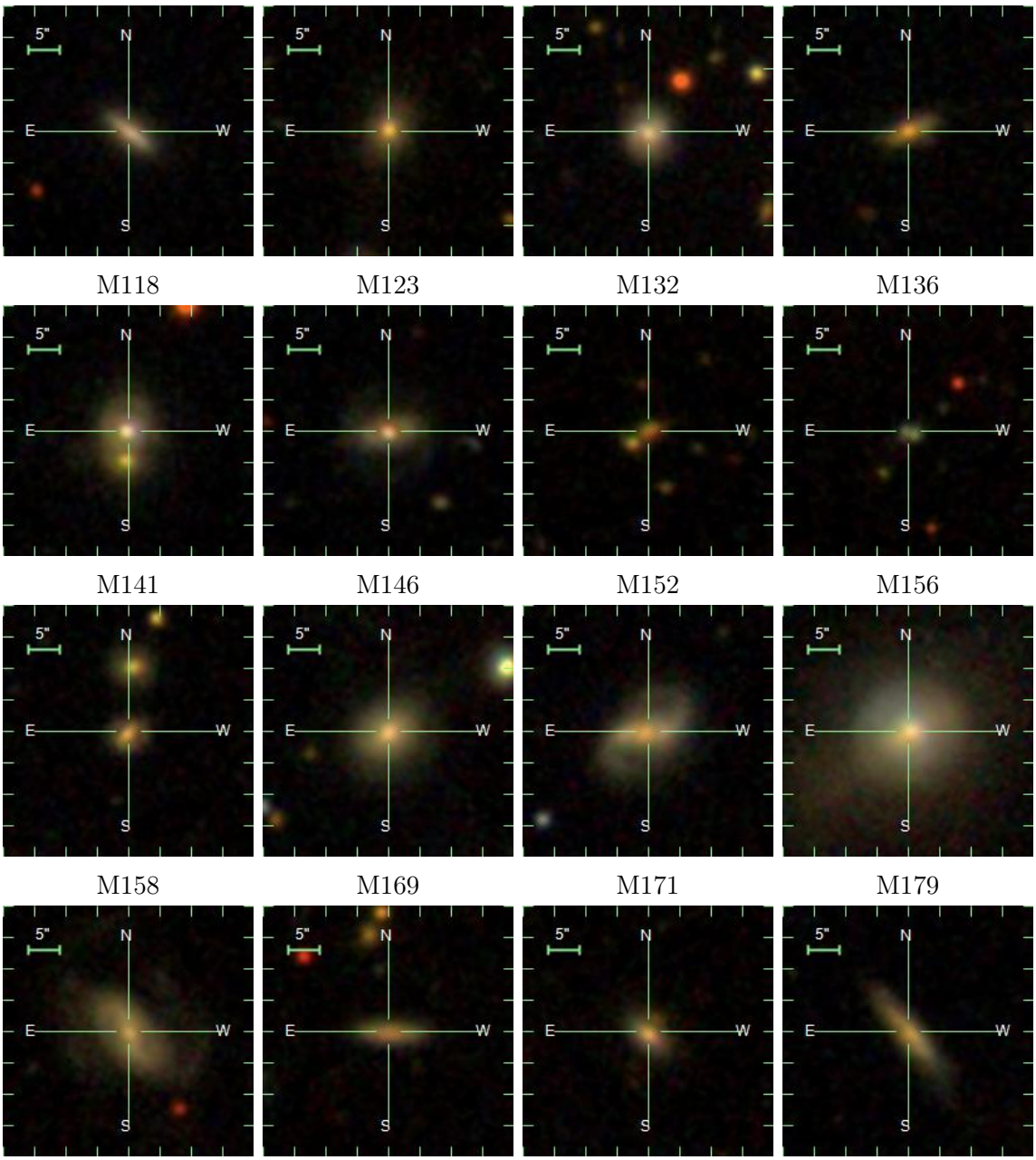

Figure E.2: Galaxy images taken from SDSS *(continued)*.

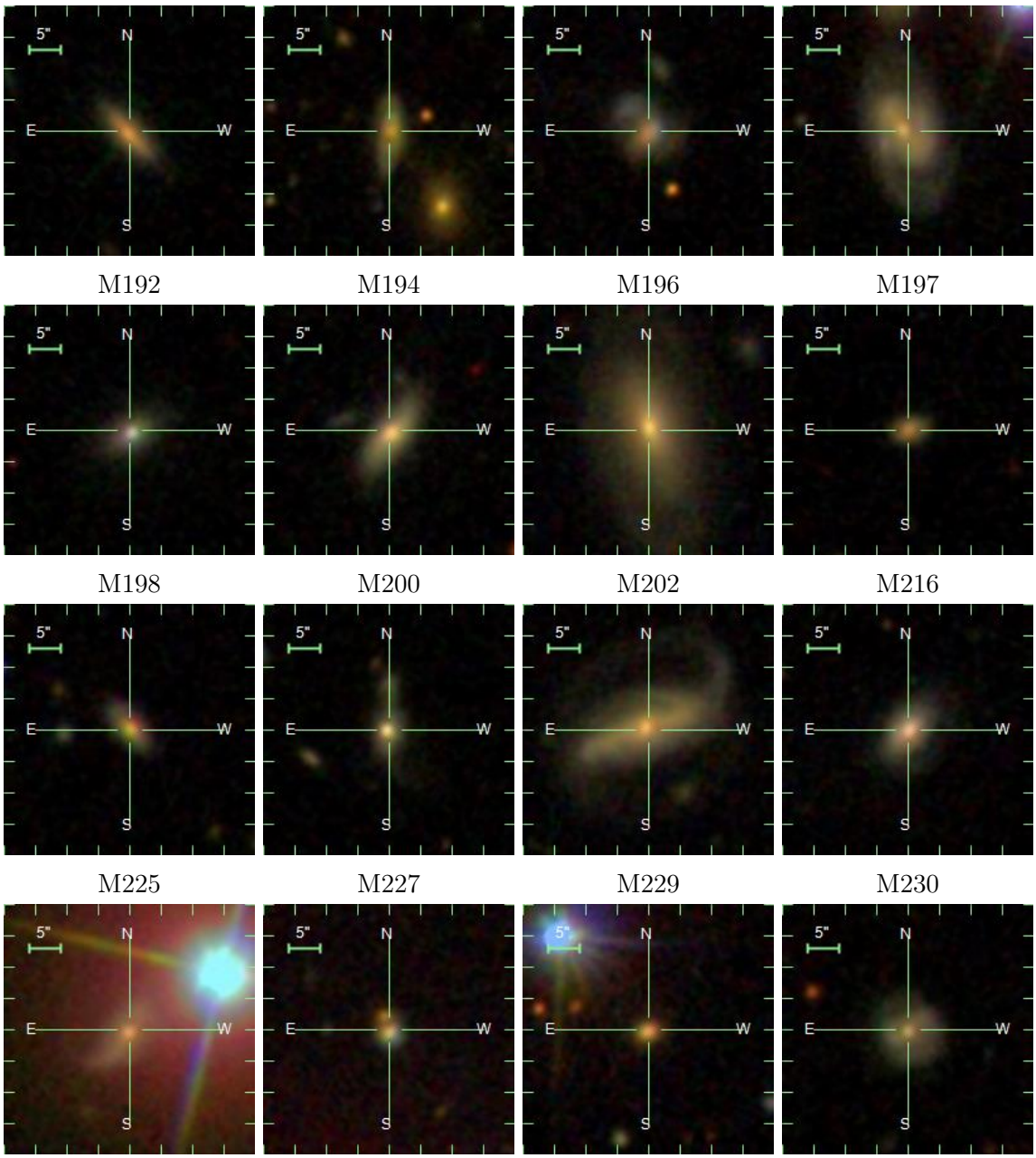

M192 M194 M196 M197

M198 M200 M202 M216

M225 M227 M229 M230

M234 M249 M250 M273

Figure E.2: Galaxy images taken from SDSS *(continued)*.

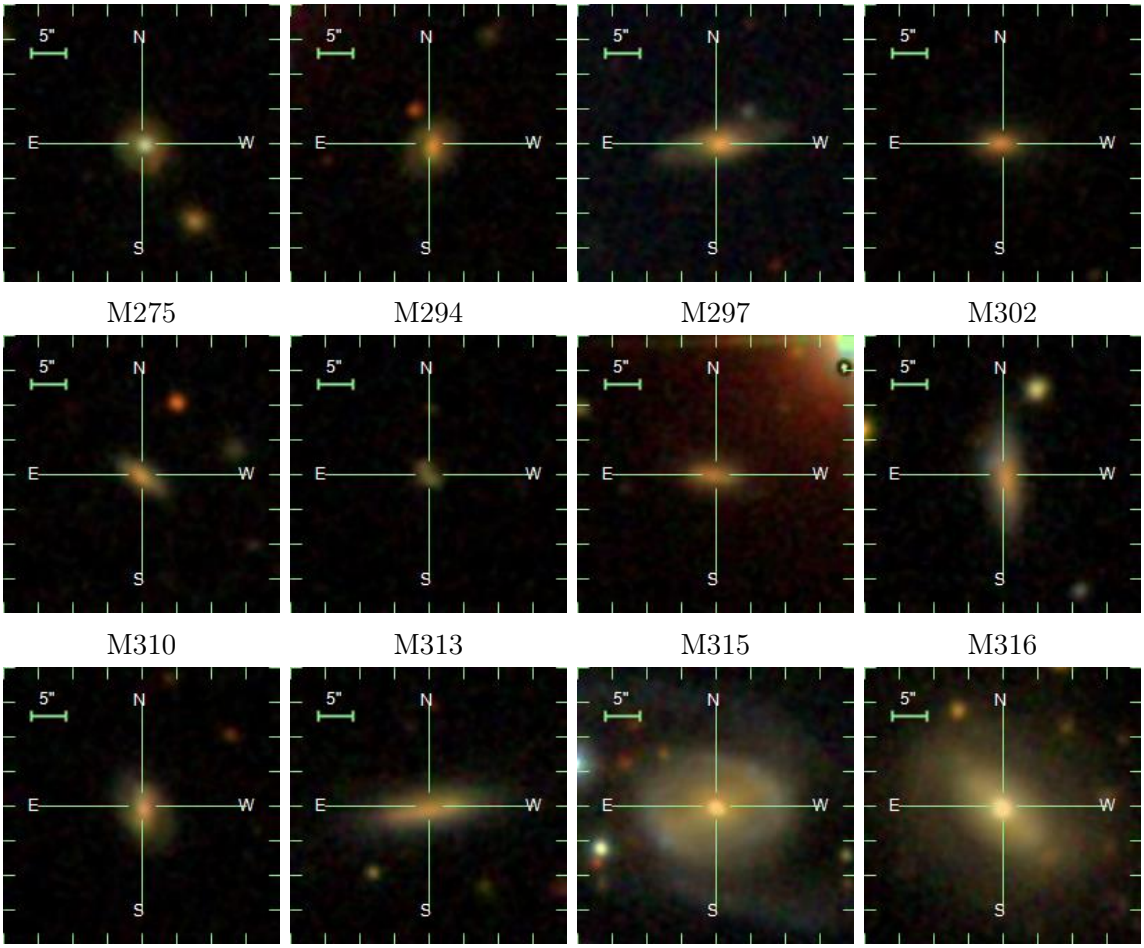

M275 M294 M297 M302

M310 M313 M315 M316

M317 M319 M328 M329

Figure E.2: Galaxy images taken from SDSS *(continued)*.

E.3 Data pertaining to Kirkpatrick *et al.* 2014

A. Kirkpatrick, *et al.* [156] measured CO(J=1→0) emission from 24 galaxies in the 5MUSES sample, 17 of which were detected above 3 σ. These galaxies were included in the analysis in Chp. 6. The data corresponding to these galaxies is listed in the tables below: the infrared properties in Table E.1, the metallicities in Table E.2, and the CO(J=1→0) results in Table E.3.

Table E.1: Target galaxies included from Kirkpatrick *et al.* 2014.

5MUSES ID	RA (J2000)	DEC (J2000)	$z_{\rm IR}^{*\dagger}$	EW$_{6.2}{}^{\dagger}$ (µm)	$\log_{10}\left(\frac{L_{\rm IR}}{L_\odot}\right)^{\dagger\ddagger}$
101	10$^{\rm h}$41'59.8"	+58°58'56.4"	0.360^b	$<$ 0.127	11.93 ± 0.02
105	10$^{\rm h}$44'32.9"	+56°40'41.6"	0.067^a	0.637 ± 0.117	10.90 ± 0.03
132	10$^{\rm h}$52'06.6"	+58°09'47.1"	0.117^b	0.661 ± 0.009	11.32 ± 0.03
136	10$^{\rm h}$54'21.7"	+58°23'44.7"	0.205^b	0.074 ± 0.001	11.41 ± 0.03
141	10$^{\rm h}$57'05.4"	+58°04'37.4"	0.140^b	0.097 ± 0.001	11.16 ± 0.03
156	15$^{\rm h}$58'33.3"	+54°59'37.2"	0.340^b	0.327 ± 0.012	12.08 ± 0.03
158	16$^{\rm h}$00'38.8"	+55°10'18.7"	0.144^b	0.637 ± 0.020	11.43 ± 0.04
169	16$^{\rm h}$04'08.3"	+54°58'13.1"	0.064^a	0.602 ± 0.009	10.81 ± 0.03
171	16$^{\rm h}$04'40.6"	+55°34'09.3"	0.078^a	0.521 ± 0.035	11.08 ± 0.04
179	16$^{\rm h}$08'03.7"	+54°53'02.0"	0.053^a	0.373 ± 0.019	10.24 ± 0.01
194	16$^{\rm h}$11'19.4"	+55°33'55.4"	0.227^a	$<$ 0.100	11.74 ± 0.03
200	16$^{\rm h}$12'50.9"	+53°23'05.0"	0.048^b	0.405 ± 0.074	10.38 ± 0.05
216	16$^{\rm h}$15'51.5"	+54°15'36.0"	0.215^b	0.445 ± 0.049	11.41 ± 0.04
225	16$^{\rm h}$17'48.1"	+55°18'31.1"	0.145^a	0.363 ± 0.030	11.11 ± 0.05
227	16$^{\rm h}$17'59.2"	+54°15'01.3"	0.135^a	0.137 ± 0.006	11.10 ± 0.06
229	16$^{\rm h}$18'19.3"	+54°18'59.1"	0.083^a	0.472 ± 0.005	11.12 ± 0.04
230	16$^{\rm h}$18'23.1"	+55°27'21.4"	0.084^a	0.613 ± 0.016	11.11 ± 0.03
234	16$^{\rm h}$19'29.6"	+54°18'41.9"	0.100^a	0.487 ± 0.048	11.05 ± 0.02
249	16$^{\rm h}$22'14.8"	+55°06'14.2"	0.237^a	0.470 ± 0.021	11.65 ± 0.02
250	16$^{\rm h}$23'13.1"	+55°11'11.6"	0.236^a	0.405 ± 0.001	11.65 ± 0.02
273	16$^{\rm h}$37'31.4"	+40°51'55.6"	0.189^a	0.404 ± 0.045	11.42 ± 0.05
275	16$^{\rm h}$37'51.4"	+41°30'27.3"	0.287^a	0.131 ± 0.011	12.02 ± 0.04
294	17$^{\rm h}$12'32.4"	+59°21'26.2"	0.210^b	0.507 ± 0.006	11.57 ± 0.04
313	17$^{\rm h}$18'52.7"	+59°14'32.1"	0.322^b	0.112 ± 0.010	11.83 ± 0.05

* Redshifts from either (a) NASA/IPAC Extragalactic Database, or (b) from the IRS spectra (as listed in Y. Wu, *et al.* [25]).
† Values from Y. Wu, *et al.* [25].
‡ Integrated from 5–1000 µm.

Target galaxies included from Kirkpatrick *et al.* 2014 (*continued*).

5MUSES ID	$\log_{10}\left(\frac{\mathrm{SFR}}{\mathrm{M_\odot\,yr^{-1}}}\right)$	$\log_{10}\left(\frac{M_*}{\mathrm{M_\odot}}\right)^{\S}$	$\log_{10}\left(\frac{\mathrm{sSFR}}{\mathrm{Gyr^{-1}}}\right)$	$\log_{10}\left(\frac{\mathrm{sSFR_{MS}}}{\mathrm{Gyr^{-1}}}\right)$
101	2.11 ± 0.02	10.86 ± 0.51	0.24 ± 0.51	-0.62
105	1.08 ± 0.03	10.79 ± 0.26	-0.72 ± 0.26	-0.88
132	1.50 ± 0.03	10.67 ± 0.03	-0.17 ± 0.04	-0.83
136	1.59 ± 0.03	11.41 ± 0.15	-0.83 ± 0.16	-0.75
141	1.34 ± 0.03	11.15 ± 0.16	-0.82 ± 0.16	-0.81
156	2.26 ± 0.03	10.17 ± 0.13	1.09 ± 0.14	-0.64
158	1.61 ± 0.04	10.99 ± 0.23	-0.38 ± 0.24	-0.81
169	0.99 ± 0.03	10.82 ± 0.22	-0.84 ± 0.22	-0.88
171	1.26 ± 0.04	10.93 ± 0.24	-0.67 ± 0.24	-0.87
179	0.42 ± 0.01	11.08 ± 0.23	-1.66 ± 0.23	-0.89
194	1.92 ± 0.03	11.19 ± 0.28	-0.28 ± 0.28	-0.73
200	0.56 ± 0.05	10.48 ± 0.32	-0.92 ± 0.32	-0.89
216	1.59 ± 0.04	10.71 ± 0.06	-0.12 ± 0.08	-0.74
225	1.29 ± 0.05	10.99 ± 0.23	-0.71 ± 0.23	-0.80
227	1.28 ± 0.06	10.73 ± 0.28	-0.46 ± 0.29	-0.81
229	1.30 ± 0.04	11.36 ± 0.15	-1.06 ± 0.16	-0.86
230	1.29 ± 0.03	10.46 ± 0.04	-0.17 ± 0.05	-0.86
234	1.23 ± 0.02	10.47 ± 0.15	-0.24 ± 0.15	-0.85
249	1.83 ± 0.02	10.96 ± 0.15	-0.14 ± 0.15	-0.72
250	1.83 ± 0.02	11.29 ± 0.19	-0.46 ± 0.19	-0.72
273	1.60 ± 0.05	10.97 ± 0.14	-0.38 ± 0.15	-0.77
275	2.20 ± 0.04	11.13 ± 0.01	0.07 ± 0.04	-0.68
294	1.75 ± 0.04	11.49 ± 0.20	-0.75 ± 0.20	-0.75
313	2.01 ± 0.05	10.64 ± 0.22	0.37 ± 0.23	-0.65

§ Masses from Y. Shi, *et al.* [169].

Table E.2: Metallicity of the galaxies from Kirkpatrick *et al.* 2014.

5MUSES ID	$\log_{10}\left(\frac{\text{[NII]}\ \lambda6583}{\text{H}\alpha}\right)^{\dagger}$	$\log_{10}\left(\frac{\text{[OIII]}\ \lambda5007}{\text{H}\beta}\right)^{\dagger}$	12+log(O/H)‡
101	–	–	–
105	-0.1323 ± 0.0122	–	–
132	-0.4306 ± 0.0082	-0.7080 ± 0.0854	9.1891
136	–	0.2892 ± 0.0871	–
141	–	–	–
156	–	–	–
158	–	-0.3644 ± 0.0516	–
169	-0.3224 ± 0.0042	-0.6212 ± 0.0700	–
171	-0.0418 ± 0.0124	–	–
179	0.1250 ± 0.0194	–	–
194	–	–	–
200	-0.0289 ± 0.0150	–	–
216	-0.3214 ± 0.0106	-0.5426 ± 0.0828	–
225	–	–	–
227	–	–	–
229	–	–	–
230	-0.3836 ± 0.0028	-0.5834 ± 0.0331	–
234	-0.2350 ± 0.0083	–	–
249	–	–	–
250	–	–	–
273	-0.1883 ± 0.0240	0.3380 ± 0.0343	–
275	–	–	–
294	–	–	–
313	–	–	–

† Derived from spectra downloaded from SDSS DR13.
‡ From C. Tremonti, *et al.* [173]. Only includes galaxies contained within SDSS DR7.

Table E.3: CO(J=1→0) results from Kirkpatrick *et al.* 2014.

5MUSES ID	$S_{\rm CO}\Delta v$ (Jy km s^{-1})	S/N	$\log_{10}\left(\frac{L'_{\rm CO}}{\rm K\,km\,s^{-1}pc^2}\right)$	$\log_{10}\left(\frac{\rm SFE}{\rm L_\odot/K\,km\,s^{-1}pc^2}\right)$
105	7.19 ± 1.27	5.66	9.20 ± 0.04	1.70 ± 0.08
132	4.28 ± 0.92	4.65	9.45 ± 0.05	1.86 ± 0.10
136	2.30 ± 0.55	4.18	9.68 ± 0.05	1.72 ± 0.10
141	3.06 ± 0.62	4.94	9.47 ± 0.04	1.69 ± 0.09
158	5.17 ± 1.23	4.20	9.73 ± 0.05	1.70 ± 0.11
169	4.47 ± 1.08	4.14	8.94 ± 0.05	1.87 ± 0.10
171	7.60 ± 1.45	5.24	9.34 ± 0.04	1.73 ± 0.09
179	11.30 ± 0.93	12.15	9.18 ± 0.02	1.06 ± 0.04
216	1.82 ± 0.36	5.06	9.63 ± 0.04	1.78 ± 0.09
225	4.52 ± 0.57	7.93	9.67 ± 0.03	1.44 ± 0.07
227	1.17 ± 0.34	3.44	9.01 ± 0.06	2.08 ± 0.13
229	11.30 ± 1.48	7.64	9.56 ± 0.03	1.56 ± 0.07
230	6.38 ± 1.25	5.10	9.33 ± 0.04	1.77 ± 0.09
234	6.24 ± 0.69	9.04	9.48 ± 0.02	1.57 ± 0.05
250	5.56 ± 0.68	8.18	10.20 ± 0.03	1.44 ± 0.05
273	1.81 ± 0.40	4.52	9.51 ± 0.05	1.90 ± 0.10
275	7.77 ± 1.38	5.63	10.52 ± 0.04	1.50 ± 0.08

References

[1] J. Garrett, *et al.*, "A 220 GHz Finline Mixer with Ultra-Wide Instantaneous Bandwidth," in *Proceedings of the Twenty-Sixth International Symposium on Space Terahertz Technology (ISSTT)*, Cambridge, MA, Mar. 2015.

[2] ——, "A 230 GHz Finline SIS Receiver with Wide IF Bandwidth," in *Proceedings of the Twenty-Seventh International Symposium on Space Terahertz Technology (ISSTT)*, Nanjing, China, Apr. 2016.

[3] J. Leech, *et al.*, "An SIS mixer based focal-plane array at 230 GHz," in *Proceedings of the Twenty-Sixth International Symposium on Space Terahertz Technology (ISSTT)*, Cambridge, MA, Mar. 2015.

[4] J. Garrett, *et al.*, "A 1x4 Focal Plane Array Using 230 GHz SIS Mixers," in *Proceedings of the Twenty-Ninth International Symposium on Space Terahertz Technology (ISSTT)*, Los Angeles, CA, Mar. 2018.

[5] I. Cortzen, *et al.*, "PAHs as tracers of the molecular gas in star-forming galaxies," submitted to *Monthly Notices of the Royal Astronomical Society*, 2018.

[6] N. Scoville, *et al.*, "ALMA Resolves the Nuclear Disks of Arp 220," *The Astrophysical Journal*, vol. 836, no. 66, p. 18, Feb. 2017.

[7] K. Sakamoto, *et al.*, "Resolved Structure of the Arp 220 Nuclei at $\lambda \approx 3$ mm," *The Astrophysical Journal*, vol. 849, no. 14, p. 11, Oct. 2017.

[8] L. Barcos-Muñoz, *et al.*, "Fast, Collimated Outflow in the Western Nucleus of Arp 220," *The Astrophysical Journal*, vol. 853, no. L28, p. 7, Feb. 2018.

[9] ALMA Partnership, *et al.*, "The 2014 ALMA Long Baseline Campaign: First Results from High Angular Resolution Observations Toward the HL Tau Region," *The Astrophysical Journal*, vol. 808, no. L3, p. 10, Jul. 2015.

[10] S. Asayama, *et al.*, "ALMA Cycle 5 Technical Handbook," ALMA Partnership, Tech. Rep., 2017.

[11] J. Tucker, "Quantum limited detection in tunnel junction mixers," *IEEE Journal of Quantum Electronics*, vol. 15, no. 11, pp. 1234–1258, Nov. 1979.

[12] J. R. Tucker and M. J. Feldman, "Quantum detection at millimeter wavelengths," *Reviews of Modern Physics*, vol. 57, no. 4, pp. 1055–1113, Oct. 1985.

[13] Y. Fujii, *et al.*, "The First Six ALMA Band 10 Receivers," *IEEE Transactions on Terahertz Science and Technology*, vol. 3, no. 1, pp. 39–49, Jan. 2013.

[14] M. Westig, *et al.*, "Improved Nb SIS devices for heterodyne mixers between 700 GHz and 1.3 THz with NbTiN transmission lines using a normal metal energy relaxation layer," *Journal of Applied Physics*, vol. 114, no. 12, p. 124504, Sep. 2013.

[15] D. Rigopoulou, *et al.*, "Science with ALMA Band 11 (1.0-1.6 THz)," *The Messenger*, vol. 153, pp. 35–37, Sep. 2013.

[16] T. G. Phillips, S. Padin, and J. Zmuidzinas, "Submillimeter Telescopes," in *Planets, Stars and Stellar Systems*, T. D. Oswalt and W. C. Keel, Eds. Dordrecht: Springer Netherlands, 2013, pp. 283–313.

[17] S. Claude, *et al.*, "The Band 3 receiver (84-116 GHz) for ALMA," in *2005 Joint 30th International Conference on Infrared and Millimeter Waves and 13th International Conference on Terahertz Electronics*, Williamsburg, 2005.

[18] S. Asayama, *et al.*, "Development of ALMA Band 4 (125-163 GHz) receiver," *Publications of the Astronomical Society of Japan*, vol. 66, no. 3, pp. 57–57, Jun. 2014.

[19] B. Billade, *et al.*, "Performance of the First ALMA Band 5 Production Cartridge," *IEEE Transactions on Terahertz Science and Technology*, vol. 2, no. 2, pp. 208–214, Mar. 2012.

[20] G. Ediss, *et al.*, "ALMA Band 6 Cartridge: Design and Performance," in *Proceedings of the Fifteenth International Symposium on Space Terahertz Technology (ISSTT)*, Northampton, MA, 2004.

[21] S. Mahieu, *et al.*, "The ALMA Band-7 Cartridge," *IEEE Transactions on Terahertz Science and Technology*, vol. 2, no. 1, pp. 29–39, Jan. 2012.

[22] W. Shan, *et al.*, "Design and Development of SIS Mixers for ALMA Band 8," *IEEE Transactions on Appiled Superconductivity*, vol. 15, no. 2, pp. 503–506, Jun. 2005.

[23] A. Baryshev, *et al.*, "The ALMA Band 9 receiver," *Astronomy & Astrophysics*, vol. 577, no. A129, p. 12, May 2015.

[24] A. Kerr, *et al.*, "Development of the ALMA Band-3 and Band-6 Sideband-Separating SIS Mixers," *IEEE Transactions on Terahertz Science and Technology*, vol. 4, no. 2, pp. 201–212, Mar. 2014.

[25] Y. Wu, *et al.*, "Infrared Luminosities and Aromatic Features in the 24 μm Flux-Limited Sample of 5MUSES," *The Astrophysical Journal*, vol. 723, no. 1, pp. 895–914, Nov. 2010.

[26] J. R. Tucker, "Predicted conversion gain in superconductor-insulator-superconductor quasiparticle mixers," *Applied Physics Letters*, vol. 36, no. 6, pp. 477–479, Mar. 1980.

[27] L. N. Cooper, "Bound Electron Pairs in a Degenerate Fermi Gas," *Physical Review*, vol. 104, no. 4, pp. 1189–1190, Nov. 1956.

[28] J. Bardeen, L. N. Cooper, and J. R. Schrieffer, "Theory of Superconductivity," *Physical Review*, vol. 108, no. 5, pp. 1175–1204, Dec. 1957.

[29] I. Giaever, "Electron Tunneling Between Two Superconductors," *Physical Review Letters*, vol. 5, no. 10, pp. 464–466, Nov. 1960.

[30] J. Nicol, S. Shapiro, and P. H. Smith, "Direct Measurement of the Superconducting Energy Gap," *Physical Review Letters*, vol. 5, no. 10, pp. 461–464, Nov. 1960.

[31] B. Josephson, "Possible new effects in superconductive tunnelling," *Physics Letters*, vol. 1, no. 7, pp. 251–253, Jul. 1962.

[32] L. Esaki, "New Phenomenon in Narrow Germanium p-n Junctions," *Physical Review*, vol. 109, no. 2, pp. 603–604, Jan. 1958.

[33] A. H. Dayem and R. J. Martin, "Quantum Interaction of Microwave Radiation with Tunneling Between Superconductors," *Physical Review Letters*, vol. 8, no. 6, pp. 246–248, Mar. 1962.

[34] P. K. Tien and J. P. Gordon, "Multiphoton Process Observed in the Interaction of Microwave Fields with the Tunneling between Superconductor Films," *Physical Review*, vol. 129, no. 2, pp. 647–651, Jan. 1963.

[35] M. Tinkham, *Introduction to Superconductivity*, 2nd ed. Dover Publications, 2004.

[36] E. Bezuglyi, *et al.*, "Subgap current in superconducting tunnel junctions with diffusive electrodes," *Physical Review B*, vol. 73, no. 22, p. 220506, Jun. 2006.

[37] B. Mitrović and L. a. Rozema, "On the correct formula for the lifetime broadened superconducting density of states," *Journal of Physics: Condensed Matter*, vol. 20, no. 1, p. 015215, Jan. 2008.

[38] R. C. Dynes, V. Narayanamurti, and J. P. Garno, "Direct Measurement of Quasiparticle-Lifetime Broadening in a Strong-Coupled Superconductor," *Physical Review Letters*, vol. 41, no. 21, pp. 1509–1512, Nov. 1978.

[39] T. Noguchi, T. Suzuki, and T. Tamura, "Subgap Tunneling Current at Low Temperature in Nb/Al-AlN/Nb SIS Junctions," *IEEE Transactions on Applied Superconductivity*, vol. 21, no. 3, pp. 756–759, Jun. 2011.

[40] T. Noguchi, *et al.*, "Contribution of the imaginary part of the superconducting gap energy on the SIS tunneling current," *Physica C: Superconductivity*, vol. 469, no. 15-20, pp. 1585–1588, Oct. 2009.

[41] W. L. McMillan, "Tunneling Model of the Superconducting Proximity Effect," *Physical Review*, vol. 175, no. 2, pp. 537–542, Nov. 1968.

[42] A. Zehnder, *et al.*, "Proximity effects in Nb/Al-AlOx-Al/Nb superconducting tunneling Junctions," *Physical Review B*, vol. 59, no. 13, pp. 8875–8886, Apr. 1999.

[43] A. Golubov, *et al.*, "Proximity effect in superconductor-insulator-superconductor Josephson tunnel junctions: Theory and experiment," *Physical Review B*, vol. 51, no. 2, pp. 1073–1089, Jan. 1995.

[44] E. Houwman, *et al.*, "Proximity effect in Nb/Al, AlOxide, Al/Nb Josephson tunnel junctions," *IEEE Transactions on Applied Superconductivity*, vol. 3, no. 1, pp. 2170–2173, Mar. 1993.

[45] N. R. Werthamer, "Nonlinear Self-Coupling of Josephson Radiation in Superconducting Tunnel Junctions," *Physical Review*, vol. 147, no. 1, pp. 255–263, Jul. 1966.

[46] H. A. Kramers, "The Quantum Theory of Dispersion," *Nature*, vol. 114, no. 2861, pp. 310–311, Aug. 1924.

[47] R. de L. Kronig, "On the Theory of Dispersion of X-Rays," *Journal of the Optical Society of America*, vol. 12, no. 6, pp. 547–557, Jun. 1926.

[48] P. W. Anderson and J. M. Rowell, "Probable Observation of the Josephson Superconducting Tunneling Effect," *Physical Review Letters*, vol. 10, no. 6, pp. 230–232, Mar. 1963.

[49] H. B. Callen and T. A. Welton, "Irreversibility and Generalized Noise," *Physical Review*, vol. 83, no. 1, pp. 34–40, Jul. 1951.

[50] D. Rogovin and D. Scalapino, "Fluctuation phenomena in tunnel junctions," *Annals of Physics*, vol. 86, no. 1, pp. 1–90, Jul. 1974.

[51] R. Blundell, R. E. Miller, and K. H. Gundlach, "Understanding noise in SIS receivers," *International Journal of Infrared and Millimeter Waves*, vol. 13, no. 1, pp. 3–14, Jan. 1992.

[52] Q. Ke and M. Feldman, "Optimum source conductance for high frequency superconducting quasiparticle receivers," *IEEE Transactions on Microwave Theory and Techniques*, vol. 41, no. 4, pp. 600–604, Apr. 1993.

[53] C. E. Tong, A. Hedden, and R. Blundell, "An Empirical Probe to the Operation of SIS Receivers – Revisiting the Technique of Intersecting Lines," in *Proceedings of the Ninteenth International Symposium on Space Terahertz Technology (ISSTT)*, Groningen, 2008, pp. 314–318.

[54] D. Woody, R. Miller, and M. Wengler, "85–115-GHz Receivers for Radio Astronomy," *IEEE Transactions on Microwave Theory and Techniques*, vol. 33, no. 2, pp. 90–95, Feb. 1985.

[55] A. Skalare, "Determining embedding circuit parameters from DC measurements on quasiparticle mixers," *International Journal of Infrared and Millimeter Waves*, vol. 10, no. 11, pp. 1339–1353, Nov. 1989.

[56] S. Withington, *et al.*, "Direct detection at submillimetre wavelengths using superconducting tunnel junctions," *Infrared Physics & Technology*, vol. 36, no. 7, pp. 1059–1075, Dec. 1995.

[57] T. Kojima, *et al.*, "Performance and Characterization of a Wide IF SIS-Mixer-Preamplifier Module Employing High-J c SIS Junctions," *IEEE Transactions on Terahertz Science and Technology*, vol. 7, no. 6, pp. 694–703, Nov. 2017.

[58] C. Tong, *et al.*, "A Distributed Lumped-Element SIS Mixer With Very Wide Instantaneous Bandwidth," *IEEE Transactions on Appiled Superconductivity*, vol. 15, no. 2, pp. 490–494, Jun. 2005.

[59] J. Schleeh, *et al.*, "Cryogenic Broadband Ultra-Low-Noise MMIC LNAs for Radio Astronomy Applications," *IEEE Transactions on Microwave Theory and Techniques*, vol. 61, no. 2, pp. 871–877, Feb. 2013.

[60] A. Akgiray, *et al.*, "Noise Measurements of Discrete HEMT Transistors and Application to Wideband Very Low-Noise Amplifiers," *IEEE Transactions on Microwave Theory and Techniques*, vol. 61, no. 9, pp. 3285–3297, Sep. 2013.

[61] S. Padin, *et al.*, "An integrated SIS mixer and HEMT IF amplifier," *IEEE Transactions on Microwave Theory and Techniques*, vol. 44, no. 6, pp. 987–990, Jun. 1996.

[62] S. Montazeri, *et al.*, "A 220-GHz SIS Mixer Tightly Integrated With a Sub-Hundred-Microwatt SiGe IF Amplifier," *IEEE Transactions on Terahertz Science and Technology*, vol. 6, no. 1, pp. 133–140, Jan. 2016.

[63] B.-K. Tan, G. Yassin, and P. Grimes, "Ultra-Wide Intermediate Bandwidth for High-Frequency SIS Mixers," *IEEE Transactions on Terahertz Science and Technology*, vol. 4, no. 2, pp. 165–170, Mar. 2014.

[64] C. Tong, *et al.*, "A wideband 240 GHz receiver for the submillimeter array," in *Proceedings Volume 9914, Millimeter, Submillimeter, and Far-Infrared Detectors and Instrumentation for Astronomy VIII*, W. S. Holland and J. Zmuidzinas, Eds., Jul. 2016, p. 99140F.

[65] ——, "Ultra-wide IF bandwidth – The next frontier for SIS receivers," in *2015 IEEE MTT-S International Microwave Symposium*. IEEE, May 2015, pp. 1–4.

[66] A. Kerr, *et al.*, "Development of Second-Generation SIS Receivers for ALMA," NRAO, Tech. Rep. 445, 2017.

[67] S. Iguchi and D. Iono, "What are scientifically valuable developments for ALMA enhancement?" in *SPIE Astronomical Telescopes + Instrumentation*, L. M. Stepp, R. Gilmozzi, and H. J. Hall, Eds., Montreal, 2014, p. 914520.

[68] D. Maier, *et al.*, "230 GHz SSB SIS mixer for band 3 of the new generation receivers for the Plateau de Bure interferometer," in *Proceedings of the Sixteenth International Symposium on Space Terahertz Technology (ISSTT)*, Göteborg, Sweden, 2005, pp. 33–36.

[69] M. Carter, *et al.*, "The EMIR multi-band mm-wave receiver for the IRAM 30-m telescope," *Astronomy & Astrophysics*, vol. 538, p. A89, 2012.

[70] T. K. Sridharan and K. Young, "SMA Observer Center," 2017. [Online]. Available: http://sma1.sma.hawaii.edu/status.html

[71] G. Yassin, *et al.*, "Broadband 230 GHz finline mixer for astronomical imaging arrays," *Electronics Letters*, vol. 33, no. 6, pp. 498–500, Mar. 1997.

[72] Y. Zhou, *et al.*, "Performance of a 230 GHz Finline SIS Mixer With a Wide IF Bandwidth," in *Proceedings of the Twenty-Third International Symposium on Space Terahertz Technology (ISSTT)*, Tokyo, Japan, 2012, pp. 111–116.

[73] C. North, G. Yassin, and P. Grimes, "Rigorous analysis of finline tapers for high performance millimetre and submillimetre detectors," in *Proceedings of the Seventeenth International Symposium on Space Terahertz Technology (ISSTT)*, Paris, France, 2006, pp. 284–287.

[74] J. Ward, F. Rice, and G. Chattopadhyay, "SuperMix : A Flexible Software Library for High-Frequency Circuit Simulation, Including SIS Mixers and Superconducting Elements," in *Proceedings of the Tenth International Symposium on Space Terahertz Technology (ISSTT)*, Charlottesville VA, 1999, pp. 269–281.

[75] D. C. Mattis and J. Bardeen, "Theory of the Anomalous Skin Effect in Normal and Superconducting Metals," *Physical Review*, vol. 111, no. 2, pp. 412–417, Jul. 1958.

[76] A. R. Kerr, "Surface Impedance of Superconductors and Normal Conductors in EM Simulators," National Radio Astronomy Observatory, Green Bank, West Virginia, Tech. Rep. 302, 1996.

[77] P. Serres, *et al.*, "The IF Output Impedance of SIS Mixers," *IEEE Transactions on Terahertz Science and Technology*, vol. 5, no. 1, pp. 1–10, 2014.

[78] M. Gurvitch, M. A. Washington, and H. A. Huggins, "High quality refractory Josephson tunnel junctions utilizing thin aluminum layers," *Applied Physics Letters*, vol. 42, no. 5, pp. 472–474, Mar. 1983.

[79] R. D. McCarty and V. D. Arp, "A New Wide Range Equation of State for Helium," in *Advances in Cryogenic Engineering*, R. Fast, Ed. Boston, MA: Springer, 1990.

[80] R. Finger, "ALMA RF membrane simulations," Atacama Large Millimeter Array (ALMA), Tech. Rep., 2007.

[81] D. J. Benford, M. C. Gaidis, and J. W. Kooi, "Optical properties of Zitex in the infrared to submillimeter," *Applied Optics*, vol. 42, no. 25, pp. 5118–2122, Sep. 2003.

[82] D. K. Finnemore, T. F. Stromberg, and C. A. Swenson, "Superconducting Properties of High-Purity Niobium," *Physical Review*, vol. 149, no. 1, pp. 231–243, Sep. 1966.

[83] P. Dhakal, *et al.*, "Superconducting DC and RF Properties of Ingot Niobium," *arXiv*, vol. 1202.0811, Feb. 2012.

[84] C. P. Poole, H. A. Farach, and R. J. Creswick, *Superconductivity*, 1st ed. Academic Press, 1995.

[85] S. Withington and E. Kollberg, "Spectral-domain analysis of harmonic effects in superconducting quasiparticle mixers," *IEEE Transactions on Microwave Theory and Techniques*, vol. 37, no. 1, pp. 231–238, Jan. 1989.

[86] A. Ermakov, *et al.*, "Broken-step Phenomenon in SIS Mixers," in *Proceedings of the Twenty-Seventh International Symposium on Space Terahertz Technology (ISSTT)*, Nanjing, 2016.

[87] A. Semenov, *et al.*, "Coherent Excited States in Superconductors due to a Microwave Field," *Physical Review Letters*, vol. 117, no. 4, pp. 1–5, 2016.

[88] R. M. Fano, "Theoretical limitations on the broadband matching of arbitrary impedances," Massachusetts Institute of Technology (MIT), Tech. Rep. 41, 1948.

[89] H. Bode, *Network Analysis and Feedback Amplifier Design*. New York: Van Nostrand, 1945.

[90] A. Kerr, "Some fundamental and practical limits on broadband matching to capacitive devices, and the implications for SIS mixer design," *IEEE Transactions on Microwave Theory and Techniques*, vol. 43, no. 1, pp. 2–13, Jan. 1995.

[91] H. Inoue, T. Noguchi, and K. Kohno, "SIS junction as a microwave noise source," *Journal of Physics: Conference Series*, vol. 234, no. 4, p. 042014, Jun. 2010.

[92] E. Sundin, A. Pavolotsky, and C. Risacher, "Cryogenic LNA Characterization with SIS Junction as Noise Source," in *Proceedings of the Sixteenth International Symposium on Space Terahertz Technology (ISSTT)*, no. January, 2006, pp. 188–190.

[93] P. Richards, *et al.*, "Quasiparticle heterodyne mixing in SIS tunnel junctions," *Applied Physics Letters*, vol. 34, no. 5, pp. 345–347, Mar. 1979.

[94] T. Shen, *et al.*, "Conversion gain in mm-wave quasiparticle heterodyne mixers," *Applied Physics Letters*, vol. 36, no. 9, pp. 777–779, May 1980.

[95] S. Rudner, *et al.*, "The antenna-coupled SIS quasiparticle array mixer," *IEEE Transactions on Magnetics*, vol. 17, no. 1, pp. 690–693, Jan. 1981.

[96] W. McGrath, *et al.*, "Large gain, negative resistance, and oscillations in superconducting quasiparticle heterodyne mixers," *Applied Physics Letters*, vol. 39, no. 8, pp. 655–658, Oct. 1981.

[97] A. Kerr, *et al.*, "Infinite available gain in a 115 GHz SIS mixer," *Physica B+C*, vol. 108, no. 1-3, pp. 1369–1370, Aug. 1981.

[98] S. Withington and P. Kennedy, "Numerical procedure for simulating the large-signal quantum behaviour of superconducting tunnel-junction circuits," *IEE Proceedings G Circuits, Devices and Systems*, vol. 138, no. 1, p. 70, Feb. 1991.

[99] M. J. Feldman and S. Rudner, "Mixing with SIS Arrays," in *Reviews of Infrared and Millimeter Waves*. Boston, MA: Springer US, 1983, pp. 47–75.

[100] P. Kittara, "The Development of a 700 GHz SIS Mixer with Nb Finline Devices: Nonlinear Mixer Theory, Design Techniques and Experimental Investigation," Doctor of Philosophy, University of Cambridge, 2002.

[101] S. Withington, P. Kittara, and G. Yassin, "Multitone quantum simulations of saturating tunnel junction mixers," *Journal of Applied Physics*, vol. 93, no. 12, pp. 9812–9822, Jun. 2003.

[102] P. Kittara, S. Withington, and G. Yassin, "Theoretical and numerical analysis of very high harmonic superconducting tunnel junction mixers," *Journal of Applied Physics*, vol. 101, no. 2, p. 024508, Jan. 2007.

[103] P. Kennedy, "Superconducting Devices for Millimetre Wavelength Astronomy," Ph.D. dissertation, University of Cambridge, 1991.

[104] K. Schuster, *et al.*, "A complete CO 2-1 map of M 51 with HERA," *Astronomy & Astrophysics*, vol. 461, no. 1, pp. 143–151, Jan. 2007.

[105] C. Groppi, *et al.*, "The Kilopixel Array Pathfinder Project (KAPPa), a 16 pixel integrated heterodyne focal plane array," in *Proceedings of the Thirty-Ninth International Conference on Infrared, Millimeter, and Terahertz waves (IRMMW-THz)*, W. S. Holland, Ed., vol. 8452, Tucson, Sep. 2012.

[106] K. Schuster, *et al.*, "A 230 GHz heterodyne receiver array for the IRAM 30 m telescope," *Astronomy & Astrophysics*, vol. 423, no. 3, pp. 1171–1177, Sep. 2004.

[107] J. M. Payne, "Multibeam receiver for millimeter-wave radio astronomy," *Review of Scientific Instruments*, vol. 59, no. 9, pp. 1911–1919, Sep. 1988.

[108] J. Payne and P. Jewell, "The Upgrade of the NRAO 8-beam receiver," in *Proceedings of the ASP Conference Series*, vol. 75, Tucson, 1995, pp. 114–148.

[109] K. Sunada, *et al.*, "Development and First Result from the NRO SIS 25 BEam Array Receiver System (BEARS)," in *Imaging at Radio through Submillimeter Wavelengths, ASP Conference Proceedings*, 2000, pp. 19–22.

[110] ——, "BEARS - SIS 25-Beam Array Receiver System for the NRO 45-m Telescope," in *Astronomical Telescopes and Instrumentation*, H. R. Butcher, Ed., vol. 4015, Jul. 2000, pp. 237–246.

[111] R. Guesten, *et al.*, "CHAMP: the Carbon Heterodyne Array of the MPIfR," in *Proc. SPIE 3357, Advanced Technology MMW, Radio, and Terahertz Telescopes*, Kona, HI, Jul. 1998, pp. 167–177.

[112] C. Walker, *et al.*, "PoleStar: An 810 GHz Array Receiver for AST/RO," in *Proceedings of the Twelfth International Symposium on Space Terahertz Technology (ISSTT)*, San Diego, Feb. 2001, pp. 540–552.

[113] K. Schuster, *et al.*, "The IRAM 230 GHz Multibeam SIS Receiver," in *Proceedings of the Eighth International Symposium on Space Terahertz Technology (ISSTT)*, Cambridge, MA, 1997, pp. 499–504.

[114] ——, "The IRAM 230 GHz Multibeam Receiver," in *Proceedings of SPIE Vol. 4015: Radio Telescopes*, H. R. Butcher, Ed., Munich, Jul. 2000, pp. 260–267.

[115] U. Graf, *et al.*, "SMART: The KOSMA sub-millimeter array receiver for two frequencies," in *Proceedings of the Thirteenth International Symposium on Space Terahertz Technology (ISSTT)*, Cambridge, Mar. 2002, pp. 143–152.

[116] ——, "Upgrade of the SMART Focal Plane Array Receiver for NANTEN2," in *Proceedings of the Ninteenth International Symposium on Space Terahertz Technology (ISSTT)*, Groningen, Apr. 2008.

[117] R. Higgins, "NANTEN2 / SMART Receiver overview," in *NANTEN Workshop*, Melbourne, 2013.

[118] C. Groppi, *et al.*, "DesertSTAR: a 7 pixel 345 GHz heterodyne array receiver for the Heinrich Hertz Telescope," in *Proceedings of SPIE - The International Society for Optical Engineering*, T. G. Phillips and J. Zmuidzinas, Eds., vol. 4855, Marseille, Feb. 2003, pp. 330–337.

[119] ——, "First results from DesertSTAR: a 7-pixel 345-GHz heterodyne array receiver for the Heinrich Hertz Telescope," in *Proc. of SPIE*, J. Zmuidzinas, W. S. Holland, and S. Withington, Eds., vol. 4855, Oct. 2004, p. 290.

[120] J. Buckle, *et al.*, "HARP/ACSIS: a submillimetre spectral imaging system on the James Clerk Maxwell Telescope," *Monthly Notices of the Royal Astronomical Society*, vol. 399, no. 2, pp. 1026–1043, Oct. 2009.

[121] C. Kasemann, *et al.*, "CHAMP+: A Powerful Submm Heterodyne Array," in *Proceedings of the Ninteenth International Symposium on Space Terahterz Technology (ISSTT)*, Groningen, Apr. 2008, pp. 166–172.

[122] C. Groppi, *et al.*, "SuperCam : A 64 pixel heterodyne array receiver for the 350 GHz Atmospheric Window," in *Proceedings of the Twentieth International Symposium on Space Terahertz Technology (ISSTT)*, Charlottesville, Apr. 2009, pp. 90–96.

[123] T. Minamidani, *et al.*, "Development of the new multi-beam 100 GHz band SIS receiver FOREST for the Nobeyama 45-m Telescope," in *Proc. SPIE 9914, Millimeter, Submillimeter, and Far-Infrared Detectors and Instrumentation for Astronomy VIII*, Edinburgh, Jul. 2016.

[124] T. Nakajima, *et al.*, "Development of a New Multi-Beam Array 2SB Receiver in 100 GHz Band for the NRO 45-m Radio Telescope," in *Proceedings of the International Symposium on Space Terahertz Technology (ISSTT)*, 2012.

[125] R. Güsten, *et al.*, "Submillimeter heterodyne arrays for APEX," in *Proc. SPIE*, W. D. Duncan, W. S. Holland, S. Withington, and J. Zmuidzinas, Eds., vol. 7020, Aug. 2008, p. 702010.

[126] S. Heyminck, "A-MKID, PI230, LAsMA: new MPIfR receivers for APEX," in *Science with the Atacama Pathfinder Experiment (APEX)2*, Schloss Ringberg, 2016.

[127] D. Maier, "230 GHz sideband-separating mixer array," in *Proceedings of the Twentieth International Symposium on Space Terahertz Technology*, Charlottesville, VA, 2009, pp. 14–18.

[128] D. Maier, *et al.*, "7-pixels prototype for a 230 GHz multi-beam receiver," in *Proceedings of the Twenty-Seventh International Symposium on Space Terahertz Technology (ISSTT)*, Nanjing, 2016.

[129] P. Goldsmith, "Studying the Formation and Development of Molecular Clouds: with the CCAT Heterodyne Array Instrument (CHAI)," in *Institut d' Astrophysique de Paris (France), CCAT Day*, Paris, 2012.

[130] "The CCAT Project," 2015.

[131] J. Yang, *et al.*, "The Superconducting Spectroscopic Array Receiver (SSAR): The Next-Generation Molecular Line Instrument," in *The 2nd Chinese-German Workshop on Star & Planet Formation*, Kiel, 2010.

[132] C. E. Groppi and J. H. Kawamura, "Coherent Detector Arrays for Terahertz Astrophysics Applications," *IEEE Transactions on Terahertz Science and Technology*, vol. 1, no. 1, pp. 85–96, Sep. 2011.

[133] A. D. Henke, S. Claude, and J. D. Francesco, "Concept Study of a Millimeter Camera for ALMA," NRC Herzberg Astronomy & Astrophysics, Victoria, Tech. Rep., 2015.

[134] P. F. Goldsmith, "Sub-Millimeter Heterodyne Focal-Plane Arrays for High-Resolution Astronomical Spectroscopy," *The Radio Science Bulletin*, vol. 2017, no. 362, pp. 53–73, Sep. 2017.

[135] C. Groppi, "Submillimeter Heterodyne Spectroscopy of Star Forming Regions," Ph.D. dissertation, University of Arizona, 2003.

[136] J. Leech, "A New 350 GHz Heterodyne Array Receiver (HARP) and Observations of Luminous Infrared Galaxies," Ph.D. dissertation, Cambridge, 2002.

[137] P. Grimes, *et al.*, "GUBBINS: A novel Millimeter-wave heterodyne interferometer," in *Proceedings of the Twentieth International Symposium on Space Terahertz Technology (ISSTT)*, no. 82-89, Charlottesville, Apr. 2009.

[138] C. F. McKee and E. C. Ostriker, "Theory of Star Formation," *Annual Review of Astronomy and Astrophysics*, vol. 45, no. 1, pp. 565–687, Sep. 2007.

[139] R. C. Kennicutt and N. J. Evans, "Star Formation in the Milky Way and Nearby Galaxies," *Annual Review of Astronomy and Astrophysics*, vol. 50, no. 1, pp. 531–608, Sep. 2012.

[140] P. Madau and M. Dickinson, "Cosmic Star-Formation History," *Annual Review of Astronomy and Astrophysics*, vol. 52, no. 1, pp. 415–486, Aug. 2014.

[141] J. Smith, *et al.*, "The Mid-Infrared Spectrum of Star-forming Galaxies: Global Properties of Polycyclic Aromatic Hydrocarbon Emission," *The Astrophysical Journal*, vol. 656, no. 2, pp. 770–791, Feb. 2007.

[142] G. Magdis, *et al.*, "Mid- to far-infrared properties of star-forming galaxies and active galactic nuclei," *Astronomy & Astrophysics*, vol. 558, p. A136, Oct. 2013.

[143] A. Tielens, "Interstellar Polycyclic Aromatic Hydrocarbon Molecules," *Annual Review of Astronomy and Astrophysics*, vol. 46, no. 1, pp. 289–337, Sep. 2008.

[144] D. J. Hollenbach and A. G. G. M. Tielens, "Dense Photodissociation Regions (PDRs)," *Annual Review of Astronomy and Astrophysics*, vol. 35, no. 1, pp. 179–215, Sep. 1997.

[145] ——, "Photodissociation regions in the interstellar medium of galaxies," *Reviews of Modern Physics*, vol. 71, no. 1, pp. 173–230, Jan. 1999.

[146] G. Bendo, *et al.*, "The relations among 8, 24 and 160 μm dust emission within nearby spiral galaxies," *Monthly Notices of the Royal Astronomical Society*, vol. 389, no. 2, pp. 629–650, Sep. 2008.

[147] F. Boulanger, *et al.*, "Small grains and IRAS colors," *The Astrophysical Journal*, vol. 332, p. 328, Sep. 1988.

[148] ——, "Variations in the abundance of transiently heated particles within nearby molecular clouds," *The Astrophysical Journal*, vol. 364, no. 1988, p. 136, Nov. 1990.

[149] G. Helou, C. Ryter, and B. T. Soifer, "Very small grains and the infrared colors of galaxies," *The Astrophysical Journal*, vol. 376, p. 505, Aug. 1991.

[150] J. Pety, *et al.*, "Are PAHs precursors of small hydrocarbons in photo-dissociation regions? The Horsehead case," *Astronomy & Astrophysics*, vol. 435, no. 3, pp. 885–899, Jun. 2005.

[151] J. Jensen, *et al.*, "PAH features within few hundred parsecs of active galactic nuclei," *Monthly Notices of the Royal Astronomical Society*, vol. 470, no. 3, pp. 3071–3094, Sep. 2017.

[152] H. Roussel, *et al.*, "Warm Molecular Hydrogen in the Spitzer SINGS Galaxy Sample," *The Astrophysical Journal*, vol. 669, no. 2, pp. 959–981, Nov. 2007.

[153] A. D. Bolatto, M. Wolfire, and A. K. Leroy, "The CO-to-H_2 Conversion Factor," *Annual Review of Astronomy and Astrophysics*, vol. 51, no. 1, pp. 207–268, Aug. 2013.

[154] C. Carilli and F. Walter, "Cool Gas in High-Redshift Galaxies," *Annual Review of Astronomy and Astrophysics*, vol. 51, no. 1, pp. 105–161, Aug. 2013.

[155] P. Solomon and P. Vanden Bout, "Molecular Gas at High Redshift," *Annual Review of Astronomy and Astrophysics*, vol. 43, no. 1, pp. 677–725, Sep. 2005.

[156] A. Kirkpatrick, *et al.*, "Early Science with the Large Millimeter Telescope: Exploring the Effect of AGN Activity on the Relationships Between Molecular Gas, Dust, and Star Formation," *The Astrophysical Journal*, vol. 796, no. 2, p. 135, Nov. 2014.

[157] A. Pope, *et al.*, "Probing the Interstellar Medium of z $\sim$ 1 Ultraluminous Infrared Galaxies Through Interferometric Observations of CO and Spitzer Mid-Infrared Spectroscopy," *The Astrophysical Journal*, vol. 772, no. 2, p. 92, Jul. 2013.

[158] D. Calzetti, *et al.*, "Star Formation in NGC 5194 (M51a): The Panchromatic View from GALEX to Spitzer," *The Astrophysical Journal*, vol. 633, no. 2, pp. 871–893, Nov. 2005.

[159] M. Schmidt, "The Rate of Star Formation." *The Astrophysical Journal*, vol. 129, p. 243, Mar. 1959.

[160] R. C. Kennicutt, "Star Formation in Galaxies Along the Hubble Sequence," *Annual Review of Astronomy and Astrophysics*, vol. 36, no. 1, pp. 189–231, Sep. 1998.

[161] R. Genzel, *et al.*, "A study of the gas-star formation relation over cosmic time," *Monthly Notices of the Royal Astronomical Society*, vol. 407, no. 4, pp. 2091–2108, Sep. 2010.

[162] E. Daddi, *et al.*, "Very High Gas Fractions and Extended Gas Reservoirs in z=1.5 Disk Galaxies," *The Astrophysical Journal*, vol. 713, no. 1, pp. 686–707, Apr. 2010.

[163] ——, "Different Star Formation Laws for Disks Versus Starbursts at Low and High Redshifts," *The Astrophysical Journal*, vol. 714, no. 1, pp. L118–L122, May 2010.

[164] L. Tacconi, *et al.*, "Submillimeter Galaxies at z $\sim$ 2: Evidence for Major Mergers and Constraints on Lifetimes, IMF, and CO-H_2 Conversion Factor," *The Astrophysical Journal*, vol. 680, no. 1, pp. 246–262, Jun. 2008.

[165] M. Regan, *et al.*, "The Radial Distribution of the Interstellar Medium in Disk Galaxies: Evidence for Secular Evolution," *The Astrophysical Journal*, vol. 652, no. 2, pp. 1112–1121, Dec. 2006.

[166] G. Bendo, *et al.*, "The JCMT Nearby Galaxies Legacy Survey - III. Comparisons of cold dust, polycyclic aromatic hydrocarbons, molecular gas and atomic gas in NGC 2403," *Monthly Notices of the Royal Astronomical Society*, vol. 402, no. 3, pp. 1409–1425, Mar. 2010.

[167] C. Lonsdale, *et al.*, "SWIRE: The SIRTF Wide-Area Infrared Extragalactic Survey," *Publications of the Astronomical Society of the Pacific*, vol. 115, no. 810, pp. 897–927, Aug. 2003.

[168] D. Fadda, *et al.*, "The Spitzer Space Telescope Extragalactic First Look Survey: 24 μm Data Reduction, Catalog, and Source Identification," *The Astronomical Journal*, vol. 131, no. 6, pp. 2859–2876, Jun. 2006.

[169] Y. Shi, *et al.*, "Extended Schmidt Law: Role of Existing Stars in Current Star Formation," *The Astrophysical Journal*, vol. 733, no. 2, p. 87, Jun. 2011.

[170] E. Murphy, *et al.*, "Calibrating Extinction-Free Star Formation Rate Diagnostics with 33 GHz Free-Free Emission in NGC 6946," *The Astrophysical Journal*, vol. 737, no. 2, p. 67, Aug. 2011.

[171] E. Daddi, *et al.*, "Multiwavelength Study of Massive Galaxies at z $\sim$2. I. Star Formation and Galaxy Growth," *The Astrophysical Journal*, vol. 670, no. 1, pp. 156–172, Nov. 2007.

[172] D. Elbaz, *et al.*, "GOODS- Herschel : an infrared main sequence for star-forming galaxies," *Astronomy & Astrophysics*, vol. 533, p. A119, Sep. 2011.

[173] C. Tremonti, *et al.*, "The Origin of the Mass-Metallicity Relation: Insights from 53,000 Star-forming Galaxies in the Sloan Digital Sky Survey," *The Astrophysical Journal*, vol. 613, no. 2, pp. 898–913, Oct. 2004.

[174] M. Pettini and B. E. J. Pagel, "[O III]/[N II] as an abundance indicator at high redshift," *Monthly Notices of the Royal Astronomical Society*, vol. 348, no. 3, pp. L59–L63, Mar. 2004.

[175] S. Veilleux and D. E. Osterbrock, "Spectral classification of emission-line galaxies," *The Astrophysical Journal Supplement Series*, vol. 63, p. 295, Feb. 1987.

[176] C. Kramer, "Calibration of spectral line data at the IRAM 30m radio telescope," Institut de radioastronomie millimétrique (IRAM), Tech. Rep., 1997.

[177] R. Kennicutt, *et al.*, "SINGS: The SIRTF Nearby Galaxies Survey," *Publications of the Astronomical Society of the Pacific*, vol. 115, no. 810, pp. 928–952, Aug. 2003.

[178] D. Dale, *et al.*, "Herschel Far-Infrared and Submillimeter Photometry for the KINGFISH Sample of Nearby Galaxies," *The Astrophysical Journal*, vol. 745, no. 1, p. 95, Jan. 2012.

[179] C. Wilson, *et al.*, "The JCMT Nearby Galaxies Legacy Survey - VIII. CO data and the LCO(3-2)-LFIR correlation in the SINGS sample," *Monthly Notices of the Royal Astronomical Society*, vol. 424, no. 4, pp. 3050–3080, Aug. 2012.

[180] M. Aravena, *et al.*, "Cold Molecular Gas in Massive, Star-Forming Disk Galaxies at z=1.5," *The Astrophysical Journal*, vol. 718, no. 1, pp. 177–183, Jul. 2010.

[181] D. Frayer, *et al.*, "Green Bank Telescope Spectrometer CO(1-0) Observations of the Strongly Lensed Submillimeter Galaxies from the Herschel Atlas," *The Astrophysical Journal*, vol. 726, no. 2, p. L22, Jan. 2011.

[182] B. Magnelli, *et al.*, "Dust temperature and CO - H_2 conversion factor variations in the SFR - M* plane," *Astronomy & Astrophysics*, vol. 548, p. A22, Dec. 2012.

[183] D. Frayer, *et al.*, "Molecular Gas in the z = 1.2 Ultraluminous Merger GOODS J123634.53+621241.3," *The Astrophysical Journal*, vol. 680, no. 1, pp. L21–L24, Jun. 2008.

[184] A. Pope, *et al.*, "Mid-Infrared Spectral Diagnosis of Submillimeter Galaxies," *The Astrophysical Journal*, vol. 675, no. 2, pp. 1171–1193, Mar. 2008.

[185] C. Casey, *et al.*, "Molecular gas in submillimetre-faint, star-forming ultraluminous galaxies at z > 1," *Monthly Notices of the Royal Astronomical Society*, vol. 415, no. 3, pp. 2723–2743, Aug. 2011.

[186] M. Bothwell, *et al.*, "A survey of molecular gas in luminous sub-millimetre galaxies," *Monthly Notices of the Royal Astronomical Society*, vol. 429, no. 4, pp. 3047–3067, Mar. 2013.

[187] R. Ivison, *et al.*, "Tracing the molecular gas in distant submillimetre galaxies via CO(1-0) imaging with the Expanded Very Large Array," *Monthly Notices of the Royal Astronomical Society*, vol. 412, no. 3, pp. 1913–1925, Apr. 2011.

[188] C. Carilli, *et al.*, "Imaging the Molecular Gas in a Submillimeter Galaxy at z=4.05: Cold Mode Accretion or a Major Merger?" *The Astrophysical Journal*, vol. 714, no. 2, pp. 1407–1417, May 2010.

[189] D. Riechers, *et al.*, "Polycyclic Aromatic Hydrocarbon and Mid-Infrared Continuum Emission in a z $>$ 4 Submillimetre Galaxy," *The Astrophysical Journal*, vol. 786, no. 1, p. 31, Apr. 2014.

[190] L. Armus, *et al.*, "Observations of Ultraluminous Infrared Galaxies with the Infrared Spectrograph on the Spitzer Space Telescope . II. The IRAS Bright Galaxy Sample," *The Astrophysical Journal*, vol. 656, no. 1, pp. 148–167, Feb. 2007.

[191] V. Desai, *et al.*, "PAH Emission from Ultraluminous Infrared Galaxies," *The Astrophysical Journal*, vol. 669, no. 2, pp. 810–820, Nov. 2007.

[192] M. Sargent, *et al.*, "Regularity Underlying Complexity: A Redshift-Independent Description of the Continuous Variation of the Galaxy-Scale Molecular Gas Properties in the Mass-Star Formation Rate Plane," *The Astrophysical Journal*, vol. 793, no. 1, p. 19, Aug. 2014.

[193] A. Leroy, *et al.*, "The Star Formation Efficiency in Nearby Galaxies: Measuring Where Gas Forms Stars Effectively," *The Astronomical Journal*, vol. 136, no. 6, pp. 2782–2845, Dec. 2008.

[194] ——, "HERACLES: The HERA CO Line Extragalactic Survey," *The Astronomical Journal*, vol. 137, no. 6, pp. 4670–4696, Jun. 2009.

[195] ——, "Molecular Gas and Star Formation in Nearby Disk Galaxies," *The Astronomical Journal*, vol. 146, no. 2, p. 19, Jun. 2013.

[196] A. Saintonge, *et al.*, "COLD GASS, an IRAM legacy survey of molecular gas in massive galaxies - II. The non-universality of the molecular gas depletion time-scale," *Monthly Notices of the Royal Astronomical Society*, vol. 415, no. 1, pp. 61–76, Jul. 2011.

[197] J. Garrett, *et al.*, "A 230 GHz finline SIS receiver with wide if bandwidth," in *Proceedings of the Twenty-Seventh International Symposium on Space Terahertz Technology (ISSTT)*, Cologne, Germany, Apr. 2017.

[198] J. W. Lamb, "Miscellaneous data on materials for millimetre and submillimetre optics," *International Journal of Infrared and Millimeter Waves*, vol. 17, no. 12, pp. 1997–2034, Dec. 1996.

[199] P. Ade, *et al.*, "Bicep2/ Keck Array . IV. Optical Characterization and Performance of the Bicep2 and Keck Array Experiments," *The Astrophysical Journal*, vol. 806, no. 2, p. 206, Jun. 2015.

[200] J. Carlstrom, *et al.*, "The 10 Meter South Pole Telescope," *Publications of the Astronomical Society of the Pacific*, vol. 123, no. 903, pp. 568–581, May 2011.

[201] A. Hector, *et al.*, "Investigating the Origin of Harmonics in a 230 GHz Local Oscillator," in *Proceedings of the Twenty-Sixth International Symposium on Space Terahertz Technology (ISSTT)*, Cambridge, MA, 2015.

[202] T. H. Lee, *The Design of CMOS Radio-Frequency Integrated Circuits*. Cambridge: Cambridge University Press, 1998.

[203] X. Qi, "High Frequency Characterization and Modeling of On-Chip Interconnects and RF IC Wire Bonds," Ph.D. dissertation, Stanford, 2001.

[204] D. M. Pozar, *Microwave engineering*, 4th ed. John Wiley & Sons, 2009.